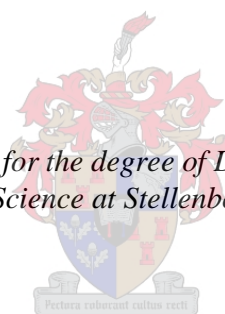# Investigating the formation of multicomponent crystals of antiplasmodial agents

by

Monica Jade Clements

Dissertation presented for the degree of Doctor of Philosophy in the
Faculty of Science at Stellenbosch University

Supervisor: Dr Margaret Blackie
Co-supervisor: Dr Tanya le Roex

April 2019

DECLARATION

By submitting this thesis electronically, I declare that the entirety of the work contained therein is my own, original work, that I am the sole author thereof (save to the extent explicitly otherwise stated), that reproduction and publication thereof by Stellenbosch University will not infringe any third party rights and that I have not previously in its entirety or in part submitted it for obtaining any qualification.

March 2019

ABSTRACT

The aim of this project was to explore the formation of multicomponent crystals of some known, as well as some novel, antiplasmodial agents and investigate and compare structures and properties of the antiplasmodials and the multicomponent crystals that they form.

A series of five known 4-aminoquinoline antiplasmodial agents were chosen and the formation of multicomponent crystals with these compounds was investigated. The use of molecular electrostatic potential surfaces (MEPS) to calculate molecular complementarity with a specific coformer allowed us to rank a list of coformers according to the probability of forming multicomponent crystals with each 4-aminoquinoline. A total of nineteen multicomponent forms were obtained by liquid-assisted grinding, and these were characterised by PXRD, IR, TGA and DSC. Possible reasons are given for why two of the five 4-aminoquinolines yielded only amorphous multicomponent products, while three yielded crystalline products. Additionally, a brief discussion is given for the reasonably low success rate (38%) of the MEPS method for coformer selection.

Attempts were then made to synthesise a series of novel aminoferrocene-containing lapatinib analogues so that the abovementioned knowledge could be applied to a novel system. While, we successfully achieved the synthesis of the precursor fragments, the key reaction that coupled the aminoferrocene fragment to the lapatinib core – the Suzuki-Miyaura reaction – proved more challenging than expected. After substantial effort, the desired product was obtained (as detected by LC-MS), however it could not be isolated, most likely due to low yields. The use of an amine or amide linker (instead of a direct carbon-carbon bond) was also investigated, however these attempts were also unsuccessful.

A series of 6-substituted quinazolin-4($3H$)-ones, formed serendipitously during the synthesis of the lapatinib analogues, were also studied for their ability to form multicomponent crystals. The MEPS method to select coformers was applied and liquid-assisted grinding was used to form eight novel multicomponent crystals. Interestingly, only one of the quinazolinone derivatives formed multicomponent crystals with the chosen coformers, while the remaining three yielded only mixtures of starting materials. Possible explanations for this were explored and it is clear that there are additional factors that play a larger role than initially thought.

This study shows that quinoline- and quinazolinone-based antiplasmodial agents warrant further attention for the formation of multicomponent crystals. The work described in this thesis provides a greater understanding of the ability of these molecules to form multicomponent crystals. Together with similar studies, this knowledge could be applied to related systems, which would one day allow for accurate predictions and the formation of multicomponent crystals of antiplasmodial agents with tailored properties.

Uittreksel

Die doel van hierdie projek was om die vorming van multikomponent kristalle van sommige bekende sowel as sommige nuwe, antiplasmodiese middels te ondersoek en om die strukure en eienskappe van die antiplasmodiese en die multikomponentkristalle wat hulle vorm, te odersoek en vergelyk.

'n Reeks van vyf bekende 4-aminokwinolien-antiplasmodiese middels is gekies en die vorming van multikomponent kristalle met hierdie verbindings is ondersoek. Die gebruik van molekulêre elektrostatiese potensiaal oppervlaktes (MEPS) om molekulêre komplementariteit met 'n spesifieke kovormer te bereken, het ons toegelaat om 'n lys van kovormers te rangskik volgens hul waarskynlikheid om multikomponent kristalle met elke 4-aminokwinolien te vorm. In totaal in negentien multikomponent vorms verkry deur middel van vloiestof-vergemaklikde meganiese chemie, en is beskryf deur PXRD, IR, TGA en DSC. Moontlike redes word gegee waarom twee van die vyf 4-aminokwinolien molekules slegs amorfiese multikomponent produkte opgelewer het, terwyl drie kristallyne produkte opgelewer het. Daarbenewens word 'n kort bespreking gegee oor die redelike lae suksessyfer (38%) van die MEPS-metode vir die keuse van kovormers.

Pogings is dan aangewend om 'n reeks nuwe aminoferroseen-bevattende lapatinib-analoë te sintetiseer sodat die bogenoemde kennis op 'n nuwe stelsel toegepas kan word. Ons het die sintese van die voorloperfragmente suksesvol voltooi, maar die sleutelreaksie wat die aminoferoseenfragment aan die lapatinib-kern koppel – die Suzuki-Miyaura-reaksie – was meer uitdagend as verwag. Na aansienlike moeite is die verlangde produk verkry (soos aangetoon deur LC-MS), maar dit kon nie geïsoleer word nie, waarskynlik as gevolg van lae opbrengste. Die gebruik van 'n amien- of amiedskakelaar (in plaas van 'n direkte koolstof-koolstofbinding) is ook ondersoek, maar hierdie pogings was ook onsuksesvol.

'n Reeks 6-gesubstitueerde kwinazolinoon wat gevorm is tydens die sintese van die lapatinib analoge, is ook bestudeer vir hul vermoë om multikomponent kristalle te vorm. Die MEPS-metode om koformers te kies is toegepas en vloiestof-vergemaklikde meganies chemie is gebruik om agt nuwe multikomponent kristalle te vorm. Slegs een van die kwinazolinoon analoge multikomponent kristalle gevorm met die gekose koformers, terwyl die oorblywende drie slegs mengsels van die uitgangsmateriaal opgelewer het. Moontlike verduidelikings hiervoor is ondersoek en dit is duidelik data daar addisionele faktore is wat 'n groter rol speel as aanvanklik gedink.

Hierdie studie toon dat kwinolien- en kwinazolinoon-gebaseerde antiplasmodiese middels verdere aandag verdien rakende die vorming van multikomponent kristalle. Die werk wat in hierdie tesis beskryf word, bied 'n groter begrip oor die vermoë van hierdie molekules om multikomponent kristalle te vorm. Saam met soortgelyke studies kan hierdie kennis toegepas word op verwante stelsels, wat eendag kan toelaat vir akkurate voorspellings en die vorming van multikomponent kristalle met antiplasmodiese middels.

ACKNOWLEDGEMENTS

Writing the acknowledgements section of a thesis is a daunting task. The sudden realisation that you just about ready to submit your thesis, as well as realising how many people have contributed to you getting to where you are today, is incredible. I consider myself extremely blessed to have met and worked with such amazing people.

First and foremost I would like to express my gratitude to my two supervisors – Dr Margaret Blackie and Dr Tanya le Roex. Thank you not only for your support and guidance during this project but also for allowing me to grow and develop outside the laboratory. You have equipped me with the necessary skills to become an independent scientist and to succeed in my career and for that I am immensely grateful.

Thank you to the supramolecular and organic chemistry groups for cherished discussions, lunches and good times over the past few years. I would like to especially thank Jonathan and Anton for their friendship and valuable discussions over a beer when things weren't going to plan in the laboratory. I would also like to thank Leigh for her wealth of knowledge on so many different things. Last but not least, I would like to thank Jeanie for providing motivation to work when I was procrastinating, and for many useful discussions on results and new ideas. A word of gratitude is also extended to Raymond, Mary, Debbie and the rest of the support and technical staff of the de Beers building. Without you, we would not function nearly half as well.

I also wish to thank Prof Pollastri and his team at Northeastern University in Boston, USA for allowing me to spend time in their laboratory. It was an incredible experience and it opened my eyes to a whole new world of R&D! I will forever cherish the memories made during that time.

To my parents, I know you don't always know exactly what it is I actually do, but I thank you for your unconditional love and support. I'm sure you will be happy to know that I will be finding a "real job" now! To my sister, Tanya, thank you for the chats (and sometimes rants), especially over the past year, and for spending time proof-reading this thesis.

To my boyfriend, and best friend, Francois, I cannot even begin to express my gratitude. I'm sure that these last few months have been especially challenging and I thank you for all the support and love you gave me when I needed it the most. I couldn't ask for a better person to enter the next chapter of my life with.

Lastly, I would like to thank the National Research Foundation (NRF) for their financial support in the form of a scholarship as well as providing me with additional funding to spend time in Prof Pollastri's laboratory in Boston in 2017. Thank you to Stellenbosch University for funding and for providing excellent facilities in which to carry out my research.

CONFERENCE ATTENDANCE

Indaba 9: Modelling of Structures and Properties

September 2018. Skukuza, Kruger National Park, South Africa.

Poster and flash oral presentation: *Forming multicomponent crystals with quinazolinones*

International Conference on the Organic Solid State (ICCOSS)

April 2017, Stellenbosch, South Africa

Poster presentation: *Structures and properties of aminoquinoline salts*

H3D Symposium – International Conference on Medicinal Chemistry

November 2016, Goudini Spa, South Africa.

Poster presentation: *Synthesis of novel Lapatinib-derived analogues as potential antiplasmodial agents*

"Two roads diverged in a wood, and I – I took the one less travelled by, and that has made all the difference." – Robert Frost, The Road Not Taken.

TABLE OF CONTENTS

ABBREVIATIONS

ADME	Adsorption, distribution, metabolism, excretion
CIF	Crystallographic Information File
CSD	Cambridge Structural Database
DCM	Dichloromethane
DMF	N,N-Dimethyl formamide
DMSO	Dimethyl sulphoxide
DSC	Differential scanning calorimetry
EAFUS	Everything Added to food in the United States
EtOAc	Ethyl acetate
FDA	Food and Drug Administration
FTIR	Fourier-transform infrared
GRAS	Generally regarded as safe
HRMS	High resolution mass spectrometry
IPA	Isopropyl alcohol
IUPAC	International Union of Pure and Applied Chemistry
LAG	Liquid-assisted grinding
LC-MS	Liquid chromatography mass spectrometry
MCC(s)	Multicomponent crystal(s)
MEPS	Molecular electrostatic potential surface
MeCN	Acetonitrile
MeOH	Methanol
m/z	Mass to charge ratio
NMR	Nuclear magnetic resonance
PXRD	Powder X-ray diffraction
R_f	Ratio of movement of solute to solvent on TLC
SAR	Structure-activity relationship
SCXRD	Single crystal X-ray diffraction
TGA	Thermogravimetric analysis
THF	Tetrahydrofuran
TLC	Thin layer chromatography
WHO	World Health Organisation

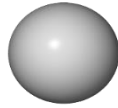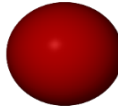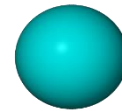# ATOM COLOURS

Carbon

Hydrogen

Oxygen

Nitrogen

Chlorine
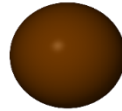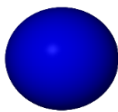
Iodine

Iron

CHAPTER 1
Introduction

1.1 MALARIA

Malaria is a mosquito-borne infectious disease that has been prevalent for millenia.[1] Predominately found in tropical climates and especially third world countries, malaria is a burden to 97 countries and over 3.2 billion people are at risk worldwide.[2] Although the number of cases of malaria has decreased globally (216 million in 2016 in comparison to 237 million in 2010), the rate of decline has plateaued and even reversed in some areas since 2014.[3] Even with current treatment options, over 1200 deaths of children under five years old are reported every day, making up a vast majority of the total annual death toll in Africa.[4] Therefore, the African continent, and more specifically sub-Saharan Africa, continues to account for the majority of malaria cases and deaths worldwide.[3]

Numerous organisations, such as the Medicines for Malaria Venture, the Bill and Melinda Gates Foundation and the Roll Back Malaria Partnership, the United Nations and World Health Organisation, have developed an updated global strategy for malaria that focuses on reducing global malaria incidents by 90% by 2030.[2] The impact that this will have on the global poverty rate as well as standard of living worldwide, is undeniable. In many of the poorer countries (especially in Africa), direct costs such as medication and health care, drain a country's economic growth. In addition, sectors such as tourism, foreign investment and trade have also been negatively affected, which in turn influences the economic status of a country.[5] Currently, increased financial support is being provided by a number of organisations not only for the distribution of preventative measures (such as bed nets) but also for research into new initiatives to combat the disease. Furthermore, increased education in rural areas to promote the correct use of medications and preventative measures is being carried out, however this is no simple task.[6] Researchers have also been studying multiple aspects of the malaria parasite, including its life cycle and potential drug targets, as a way to one day be able to eradicate this disease.

Malaria is caused by members of the *Plasmodium* genus and are commonly transmitted to a human host by approximately 40 species of the female *Anopheles* mosquito.[7] There are five species of the *Plasmodium* parasite that are known to infect humans – *P. falciparum*, *P. vivax*, *P. ovale*, *P. malariae* and *P. knowlesi*. Of these five *Plasmodium* species, *P. falciparum* is most prevalent and deadly, with roughly 90% of worldwide infections occurring in sub-Saharan Africa.[7] The manifestation of the disease within the human host is dependent on the species of *Plasmodium* as well as the life cycle of the parasite, amongst other reasons.

1.2 THE LIFE CYCLE OF THE MALARIA PARASITE

The malaria parasite is spread through the infection of two hosts – mosquitoes and humans (Figure 1.1).[8] The life cycle of the parasite can be divided into three stages: one sexual stage (in the mosquito) and two asexual stages that occur in the human host (one in liver cells and one in red blood cells). When the female *Anopheles* mosquito feeds on human blood, she injects sporozoites into the human host's blood stream that are rapidly taken up by the liver cells. These then further develop within the liver to form merozoites. In two of the five *Plasmodium* species, namely *P. ovale* and *P. vivax*, a portion of these parasites stay dormant in the liver for months or even years that could lead to a relapse in malaria symptoms even after treatment. Once the liver cells lyse, the merozoites enter the bloodstream and red blood cells. At this stage, the parasites replicate asexually and can consume the contents of the erythrocytes (red blood cells).[9] The red blood cells eventually lyse, releasing the merozoites back into the blood stream. This asexual cycle repeats every 48 hours and gives rise to the clinical symptoms associated with malaria, such as periodic fever and chills. After several asexual cycles, some of the merozoites further develop into gametocytes within the human's blood stream. When a mosquito takes another blood meal, these gametocytes enter the mosquitoes blood stream, where they undergo fusion to develop zygotes. These zygotes further develop to form sporozoites, which begins the cycle afresh.[1,7] Understanding the life cycle of the parasite is critical to developing new antiplasmodial agents as it allows researchers to target specific stages of the life cycle and therefore treat the patient at various stages of infection.
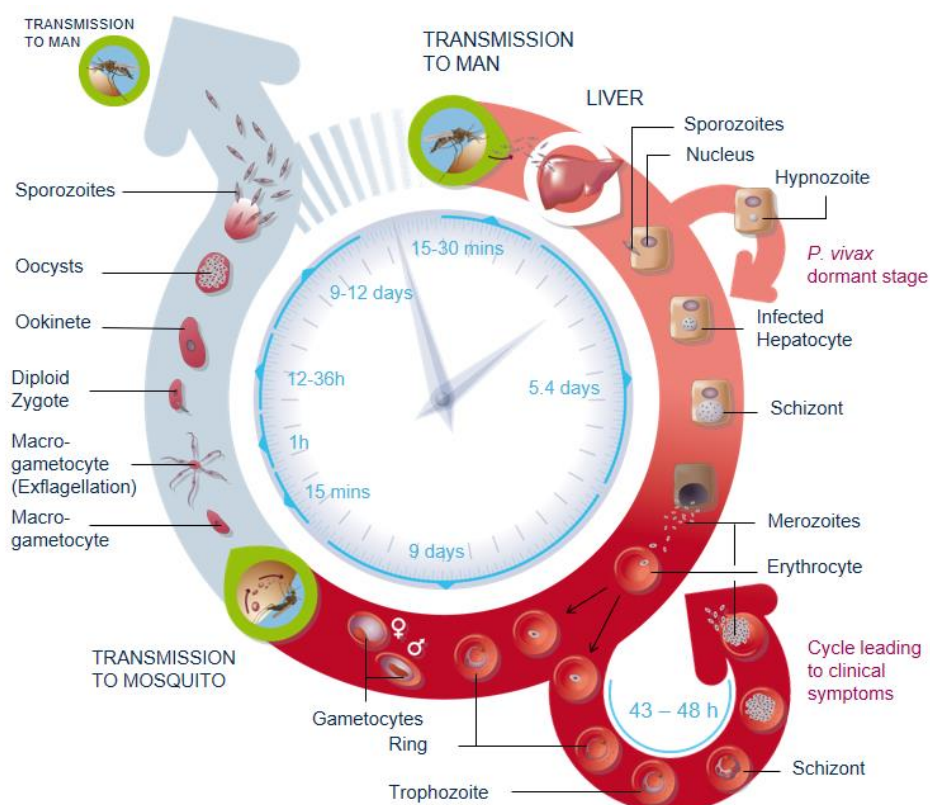

Figure 1.1: Life cycle of the *Plasmodium* parasite. Taken from Medicines for Malaria Venture online resources.[8]

1.3 MODES OF ACTION OF ANTIMALARIAL DRUGS

Antimalarial agents can be classified into three broad categories based on their mode of action – the antifolates (that target dihydrofolate reductase, DHFR), the endoperoxides (formation of radical species) and the quinolines (β-hematin inhibitors).[10]

1.3.1 The antifolates

Humans are incapable of synthesising folate derivatives and therefore require dietary sources in the form of essential nutrients. However, protozoa, such as *Plasmodium*, make use of pteridine, *p*-aminobenzoic acid and mono-L-glutamate as precursors in the biosynthesis of folate derivatives, rather than dietary sources. This pathway is therefore an attractive target for antiplasmodial drug development. Therefore, the antifolate class of antimalarial drugs target one of two folate pathways in the malaria parasite – either folate salvage (inhibition of dihydrofolate reductase) or *de novo* folate synthesis (inhibition of dihydropteroate synthase, DHPS). It is however, important to note that these two classes are synergistic and are therefore often used in combination to treat malaria.[11]

Both DHFR and DHPS catalyse the synthesis of tetrahydrofolate – a co-factor in the synthesis of pyrimidines, which are responsible for deoxyribonucleic acid (DNA) synthesis.[12,13] In the case of the DHFR class, it is thought that the drug molecule (such as pyrimethamine or proguanil, Figure 1.2a and 1.2b) competes with dihydrofolate by mimicking its pteridine structure. The "sulfa drugs" (such as sulphadoxine, Figure 1.2c) that target the inhibition of DHPS act by mimicking *p*-aminobenzoic acid that targets the active site of DHPS. In this way, folate formation is inhibited, thereby depriving the parasite of essential folate co-factors required for growth and proliferation.[14]
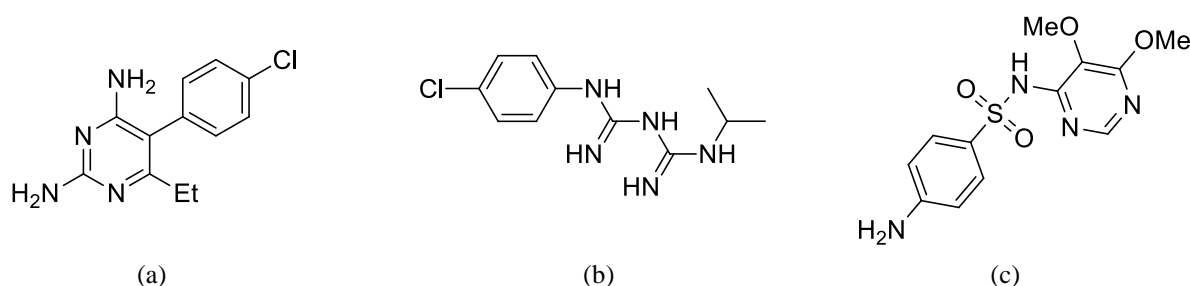
Figure 1.2: Structure of (a) pyrimethamine, (b) proguanil and (c) sulphadoxine.

One of the major drawbacks of the antifolate class of antimalarial agents is that resistance to these compounds is widespread. In addition, these compounds often have negative side effects, low bioavailability and high toxicity. For these reasons, they are currently only used in combination with other classes of antimalarial agents as alternative treatment options.[15,16]

1.3.2 The endoperoxides

Today the endoperoxide class of antimalarial agents, and more specifically artemisinin and its semi-synthetic derivatives (Figure 1.3), are the World Health Organisation's recommended choice in the treatment of malaria caused by *P. falciparum*, including multi-drug resistant infections.[17] This class of drugs target different membrane structures within infected cells, such as the digestive vacuole membrane, the plasma membrane and the nuclear envelope.[18]
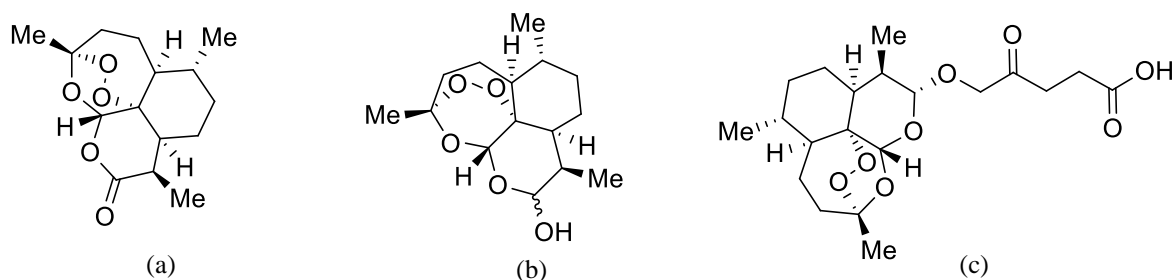

Figure 1.3: Structure of (a) artemisinin, (b) dihydroartemisinin and (c) artesunate.

While this class is considered to be the most effective for malaria treatment, the exact mode of action is still under debate.[19] It is hypothesised that the free heme or iron within infected cells interacts with the endoperoxide bridge of the drug molecule and in doing so, releases free radicals that disrupt parasitic cell membranes.[20,21] An alternative suggestion is that these free radical species interact with free heme to form a more lethal form of heme thereby causing parasite death.[22] It is this mode of action that results in a drug that is efficient, fast-acting and has few side effects.[23] Unfortunately, some countries have reported that strains of *P. falciparum* are showing signs of resistance to these drugs too.[24,25]

1.3.3 β-hematin inhibitors

Once the sporozoites enter the red blood cell, they feed on host hemoglobin, where it is broken down in the digestive vacuole of the parasite to provide the amino acids that are necessary for growth.[26] It is at this stage that the iron centre of hemoglobin is oxidised, whereupon free heme is released. This heme (ferriprotoporphyrin IX) is toxic to the parasite and is therefore crystallised into a non-toxic form (called hemozoin) by the parasite. Hemozoin has a distinctive brown pigmentation that is characteristic of malaria-infected red blood cells and is the tell-tale sign of infection.[27]

The quinoline-based antimalarial agents, such as quinine and chloroquine, target this conversion of free heme to hemozoin. It is well-known that the quinoline moiety is essential for the efficacy of this class of compounds.[27–29] It is postulated that because of the weak basicity of the nitrogen atom in the quinoline ring, the drug enters the acidic food vacuole of the parasite, where it is protonated and subsequently cannot be removed by efflux pumps out of the vacuole. This method, known as pH-trapping, allows a high concentration of the drug molecule to accumulate within the vacuole, where it can then inhibit the

formation of hemozoin (or the synthetic derivative, β-hematin). The amino side chains of many antimalarial agents also aid in this pH trapping mechanism.[30] It is also suggested that the quinoline drug, once inside the digestive vacuole, adsorbs onto the hemozoin crystal surface, which hinders further crystal growth, thereby killing the parasite through a build-up of toxic heme in the digestive vacuole.[27,31,32] However, there are still gaps in the understanding of the exact mechanism of action of how these antimalarial compounds interfere with the crystallisation process within the parasite and is therefore still currently being explored.[31–34]

While still being studied, the current β-hematin class of antiplasmodials are widely inactive in most parts of Sub-Saharan Africa for the treatment of malaria caused by *P. falciparum* as the parasite has developed resistance them, especially chloroquine (Figure 1.4b).[35] A mutant protein called *Plasmodium falciparum* chloroquine resistance transporter (PfCRT) increases the efflux of chloroquine across the digestive vacuole and as a result leads to a diminished accumulation of the drug to inhibit the formation of hemozoin.[36,37] Having said this, new compounds are currently being developed that can overcome this resistance.[38,39]

1.4 CURRENT ANTIPLASMODIAL AGENTS

Over the last century, many natural and synthetic compounds have been used to treat malaria. The first antimalarial agent on the market was quinine (Figure 1.4a) – a quinoline-based drug that was isolated from the bark of the *cinchona* tree and initially used to treat fever from as early as the 1600s.[40] Perhaps one of the most well-known and most effective antimalarial agents to date is chloroquine (Figure 1.4b), which was developed by Bayer Pharmaceuticals in 1934.[41] During World War II, chloroquine (under the brand name *Resochin*) was primarily used as a prophylaxis and treatment option for malarial infections caused by *P. falciparum.* Over twenty generic brands of chloroquine are currently on the market and the World Health Organisation still recommends that chloroquine remain on the List of Essential Medicines. These days, however, it is mainly used for the prevention and treatment of malaria caused by *P. vivax*, *P. ovale* and *P. malariae* due to the widespread resistance to *P. falciparum*.[17]

Various antiplasmodial and antimalarial drugs have thus been developed to compensate for the widespread resistance. It is at this point that it is important to note that there is a distinction between *antimalarial* and *antiplasmodial* drugs. Antimalarial refers to a marketed drug that treats or prevents malarial infections, such as the quinoline-based agents described above and artemisinin combination therapies, while antiplasmodial describes a broad class of compounds that are efficacious against the *Plasmodium* parasite.

Over the last decade, a flurry of research into quinoline-based agents was carried out in an attempt to overcome this resistance.[28,39,42,43] Quinoline-methanols, 4-aminoquinolines and acridines, which are all

potent against *P. falciparum*, were developed as a result. Most notable is amodiaquine (Figure 1.4c) and mefloquine (Figure 1.4d), which are currently available in some combination therapies.
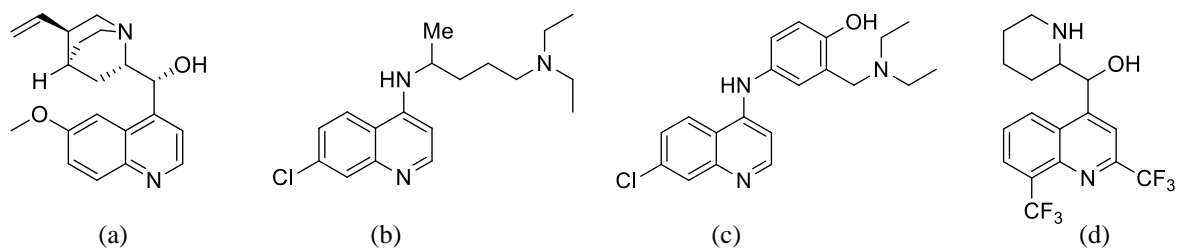

Figure 1.4: Structure of (a) quinine, (b) chloroquine, (c) amodiaquine and (d) mefloquine.

Aminoquinolines have been successful because they generally have low toxicity and reasonable efficacy values. They are also relatively simple and cheap to synthesise and so the cost per treatment is affordable.[44] Even though resistance is becoming more prevalent with this class, they remain a target for novel antiplasmodial therapies.[10,18,45] There are currently thirteen compounds in clinical trials, with a number of compounds in pre-clinical stages that look promising.[46] These include Tafenoquine (an 8-aminoquinoline), AQ-13 (a simple derivative of chloroquine), and MMV30048 (a 2-aminopyridine). Most promising, however, is artefenomel-ferroquine and lumafantrine-KAF156, both of which are currently in phase 2b clinical trials.[46]

Due to the rapid development of resistance of *Plasmodium* to quinoline-based agents, the World Health Organisation recommends the use of artemisinin combination therapies (ACTs) to treat patients.[17] By combining the fast-acting and highly efficacious artemisinin-type compounds with slower-acting quinoline-type compounds, a three-day dosage can be administered that will improve the cure rate and also lower resistance development.[47] Currently, the most used combinations include artemether-lumafantrine (Coartem®), dihydroartemisinin-piperaquine (DuoCotecxin®) and artesunate-amodiaquine (Camoquin®).[25]

In July 2015, the world's first malaria vaccine (Mosquirix™) was approved by the European Medicines Agency, following 30 years of development by GlaxoSmithKline.[48] However, the vaccine is to be cautiously recommended, according to the World Health Organisation advisory committee.[49] They report that in trials of over 15 000 children, a series of four shots only reduced the number of malaria cases by 36% in young children. The vaccine has, however, still been recommended for pilot programmes in Africa where it will be assessed as a complementary tool that could be added to the current arsenal of preventative and treatment measures.[50] In May 2018, the African Vaccine Regulatory Forum in conjunction with Ghanaian, Kenyan and Malawian regulatory authorities authorised the vaccine for pilot immunisation programmes for young children. This programme is set to begin in 2019 in these three countries.[51]

While the vaccine may not be as effective as initially anticipated, the hope is that a more potent vaccine will be developed in time. Until then, we rely on treatment options such as the ACTs described above. But with the development of resistance to even these treatments,[25] the need for new antimalarial drugs becomes ever more apparent.

1.4.1 Synthesising novel compounds

By studying structure-activity relationships, we can gain knowledge on the types and positions of moieties on scaffolds that could either improve or diminish various properties of the compound such as efficacy, solubility and toxicity. By understanding these relationships, specific fragments can be combined in an attempt to synthesise molecules with desirable properties. In fact, the majority of compounds available on the market today are available as a result of extensive structure-activity relationship studies on previously reported candidates. Compounds such as AQ-13, primaquine and amodiaquine (Figure 1.5) all stem from chemical modifications of quinine.[10]
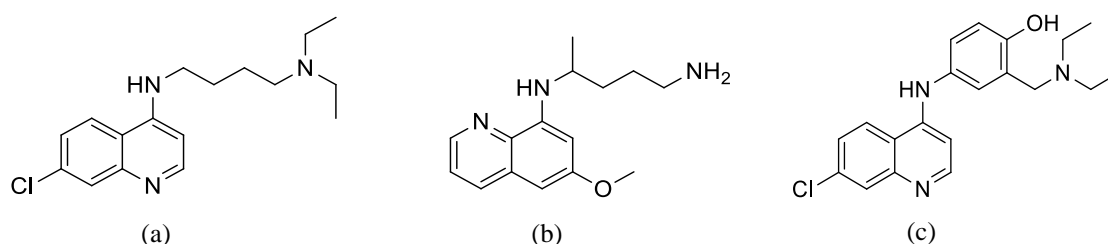
Figure 1.5: Structure of (a) AQ-13, (b) primaquine and (c) amodiaquine.

By far the most widely studied antiplasmodial structure-activity relationships are with the quinoline (β-hematin inhibitor) class.[45] This is most likely because these compounds are simpler and cheaper to synthesise, usually have low toxicity and have a known target (inhibition of β-hematin).[52] The 4-aminoquinoline class (Figure 1.6) has been extensively studied. It was found that the 7-position is optimal for substituents, and halogens (especially chlorine) at this position outperform other functional groups when comparing efficacies.[30] It was also determined that the secondary amine at the 4-position is important. Replacing this group with a tertiary amine, or other linkers, has a detrimental effect on the efficacy of the drug.[53] The amino side chain has been shown to assist in the mode of action of the drug, but changes in the linker between this amino group and the 4-aminoquinoline scaffold are more tolerable. Linkers such as phenyl rings,[54] branched and unbranched alkyl chains,[55,56] 5-membered heterocycles such as oxazoles[57] or triazoles[58] and even metallocenes[59,60] have all be investigated and some are showing promising results.

Figure 1.6: The 4-aminoquinoline class of antiplasmodial agents.

Ferroquine, an antiplasmodial agent currently in clinical trials, was also developed as a result of extensive structure-activity relationship studies and continuation with further studies has shown 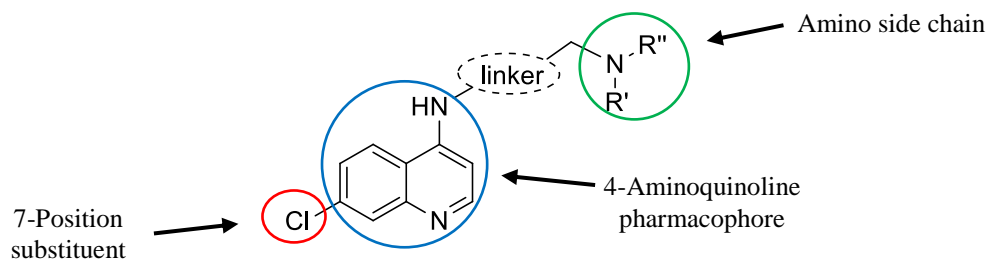a mix of results. Jacobs *et al.* synthesised a series of ferroquine analogues with varying alkyl chain lengths as well as oxalamide linkers between the 4-aminoquinoline and ferrocene moieties.[61] Some compounds displayed efficacies superior to that of chloroquine, the standard used for testing. Amino alcohol side chains[62] have also been studied, as well as the use of other metallocenes such as ruthenocene.[60] In addition, for these aminoquinoline-type compounds, the location of the ferrocene moiety is important. Work by Biot *et al.* indicates that the ferrocene moiety should be flanked by the aminoquinoline and an alkyl amino side chain.[63]

A more recently investigated route is the use of molecular hybridisation. This involves the design of compounds by combining two or more different pharmacophores into one molecule using covalent linkers.[10,64] This approach is thought to improve efficacy and reduce the onset of resistance because two modes of action are targeted simultaneously. In some cases, such as the artemisinin-quinine hybrid shown in Figure 1.7, the efficacy of the new compound is far superior to that of the individual pharmacophores, as well as a 1:1 physical mixture of artemisinin and quinine.[65] It should be noted that hybridisation is different to the combination therapies described in the previous section. In the latter, the drug compounds are merely combined as a physical mixture into a specific formulation, while for hybridisation, a new molecule is synthesised through covalent linkage of two compounds (or parts of compounds).
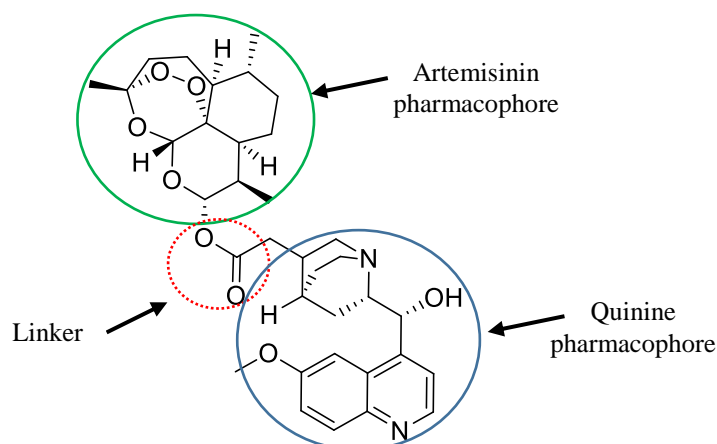

Figure 1.7: Hybrid compound formed by linking quinine and artemisinin pharmacophores with an ester linkage.

Structure-activity relationships and the synthetic derivatives produced from these studies are imperative in the search for antiplasmodial agents that can overcome the current resistance issues, whilst maintaining efficacy. However, these studies can be time-consuming, costly and less than one percent of the compounds synthesised in these studies, and deemed as possible clinical candidaates, make it onto the market.

It is clear that a delicate balance of functional groups and their positions on the molecule is required to achieve optimal efficacy and physicochemical properties and that, while scientists are gaining knowledge in this field, we are far from being able to apply a standard recipe for novel clinical candidates from a pantry of pharmacophores and functional groups.

1.5 PROBLEMS ASSOCIATED WITH ANTIMALARIAL DRUG DEVELOPMENT

Despite substantial progress made toward fundamental knowledge used during the drug discovery and development pipeline, tropical infectious diseases (such as malaria) continue to plague the developing world. Socio-economic issues have also played a role in the lack of progress in eliminating the disease. Malaria is prevalent in underdeveloped and poorer regions where education lacks. In many cases, patients have little to no access to hospital environments or clinics. As a result, drug candidates need to be well tolerated in humans, have very few side effects and ideally be offered as a single dose in tablet form.[46,66,67]

The development of drug candidates to treat malaria was initially driven by the Western world during the first part of the 20th century, but as their interests drifted away from these regions, so did the development of novel treatment strategies.[68] Given how long the drug discovery process takes, as well as the financial input required, it is not surprising that the pharmaceutical industry is hesitant to engage in these research endeavours simply because it is not profitable for them.[69] Having said that, new partnerships with the private sector (in particular the Bill and Melinda Gates Foundation) and academia have seen an increase in research aimed towards malaria and other neglected tropical diseases. Open Source Malaria Project, led by Matthew Todd of the University of Sydney, is an online platform for antimalarial drug discovery based on contributions from a number of researchers. This project, in collaboration with Medicines for Malaria Venture and other funding agencies, is an open access project that focuses on phenotypic hit-to-lead phase drug discovery and is making significant contributions to the fight against malaria.[70,71] There are, however, other issues that plague the advancement of drug candidates to the marketplace.[68] Some of these are discussed below, along with some of the current methods to at least partially overcome these challenges.

1.5.1 The lengthy drug discovery and development timeline

For a drug candidate to reach the market, numerous testing phases need to be passed. The early drug discovery pipeline (Figure 1.8) includes initial *in vitro* testing against the parasite to determine efficacies. Compounds that display superior efficacies (usually comparable to those currently on the market) are chosen for further evaluation and development, which includes additional *in vitro* and *in vivo* testing to determine its pharmacokinetic profile. Once the compound passes these tests, it moves from being a "hit" compound to a "lead" compound. At this point, a lead optimisation phase and preclinical trials take place that determine safety and toxicity. A further three phases of clinical trials that evaluate the drug candidate in humans must be carried out before the drug can be approved for the market. In the majority of cases, compounds do not pass the pre-clinical trial phase and are discarded due to a variety of reasons including low efficacy, poor solubility and bioavailability, high toxicity or negative side effects.[72]
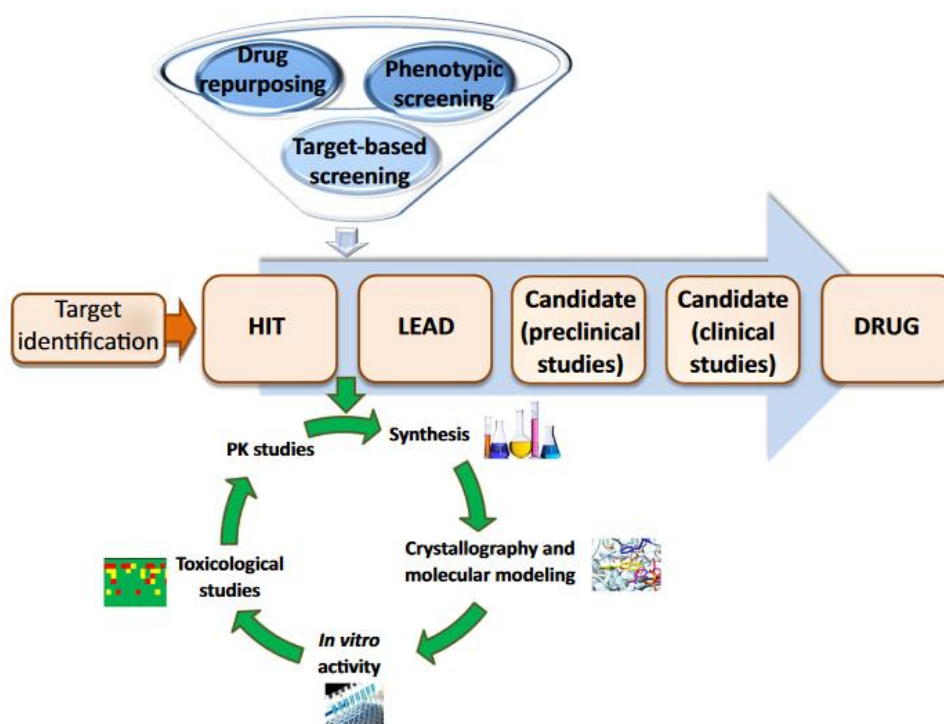
Figure 1.8: Illustration of the drug discovery and development process. Taken from Pierce *et al.*[73]

Because the majority of the discovery and development process for malaria drug candidates is performed in academic environments (without the financial and technical resources of large pharmaceutical companies), some researchers have turned to "drug repurposing" to overcome some of these hurdles.[74–76] Klug *et al.* propose four main categories that fall under repurposing – drug repurposing, target repurposing, target class repurposing and lead repurposing.[77] A brief description of each category, as well as the associated advantages and disadvantages, are described below.

Drug repurposing is characterised by the lack of additional optimisation needed for the repurposed chemical entity. As a result, Food and Drug Administration (FDA) approved compounds initially intended for a certain purpose are used for a second indication without structural modification. One of the advantages is that because it has already gone through safety testing and pharmacokinetic profiling, the cost and development time to the drug is considerably reduced. It should be noted, though, that dosing and formulation studies still need to be carried out, as well as modified clinical trials for the new purpose.

Target repurposing involves a compound that is approved (or a clinical candidate) for one use, but is then used as a starting point to develop compounds that target the parasite. This differs from drug repurposing as the initial compound is often modified synthetically to optimise the selectivity and efficacy against the target parasite.

Target class repurposing differentiates from target repurposing in the sense that the target (and therefore the mode of action) of the compound is not known. Instead, a phenotypic assay (often parasite cell death) is used to determine efficacy. While this approach has the disadvantage of hindering the 'rational design' optimisation process, it does provide a more robust approach to discovering novel modes of action and finding targets that are distinctive to that parasite.

Lead repurposing focuses on early-stage drug candidates, rather than approved or clinical candidates. The process begins with a high-throughput screen of a class of lead molecules (for example, kinase inhibitors) that are screened for a specific target parasite, often making use of phenotypic assays to assess the efficacy of the compounds. The advantage of this strategy is that it is more likely to give a variety of chemotypes that can be further pursued and is more unbiased in comparison to the other three repurposing strategies.

To date, there are no compounds that have been approved as a repurposed drug for the treatment of malaria; however, there are some candidates that have potential.[75] One such compound is lapatinib – an anticancer drug that was identified as a potent antiplasmodial agent (Figure 1.9).[78] Currently the Pollastri laboratory (Northeastern University), amongst others, are investigating derivatives of lapatinib for neglected tropical diseases, including malaria.[79]
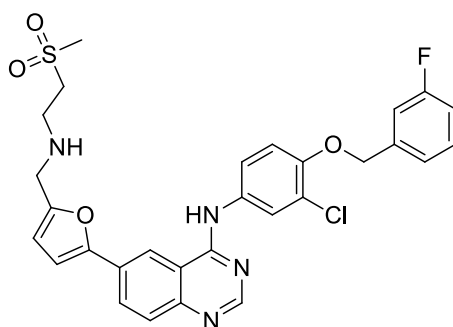

Figure 1.9: Structure of lapatinib.

This approach has the advantage of reduced financial costs associated with drug discovery, as well as a decrease in time from bench to clinic for these compounds.[80] Therefore, this approach is attractive for finding alternative compounds to combat malaria. Given the widespread use of antimalarial agents for the treatment or prevention of infections in children, repurposing becomes challenging, as stringent safety requirements are needed. Another challenge contributing to this includes ineffective therapeutic concentrations due to poor bioavailability.[81]

1.5.2 Poor physicochemical properties

The second, and arguably the largest problem associated with the development of drug candidates is the achievement of appropriate physicochemical properties. It is well-known that less than one percent of potential drug candidates make it onto the market.[82,83] While poor efficacy and toxicity is sometimes to blame, many candidates are discarded due to poor aqueous solubility and low bioavailability.[84]

While the synthesis of analogues is important to obtain structure-property relationships, it can also be worthwhile to investigate improving these undesirable physicochemical properties without redesigning the molecule (and risking a loss in efficacy). Due to the cost associated with the discovery and development process, reviving candidates that displayed adequate efficacies, but were discarded due to solubility and bioavailability issues could be a worthwhile endeavour.

Various methods to improve some of the physicochemical and pharmacokinetic properties of potential drug candidates are currently being investigated, including nanotechnology,[85] emulsifications[86] and polymer drug delivery systems.[87] Other methods that are being studied include incorporating the drug molecule into porous materials such as metal-organic frameworks[88,89] or cyclodextrins.[90,91] Another method that has become popular is the inclusion of the drug molecule in multicomponent crystals (such as salts and cocrystals).[92–94] This method is advantageous because it allows for a change in some of the physicochemical properties of the drug molecule, without changing the drug's structure. In this way, the drug's efficacy can be retained while properties such as solubility, bioavailability, stability and other mechanical properties can be improved.[83,95,96] In addition, drug-drug multicomponent crystals could be formed that have the ability to target two pathways simultaneously; however, factors such as therapeutic dosages and synergistic or antagonistic effects would need to be studied first.[97]

It should be noted that inclusion of a drug molecule in multicomponent crystals will not overcome drug resistance by the disease that the drug candidate is targeting. In addition, the formation of multicomponent crystals with a specific coformer to give certain physicochemical properties is still unpredictable.[98] As a result, research is currently being conducted to increase the knowledge in this field. However, there is little knowledge on the formation of multicomponent crystals of antiplasmodial agents, despite the potential these molecules may have.[99]

1.6 MULTICOMPONENT CRYSTALS

The field of multicomponent crystals (pharmaceutical and otherwise) falls under the term "supramolecular chemistry" which focuses on interactions between molecules and how they assemble on a molecular level.[84] While it should be noted that supramolecular chemistry certainly takes place in solution as well, only the solid-state supramolecular chemistry will be discussed here, as it is the focus of this thesis. Under the umbrella of supramolecular chemistry, lies the field of crystal engineering, which involves the design of new materials with a specific property (or purpose) through the application of knowledge obtained from known systems. We attempt to rationalise how molecules interact in the solid state by studying patterns in known structures (and also how this effects the properties of the system) and then apply this knowledge to deduce patterns and 'rules'.[100] In this way, we are working towards one day being able to tailor-make multicomponent crystals and other materials with specific properties.

A multicomponent crystal is defined as a crystal that contains more than one type of chemical entity in the crystal lattice.[101] Each entity can be classified as an ion, solvent or coformer and the combination of these in the crystal lattice gives rise to the types of multicomponent crystals discussed below. In the context of pharmaceutical multicomponent crystals, the coformer, ion or solvent needs to be safe for human consumption.[93] These coformers can be chosen from EAFUS (Everything Added to Food in the United States) and GRAS (Generally Regarded As Safe) databases.[102,103]

1.6.1 Types of multicomponent crystals

In a broad sense, the term 'multicomponent crystal' encompasses three categories – cocrystals, salts and solvates; however, other intermediary categories have also been suggested in an attempt to be more specific in the description. These other categories include salt solvates, cocrystal solvates, cocrystal salts and cocrystal salt solvates (Figure 1.10). The definition of many of these terms (especially cocrystals) is currently still under debate.[104] It is important to note that while there may be slightly different definitions for these terms, the ones given below are most commonly used in the literature,[93,101,105] and will be used throughout this thesis.
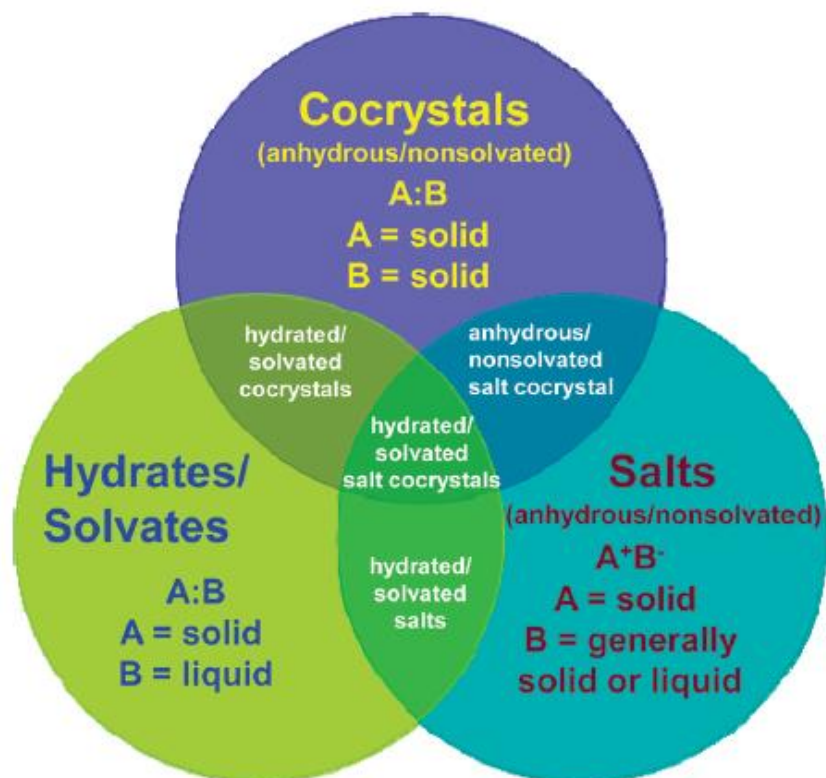
Figure 1.10: Multicomponent forms and how they overlap. Taken from Aitipamila *et al*.[105]

The formation of simple salts of drug molecules is a common practice in the pharmaceutical industry as a way to improve solubility. It is estimated that about half of all marketed drugs are sold in salt form.[106] The main reason for this is the relative ease of synthesis and the reliability of the product that forms. The definition of a salt, according to the International Union of Pure and Applied Chemistry (IUPAC), is a "*chemical compound consisting of an assembly of cations and anions*".[107] Reviews are available that focus on the use of counter ions such as chloride and sodium ions, as well as the administration routes and daily dosages.[108,109] The use of organic molecules as coformers could also result in the formation of salts (such as carboxylic acid coformers with basic drug molecules). In some cases, however, it is difficult to predict whether proton transfer will take place or not. The use of the ΔpKa rule is often used to assist in this regard, where a salt is expected to form when $\Delta pKa > 3$ and a cocrystal when $\Delta pKa < 0$. When the ΔpKa is between 0 and 3, there is uncertainty as to whether a salt or cocrystal will form or even a product in which partial proton transfer may occur.[110] In some cases, however, drug molecules are not ionisable and as a result, exploration into the formation of cocrystals becomes valid.[111]

The definition of a cocrystal has had much debate over the last decade, but in 2018 the FDA released a document on pharmaceutical cocrystals in which they make use of the following definition: "*pharmaceutical cocrystals are crystalline materials composed of two or more different molecules, one of which is the API (active pharmaceutical ingredient), in a defined stoichiometric ratio within the same crystal lattice that are associated by non-ionic and noncovalent bonds.*"[112] This definition, however,

could include solvates or hydrates. Another definition previously proposed by Vioglio *et al.* is more specific, stating that, in addition to the above criteria, all components must be in the solid state (in other words no solvent molecules in the lattice).[113]

In some cases, solvent molecules can be included into the crystal lattice. For these multicomponent crystals, if there is only one other molecule present, they would be considered solvates (or hydrates if the solvent is water). It is also possible to form a cocrystal solvate (or hydrate), a salt solvate, or even a cocrystal salt solvate (or hydrate).[114] These forms are illustrated in Figure 1.11 along with simpler cocrystals and salts.

For clarity and simplicity within this thesis, when the multicomponent crystal contains neutral drug and coformer molecules only, it will be termed a cocrystal. When there is charge transfer between the two (or more) molecules or atoms, it will be termed a salt and in cases where solvent is included, the multicomponent crystal will be termed a solvate (or hydrate when the solvent is water).

While not classified as a multicomponent crystal, it is also important to define amorphous materials as they are frequently seen in the literature, as well as in the pharmaceutical industry.[115–118] An amorphous material differs from a crystalline material in that there is no long-range order of the packing of molecules in the solid state.[119] There is still, however, short-range ordering and intermolecular interactions between the molecules, but in no uniform fashion that would form a crystal lattice.[119] Advantages of amorphous materials include improved solubility, dissolution rates and occasionally improved compression characteristics in comparison to crystalline forms.[120] Conversely, the physical and chemical stability of amorphous material is often poor in comparison to crystalline forms.[120]
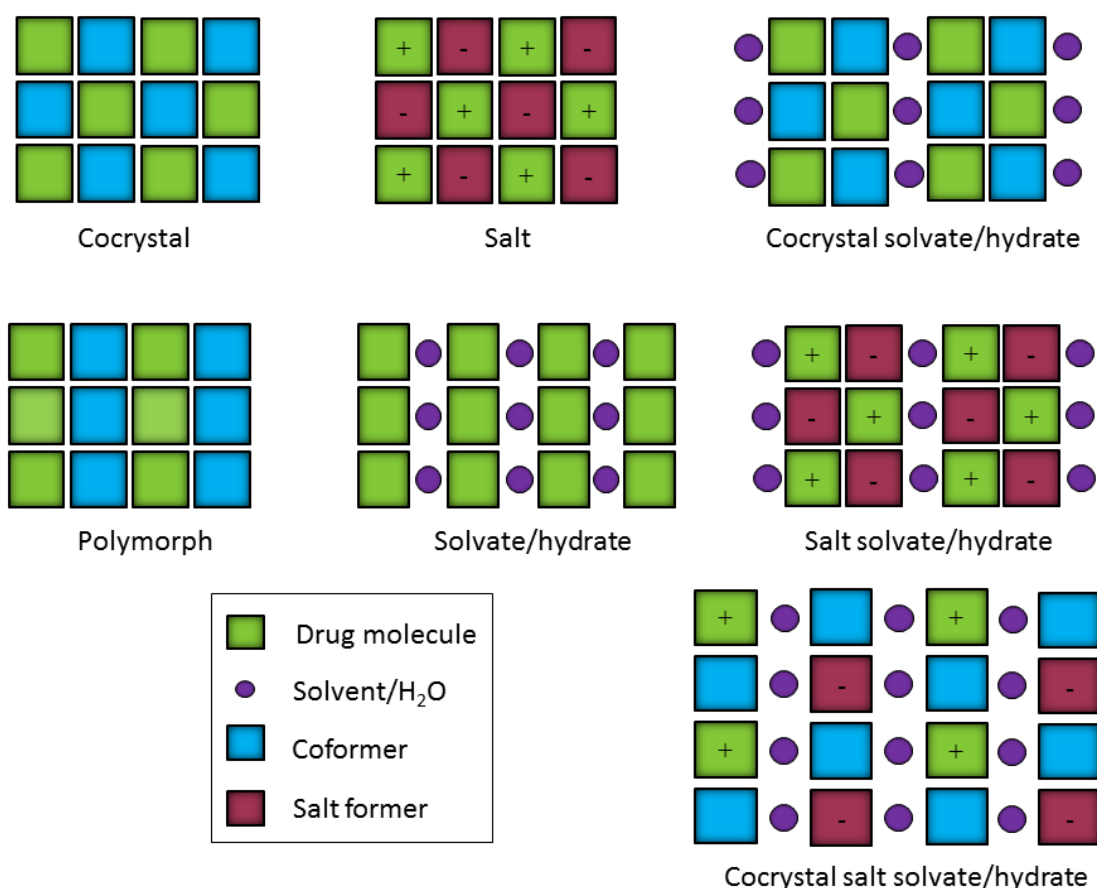
Figure 1.11: Types of multicomponent crystals. Image adapted from Voiglio *et al.*[113] and Duggirala *et al.*[93]

1.6.2 Multicomponent crystals as intellectual property

In addition to their physicochemical advantages, multicomponent crystals have been a hot topic in terms of intellectual property over the past decade.[121,122] In 2007, Trask reviewed the then-current position of pharmaceutical cocrystals as intellectual property.[122] He suggests that cocrystals satisfy the criteria for patent approval – namely novelty, utility and non-obviousness. This has been more recently reviewed by Braga *et al.* in relation to crystal engineering in the patent and regulatory literature.[123] There are a number of patents that describe multicomponent forms of drug molecules, as well as their preparation.[124]

Regulatory approval, however, is the challenging step in drug development.[82] In 2013, the FDA stated that cocrystals should be regarded as "drug product intermediates" rather than new active pharmaceutical ingredients.[125] In early 2018, however, they released more detailed guidelines on the topic. The FDA now requires that applications that claim new cocrystal forms of APIs submit evidence for this in the form of three points: evidence that the API and coformer are present in the unit cell, that they are both neutral species and interact non-ionically and that there is significant dissociation of the API from the cocrystal before it reaches its target site. They also state that APIs that satisfy these points

are analogous to a polymorphic form of the API, rather than a new API. In addition, drug-drug cocrystals should be thought of as fixed-dose combination products, rather than new single APIs.[112]

In 2015, the European Medicines Agency (EMA) also released their reflection paper on the topic of pharmaceutical cocrystals, however their stance on the matter is slightly different.[112] They state that cocrystals would not be classed as 'New Active Substances' unless they demonstrate different safety or efficacy data in comparison to the API itself. They consider cocrystals to be similar to polymorphic forms, salts, hydrates or solvates and should be treated as such, unless they differ in their safety or efficacy data. Cocrystals are therefore considered eligible for drug product applications in a similar manner to that of other multicomponent crystals (salts, hydrates etc.).

Although the FDA and EMA differ slightly on their position of pharmaceutical cocrystals, the fact that there are now more detailed guidelines for industry means that the advancement of cocrystal drug development is warranted. Furthermore, it will promote the application of cocrystal drug products to regulatory bodies and as a result, more drug molecules could be available on the market in their multicomponent forms.[126,127]

1.6.3 Designing multicomponent crystals

In order to obtained new multicomponent crystals, some knowledge of the individual components is first required, as well as an understanding of the types of interactions that could form when trying to combine the components to form a multicomponent crystal.[128]

1.6.3.1 Intermolecular interactions

Intermolecular interactions are those forces that are present between atoms that are not directly bonded to each other and are reversible.[84] For this reason they are also referred to as non-covalent interactions. They play a large role in the way molecules assemble in the solid state and can also influence properties such as solubility, thermal stability and density. There are numerous intermolecular interactions that have been observed and described in the literature, including dispersion interactions, electrostatic interactions, π-π interactions as well as hydrogen- and halogen-bonding interactions.[84] In the solid state, these interactions can be present in varying proportions and need not be strong interactions – many weak interactions could have a larger effect than one strong interaction.[129] As this thesis focuses primarily on multicomponent crystals that are formed through hydrogen bonding and π-π interactions, these two interactions will be the focus of this section. In addition, halogen bonding is becoming increasingly popular in crystal engineering and the pharmaceutical industry and will therefore also be briefly discussed.[130]

The hydrogen bond is considered one of the most common non-covalent interactions found in the literature and certainly the most widely-studied, especially in the pharmaceutical industry.[131–133] In 2011, IUPAC defined the hydrogen bond[104] as "*an attractive interaction between a hydrogen atom from a molecule or molecular fragment D–H in which D is more electronegative than H, and an atom or group of atoms in the same or different molecule, in which there is evident of bond formation.*" The hydrogen bond (shown in Figure 1.12) therefore comprises a hydrogen bond donor (D–H) and an acceptor (A–Y) and is described by the distance (d) between A and H and the angle (θ) DĤA. When there is proton transfer between the donor and acceptor, it is known as a charge-assisted hydrogen bond. The hydrogen bond is considered to be the strongest of the intermolecular interactions and has been shown to have directionality and a distinct effect on the packing of molecules in the solid state.[134] In addition, the hydrogen bond is important in many biological systems with the most common interaction being C–H···O (or N).[135]

(a)   (b)

Figure 1.12: (a) Hydrogen bond and (b) charge-assisted hydrogen bond (salt formation).

A second type of interaction, known as the π-π interaction, occurs between aromatic molecules (as shown in Figure 1.13). The delocalised π electrons of the aromatic ring can form dispersion interactions due to their polarisability.[136] Because the C–H bond is slightly polarised, the centre of the aromatic ring has a slight negative charge, while the rim of the ring (σ-framework) has a slight positive charge. These interactions are common, however not as strong or directional as hydrogen bonds.[137] In cases where hydrogen bonding between molecules is absent or very weak, π-π interactions can play a large role in the packing of the molecules.[138]

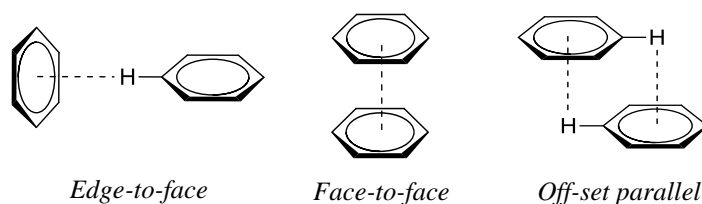*Edge-to-face*   *Face-to-face*   *Off-set parallel*

Figure 1.13: Types of π-π interactions.

The halogen bond (Figure 1.14) is considerably less-studied than the previous two forms of intermolecular interactions, however it is becoming progressively more common not only in the crystal engineering field but in medicinal chemistry too.[130,139–141] IUPAC defines the halogen bond, R–X···Y–Z, as "*a net attractive interaction between an electrophilic region on a halogen atom X belonging to a molecule or molecular fragment, R–X and a nucleophilic region of a molecule or molecular fragment, Y–Z.*"[142] The halogen bond is considered to be highly directional and often the distance between the donor and acceptor atoms is much shorter than the sum of their van der Waals radii. The halogen-bonding ability of the halogen is dependent on its polarisability (F << Cl << Br << I).[121] Unfortunately, the use of halogen bonding to form multicomponent crystals in the pharmaceutical industry has been scarcely explored because the halogen donor molecules that act as coformers are often considered toxic and not safe for human consumption.[140]
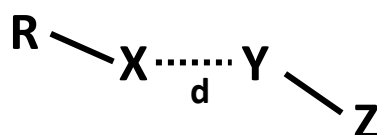

Figure 1.14: A scheme of the halogen bond where X is the halogen, R is the rest of the molecule, Y is the nucleophile of a second molecule and Z is the rest of that molecule.

A summary of these intermolecular interactions as well as acceptable distances between the relevant atoms is given in Table 1.1 below.

Table 1.1: Types of intermolecular interactions with ranges of acceptable distances between relevant atoms

Type of interaction	Relevant atoms	Distance (between relevant atoms or centroid to centroid)
Hydrogen bond	D–H···A	2.2 – 3.0 Å[84]
Halogen bond	R–X···Y	2.6 – 3.3 Å[143]
π-π interaction (face-to-face and offset face-to-face)	Centroid to centroid	3.3 – 3.8 Å[144]
π-π interaction (edge-to-face)	Centroid to centroid	Up to 5 Å[144]

D = donor atom; A = acceptor atom; R = rest of molecule, X = halogen, Y = nucleophile

1.6.3.2 The synthon approach to selecting coformers

One of the most common methods of forming multicomponent crystals is using the synthon approach, which relies on the abovementioned intermolecular interactions that are present between functional

groups.[145] A synthon can be described as "*the repeating structural unit that directs how molecules interact with each other in the solid state*."[146] Figure 1.15 shows selected synthons used in crystal engineering. The use of carboxylic acids and amides are popular for forming multicomponent crystals as they form strong hydrogen bonds. The acid-amide interaction is said to be the most common on the Cambridge Structural Database (CSD), followed by the amide-amide and acid-acid interaction.[147]
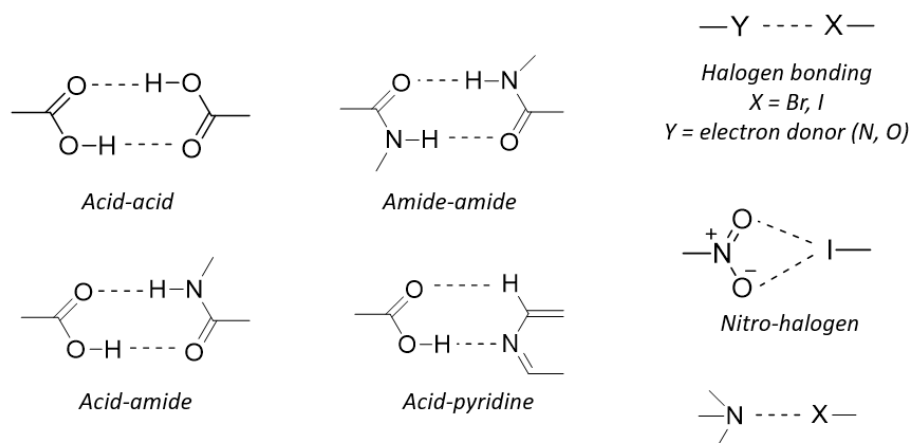

Figure 1.15: Selected synthons in crystal engineering strategies.

1.6.3.3 Using computational tools to aid in coformer selection

One of the main disadvantages of the use of multicomponent crystals to improve physicochemical properties of drug molecules is the lack of predictability in forming them in the first place. In this sense, the most challenging aspect is accurately choosing a coformer that will result in the formation of the correct multicomponent crystal. While some focus on the synthon approach to choose coformers, others turn to computational methods to assist in the selection process.[148] Some focus on modified crystal structure prediction methods[149] that investigate lattice energies and stable packing arrangements of cocrystals in comparison to the individual components.[150–152] It is generally thought that a multicomponent crystal is the thermodynamically favoured product and therefore would only form if it is more stable than the crystals of the individual components.[152] Using this assumption, density functional theory is used to determine lattice energies of each component and the multicomponent crystal. The comparison of component and cocrystal stability is used to determine whether or not the coformer is a suitable choice. These methods, however, can be computationally expensive as they require new calculations for each set of potential components.

The use of hydrogen bond propensity calculations have also been carried out as a way to predict the likelihood of successful cocrystallisations by statistically analysing the occurrence of hydrogen bonds between particular fragments in the CSD.[153,154] The software used searches the CSD for structures that have similar functional groups to that of the input molecule and quantifies the probability of the occurrence of hydrogen bonds between the components. If the hydrogen bonds of highest propensity are

found to occur between functional groups found on the coformer and the drug molecule, then the possibility of the formation of multicomponent forms is high. It should be noted that the software does not take into consideration factors such as aromaticity, steric hindrance between functional groups or the chemical environment of the donor-acceptor groups.[110]

Fluid-phase thermodynamics theory conductor-like screening model for real solvents (COSMO-RS theory)[155,156] has also become popular for the screening of coformers. It has been used to calculate the difference in excess enthalpies between the multicomponent form and the individual components. COSMO-RS assumes that the interactions between components in the solid phase are equivalent to that of a super-cooled liquid phase.[157]

Another method is to calculate gas-phase molecular electrostatic potential surfaces (MEPS) for each molecule (API and coformer) to evaluate molecular complementarity. This method employs an electrostatic model to identify a set of surface site interaction points (SSIPs), which can be described as H-bond donor and H-bond acceptor parameters.[158,159] Using the MEPS approach, the probability of the formation of multicomponent forms are estimated through the comparison of the calculated energy of the multicomponent form and that of the pure components. This difference in energy between the pure and multicomponent forms provides a measure of the thermodynamic driving force for multicomponent crystal formation.[157,160]

The COSMO-RS and MEPS approach have been compared by Grecu *et al.* and found to yield similar results when used as a virtual cocrystal screening tool.[160] While these methods may seem crude and have major approximations, the advantage is that they are simple, fast and do not require crystal structure data. For these reasons, these methods are suitable for screening of large libraries of potential coformers, but have the disadvantage of reliability in the predictions.[160]

The effectiveness of prediction methods is directly related to the complexity of the system (conformational flexibility, number of molecules in the asymmetric unit and the presence of heavy elements). As a result, current computational methods do not always take into account long-order packing contributions that could be playing an important role in the stabilisation of the system.[161] These aspects, together with other assumptions described above that are needed for the various computational methods, could provide an explanation for why we are not yet at the point where we can accurately predict the formation of multicomponent crystals. Possibly a combined approach of experimentally-obtained data and computational calculations is the key for more accurate predictions in the future.

1.6.3.4 Methods used to form multicomponent crystals

The most commonly used method for the preparation of multicomponent crystals is the solvent evaporation method.[162] In a typical solution cocrystallisation, the individual components are dissolved in a minimum amount of a common solvent, often with gentle heating and stirring. The vial is then

placed in an area with little vibration or movement and the solvent is allowed to slowly evaporate. This method allows for the formation of single crystals that can be studied using single crystal X-ray diffraction. In some cases, however, one or more of the components can crystallise out separately and the multicomponent form is not obtained. This could be due to the solubility, or that the formation of the multicomponent product is not favourable over the individual components.

Another solution-based method is a layering technique that could overcome the differences in solubility of the individual components. In this method, one of the components is dissolved in one solvent, and the other in a second solvent. The one is gently pipetted over the first so that a two-layer system is obtained. By slow diffusion of the solvents, the components interact and can form multicomponent crystals. Alternatively, a solvent in which neither component is soluble can be layered over the solution of components in a similar two-layer system. In this way, it is hoped that crystals will grow at the interface between the layers.

The use of mechanochemistry has also been reported for the formation of multicomponent crystals. In this method, mechanical force is applied through grinding or milling to induce interactions between components.[163] The use of a mortar and pestle is often used; however, ball mills are becoming more popular as they are more reliable. Liquid-assisted grinding – where catalytic amounts of solvent are used to accelerate the reaction – is a more popular choice for the formation of multicomponent crystals, especially as a screening tool, as it is fast and efficient and overcomes solubility differences between components.[164] One of the disadvantages of this method is that it does not allow for the formation of single crystals and therefore other methods are required to obtain single crystal data.

A less-studied method is the co-sublimation of components. This method relies on the ability of the components to enter the gas phase where they can interact and potentially form as a new solid material. The advantage of this method is that it is solvent-free and allows for the formation of single crystals. However, not all compounds are able to sublime directly to vapour on heating and the temperature at which the components sublime could be very different. This could influence the formation of multicomponent crystals.[165]

Alternative methods for the preparation of multicomponent crystals include melt crystallisation,[166] twin screw extrusion,[167] spray drying,[168] freeze-drying[169] and slurry methods;[170] however, these are not as widely used.

1.6.3.5 Other factors to consider

While synthons and their ability to form intermolecular interactions are known to drive the formation of multicomponent crystals, other factors such as molecular shape and the affinity of molecules to close pack can play a role in crystal packing and the ability to form multicomponent crystals.[171] In general, organic molecules will typically pack in such a way as to fill the space as efficiently as possible. This is

due to van der Waals interactions present between molecules that have a stabilising effect according to the contact area.[104,172]

It is also important to consider the physicochemical properties of the components in relation to the experimental method that will be used to obtain the multicomponent crystals.[173] Solution methods are popular, but issues such as solubility of the component in solvents can result in one of the components 'crashing out' instead of forming the intended multicomponent crystal. Mechanochemical methods could prove problematic for compounds that have stability issues – where the force from milling or grinding could decompose one of the components. It should also be noted that the use of various cocrystallisation methods could potentially give rise to polymorphs, or even different types of multicomponent crystals (for example salts or cocrystals) depending on the method used.[174,175]

1.6.4 Current pharmaceutical multicomponent crystals

The formation of multicomponent crystals has been well-documented for the improvement of certain physicochemical properties, but because of uncertainty in their classification until recently, it has not been well taken up by the pharmaceutical industry in terms of marketing drugs as their multicomponent forms. In addition, the lack of suitable production methods on large scale, as well as predictability issues has dampened full-scale research efforts by pharmaceutical companies.[119]

Excluding simple salts (such as chloride or sodium salts), there are currently only three multicomponent forms of drug molecules that are on the market.[176] The first is escitalopram oxalate, which was approved by the FDA in 2009 for the treatment of anxiety and depression and is marketed as Lexapro®. It is classified as a cocrystal salt hydrate as it comprises two escitalopram cations, charge-balancing oxalate anions, as well as a neutral molecule of oxalic acid and one molecule of water per asymmetric unit.[177] The second is a valproate sodium cocrystal with valproic acid, licensed in 2012 and marketed as Depakote®. It is marketed by Novartis to treat disorders such as seizures and manic depression. It comprises a 1:1 molar ratio of the sodium valproate salt and valproic acid, resulting in a crystalline, non-hygroscopic solid form.[178] The third is Entresto® (sacubitril-valsartan), a 1:1 molar ratio of sacubitril and valsartan, both present as the anionic form stabilised by three sodium cations and water molecules. It is currently used for the treatment of chronic heart failure.[179] In addition, the cocrystal of the anti-diabetic drug, Ertugliflozin and coformer 5-oxo-proline, is currently in clinical trials. This drug has also been cocrystallised with other coformers, including pyroglutamic acid and *L*-proline.[180]

Investigation into improving physicochemical properties of drug molecules through the formation of multicomponent crystals has increased substantially over the past decade.[82] Some of these drug molecules include ibuprofen that exhibits an 8-fold improvement in the dissolution rate when cocrystallised with nicotinamide.[181] Carbamazepine has been cocrystallised with saccharin[182,183] and a

number of carboxylic acid coformers,[184] and many of these cocrystals showed improvements to the solubility and bioavailability of the drug molecule. Smith *et al.* investigated the formation of the multicomponent crystal of quercetin with isonicotinamide, caffeine and theobromine, all of which displayed improved solubility and absorption of the drug *in vivo*.[185] Lapatinib, an anticancer drug, has also been cocrystallised with caproic acid, caprylic acid and adipic acid to form salts in each case.[186]

While multicomponent forms of drug molecules have received considerable attention, there has been a neglect with antiplasmodial drug molecules, despite the urgent need to improve the physicochemical properties of some of them.[99] Having said this, there are a few reported cases of multicomponent forms of some known antiplasmodial agents. Some of these are described below.

Pyrimethamine, an antifolate antiplasmodial agent, has been well studied by a number of researchers.[110,187,188] Delori *et al.* made use of the ΔpKa rule and hydrogen bond propensity calculations to screen for potential coformers. Multicomponent forms of pyrimethamine were obtained with theophylline, aspirin, α-ketoglutaric acid, saccharin, *p*-coumaric acid, succinimide and *L*-leucine.[110] Stanley *et al.* reported two salts formed from pyrimethamine and glutaric acid (Figure 1.16a) or formic acid (both in a 1:1 ratio of API to coformer).[188] Sethuraman *et al.* reported a further four salts formed from pyrimethamine with maleic acid, succinic acid, phthalic acid or fumaric acid (Figure 1.16b).[189] In the majority of these cases where carboxylic acid coformers are used, the acid-aminopyridine heterosynthon is observed to be the driving force behind cocrystallisation.
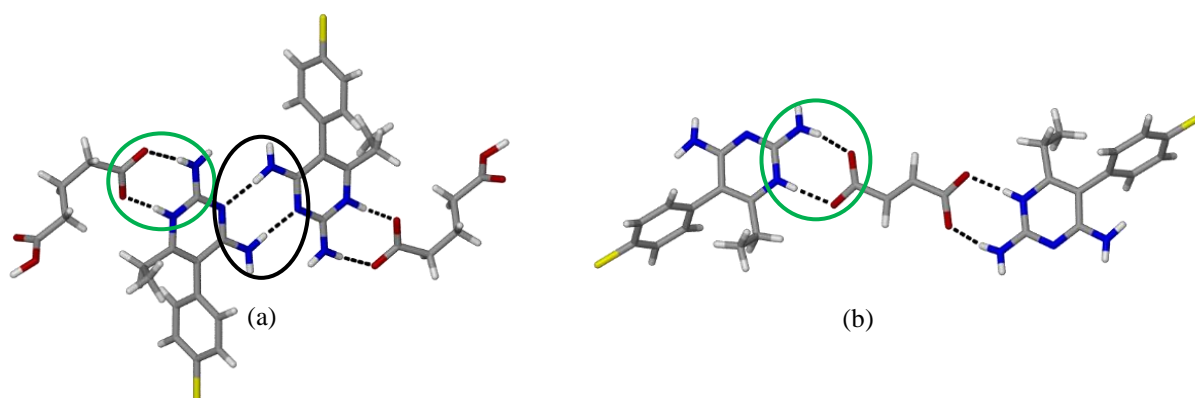

(a)   (b)

Figure 1.16: Structure of the salt of pyrimethamine formed with (a) glutaric acid (CSD ref: UHAYEH) and (b) fumaric acid (CSD ref: ULAXIO). Circled in green is the acid-aminopyridine heterosynthon and in black is the aminopyridine homosynthon.

A second antifolate drug that was developed but discarded before clinical use is MMP – a methyl suphonyl aminopyridine antiplasmodial agent developed by Chibale and coworkers.[190] This compound showed excellent potency against *P. falciparum*, but exhibited poor aqueous solubility (10 µg/mL at pH = 7.4). Investigation into the formation of multicomponent forms of this compound led to the formation of five salts and one cocrystal with various coformers, including salicylic acid, oxalic acid and adipic

acid (Figure 1.17). These multicomponent forms showed similar hydrogen-bonding motifs to those of pyrimethamine described above. The acid-aminopyridine heterosynthon is highlighted in green in Figure 1.17. For three of the salts obtained, improved solubility of up to 200 µg/mL at pH = 7.4 was observed.
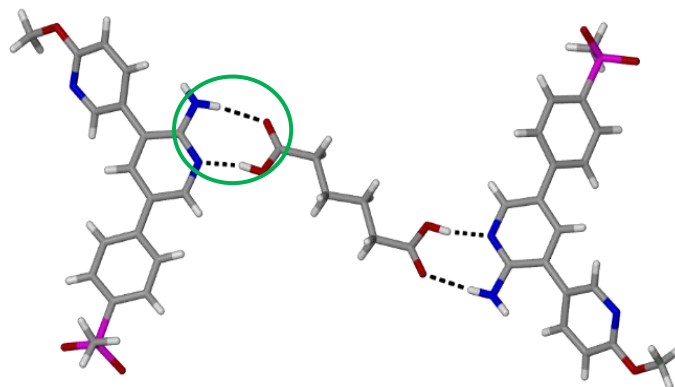

Figure 1.17: Structure of the cocrystal formed from MMP and adipic acid (CSD ref: PIWWEZ). Cirlcled in green is the acid-aminopyridine heterosynthon.

Two multicomponent forms of artemisinin have been reported by Karki *et al.*[191] The use of orcinol and resorcinol as coformers yielded two cocrystals with artemisinin. In both cases, O–H···O hydrogen bonding is observed (as seen in Figure 1.18) between the API and coformer, but the packing arrangement is different. In addition, a co-amorphous solid of curcumin-artemisinin has recently been reported by Mannava *et al.*, which showed improved solubility and bioavailability in comparison to artemisinin.[192]
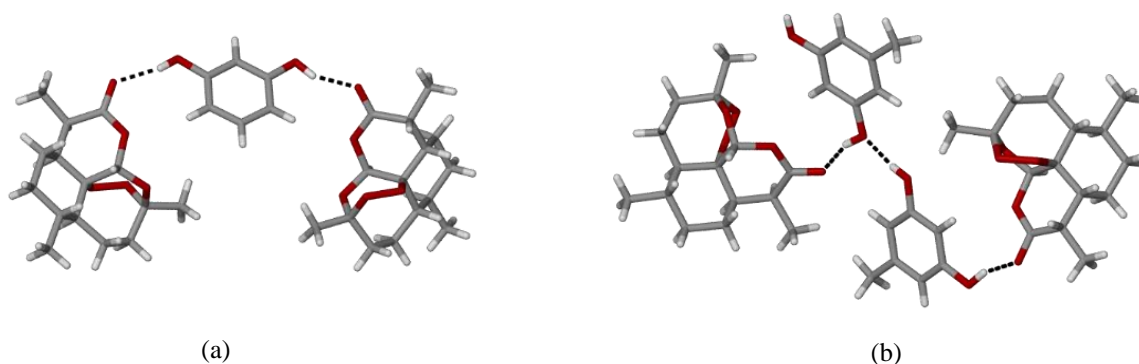

(a)   (b)

Figure 1.18: Structure of the cocrystal of artemisinin formed with (a) resorcinol (CSD ref: TALCOA) and (b) orcinol (CSD ref: TALCUG).

The quinoline-containing class of antiplasmodial agents has received more attention in the literature and has been shown to form multicomponent crystals with a number of coformers.[193–195] In most of these cases, linear and aromatic carboxylic acids were used as coformers. However, in some instances saccharin and certain binaphthyl derivatives were able to form multicomponent crystals. For the

multicomponent crystals obtained with mefloquine and amodiaquine, an improvement in the solubility and *in vitro* dissolution rates were observed in comparison to the parent API. Unfortunately, the authors did not obtain crystal structures of these forms.

While there have been many more reports of multicomponent forms of quinine,[196–199] the physicochemical properties of these forms have not yet been investigated. In these cases, crystal structures show hydrogen bonding between the nitrogen atom in the amino side chain of the API and the coformer, as shown in Figure 1.19.

(a)   (b)

Figure 1.19: Structure of the salt of quinine formed from (a) 2-chlorobutyrate (CSD ref: VAZCUZ) and (b) saccharin (CSD ref: YANNIL).

Previously, we have reported salts of 1,2,3-triazole-containing quinolines and aromatic acids such as salicylic acid and pamoic acid (Figure 1.20).[200] Hydrogen bonding takes place between the carboxylic acid and the nitrogen in the amino side chain, as well as with the quinoline nitrogen atom. Interestingly, here the choice of coformer seems to influence the efficacy of the compound. However, further work needs to be conducted before any definitive claims can be made.
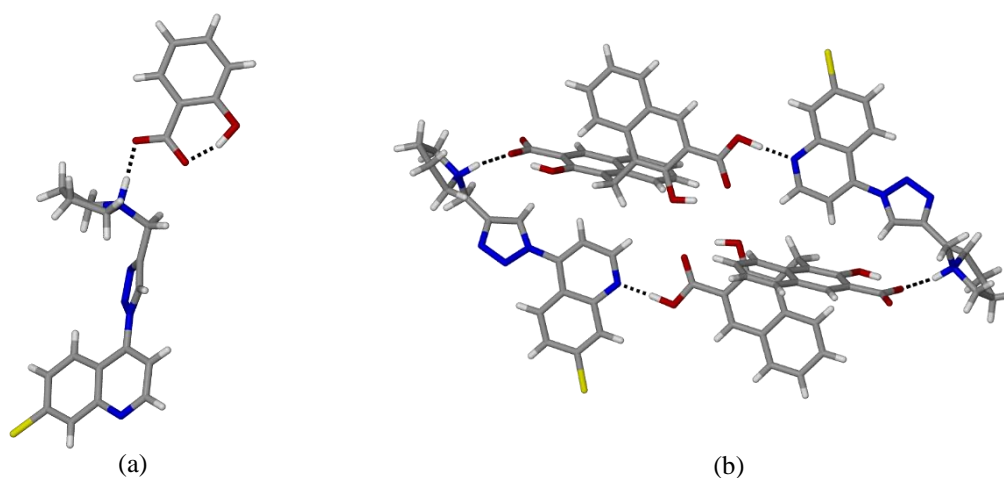

(a)   (b)

Figure 1.20: Structure of the salt of 7-chloro-4-(4-(pyrrolidin-1-ylmethyl)-1*H*-1,2,3-triazole-1-yl)quinoline formed with (a) salicylic acid and (b) pamoic acid, showing the proton transfer between the salicylate and amino groups. Solvent molecules (DMSO and H_2O) from (b) have been removed for clarity.

While these cases seem to promote the fact that antiplasmodial agents have the potential to form multicomponent crystals as a way of improving physicochemical properties, it is unfortunate that there is possibly a bias in the literature toward positive results. It may well be that there are many cases where the use of multicomponent crystals has a detrimental effect on the physicochemical properties of the parent drug molecule, but these results may not have been published. In addition, the majority of the negative cocrystallisation attempts do not make it into peer-reviewed journals and so the bias toward the potential that some molecules have to forming multicomponent crystals is skewed. It was therefore our goal to explore this further and to gain insight into this field.

1.7 INTRODUCING OUR STRATEGY

In an ideal situation, a chemist should be able to use the knowledge available to assess the molecule at hand, select the appropriate coformer that will improve the specific property required and to form the multicomponent form of the API with the desired properties. Unfortunately, the present knowledge on forming multicomponent crystals is simply not sufficient to allow for accurate prediction. In addition, there is a lack of knowledge on the structure-property relationship between the chosen coformer and the newly-formed multicomponent crystal. These two factors are currently hindering the ability to tailor-make multicomponent crystals with specific properties.

1.7.1 The aims and objectives of this study

The aim of this work was to investigate the formation of multicomponent crystals of known and novel antiplasmodial agents. By doing so, we aimed to contribute to the current knowledge that will one day allow for accurate predictions for tailor-made properties. In order to achieve this, some objectives were set for this project.

Our initial strategy was to make use of a combined theoretical and experimental approach to investigate the formation of multicomponent crystals of known antiplasmodial agents. For this, five compounds were selected, namely ferroquine, phenylequine, amodiaquine, *N*-(7-chloroquinolin-4-yl)ethane-1,2-diamine and *N*-(7-chloroquinolin-4-yl)propane-1,3-diamine (Figure 1.21). These molecules were chosen because they have been shown to have reasonably poor solubility, are simple to synthesise or purchase and are similar in structure so that comparisons can be made about the types of intermolecular interactions that form.
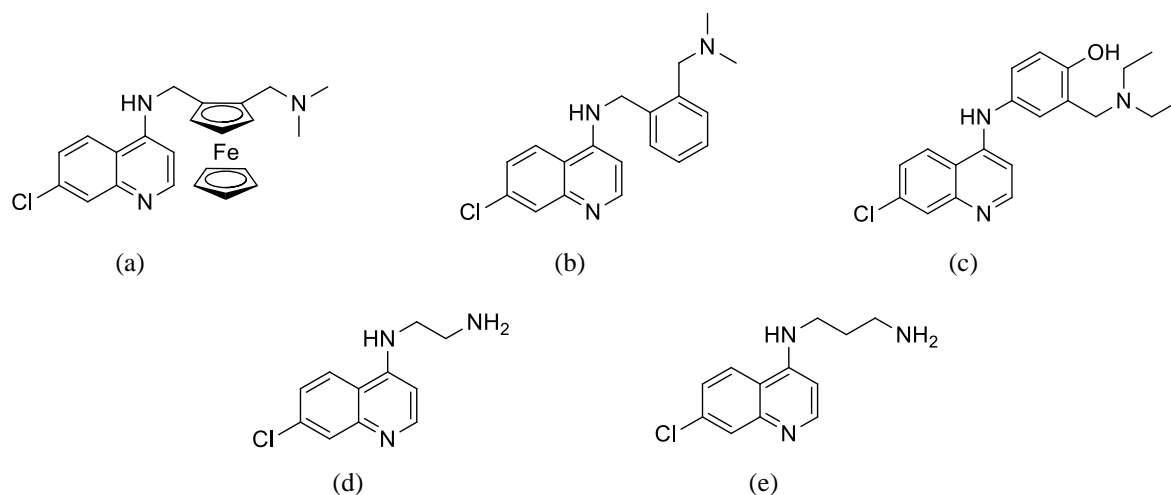
Figure 1.21: Structure of (a) ferroquine, (b) phenylequine, (c) amodiaquine, (d) *N*-(7-chloroquinolin-4-yl)ethane-1,2-diamine and (e) *N*-(7-chloroquinolin-4-yl)propane-1,3-diamine.

While we are able to make or purchase these compounds on gram-quantity scale, the application of the multicomponent crystal method to the drug discovery process would need to be carried out on much smaller sample sizes – sometimes only up to 50 mg of sample. Therefore, complete screening methods for finding multicomponent crystals from a wide range of coformers is challenging. For this reason, we sought to determine whether the use of computational methods could assist us in the selection of coformers that would likely yield multicomponent crystals with our chosen APIs. We thus decided to make use of molecular electrostatic potential surface calculations as carried out by Grecu *et al*.[160] Once a ranked list of coformers is obtained, experimental screening could be carried out using a variety of methods to determine the reliability of the computational calculations, as well as to determine if there are trends in the types of coformers used that form multicomponent crystals, as well as the types of interactions formed.

Provided this method gives multicomponent products, we would apply it to other compounds that are not as easily obtained in large quantities. For this we turned to lapatinib derivatives as they have been shown to display good efficacies against *P. falciparum*, but suffer from low solubility.[201] The advantage of this approach is that the majority of the synthetic methodology is already established.[202] In addition, inspired by Ferroquine, we sought to introduce substituted ferrocene moieties into the lapatinib compound, as shown in Figure 1.22.
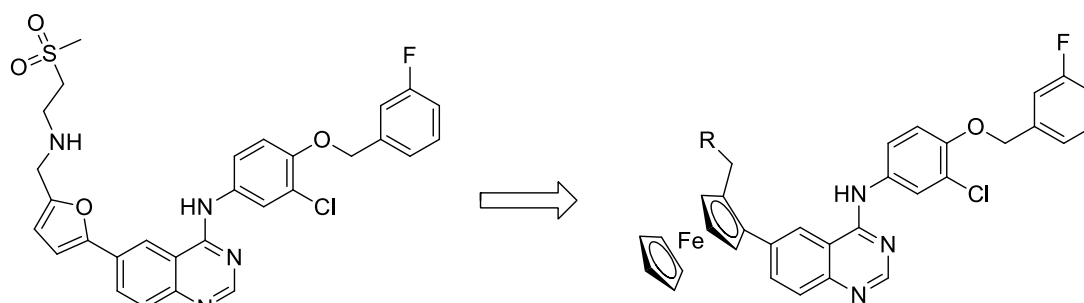
Figure 1.22: Structure of lapatinib (left) and the incorporation of an aminoferrocene moiety (right), where the R-group is a tertiary amine (dimethyl, pyrrolidyl, morpholinyl etc.).

At this point, the mode of action of the lapatinib analogues against *P. falciparum* is unknown. It is suggested that it could be targeting one or more kinases within the parasite, but could also be acting as a β-hematin inhibitor.[79] The efficacy results that have been obtained are based on phenotypic assays that assess the ability of the drug molecule to inhibit the growth of the parasite. Further studies would therefore need to be conducted to confirm the mode of action, but this is beyond the scope of this project.

By incorporating a synthetic approach into the project we expected to contribute to the structure-activity relationship studies on these compounds. We were also interested to see what effect small modifications to the structure would have on its ability to form multicomponent crystals. Initially, the R-groups described above would be investigated, and then including linkers such as amides between the quinazoline scaffold and the ferrocene tail group. In this way, a greater knowledge on structure-property relationships could be obtained.

1.8 REFERENCES

(1)   Cox, F. E. G. *Parasites Vectors* **2010**, *3* (5), 1–9.

(2)   World Health Organisation. *Global technical strategy for malaria 2016-2030*; Available at: http://www.who.int/malaria/publications/atoz/9789241564991/en/ (accessed 26 August 2018).

(3)   World Health Organisation. *World Malaria Report 2017*; Available at: http://apps.who.int/iris/discover?query=world+malaria+report+2017 (accessed 26 August 2018).

(4)   Maitland, K. *N. Engl. J. Med.* **2016**, *375* (25), 2416–2417.

(5)   Sachs, J.; Malaney, P. *Nature* **2002**, *415* (6872), 680–685.

(6)   Gallup, J.; Sachs, J. *The Intolerable Burden of Malaria: A New Look at Numbers*; American Society of Tropical Medicine and Hygiene: Northbrook, 2001.

(7)   White, N. J.; Pukrittayakamee, S.; Hien, T. T.; Faiz, M. A.; Mokuolu, O. A.; Dondorp, A. M. *Lancet* **2014**, *383*, 723–735.

(8)   Medicines for Malaria Venture. Animated lifecycle of the malaria parasite, power point slide. Available at https://www.mmv.org/malaria-medicines/parasite-lifecycle (accessed 16 August 2018).

(9)   Gardner, M. J.; Hall, N.; Fung, E.; White, O.; Berriman, M.; Hyman, R. W.; Carlton, J. M.; Pain, A.; Nelson, K. E.; Bowman, S.; Paulsen, I. T.; James, K.; Eisen, J. A; Rutherford, K.; Salzberg, S. L.; Craig, A.; Kyes, S.; Chan, M.-S.; Nene, V.; Shallom, S. J.; Suh, B.; Peterson, J.; Angiuoli, S.; Pertea, M.; Allen, J.; Selengut, J.; Haft, D.; Mather, M. W.; Vaidya, A. B.; Martin, D. M. A; Fairlamb, A. H.; Fraunholz, M. J.; Roos, D. S.; Ralph, S. A; McFadden, G. I.; Cummings, L. M.; Subramanian, G. M.; Mungall, C.; Venter, J. C.; Carucci, D. J.; Hoffman, S. L.; Newbold, C.; Davis, R. W.; Fraser, C. M.; Barrell, B. *Nature* **2002**, *419*, 498–511.

(10)   Mishra, M.; Mishra, V. K.; Kashaw, V.; Iyer, A. K.; Kashaw, S. K. *Eur. J. Med. Chem.* **2016**, *125*, 1300–1320.

(11)   Nzila, A. *J. Antimicrob. Chemother.* **2006**, *57* (6), 1043–1054.

(12)   Hyde, J. E. *Acta Trop.* **2005**, *94* (3), 191–206.

(13)   Yuthavong, Y.; Tarnchompoo, B.; Vilaivan, T.; Chitnumsub, P.; Kamchonwongpaisan, S.; Charman, S. A; McLennan, D. N.; White, K. L.; Vivas, L.; Bongard, E.; Thongphanchang, C.; Taweechai, S.; Vanichtanankul, J.; Rattanajak, R.; Arwon, U.; Fantauzzi, P.; Yuvaniyama, J.; Charman, W. N.; Matthews, D. *Proc. Natl. Acad. Sci. U. S. A.* **2012**, *109* (42), 16823–16828.

(14)   Olliaro, P. *Pharmacol. Ther.* **2001**, *89* (2), 207–219.

(15)   Sirawaraporn, W.; Yongkiettrakul, S.; Sirawaraporn, R.; Yuthavong, Y.; Santi, D. V. *Exp. Parasitol.* **1997**, *87*, 245–252.

(16)   Klein, E. Y. *Int. J. Antimicrob. Agents* **2013**, *41* (4), 311–317.

(17)   World Health Organisation. *Overview of Malaria Treatment*, Available at: http://www.who.int/malaria/areas/treatment/overview/en/ (accessed 26 August 2018).

(18)   Barnett, D. S.; Guy, R. K. *Chem. Rev.* **2014**, *114* (22), 11221–11241.

(19)   Neill, P. M. O.; Barton, V. E.; Ward, S. A. *Molecules* **2010**, *15*, 1705–1721.

(20)   Meshnick, S. R. *Trans. R. Soc. Trop. Med. Hyg.* **1989**, *88*, 31–32.

(21)   Patel, H. D.; Christian, D. J. *Indian J. Chem.* **2014**, *53*, 835–857.

(22)   Meshnick, S. R.; Dobson, M. J. *Antimalarial Chemotherapy: Mechanisms of Action, Resistance, and New Directions in Drug Discovery*; Rosendthal, P. J. (editor), 2nd Edition; Humana Press, 2001.

(23)   Antoine, T.; Fisher, N.; Amewu, R.; O'Neill, P. M.; Ward, S. A.; Biagini, G. A. *J. Antimicrob. Chemother.* **2014**, *69* (4), 1005–1016.

(24)   World Health Organisation. *World Malaria Report 2005*; Available at: https://www.who.int/malaria/publications/atoz/9241593199/en/ (accessed 26 August 2018).

(25)   Phillips, M. A.; Burrows, J. N.; Manyando, C.; Van Huijsduijnen, R. H.; Van Voorhis, W. C.; Wells, T. N. C. *Nat. Rev. Dis. Prim.* **2017**, *3*, 1–24.

(26)   Egan, T. J.; Combrinck, J. M.; Egan, J.; Hearne, G. R.; Marques, H. M.; Ntenteni, S.; Sewell, B. T.; Smith, P. J.; Taylor, D.; van Schalkwyk, D. A; Walden, J. C. *Biochem. J.* **2002**, *365*, 343–347.

(27)   Sullivan, D. J. *Int. J. Parasitol.* **2002**, *32* (13), 1645–1653.

(28)   Kaur, K.; Jain, M.; Reddy, R. P.; Jain, R. *Eur. J. Med. Chem.* **2010**, *45* (8), 3245–3264.

(29)   Foley, M.; Tilley, L. *Pharmacol. Ther.* **1998**, *79* (1), 55–87.

(30)   Kaschula, C. H.; Egan, T. J.; Hunter, R.; Basilico, N.; Parapini, S.; Taramelli, D.; Pasini, E.; Monti, D. *J. Med. Chem.* **2002**, *45* (16), 3531–3539.

(31)   Sullivan, D. J. *Proc. Natl. Acad. Sci. Commentary*, **2017**, 1-3.

(32)   de Villiers, K. A.; Osipova, M.; Mabotha, T. E.; Solomonov, I.; Feldman, Y.; Kjaer, K.; Weissbuch, I.; Egan, T. J.; Leiserowitz, L. *Cryst. Growth Des.* **2009**, *9* (1), 626–632.

(33)   Straasø, T.; Kapishnikov, S.; Kato, K.; Takata, M.; Als-Nielsen, J.; Leiserowitz, L. *Cryst. Growth Des.* **2011**, *11* (8), 3342–3350.

(34)   Kuter, D.; Mohunlal, R.; Fitzroy, S. M.; Asher, C.; Smith, P. J.; Egan, T. J.; de Villiers, K. A. *CrystEngComm* **2016**, *18* (27), 5177–5187.

(35)   Chinappi, M.; Via, A.; Marcatili, P.; Tramontano, A. *PLoS One* **2010**, *5* (11), 1–12.

(36)   Martin, R. E.; Marchetti, R. V; Cowan, A. I.; Howitt, S. M.; Bröer, S.; Kirk, K. *Science* **2009**, *325* (5948), 1680–1682.

(37)   Ecker, A.; Lehane, A. M.; Clain, J.; Fidock, D. A. *Trends Parasitol.* **2012**, *28* (11), 504–514.

(38)   van Schalkwyk, D. A.; Walden, J. C.; Smith, P. J. *Antimicrob. Agents Chemother.* **2001**, *45* (11), 3171–3174.

(39)   Burgess, S. J.; Kelly, J. X.; Shomloo, S.; Wittlin, S.; Brun, R.; Liebmann, K.; Peyton, D. H. *J. Med. Chem.* **2010**, *53* (17), 6477–6489.

(40)   Achan, J.; Talisuna, A. O.; Erhart, A.; Yeka, A.; Tibenderana, J. K.; Baliraine, F. N.; Rosenthal, P. J.; D'Alessandro, U. *Malar. J.* **2011**, *10* (144), 1–12.

(41)   Krafts, K.; Hempelmann, E. *Parisitol. Res.* **2012**, *111*, 1–6.

(42)   Ridley, R. G.; Hofheinz, W.; Matile, H.; Jaquet, C.; Dorn, A.; Jolidon, S. E.; Richter, W. F.; Guenzi, A.; Masciadri, R.; Girometta, M.; Urwyler, H.; Huber, W.; Thaithong, S.; Peters, W. *Antimicrob. Agents Chemother.* **1996**, *40* (8), 1846–1854.

(43)   Pou, S.; Winter, R. W.; Nilsen, A.; Kelly, J. X.; Li, Y.; Doggett, J. S.; Riscoe, E. W.; Wegmann, K. W.; Hinrichs, D. J.; Riscoe, M. K. *Antimicrob. Agents Chemother.* **2012**, *56* (7), 3475–3480.

(44)   O'Neill, P. M.; Bray, P. G.; Hawley, S. R.; Ward, S. A.; Park, B. K. *Pharmacol. Ther.* **1998**, *77* (1), 29–58.

(45)   Lawrenson, A. S.; Cooper, D. L.; O'Neill, P. M.; Berry, N. G. *J. Mol. Model.* **2018**, *24* (237), 1-11.

(46)   Ashley, E. A.; Phyo, A. P. *Drugs* **2018**, *78* (9), 861–879.

(47)   Wells, T. N. C.; Van Huijsduijnen, R. H.; Van Voorhis, W. C. *Nat. Rev. Drug Discov.* **2015**, *14* (6), 424–442.

(48)   The RTS,S Clinical Trials Partnership. *N. Engl. J. Med.* **2012**, *367* (24), 2284–2295.

(49)   World Health Organisation. *Wkly. Epidemiol. Rec.* **2016**, *91* (4), 33–52.

(50)   World Health Organisation. *A potential new tool for child health and improved malaria control*, Available at: http://www.who.int/malaria/media/malaria-vaccine-implementation-qa/en/ (accessed 28 August 2018).

(51)   Callaway, E., Maxman, A. *Malaria vaccine cautiously recommended for use in Africa,* Available at: https://www.nature.com/news/malaria-vaccine-cautiously-recommended-for-use-in-Africa-1.18638 (accessed 17 August 2018).

(52)   Winstanley, P. A. *Parasitol. Today* **2000**, *16* (4), 146–153.

(53) Pereira, G. R.; Brandão, G. C.; Arantes, L. M.; De Oliveira, H. A.; De Paula, R. C.; Do Nascimento, M. F. A; Dos Santos, F. M.; Da Rocha, R. K.; Lopes, J. C. D.; De Oliveira, A. B. *Eur. J. Med. Chem.* **2014**, *73*, 295–309.

(54) Blackie, M. A. L.; Yardley, V.; Chibale, K. *Bioorg. Med. Chem. Lett.* **2010**, *20* (3), 1078–1080.

(55) Solomon, V. R.; Haq, W.; Srivastava, K.; Puri, S. K.; Katti, S. B. *J. Med. Chem.* **2007**, *50* (2), 394–398.

(56) Yearick, K.; Ekoue-kovi, K.; Iwaniuk, D.; Natarajan, J. K.; Dios, A. C. De; Roepe, P. D.; Wolf, C. *J. Med. Chem.* **2008**, *51* (7), 1995–1998.

(57) Musonda, C. C.; Little, S.; Chibale, K. *Bioorg Med. Chem. Lett.* **2007**, *17*, 4733–4736.

(58) Taleli, L.; de Kock, C.; Smith, P. J.; Pelly, S. C.; Blackie, M. A. L.; van Otterlo, W. A. L. *Bioorg. Med. Chem.* **2015**, *23* (15), 4163–4171.

(59) Biot, C.; Glorian, G.; Maciejewski, L. A.; Brocard, J. S.; Domarle, O.; Blampain, G.; Millet, P.; Georges, A. J.; Lebibi, J. *J. Med.Chem.* **1997**, *40* (23), 3715–3718.

(60) Blackie, M. A. L.; Beagley, P.; Croft, S. L.; Kendrick, H.; Moss, J. R.; Chibale, K. *Bioorg. Med. Chem.* **2007**, *15* (20), 6510–6516.

(61) Jacobs, L.; De Kock, C.; De Villiers, K. A.; Smith, P. J.; Smith, V. J.; van Otterlo, W. A. L.; Blackie, M. A. L. *ChemMedChem* **2015**, *10* (12), 2099–2110.

(62) Roux, C.; Biot, C. *Future Med. Chem.* **2012**, *4* (6), 783–797.

(63) Biot, C.; Daher, W.; Ndiaye, C. M.; Melnyk, P.; Pradines, B.; Chavain, N.; Pellet, A.; Fraisse, L.; Pelinski, L.; Jarry, C.; Brocard, J.; Khalife, J.; Forfar-Bares, I.; Dive, D. *J. Med. Chem.* **2006**, *49* (15), 4707–4714.

(64) Muregi, F.; Ishih, A. *Drug Dev. Res.* **2010**, *71*, 20–32.

(65) Walsh, J. J.; Coughlan, D.; Heneghan, N.; Bell, A. *Bioorg. Med. Chem. Lett.* **2007**, *17*, 3599–3602.

(66) Nwaka, S.; Hudson, A. *Nat. Rev. Drug Discov.* **2006**, *5*, 941–955.

(67) Burrows, J. N.; van Huijsduijnen, R. H.; Möhrle, J. J.; Oeuvray, C.; Wells, T. N. C. *Malar. J.* **2013**, *12 (187)*, 1-20.

(68) Pink, R.; Hudson, A.; Mouriès, M. A.; Bendig, M. *Nat. Rev. Drug Discov.* **2005**, *4* (9), 727–740.

(69) Trouiller, P.; Olliaro, P.; Torreele, E.; Orbinski, J.; Laing, R.; Ford, N. *Lancet* **2002**, *359* (9324),

2188–2194.

(70)   Robertson, M. N.; Ylioja, P. M.; Williamson, A. E.; Woelfle, M.; Robins, M.; Badiola, K. A.; Willis, P.; Olliaro, P.; Wells, T. N. C.; Todd, M. H. *Parasitology* **2014**, *141* (1), 148–157.

(71)   Todd, M. *Open Source Malaria Project*. Available at: http://opensourcemalaria.org/ (accessed 13 September 2018).

(72)   Hughes, J. P.; Rees, S. S.; Kalindjian, S. B.; Philpott, K. L. *Br. J. Pharmacol.* **2011**, *162*, 1239–1249.

(73)   Pierce, R. J.; MacDougall, J.; Leurs, R.; Costi, M. P. *Trends Parasitol.* **2017**, *33* (8), 581–583.

(74)   Njoroge, M.; Njuguna, N. M.; Mutai, P.; Ongarora, D. S. B.; Smith, P. W.; Chibale, K. *Chem. Rev.* **2014**, *114* (22), 11138–11163.

(75)   Teixeira, C.; Vale, N.; Pérez, B.; Gomes, A.; Gomes, J. R. B.; Gomes, P. *Chem. Rev.* **2014**, *114* (22), 11164–11220.

(76)   Oprea, T. I.; Bauman, J. E.; Bologa, C. G.; Buranda, T.; Chigaev, A.; Edwards, B. S.; Jarvik, J. W.; Gresham, H. D.; Haynes, M. K.; Hjelle, B.; Hromas, R.; Hudson, L.; MacKenzie, D. A.; Muller, C. Y.; Reed, J. C.; Simons, P. C.; Smagley, Y.; Strouse, J.; Surviladze, Z.; Thompson, T.; Ursu, O.; Waller, A.; Wandinger-Ness, A.; Winter, S. S.; Wu, Y.; Young, S. M.; Larson, R. S.; Willman, C.; Sklar, L. A. *Drug Discov. Today: Ther. Strategies* **2012**, *8* (3–4), 61–69.

(77)   Klug, D. M.; Gelb, M. H.; Pollastri, M. P. *Bioorg. Med. Chem. Lett.* **2016**, *26* (11), 2569–2576.

(78)   Patel, G.; Karver, C. E.; Behera, R.; Guyett, P. J.; Sullenberger, C.; Edwards, P.; Roncal, N. E.; Mensa-Wilmot, K.; Pollastri, M. P. *J. Med. Chem.* **2013**, *56* (10), 3820–3832.

(79)   Mehta, N.; Ferrins, L.; Leed, S. E.; Sciotti, R. J.; Pollastri, M. P. *ACS Infect. Dis.* **2018**, *4* (4), 577–591.

(80)   Ekins, S.; Williams, A. J. *Pharm. Res.* **2011**, *28* (8), 1785–1791.

(81)   Lotharius, J.; Gamo-Benito, F. J.; Angulo-Barturen, I.; Clark, J.; Connelly, M.; Ferrer-Bazaga, S.; Parkinson, T.; Viswanath, P.; Bandodkar, B.; Rautela, N.; Bharath, S.; Duffy, S.; Avery, V. M.; Möhrle, J. J.; Guy, R. K.; Wells, T. *Malar. J.* **2014**, *13* (143), 1–15.

(82)   Dai, X.-L.; Chen, J.-M.; Lu, T.B. *CrystEngComm* **2018**, 20, 5292-5316.

(83)   Steed, J. W. *Trends Pharmacol. Sci.* **2013**, *34* (3), 185–193.

(84)   Steed, J. W.; Atwood, J. L. *Supramolecular Chemistry*, 2nd Edition; John Wiley & Sons Ltd: Chichester, United Kingdom, 2009.

(85) Farokhzad, O. C.; Langer, R. *ACS Nano* **2009**, *3* (1), 16–20.

(86) Leuner, C.; Dressman, J. *Eur. J. Pharm. Biopharm.* **2000**, *50* (1), 47–60.

(87) Priya James, H.; John, R.; Alex, A.; Anoop, K. R. *Acta Pharm. Sin. B* **2014**, *4* (2), 120–127.

(88) Huxford, R. C.; Della Rocca, J.; Lin, W. *Curr. Opin. Chem. Biol.* **2010**, *14* (2), 262–268.

(89) McKinlay, A. C.; Morris, R. E.; Horcajada, P.; Férey, G.; Gref, R.; Couvreur, P.; Serre, C. *Angew. Chem. Int. Ed.* **2010**, *49* (36), 6260–6266.

(90) Hirayama, F.; Uekama, K. *Adv. Drug Deliv. Rev.* **1999**, *36* (1), 125–141.

(91) Fan, Z.; Diao, C. H.; Song, H. Bin; Jing, Z. L.; Yu, M.; Chen, X.; Guo, M. J. *J. Org. Chem.* **2006**, *71* (6), 1244–1246.

(92) Shan, N.; Zaworotko, M. J. *Drug Discovery Today* **2008**, *13* (9–10), 440–446.

(93) Duggirala, N. K.; Perry, M. L.; Almarsson, Ö.; Zaworotko, M. J. *Chem. Commun.* **2016**, *52* (4), 640–655.

(94) Blagden, N.; Coles, S. J.; Berry, D. J. *CrystEngComm.* **2014**, 5753–5761.

(95) Miroshnyk, I.; Mirza, S.; Sandler, N. *Expert Opin. Drug Deliv.* **2009**, *6*, 333–341.

(96) Schultheiss, N.; Newman, A. *Cryst. Growth Des.* **2009**, *9* (6), 2950–2967.

(97) Thipparaboina, R.; Kumar, D.; Chavan, R. B.; Shastri, N. R. *Drug Discovery Today* **2016**, *21* (3), 481–490.

(98) Corpinot, M. K.; Stratford, S. A.; Arhangelskis, M.; Anka-Lufford, J.; Halasz, I.; Judaš, N.; Jones, W.; Bučar, D. K. *CrystEngComm* **2016**, *18* (29), 5434–5439.

(99) Clements, M.; Le Roex, T.; Blackie, M. A. L. *ChemMedChem.* **2015**, 10, 1786–1792.

(100) Vittal, J. J., Tiekink, E.R.T. (editors), *Frontiers in Crystal Engineering*; John Wiley & Sons Ltd., Chichester, England, 2006.

(101) Grothe, E.; Meekes, H.; Vlieg, E.; Ter Horst, J. H.; De Gelder, R. *Cryst. Growth Des.* **2016**, *16* (6), 3237–3243.

(102) Generally Regarded as Safe (GRAS) database. Available at: http://www.accessdata.fda.gov/scripts/fdcc/?set=GRASNotices (accessed 14 April 2015).

(103)   Everything added to Food in the United States (EAFUS) database. Available at: http://www.accessdata.fda.gov/scripts/fcn/fcnNavigation.cfm?rpt=eafusListing (accessed 14 April 2015).

(104)   Berry, D. J.; Steed, J. W. *Adv. Drug Deliv. Rev.* **2017**, *117*, 3–24.

(105)   Aitipamula, S.; Banerjee, R.; Bansal, A. K.; Biradha, K.; Cheney, M. L.; Choudhury, A. R.; Desiraju, G. R.; Dikundwar, A. G.; Dubey, R.; Duggirala, N.; Ghogale, P. P.; Ghosh, S.; Goswami, P. K.; Goud, N. R.; Jetti, R. R. K. R.; Karpinski, P.; Kaushik, P.; Kumar, D.; Kumar, V.; Moulton, B.; Mukherjee, A.; Mukherjee, G.; Myerson, A. S.; Puri, V.; Ramanan, A.; Rajamannar, T.; Reddy, C. M.; Rodriguez-Hornedo, N.; Rogers, R. D.; Row, T. N. G.; Sanphui, P.; Shan, N.; Shete, G.; Singh, A.; Sun, C. C.; Swift, J. A.; Thaimattam, R.; Thakur, T. S.; Kumar Thaper, R.; Thomas, S. P.; Tothadi, S.; Vangala, V. R.; Variankaval, N.; Vishweshwar, P.; Weyna, D. R.; Zaworotko, M. J. *Cryst. Growth Des.* **2012**, *12* (5), 2147–2152.

(106)   Serajuddin, A. T. M. *Adv. Drug Deliv. Rev.* **2007**, *59* (7), 603–616.

(107)   McNaught, A.D., Wilkinson, A. *Definition of a Salt*, 2nd edition.; Blackwell Scientific Publications, 2014.

(108)   Saal, C.; Becker, A. *Eur. J. Pharm. Sci.* **2013**, *49* (4), 614–623.

(109)   Kawakami, K. *Adv. Drug Deliv. Rev.* **2012**, *64* (6), 480–495.

(110)   Delori, A.; Galek, P. T. A.; Pidcock, E.; Patni, M.; Jones, Wi. *CrystEngComm* **2013**, *15*, 2916–2928.

(111)   Elder, D. P.; Holm, R.; Diego, H. L. De. *Int. J. Pharm.* **2013**, *453* (1), 88–100.

(112)   Food and Drug Administration (FDA), *Guidance for Industry Regulatory Classification of Pharmaceutical Co-Crystals 2018.* Available at: http://www.fda.gov/downloads/Drugs/Guidances (accessed 31 August 2018).

(113)   Cerreia Vioglio, P.; Chierotti, M. R.; Gobetto, R. *Adv. Drug Deliv. Rev.* **2017**, *117*, 86–110.

(114)   Aitipamula, S.; Banerjee, R.; Bansal, A. K.; Biradha, K.; M.L., C.; Choudhury, A. R. *Cryst. Growth Des.* **2012**, *12*, 2147–2152.

(115)   Dalpiaz, A.; Pavan, B.; Ferretti, V. *Drug Discovery Today* **2017**, *22* (8), 1134–1138.

(116)   Vrani, E. *Bosn. J. Basic Med. Sci.* **2004**, *4* (3), 35–39.

(117)   Newman, A.; Hastedt, J. E.; Yazdanian, M. *AAPS Open* **2017**, *3* (7), 1-14.

(118)   Hancock, B. C.; Zografi, G. *J. Pharm. Sci.* **1997**, *86* (1), 1–12.

(119)   Byrn, S. R.; Zografi, G.; Chen, X. *Solid-state properties of pharmaceutical materials*, 1st edition.; John Wiley & Sons Ltd, Chichester, England, 2017.

(120)   Yu, L. *Adv. Drug Deliv. Rev.* **2001**, *48* (1), 27–42.

(121)   Aakeröy, C. B.; Wijethunga, T. K.; Desper, J. *J. Mol. Struct.* **2014**, *1072* (1), 20–27.

(122)   Trask, A. V. *Mol. Pharm.* **2007**, *4* (3), 301–309.

(123)   Braga, D.; Grepioni, F.; Gavezzotti, A.; Bernstein, J. *Cryst. Growth Des.* **2017**, *17* (3), 933–939.

(124)   Desiraju, G. R.; Nangia, A. *Cryst. Growth Des.* **2016**, *16* (10), 5585–5587.

(125)   Food and Drug Administration (FDA). *Guidance for Industry: Regulatory Classification of Pharmaceutical Co-crystals 2013*, Available at: http://www.fda.gov/downloads/Drugs/Guidances/UCM09827.pdf (accessed Aug 31, 2018).

(126)   Aakeröy, C. B.; Forbes, S.; Desper, J. *J. Am. Chem. Soc.* **2009**, *131* (47), 17048–17049.

(127)   Lara-Ochoa, F.; Espinosa-Perez, G. *Cryst. Growth Des.* **2007**, *7* (7), 1213–1215.

(128)   Desiraju, G. R. *J. Am. Chem. Soc.* **2013**, *135* (27), 9952–9967.

(129)   Desiraju, G. R.; Vittal, J. J.; Ramanan, A. *Crystal Engineering: A Textbook*; World Scientific Publishing Co. Ltd.: Singapore, 2011.

(130)   Cavallo, G.; Metrangolo, P.; Milani, R.; Pilati, T.; Priimagi, A.; Resnati, G.; Terraneo, G. *Chem. Rev.* **2016**, *116* (4), 2478–2601.

(131)   Bernstein, J.; Davis, R. E.; Shimoni, L.; Chang, N.-L. *Angew. Chem Int. Ed.* **1995**, *34* (15), 1555–1573.

(132); Grabowski, S. J. (Editor). *Hydrogen Bonding - New Insights*, 1st edition. Springer, Dordrecht: Poland, 2006.

(133)   Kollman, P. A.; Allen, L. C. *Chem. Rev.* **1972**, *72* (3), 283–303.

(134)   Steed, J. W.; Turner, D. R.; Wallace, K. J. *Core Concepts in Supramolecular Chemistry and Nanochemistry*; John Wiley & Sons Ltd: England, 2007.

(135)   Jeffrey, G. A.; Saenger, W. *Hydrogen Bonding in Biological Systems*; Springer, Berlin, 1991.

(136)   Jennings, W. B.; Farrell, B. M.; Malone, J. F. *Acc. Chem. Res.* **2001**, *34* (11), 885–894.

(137)   Hunter, C. A.; Sanders, J. K. M. *J. Am. Chem. Soc.* **1990**, *112* (14), 5525–5534.

(138) Colombo, V.; Lo Presti, L.; Gavezzotti, A. *CrystEngComm* **2017**, *19* (17), 2413–2423.

(139) Politzer, P.; Murray, J. S.; Clark, T. *Phys. Chem. Chem. Phys.* **2013**, *15* (27), 11178–11189.

(140) Choquesillo-Lazarte, D.; Nemec, V.; Cinčić, D. *CrystEngComm* **2017**, *19* (35), 5293–5299.

(141) Wilcken, R.; Zimmermann, M. O.; Lange, A.; Joerger, A. C.; Boeckler, F. M. *J. Med. Chem.* **2013**, *56*, 1363–1388.

(142) Desiraju, G. R.; Ho, P. S.; Kloo, L.; Legon, A. C.; Marquardt, R.; Metrangolo, P.; Politzer, P.; Resnati, G.; Rissanen, K. *Pure Appl. Chem.* **2013**, *85* (8), 1711–1713.

(143) Forni, A.; Metrangolo, P.; Pilati, T.; Resnati, G. *Cryst. Growth Des.* **2004**, *4* (2), 291–295.

(144) Tiekink, E. R. T., Zukerman-Schpector, J. (editors), *The Importance of Pi-Interactions in Crystal Engineering*; John Wiley & Sons Ltd, Chichester, England, 2012.

(145) Mukherjee, A. *Cryst. Growth Des.* **2015**, *15* (6), 3076–3085.

(146) Desiraju, G. R. *Angew. Chem. Int. Ed.* **1995**, *34*, 2311–2327.

(147) Lombard, J.; Loots, L.; Le Roex, T.; Haynes, D. A. *CrystEngComm* **2018**, *20* (1), 25–34.

(148) Thakur, T. S.; Desiraju, G. R. *Cryst. Growth Des.* **2008**, *8* (11), 4031–4044.

(149) Price, S. L. *Chem. Soc. Rev.* **2014**, *43* (7), 2098–2111.

(150) Taylor, C. R.; Day, G. M. *Cryst. Growth Des.* **2018**, *18* (2), 892–904.

(151) Karamertzanis, P. G.; Kazantsev, A. V; Issa, N.; Gareth, W. A; Adjiman, C. S.; Pantelides, C. C.; Price, S. L. *J. Chem. Theory Comput.* **2009**, *5*, 1432–1448.

(152) Issa, N.; Karamertzanis, P. G.; Welch, G. W. A.; Price, S. L. *Cryst. Growth Des.* **2009**, *9* (1), 442–453.

(153) Wood, P. A.; Feeder, N.; Furlow, M.; Galek, P. T. A.; Groom, C. R.; Pidcock, E. *CrystEngComm* **2014**, *16*, 5839–5848.

(154) Delori, A.; Galek, P. T. A; Pidcock, E.; Jones, W. *Chem. – Eur. J.* **2012**, *18* (22), 6835–6846.

(155) Abramov, Y. A.; Loschen, C.; Klamt, A. *J. Pharm. Sci.* **2012**, 1–11.

(156) Klamt, A. *J. Cheminform.* **2012**, *4*, O14.

(157) Musumeci, D.; Hunter, C. A.; Prohens, R.; Scuderi, S.; McCabe, J. F. *Chem. Sci.* **2011**, *2* (5), 883–890.

(158) Hunter, C. A. *Angew. Chem. Int. Ed.* **2004**, *43* (40), 5310–5324.

(159) Hunter, C. A. *Chem. Sci.* **2013**, *4* (4), 1687–1700.

(160) Grecu, T.; Hunter, C. A.; Gardiner, E. J.; McCabe, J. F. *Cryst. Growth Des.* **2014**, *14* (1), 165–171.

(161) Ryan, K.; Lengyel, J.; Shatruk, M. *J. Am. Chem. Soc.* **2018**, 140 (32), 10158-10168.

(162) Qiao, N.; Li, M.; Schlindwein, W.; Malek, N.; Davies, A.; Trappitt, G. *Int. J. Pharm.* **2011**, *419*, 1–11.

(163) Delori, A.; Friščić, T.; Jones, W. *CrystEngComm* **2012**, *14* (7), 2350–2362.

(164) Friščić, T. *J. Mater. Chem.* **2010**, *20* (36), 7599-7605.

(165) Zhang, T.; Yu, Q.; Li, X.; Ma, X. *J. Cryst. Growth Des*. **2017**, *469*, 114–118.

(166) Dhumal, R. S.; Kelly, A. L.; York, P.; Coates, P. D.; Paradkar, A. *Pharm. Res.* **2010**, *27* (12), 2725–2733.

(167) Medina, C.; Daurio, D.; Nagapudi, K.; Alvarez-nunez, F. *J. Pharm. Sci.* **2010**, *99* (4), 1693–1696.

(168) Alhalaweh, A.; Kaialy, W.; Buckton, G.; Gill, H.; Nokhodchi, A.; Velaga, S. P. *AAPS PharmSciTech* **2013**, *14* (1), 265–276.

(169) Eddleston, M. D.; Patel, B.; Day, G. M.; Jones, W. *Cryst. Growth Des.* **2013**, *13* (10), 4599–4606.

(170) Setyawan, D. W. I.; Sari, R.; Yusuf, H.; Primaharinastiti, R. *Asian J. Pharm. Clin. Res.* **2014**, *7*, 62–65.

(171) Fábián, L. *Cryst. Growth Des.* **2009**, *9* (3), 1436–1443.

(172) Kitaigorodsky, A. (editor), *Molecular Crystals and Molecules*, 1st edition; Elsevier Inc; Academic Press, New York, USA, 1973.

(173) Malamatari, M.; Ross, S. A.; Douroumis, D.; Velaga, S. P. *Adv. Drug Deliv. Rev.* **2017**, *117*, 162–177.

(174) Losev, E. A.; Boldyreva, E. V. *CrystEngComm* **2018**, *20* (16), 2299–2305.

(175) Losev, E. A.; Mikhailenko, M. A.; Achkasov, A. F.; Boldyreva, E. V. *New J. Chem.* **2013**, *37* (7), 1973–1981.

(176)   Karagianni, A.; Malamatari, M.; Kachrimanis, K. *Pharmaceutics* **2018**, *10* (1), 1–30.

(177)   Harrison, W. T. A.; Yathirajan, H. S.; Bindya, S.; Anilkumar, H. G.; Devaraju. *Acta Crystallogr. Sect. C Cryst. Struct. Commun.* **2007**, *63* (2), 129–131.

(178)   Petruševski, G.; Naumov, P.; Jovanovski, G.; Bogoeva-Gaceva, G.; Seik, W. N. *ChemMedChem* **2008**, *3* (9), 1377–1386.

(179)   Bolla, G.; Nangia, A. *Chem. Commun.* **2016**, *52* (54), 8342–8360.

(180)   Abiraj, K.; Gowda, D. C. *J. Chem. Res.* **2003**, *2003* (6), 332–333.

(181)   Chow, S. F.; Chen, M.; Shi, L.; Chow, A. H. L.; Sun, C. C. *Pharm. Res.* **2012**, *29*, 1854–1865.

(182)   Gao, Y.; Zu, H.; Zhang, J. *J. Pharm. Pharmacol.* **2011**, *63*, 483–490.

(183)   Hickey, M. B.; Peterson, M. L.; Scoppettuolo, L. A.; Morrisette, S. L.; Vetter, A.; Guzmán, H.; Remenar, J. F.; Zhang, Z.; Tawa, M. D.; Haley, S.; Zaworotko, M. J.; Almarsson, Ö. *Eur. J. Pharm. Biopharm.* **2007**, *67*, 112–119.

(184)   Childs, S. L.; Rodríguez-Hornedo, N.; Reddy, L. S.; Jayasankar, A.; Maheshwari, C.; McCausland, L.; Shipplett, R.; Stahly, B. C. *CrystEngComm* **2008**, *10* (7), 856–864.

(185)   Smith, A. J.; Kavuru, P.; Wojtas, L.; Zaworotko, M. J.; Shytle, R. D. *Mol. Pharm.* **2011**, *8*, 1867–1876.

(186)   Tesson, N.; Segade Rodriquez, A. *Cocrystals of Lapatinib* - EP2937346A1, Available at: https://patents.google.com/patent/EP2937346A1. (accessed 22 September 2018).

(187)   Sethuraman, V.; Thomas Muthiah, P. *Acta Crystallogr., Sect. E: Struct. Rep. Online* **2002**, *58* (8), o817–o818.

(188)   Stanley, N.; Sethuraman, V.; Thomas Muthiah, P.; Luger, P.; Weber, M. *Cryst. Growth Des.* **2002**, *2*, 631–635.

(189)   Sethuraman, V.; Stanley, N.; Muthiah, P. T.; Sheldrick, W. S.; Winter, M.; Luger, P.; Weber, M. *Cryst. Growth Des.* **2003**, *3*, 823–828.

(190)   Cruickshank, D. L.; Younis, Y.; Njuguna, N. M.; Ongarora, D. S. B.; Chibale, K.; Caira, M. R. *CrystEngComm* **2014**, *16* (26), 5781–5792.

(191)   Karki, S.; Friščić, T.; Fábián, L.; Jones, W. *CrystEngComm* **2010**, *12* (12), 4038–4041.

(192)   Mannava, M. K. C.; Suresh, K.; Bommaka, M. K.; Konga, D. B.; Nangia, A. *Pharmaceutics* **2018**, *10* (7), 1–16.

(193)   Yadav, A. .; Dabke, A. P.; Shete, A. S. *Drug Dev. Ind. Pharm.* **2010**, *36* (9), 1036–1045.

(194)   Partogi, T.H.;Soewandhi, S.N.; Jessie, S.P.; Wikarsa, S.H.; *Int. J. Pharm. Pharm. Sci.* **2013**, *5* (3), 7–11.

(195)   Oleksyn, B. J.; Serda, P. *Acta Crystallogr. Sect. B Struct. Sci.* **1993**, *49* (1989), 530–534.

(196)   Jacobs, A.; Nassimbeni, L. R.; Sayed, A.; Weber, E. *J. Chem. Crystallogr.* **2011**, *41*, 854–857.

(197)   Khan, M.; Enkelmann, V.; Brunklaus, G. *CrystEngComm* **2011**, *13* (9), 3213–3223.

(198)   Khan, M.; Enkelmann, V.; Brunklaus, G. *J. Am. Chem. Soc.* **2010**, *132* (14), 5254–5263.

(199)   Gjerløv, A. B.; Larsen, S. *Acta Crystallogr. Sect. C Cryst. Struct. Commun.* **1997**, *53* (1982), 1505–1508.

(200)   Clements, M. J., MSc thesis: *Synthesis of quinoline derivatives as potential antiplasmodial agents and investigation into their supramolecular properties*. Stellenbosch University, 2015.

(201)   Gao, H.; Wang, Y.; Chen, C.; Chen, J.; Wei, Y.; Cao, S.; Jiang, X. *Int. J. Pharm.* **2014**, *461*, 478–488.

(202)   Erickson, G.; Guo, J.; McClure, M.; Mitchell, M.; Salaun, M. C.; Whitehead, A. *Tetrahedron Lett.* **2014**, *55* (43), 6007–6010.

CHAPTER 2

Forming multicomponent crystals of known antiplasmodial agents

2.1 INTRODUCTION

One of the most challenging aspects of crystal engineering (in a pharmaceutical field and otherwise) is choosing the right coformer that would result in the formation of a multicomponent crystal with specific properties. In order to do this, studying the individual components is first required to understand what intra-and inter-molecular interactions are present and how these can be used to form multicomponent crystals. For the purpose of this study, we selected five 4-aminoquinoline derivatives, structures of which are shown in Figure 2.1 below. These five compounds have previously been reported in the literature[1–4] and are therefore relatively simple to synthesise and require starting materials that are reasonably inexpensive.
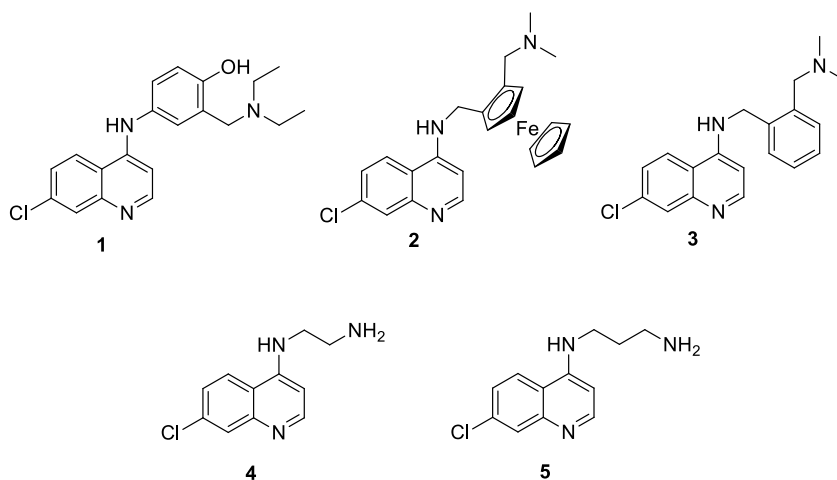
Figure 2.1: Chemical structures of the five 4-aminoquinoline antiplasmodial agents (**1 – 5**) used in this study.

Compound **1** (amodiaquine) is commercially available as the dihydrochloride dihydrate salt and is used in some combination therapies to treat malaria.[5] Compound **2** (ferroquine) is the first metallocene-containing antiplasmodial to reach clinical trials and is currently in phase II clinical trials for the treatment of malaria.[6] Compound **3** (phenylequine), the phenyl analogue of **2**, has been shown to have a similar efficacy to **2** against *P. falciparum*.[3] While possessing reasonable *in vitro* efficacies, compounds **4** and **5** were discarded as drug candidates due to poor physicochemical properties. We therefore thought that this series of five 4-aminoquinolines would be interesting to study in terms of the ability of these compounds to form multicomponent crystals, as well as what effect changes to the

structure would have on this ability. In addition to these reasons, these compounds all possess suitable functional groups to allow for intramolecular interactions with small organic coformers.

The first of these functional groups is the 4-amino moiety in each compound that can act as a hydrogen-bond donor or acceptor. Each compound also contains a quinoline ring that is known to form π-π interactions in the solid state.[7,8] Furthermore, the nitrogen atom in this ring can act as a hydrogen-bond acceptor. The tertiary nitrogen atom in the side chain of compounds **1 – 3** can act as a hydrogen-bond acceptor. Compound **1** contains an additional phenolic OH moiety that can form intermolecular interactions with a hydrogen-bond donor or acceptor. Finally, compounds **4** and **5** contain a primary amine, rather than a tertiary amine tail, that can act as a hydrogen-bond donor or acceptor.

Compounds **2** and **3** were chosen because we were interested in seeing what effect the ferrocene linker (in **2**) has on the ability to form multicomponent crystals in comparison to the phenyl linker (in **3**). Compounds **4** and **5** were chosen because they have a short alkyl chain as a linker instead of the phenyl or ferrocene moiety. We also wanted to see whether the length of the alkyl chain (and therefore the increased rotation in that chain) would influence the ability to form multicomponent crystals with these compounds.

With this series of compounds, we were confident that we would be able to obtain some insight into their ability to form multicomponent crystals and hopefully observe trends in which coformers resulted in the formation of these multicomponent crystals. Our first goal was to synthesise the desired compounds before choosing coformers to form multicomponent crystals.

2.2 SYNTHESIS OF THE ANTIPLASMODIAL AGENTS

Each of the five antiplasmodial agents have been synthesised previously and therefore the literature procedures were followed for each synthesis as discussed in the relevant sections below. In some cases, yields were lower than those obtained in the literature, but as sufficient amounts of the desired product was obtained in each case, no optimisation was attempted for any of the steps. Only a brief discussion of the synthesis of each compound is given below. Detailed synthetic procedures and characterisation data can be found in Chapter 6 (pages 123 – 131).

*2.2.1 Synthesis of amodiaquine free base (**1**)*

Amodiaquine dihydrochloride dihydrate was bought from Sigma-Aldrich (now Merck) and converted into the free base by stirring the salt in ammonia solution (25%) for 2 hours, followed by extraction into ethyl acetate. The solvent was removed under reduced pressure before the product was dissolved in a minimum amount of methanol (MeOH). After placing the vial in the fridge overnight, a pale yellow

precipitate was obtained, which was filtered and dried under high vacuum (88% yield).[9] [1]H nuclear magnetic resonance (NMR) spectroscopy confirmed that the desired product was obtained. Powder X-ray diffraction (PXRD), thermogravimetric analysis (TGA) and differential scanning calorimetry (DSC) were used to characterise the free base and results were compared to that of the hydrochloride salt (see Chapter 6, page 123) to prove that the product was no longer the salt. The crystal structure of the dihydrochloride dihydrate salt (CSD ref code: GIWLII01), as well as a propanol solvate of the free base (CSD ref code: SENJIF01) is available in the CSD. We attempted to form suitable single crystals of the free base using a variety of methods, but were unfortunately unable to obtain a crystal structure.

2.2.2 Synthesis of ferroquine (2)

The synthesis of ferroquine was carried out according to literature procedures as shown in Scheme 2.1.[10,11]
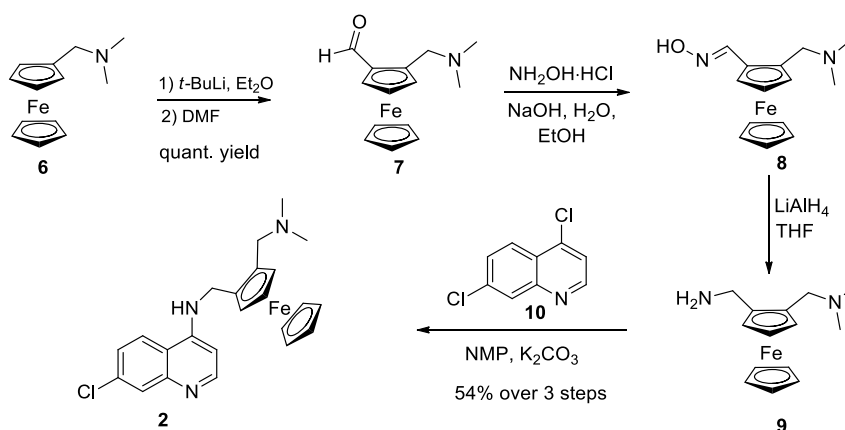
Scheme 2.1: Synthesis of **2**.

Commercially available *N,N*-dimethylaminomethyl ferrocene (**6**) was *ortho*-lithiated with 1.0 equivalent of freshly-titrated *tert*-butyllithium (*t*-BuLi) under a nitrogen atmosphere. It should be noted that while the use of *n*-butyllithium (*n*-BuLi) has been reported in the literature for these reactions,[11] the use of *t*-BuLi significantly reduces reaction times.[12] Because aldehyde product **7** can degrade over time, especially in solution,[12] minimising the reaction time results in an improvement of the yield of this reaction. Two hours after the *ortho*-lithiation of **6**, the bright orange suspension was quenched with anhydrous dimethyl formamide (DMF) forming the desired product in quantitative yield. The conversion of the aldehyde moiety into primary amine **9** was carried out via the formation of oxime **8**, without purification of the oxime intermediate. Finally, ferrocenyl amine **9** was coupled to commercially available 4,7-dichloroquinoline (**10**) to give ferroquine in a 54% yield after purification by flash column chromatography and subsequent recrystallisation from dichloromethane (DCM)/Hexane.
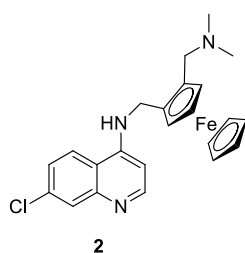
The ^{1}H NMR spectrum of **2** shows the characteristic singlet at 4.15 ppm integrating for 5H that corresponds to the unsubstituted cyclopentadiene ring of ferrocene. The characteristic splitting of the CH$_2$ protons in the ^{1}H NMR spectrum due to chirality, is also noted. The singlet integrating for 6H at 2.23 ppm corresponds to the two N-methyl groups. Five peaks were observed in the aromatic region, each integrating for 1H, which corresponds to the protons on the quinoline ring. All other protons were accounted for. It should be noted that the data correlated well with that reported in the literature.[11]

It is worth noting that 1,2-disubstituted metallocenes such as ferroquine (**2**) exhibit planar chirality and are therefore subject to a variation of the (*R*,*S*) nomenclature.[13] In Figure 2.3 below, the *R* and *S* configurations are shown for ferroquine. The synthesis described above results in the formation of the racemate, which can be resolved using *L*-tartaric acid.[12] It has, however, been shown that the racemate has slightly improved *in vitro* efficacy against *P. falciparum* in comparison to either enantiomer.[14] Because *in vivo* testing and clinical trials has made use of the racemate,[2] it was decided to continue with the formation of multicomponent forms of **2** without first resolving the racemate.
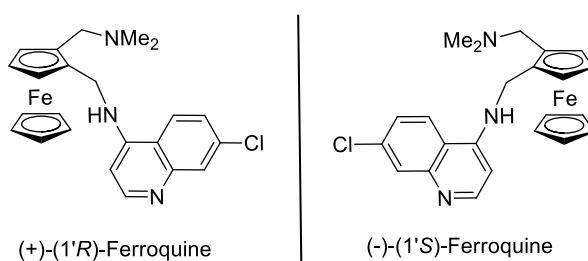
Figure 2.3: Enantiomers of **2**.

Single crystals of **2** were also obtained and the unit cell parameters of these crystals correlated well with the crystal structure of the racemate of ferroquine in the CSD. A powder X-ray diffraction (PXRD) pattern of the bulk material also correlated well with that of the predicted pattern obtained from single crystal data. While this structure is known, it is useful to study its inter- and intra-molecular interactions and packing in the solid state. Figure 2.2 shows the asymmetric unit of **2** (with the intramolecular hydrogen bond shown in black) as well as the packing of **2** viewed down the *a* axis.

(a)   (b)
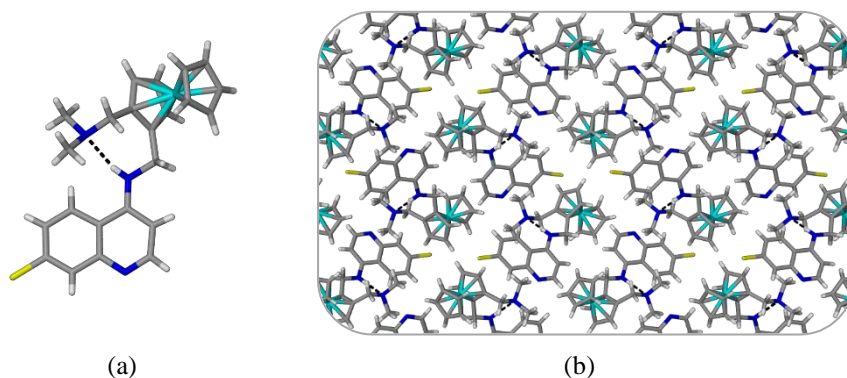
Figure 2.2: (a) The asymmetric unit of **2** showing the intramolecular hydrogen bond; (b) packing of **2** viewed down the *a* axis. CSD ref code: LEZNIO.

The dominant hydrogen bond present in the crystal structure of **2** is the intramolecular N–H⋯N interaction between the secondary amine (4-amino moiety) and the side chain nitrogen atom of the molecule. Other weaker interactions are present and contribute to the overall packing and stability of molecules in the solid state.

2.2.3 Synthesis of phenylequine (*3*)

The synthesis of **3** follows similar procedures as for ferroquine, which can be seen in Scheme 2.2, but begins with commercially available *N,N*-dimethylaminomethyl benzene (**11**).[12] The final product was obtained as a white crystalline powder in 48% yield over the last three steps after purification by flash column chromatography and subsequent recrystallisation from DCM/Hexane.
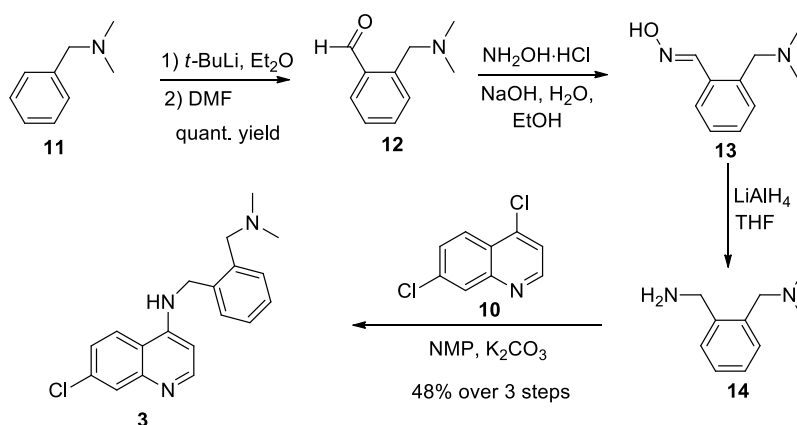
Scheme 2.2: Synthesis of **3**.
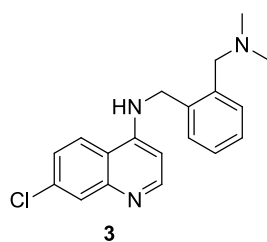
The ^{1}H NMR spectrum of **3** shows a singlet integrating for 6H corresponding to the methyl protons as well as the five peaks, each integrating for 1H, in the aromatic region that corresponds to the protons on the quinoline ring. Here, the splitting of the CH_2 protons is not observed (as for **2**) as there is no chirality. Instead the two singlets, each integrating for 2H, at 4.47 ppm and 2.29 ppm, correspond to the two CH_2 groups on **3**. All other protons are accounted for and the data compared well with the values found in the literature.[3]

A crystal structure was obtained from crystals that grew from the NMR spectroscopy sample of **3**. Compound **3** packs in the tetragonal space group $P\bar{4}2_1/c$. An N–H···N hydrogen bond (2.900 Å) between the *NH*-moiety of one molecule and the quinoline nitrogen atom of a second molecule results in the formation of chains of molecules that extend parallel to the crystallographic *c* axis (Figure 2.4). These chains of molecules then pack in three dimensions, resulting in the solid-state structure. Selected crystallographic data can be found in Table 2.1. Hydrogen-bonding geometries can be found in Chapter 6, page 130.

(a)   (b)

(c)
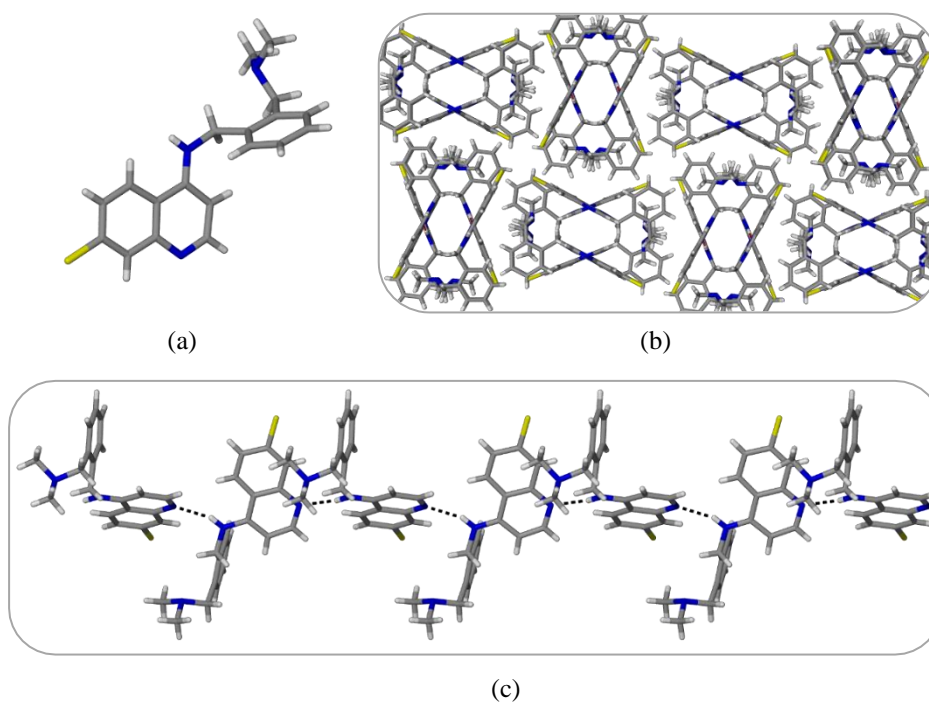
Figure 2.4: (a) The asymmetric unit of **3**; (b) packing of **3** viewed down the *c* axis and (c) hydrogen-bonded chains of **3** viewed down the *a* axis.

Table 2.1: Selected crystallographic details for **3**.

	3
Molecular formula	$C_{19}H_{20}N_3Cl$
Formula weight (g/mol)	325.83
Crystal system	Tetragonal
Space group	$P\bar{4}2_1/c$
Z	8
a (Å)	15.932(2)
b (Å)	15.932(2)
c (Å)	13.334(1)
α (°)	90
β (°)	90
γ (°)	90
Volume (Å^3)	3377.0(5)
Temperature (K)	100(2)
R_{int}	0.054
R_1 [I>2σ(I)]	0.025
wR_2	0.065
GoF	1.08

Surprisingly, the hydrogen-bonding interactions within the solid-state structure of **2** (CSD ref code: LEZNIO) are remarkably different to those of **3**. While it was expected that the ferrocene moiety would influence the packing of the molecules in the solid state, it seemed likely that a similar intramolecular hydrogen-bonding motif between the secondary amine (4-amino moiety) and the amino side chain (Figure 2.5a) would be observed in **3**. This, however, is not the case. Rather, the dominant interaction in **3** is the intermolecular hydrogen bond between the 4-amino moiety and the quinoline nitrogen atom of two molecules (Figure 2.5b).

(a)   (b)
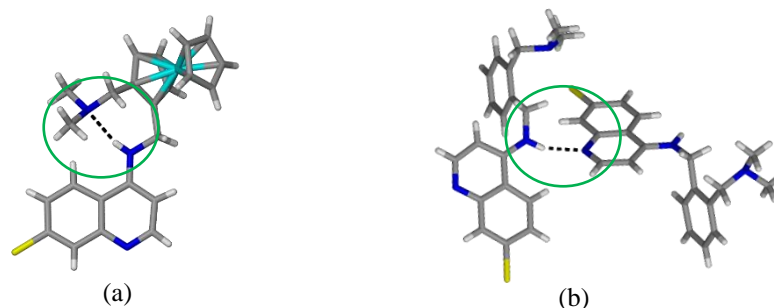
Figure 2.5: The structure of (a) **2** (CSD ref code: LEZNIO) and (b) **3** obtained from single crystal X-ray diffraction data. Circled in green is the dominant hydrogen-bonding interaction for each molecule.

This intramolecular hydrogen bond in **2** has been observed in solution as well as in the solid state.[15] While the intermolecular interactions found in **3** may well be seen in solution too, these assumptions cannot be made with only this data. The differences in the efficacy of these two compounds could be related to the intra- or intermolecular bonding; however, it would be inaccurate to infer this solely based on the crystal structure of each compound. While this would be interesting to study further, it would require extensive pharmaceutical investigation, which is beyond the scope of this study. Rather, we chose to focus on what difference these interactions have on the ability of these compounds to form multicomponent crystals.

*2.2.4 Synthesis of N^1-(7-chloroquinolin-4-yl)ethane-1,2-diamine (**4**)*

The synthesis of **4** follows a one-step procedure (Scheme 2.3) where 4,7-dichloroquinoline (**10**) was added to an excess of 1,2-diaminoethane and, after neutralising with a saturated solution of sodium carbonate, afforded the desired product as a pale yellow crystalline solid in 58% yield.
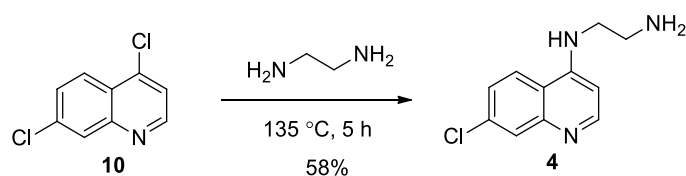
Scheme 2.3: Synthesis of **4**.
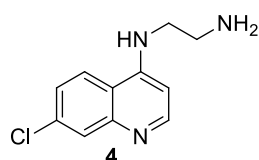
The ^{1}H NMR spectrum of **4** confirmed that the desired product was obtained. Two triplets at 3.31 ppm and 2.68 ppm, each integrating for 2H, corresponded to the two methylene protons in the side chain. The five peaks in the aromatic region, each integrating for 1H, correlated to the protons on the quinoline ring. The infrared spectrum shows a primary amine stretch at 3247 cm^{-1}. Finally, the spectroscopic data correlates well with that obtained from the literature.[4,16]

*2.2.5 Synthesis of N^1-(7-chloroquinolin-4-yl)propane-1,2-diamine (**5**)*

The synthesis of **5** follows the same procedure described for **4** above, but uses 1,3-diaminopropane as the nucleophile in the coupling reaction. As a result, the desired product was obtained as a pale yellow powder in 71% yield.
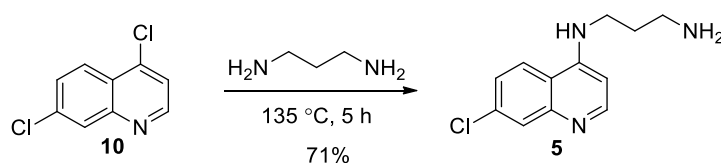
Scheme 2.4: Synthesis of **5**.
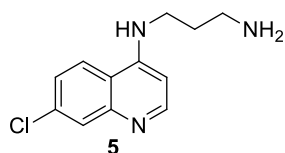
The ^{1}H NMR spectrum of **5** showed three peaks corresponding to the protons on the alkyl chain – one multiplet (1.77 – 1.68 ppm) and two triplets (at 3.32 ppm and 2.68 ppm) – each integrating for 2H. The five peaks in the aromatic region, each integrating for 1H, correspond to the protons on the quinoline ring. The primary amine stretch in the infrared spectrum was observed at 3350 cm^{-1}. These data corresponded well with the literature values.[4,16]

As the crystal structures of **4** and **5** are not available on the CSD, attempts were made to obtain diffraction-quality single crystals for each of them using a variety of solvents as well as sublimation techniques; however, all attempts so far have been unsuccessful. Despite this lack of crystal data, we set out to form multicomponent crystals of each of the five antiplasmodial compounds, using a variety of coformers.

2.3 *SELECTION OF COFORMERS*

Having synthesised the five antiplasmodial agents, our next step was to form multicomponent crystals with each of them. Before this could be done however, we would need to select appropriate small organic molecules (coformers), which would be used to form the multicomponent crystals.

In the field of pharmaceuticals, only certain coformers are allowed to be used that are known to be safe for human consumption. There are two main databases available – GRAS (generally regarded as safe) and EAFUS (everything added to food in the United States) that provide a list of tested compounds that can be used in food and medication, amongst other things.[17,18] Many of the potential drug molecules (including antiplasmodial agents) that are synthesised require a multistep synthesis and therefore a full experimental screen with many coformers is simply not feasible as it requires large quantities of the drug molecule. This can thus be an expensive endeavour. While the use of only 'safe' molecules limits the number of coformers that could be used to form multicomponent crystals of our molecules, there are still far too many compounds on these lists and therefore an additional method would be needed to further refine our list.

The most widely used method of choosing coformers is the synthon approach that involves molecular complementarity between functional groups on each molecule.[19] By identifying the types of functional groups on our molecules (as discussed in the beginning of this chapter), coformers with complementary functional groups can be identified. In our molecules, the aromatic rings can form π-π interactions with aromatic coformers. The quinoline nitrogen atom, the 4-amino moiety and the side chain nitrogen atom can form intermolecular interactions with alcohols, amides or carboxylic acids, with carboxylic acids being most prevalent in the literature.[20] Based on this logic, coformers containing either a carboxylic acid moiety, or aromatic ring (or both), would be likely to yield multicomponent crystals; however, there

is no guarantee of this. In addition to favoured intermolecular interactions, the shape of both the antiplasmodial compound and the coformer can have a large influence on the outcome of cocrystallisation.[21] The compromise between a number of variables dictates, in each case, the outcome of the attempted cocrystallisation. Essentially, this means that the multicomponent crystal will only form if it is more favourable than the crystallisation of the single components.

Despite narrowing down the list of coformers to choose from, there is still a great deal of uncertainty in which might be successful. Hence, being able to at least somewhat predict the likelihood of whether a multicomponent form of the drug can be obtained with a specific coformer would be valuable. Unfortunately, the current knowledge on crystal structure prediction does not allow for accurate predictions in a high throughput fashion.[22]

Nonetheless, in pursuit of marginal gains of predictability, and to further narrow our choice of coformers, we decided to investigate the use of a "virtual" screening method based on computational calculations to provide a list of coformers that are more likely to form multicomponent forms of each of the five molecules discussed above. A method described by Hunter and coworkers makes use of molecular electrostatic potential surfaces (MEPS) to calculate surface site interaction points on each molecule that, after some simple calculations, provides a ranked list of coformers that would be more likely to form multicomponent crystals.[23,24] This method has been used successfully in obtaining multicomponent forms of some drug molecules, including caffeine, carbamazepine, nalidixic acid and spironolactone.[25–28]

A key advantage of this method is that prior knowledge of the crystal structure and intra- and inter-molecular interactions of the components is not required. While this does not necessarily give the most accurate depiction of the solid-state geometries, it does provide a robust method that can be applied to any drug molecule and coformer of choice. A second advantage of this approach is that both conventional hydrogen-bonding interactions, as well as weaker electrostatic interactions are taken into account through the identification of the surface site interaction points on each molecule. This gives a reasonable mathematical description of the surface properties of the molecule that can then be used to calculate the total interaction of the molecule with its surrounding environment.

Because this approach makes use of gas-phase calculations, there is some degree of inaccuracy since the experimental screening would most likely take place in the solid or solution state. This approach also assumes that all possible interactions that can be made, are made and the molecular shape and packing within a crystal lattice is of lesser importance than the interactions between donor and acceptor sites. However, the advantage of efficiency and straight forward calculations makes this method viable for use with larger libraries of potential coformers. We therefore decided to make use of this method in our attempt to narrow down the list of potential coformers, so that experimental screening could be limited to the most likely candidates.

To this end, each antiplasmodial agent and potential coformer was drawn in ChemCraft and a geometry optimisation was performed in Gaussian 09 at the B3LYP/6-31+G* level of theory.[25,29] This level of theory is limited to the first 36 elements of the periodic table (H – Kr) and therefore there is a limitation in the types of molecules that can be investigated. Alternative basis sets are available that accommodate heavier atoms, but the geometry optimisations for all molecules (drug and coformers) would need to be carried out with this basis set in order to accurately complete the calculations. Once optimised, the molecular electrostatic potential was mapped onto the 0.002 Bohr Å^{-3} isodensity surface using AIMAll software.[30] Figure 2.6 gives an example of the MEPS of **1** and oxalic acid (set to the same colour scale for comparative purposes).

(a)   (b)
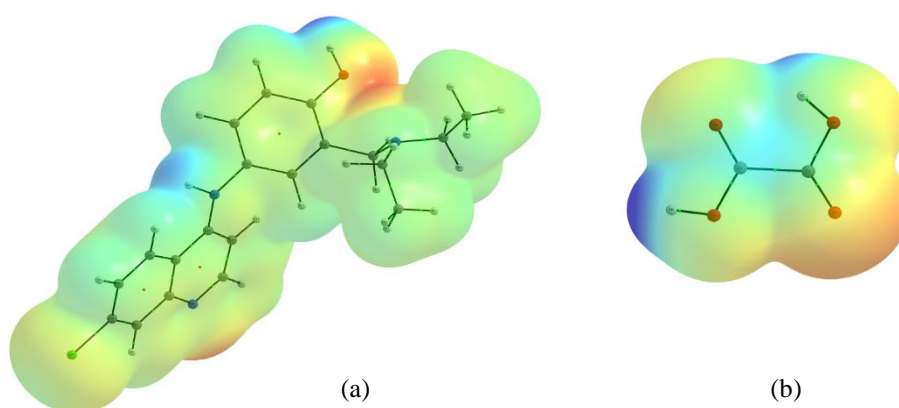
Figure 2.6: (a) Molecular electrostatic potential surface of (a) **1** and (b) oxalic acid indicating the local maxima and minima (blue +315 kJ mol^{-1} to red -207 kJ mol^{-1}) used to determine the hydrogen-bond interaction sites, α and β.

Local minima and maxima were located for each molecule on the MEPS surface and equations (1) and (2) were used to calculate the hydrogen-bond interaction sites, α and β, at each minimum and maximum.

$$\alpha = 0.0000162\ MEP_{max}^2 + 0.00962\ MEP_{max} \qquad (1)$$
$$\beta = 0.000146\ MEP_{min}^2 - 0.00930\ MEP_{min} \qquad (2)$$

where MEP_{max} and MEP_{min} are local maxima and minima on the MEPS in kJ mol^{-1}.

The highest α value corresponds to the best donor site, while the highest β value corresponds to the best acceptor site. Assuming that the highest α value will interact with the highest β value and so forth, the list of α and β values for each molecule were arranged in descending order. This allowed us to calculate the total interaction site pairing energy of each solid, E, using equation (3).

The likelihood of a multicomponent crystal forming between the two components (ΔE) can be calculated by simply subtracting the energy of each component from that of the multicomponent form using equation (4).

$$E = -\sum_{ij} \alpha_i \beta_j \qquad (3)$$

$$\Delta E = E_{cc} - nE_1 - mE_2 \qquad (4)$$

where E_1 is the interaction site pairing energy of the pure form of the antiplasmodial agent (component 1) and E_2 is the interaction site pairing energy of the pure form of the coformer (component 2). The interaction site pairing energy of the multicomponent product of component 1 and is given by E_{cc}. Stoichiometry can be included by varying the *n* and *m* values.

The ΔE values for each combination of antiplasmodial agent and coformer in a 1:1 ratio were then calculated. The more negative the ΔE value, the more likely it is to form a multicomponent product with those two components. Therefore, these values were arranged in descending order to provide a ranked list of potential coformers that would most likely form multicomponent crystals with each antiplasmodial compound. The top ten coformers are reported in Table 2.2 for each compound, along with the ΔE values associated with them. The full list of 32 potential coformers and their corresponding ΔE values can be found in Chapter 6 (page 132).

Table 2.2: Ranked list of top ten coformers for each antiplasmodial compound and their corresponding ΔE values (kJ mol^{-1}).

1		2		3		4		5	
coformer	-ΔE	coformer	-ΔE	coformer	-ΔE	coformer	-ΔE	coformer	-ΔE
OXA	12.1	OXA	24.5	OXA	14.6	OXA	15.5	FUM	22.5
DHBA	9.0	DHBA	19.0	DHBA	10.7	PAM	10.3	OXA	18.4
TRIM	8.4	FUM	18.4	FUM	9.1	TRIM	10.0	TRIM	13.5
FUM	7.6	TRIM	17.0	IND	8.5	BIPY	9.0	DHBA	13.2
PAM	6.9	MAL	16.8	PAM	8.2	PYZ	8.2	PAM	12.9
RES	6.7	PAM	16.8	TRIM	8.1	DHBA	8.1	RES	10.9
IND	6.4	IND	16.2	RES	7.7	FUM	7.7	IND	9.9
MAL	4.9	RES	16.1	MAL	7.3	IND	7.5	MAL	9.2
TERE	4.9	TERE	15.7	TERE	6.6	RES	7.2	TERE	8.7
SAL	4.3	SUC	15.2	*p*ABA	6.1	VAN	6.8	SUC	7.7

Coformer codes: OXA – oxalic acid, DHBA – 3,5-dihydroxybenzoic acid, TRIM – trimesic acid, FUM – fumaric acid, PAM – pamoic acid, RES – resorcinol, IND – indole, MAL – malonic acid, TERE – terephthalic acid; SAL – salicylic acid, SUC – succinic acid, *p*ABA – *p*-aminobenzoic acid, BIPY – 4,4-bipyridine, PYZ – pyrazine, VAN – vanillin.

Looking at the outcome of the virtual screening methods, it is noted that there is a large degree of overlap in the types of coformers that are likely to form multicomponent crystals with each antiplasmodial agent. It is evident that carboxylic acids, in most cases, dicarboxylic acids, are most favourable in terms of forming multicomponent crystals with **1** to **5**. This is not surprising, given that each antiplasmodial compound contains at least one nitrogen atom that can act as a hydrogen-bond acceptor for the OH moiety on the carboxylic acid coformer. Having said this, there are still a large number of possible carboxylic acid coformers that could have been used. This method, then, provided a starting point for which carboxylic acid coformers to try first. What is somewhat unexpected, however, is the inclusion of coformers such as indole, 4,4-bipyridine and pyrazine. As most of the functional groups on our molecules are hydrogen-bond acceptors, pairing them with other hydrogen-bond acceptors such as pyrazine does not seem likely to result in a multicomponent product. Here, however, it is likely that π-π interactions would play a more dominant role if multicomponent products are obtained with these coformers. With our list in hand, we set out to validate this computational screening method by carrying out experimental cocrystallisations with these coformers to form multicomponent crystals.

2.4 FORMATION OF MULTICOMPONENT CRYSTALS

There are a number of methods that can be used to form multicomponent crystals.[31] Two of the more popular methods are solvent evaporation or mechanochemistry. The antiplasmodial compounds in this study (especially **1**, **4** and **5**) are not very soluble in many organic solvents (with the exception of hot MeOH and DMSO). Therefore, while solution cocrystallisations would be possible, it is likely that the antiplasmodial agent would simple "crash out" of solution in each case, as it is substantially less soluble than the coformers. The use of mechanochemisty – grinding the components together – avoids solubility issues like these and is therefore a more versatile method. In addition, mechanochemistry is faster than solution-based methods for forming multicomponent products.[32] For these reasons, mechanochemistry (and specifically liquid-assisted grinding methods) was chosen for our experimental screening, together with PXRD to analyse the outcome.

Mechanochemical cocrystallisation can be carried out manually (using a mortar and pestle) or using a ball mill. We opted to make use of manual grinding, since considerably less sample is needed in comparison to the ball mill. In cases where cocrystallisation is successful, upscaling to form more product is then possible with the ball mill.

For the purpose of this study, the top ten coformers for each drug molecule were chosen from the virtual screening to perform the experimental screening. Stoichiometric amounts (1:1 ratio) of each compound (10 mg) and coformer were thus ground together in a mortar and pestle for 5 minutes with a few drops of MeOH. While other ratios are certainly possible, we chose to start with a 1:1 ratio due to simplicity. This could be expanded to other ratios at a later stage should it be necessary. PXRD was then used to

determine whether a new form had been obtained or whether only a mixture of starting materials remained by comparing the PXRD pattern of the new powder to that of each individual component. The outcomes of the experimental screening are discussed below.

Each of the five antiplasmodial compounds, as well as the coformers, were individually ground using the same conditions as described above to confirm that a new product (such as a polymorph, solvate, hydrate etc.) is not obtained simply by grinding the individual components. Grinding could also result in the amorphisation of the sample and therefore this needed to be established before beginning the cocrystallisation screening.[33] In all cases, the PXRD pattern obtained after grinding the component matched that of the pre-ground material, indicating that no new or amorphous product is obtained from individual components under these conditions.

2.4.1 Outcome of liquid-assisted grinding experiments

For each grinding experiment, the PXRD pattern of the product was compared to that of the individual components to determine whether or not a new product was obtained. The PXRD patterns of the successful attempts can be found in Chapter 6 (page 134 to 140). The remaining combinations only yielded starting material after liquid-assisted grinding, even after grinding for an additional 5 minutes.

As an example, one of the successful attempts are discussed in this chapter in detail, and a summary of the remaining successful combinations given. In Figure 2.7, the PXRD patterns of **4** (blue), pamoic acid (green) and the new multicomponent form obtained after grinding the components for 5 minutes in a mortar and pestle with a few drops of methanol (maroon) are shown. It can be seen that the new pattern does not correspond to a physical mixture that of the two individual components. It is also evident that there is no remaining starting material present in the product's PXRD pattern, indicating that a 1:1 ratio of each component is present in the new multicomponent product.
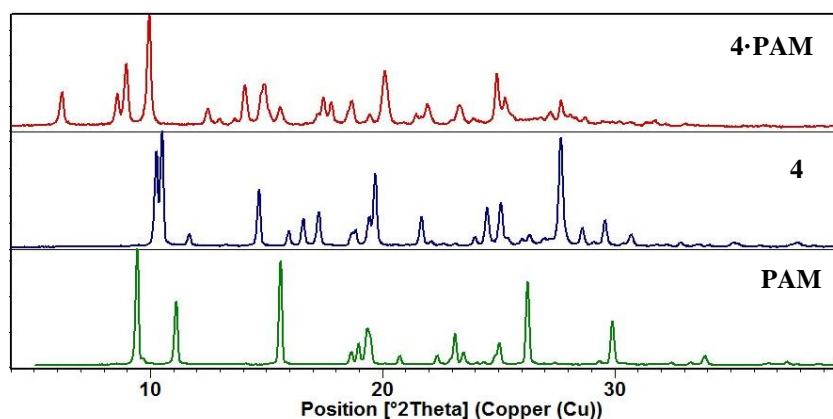
Figure 2.7: Comparison of the PXRD patterns of the two individual components, **4** (blue) and pamoic acid (**PAM**, green), and the new multicomponent form produced from LAG (**4·PAM**, maroon).

In total, 19 new products were obtained, 13 of which were crystalline and 6 of which were amorphous, as determined by PXRD. This results in a 38% success rate in forming new multicomponent forms of these antiplasmodial agents with the top ten coformers identified by the computational screening. A summary of the successful attempts can be seen in Table 2.3 (for compounds **1** – **3**) and Table 2.4 (for compounds **4** and **5**).
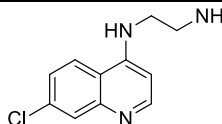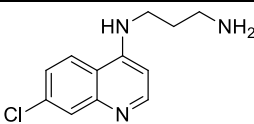
Table 2.3: Outcomes of experimental screening of the top ten coformers with **1 – 3**.

1			**2**			**3**		
Coformer*	**-ΔE** **(kJ mol⁻¹)**	**LAG** **outcome****	**Coformer***	**-ΔE** **(kJ mol⁻¹)**	**LAG** **outcome****	**Coformer***	**-ΔE** **(kJ mol⁻¹)**	**LAG** **outcome****
OXA	12.1	MCC	OXA	24.5	A	OXA	14.6	MCC
DHBA	9.0	SM	DHBA	19.0	SM	DHBA	10.7	MCC
TRIM	8.4	A	FUM	18.4	SM	FUM	9.1	SM
FUM	7.6	MCC	TRIM	17.0	A	IND	8.5	MCC
PAM	6.9	SM	MAL	16.8	SM	PAM	8.2	SM
RES	6.7	SM	PAM	16.8	SM	TRIM	8.1	SM
IND	6.4	SM	IND	16.2	SM	RES	7.7	MCC
MAL	4.9	SM	RES	16.1	SM	MAL	7.3	MCC
TERE	4.9	MCC	TERE	15.7	SM	TERE	6.6	SM
SAL	4.3	SM	SUC	15.2	SM	*p*ABA	6.1	SM

*Coformer codes: OXA – oxalic acid, DHBA – 3,5-dihydroxybenzoic acid, TRIM – trimesic acid, FUM – fumaric acid, PAM – pamoic acid, RES – resorcinol, IND − indole, MAL – malonic acid, TERE – terephthalic acid; SAL – salicylic acid, , SUC – succinic acid, *p*ABA – *p*-aminobenzoic acid.

**LAG outcome: MCC = new multicomponent crystalline material, A = amorphous product and SM = only starting materials remained after grinding.

Table 2.4: Outcomes of experimental screening of the top ten coformers with **4** and **5**.

Coformer*	-ΔE (kJ mol⁻¹)	LAG outcome**	Coformer*	-ΔE (kJ mol⁻¹)	LAG outcome**
OXA	15.5	MCC	FUM	22.5	SM
PAM	10.3	MCC	OXA	18.4	A
TRIM	10.0	MCC	TRIM	13.5	SM
BIPY	9.0	SM	DHBA	13.2	SM
PYZ	8.2	SM	PAM	12.9	SM
DHBA	8.1	SM	RES	10.9	SM
FUM	7.7	MCC	IND	9.9	SM
IND	7.5	MCC	MAL	9.2	A
RES	7.2	SM	TERE	8.7	SM
VAN	6.8	SM	SUC	7.7	A

*Coformer codes: OXA – oxalic acid, PAM – pamoic acid, TRIM – trimesic acid, BIPY – 4,4-bipyridine, PYZ − , pyrazine, DHBA – 3,5-dihydroxybenzoic acid, FUM – fumaric acid, IND – indole, RES – resorcinol, VAN – vanillin; MAL – malonic acid, TERE – terephthalic acid; SUC – succinic acid.
**LAG outcome: MCC = new multicomponent crystalline material, A = amorphous product and SM = only starting materials remained after grinding.

Compound **1** yielded four new multicomponent forms, all with carboxylic acid coformers. Three of these forms were crystalline and only one was amorphous. Compound **2** yielded only two multicomponent forms, both of which were amorphous. Compound **3** yielded five multicomponent forms, all of which were crystalline. Three of the coformers were carboxylic acids, while one was a phenol and the other an indole. Compound **4** yielded five new multicomponent crystals, all of which were crystalline. All except for one made use of carboxylic acids as coformers. Compound **5** yielded three multicomponent forms, all of which were amorphous and made use of carboxylic acid coformers.

It is interesting that compounds **2** and **5** give only amorphous products, while **3** and **4** give only crystalline products. Since each component remains crystalline after grinding them separately under the same conditions, the formation of the multicomponent product for **2** and **5** is likely inducing amorphisation, rather than the grinding. For compound **2**, the shape of the molecule or the fact that it is racemic could be influencing the amorphous outcome. Compound **5** contains the extended alkyl chain that, due to the rotational freedom, could be causing a disruption in the packing of these molecules in a uniform manner when the coformer is included.

It should be highlighted that obtaining an amorphous multicomponent product is not considered a failure from a pharmaceutical point of view. Amorphous materials are often prepared using mechanochemistry

to improve the dissolution of a drug molecule.[34–36] Unfortunately, obtaining amorphous material makes studying the intermolecular interactions challenging as they cannot be analysed with X-ray diffraction.

For the 7 amorphous multicomponent forms, extended grinding times were also investigated because, in some cases, the formation of multicomponent forms of molecules are known to go through an amorphous phase before crystallisation as the new multicomponent form.[37,38] In our case, however this was not observed after an additional 10 minutes of grinding.

When comparing the outcomes of **2** and **3**, the obvious difference is that **2** only forms two multicomponent forms (both of which are amorphous), while **3** forms five (all of which are crystalline). The ferrocene moiety in **2**, in comparison to the phenyl moiety in **3**, is likely the reason for this outcome. The bulkiness of the ferrocene moiety might be playing a role as well as the intra- and inter-molecular interactions in each compound. In the case of **2**, the quinoline nitrogen atom is inaccessible through an intramolecular hydrogen bond with the NH moiety at the 4-position of the quinoline. While it is possible that some coformers could give rise to intermolecular interactions that are more favourable than the N–H⋯N intramolecular interaction, it seems that for the majority of the coformers that we tried, this was simply not the case. In compound **3**, however, this intramolecular interaction is not present, leaving that nitrogen atom available to interact with other molecules.

When comparing compounds **4** and **5**, it seems that the shorter side chain increases the ability of the compound to form crystalline multicomponent products. In addition, the additional rotational freedom of the side chain of **5** could be hindering efficient packing of the molecules during cocrystallisation.

2.4.2 Characterising the new multicomponent products

Attempts were made to form single crystals of each of the newly-formed multicomponent products by dissolving them in hot MeOH. In many cases, the product was insoluble in MeOH and therefore DMSO was used; however, this was also unsuccessful in dissolving many of the products. In cases where the product did dissolve, allowing the solvent to slowly evaporate did not yield any single crystals. In the majority of the attempts, a sticky residue was obtained that could not be analysed by PXRD. For some attempts, a powdered product was obtained and PXRD confirmed that the same product was formed as obtained in the liquid-assisted grinding (LAG) experiment.

Because we could not obtain single crystals and therefore could not characterise these new products using single crystal X-ray diffraction, it was necessary to make use of other spectroscopic and analytical techniques to provide additional insight into these systems. Fourier-transform infrared (FT-IR) spectroscopy was used to establish if proton transfer had taken place between the carboxylic acid coformer and the antiplasmodial agent during the formation of the new multicomponent product. Studying the carboxylic acid/carboxylate stretch in the IR spectrum of the coformer and new

multicomponent product, we could suggest whether proton transfer had occurred or not.[31] If proton transfer had occurred, the multicomponent product is classified as a salt, while if no proton transfer occurs, it is classified as a cocrystal. It should be noted that proton transfer is not always observed discretely, but that rather a continuum exists between the two extremes.[39] Therefore it is also possible to observe partial proton transfer between the two components. In these cases, it is difficult to observe a distict shift in the C=O stretch on the FT-IR spectrum.

The FT-IR spectra for the multicomponent products of each antiplasmodial agent with oxalic acid is shown as an example below. The carbonyl stretch of the carboxylic acid has shifted in wavenumbers after grinding, as highlighted by the blue shaded block in Figure 2.8. This blue shift indicates that proton transfer has taken place between the carboxylic acid moiety and one of the nitrogen atoms on the antiplasmodial agent. Unfortunately, it is difficult to say with certainty which nitrogen atom is acting as the hydrogen-bond acceptor; however, it is likely to be the tertiary nitrogen atom in the side chain as it is most basic in nature. In addition, the phenolic OH stretch of the carboxylic acid is no longer seen (green shaded area in Figure 2.7), which further indicates that a salt has formed. The FT-IR spectra for all multicomponent products obtained can be found in Addendum B (electronic supplementary information).
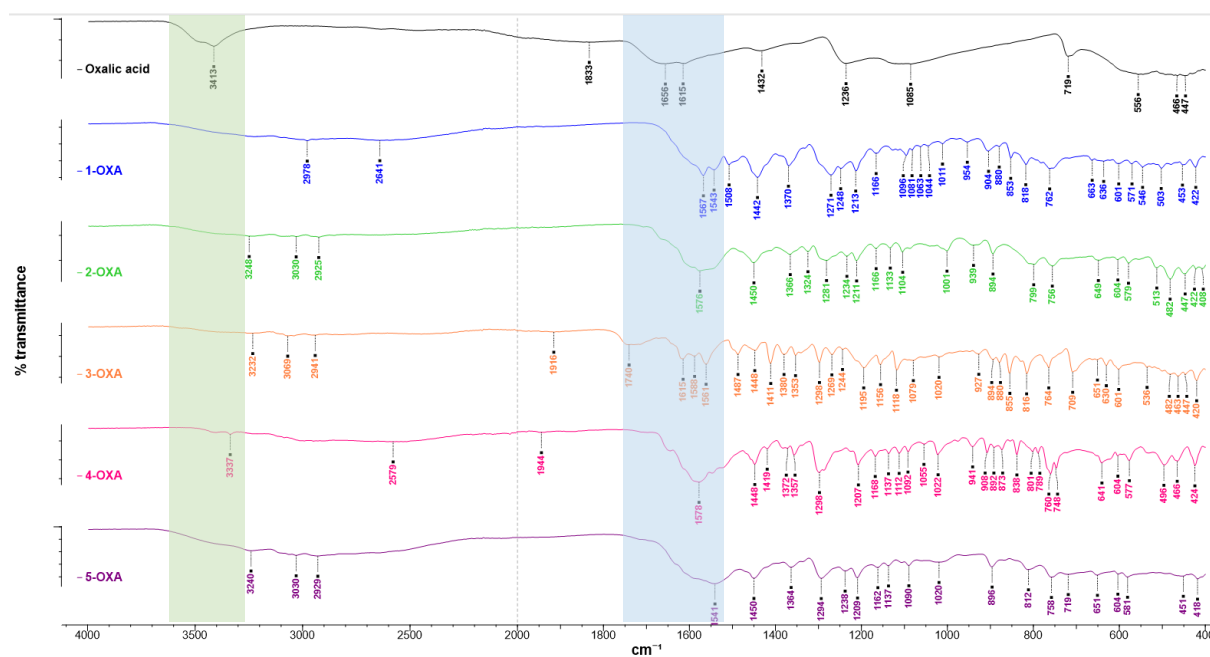
Figure 2.8: Comparison of the FT-IR spectrum of oxalic acid and the multicomponent forms obtained with compounds **1 – 5**. Highlighted in the blue shaded block is the carboxylic acid/carboxylate C=O stretch region. Highlighted in the green shaded block is the carboxylic acid OH stretch region.

Table 2.4 summarises whether each multicomponent form obtained with carboxylic acid coformers in particular, is a salt or cocrystal, based on the shift in the carboxylic acid C=O stretch. For the majority of the multicomponent forms, proton transfer was evident. For **3·MAL** and **4·PAM**, no significant change in the carbonyl stretch was noted, indicating cocrystal formation. For **4·FUM** and **4·TRIM**, the shift in the peak was not as prominent and it is likely that partial proton transfer is occurring in these compounds.

Table 2.4: Summary of multicomponent forms of **1** – **5** obtained with carboxylic acid coformers – salt versus cocrystal outcomes.

Multicomponent form	C=O stretch of coformer (cm⁻¹)	C=O stretch of multicomponent form (cm⁻¹)	Salt / coformer
1·OXA		1567	Salt
2·OXA*		1592	Salt
3·OXA	1656	1588	Salt
4·OXA		1578	Salt
5·OXA*		1541	Salt
1·FUM	1658	1567	salt
4·FUM		1617	Salt/cocrystal†
1·TRIM*		1607	Salt
2·TRIM*	1691	1607	Salt
4·TRIM		1646	Salt/cocrystal†
3·MAL	1693	1697	Cocrystal
5·MAL*		1539	Salt
1·TERE	1673	1547	Salt
3·DHBA	1681	1588	Salt
4·PAM	1647	1637	Cocrystal
5·SUC*	1683	1537	Salt

* amorphous products

† Shift in the C=O stretch is not as pronounced as for the other cases and it is likely that there is only partial proton transfer in these cases.

Non-acidic coformers were used in the formation of **3·IND**, **3·RES** and **4·IND** and therefore a salt is not likely to have formed. For **3·RES**, the phenolic OH moiety of resorcinol is most likely hydrogen bonding to one of the nitrogen atoms in **3**, resulting in the formation of a cocrystal. The IR spectrum of **3·RES** shows an OH-stretch at 3063 cm⁻¹, slightly lower in wavenumber to that of the OH peak in

Stellenbosch University https://scholar.sun.ac.za

Chapter 2: Forming multicomponent crystals of known antiplasmodial agents

resorcinol. For **3·IND** and **4·IND**, the NH stretch at 3394 cm^{-1} of indole can be seen in the IR spectrum of **3·IND** at 3397 cm^{-1}, indicating no proton transfer.

We also investigated the thermal stability of these systems in comparison to their individual components. This was carried out using TGA and DSC. Figure 2.9 shows the thermal analysis for **4·OXA** in comparison to the two individual components. Oxalic acid melts at 102.5 °C, while **4** melts at 138.3 °C. The multicomponent form has increased thermal stability, with the first endotherm in the DSC being observed at 162.9 °C. This correlates to the melt (as observed visually with a melting point machine) and followed soon after by decomposition of the material. The thermal analysis for the remaining multicomponent forms can be found in Chapter 6 (page 141 – 150).
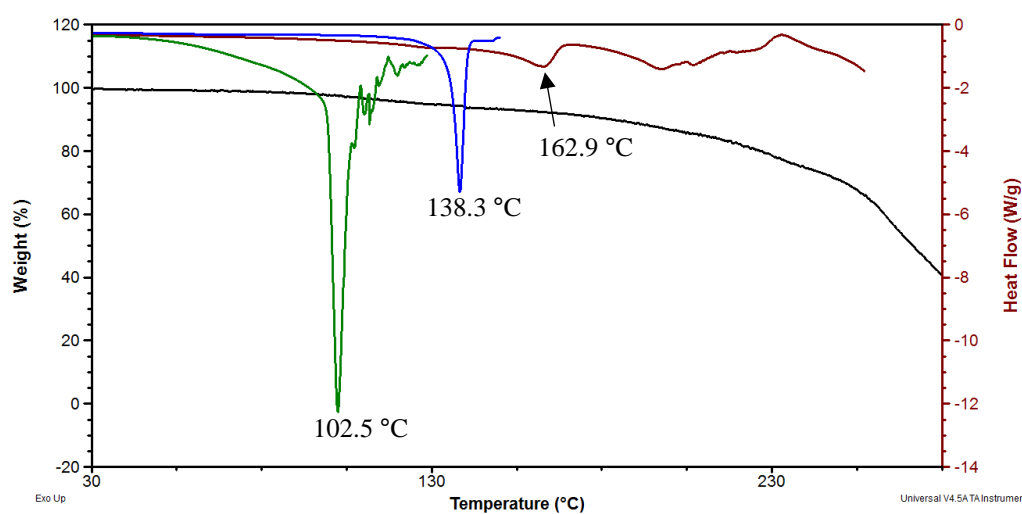
Figure 2.9: Thermal analysis of **4·OXA** in comparison to its individual components. The TGA trace of **4·OXA** is shown in black, the DSC trace of **4·OXA** is shown in maroon, the DSC trace of **4** is shown in blue and the DSC trace of oxalic acid is shown in green.

For many of the multicomponent forms, an initial mass loss on the TGA indicated that solvent is removed upon heating. Calculations suggest that it is most likely H_2O or MeOH, or a combination of both. This was also observed visually using a hot-stage microscope where a small amount of the powder was placed under oil and heated. Bubbles were observed at temperatures corresponding to the initial mass loss indicated in the TGA analysis, proving that MeOH or H_2O was indeed being released. After the release of the MeOH or H_2O molecules, a melt is observed on the DSC followed, often immediately, by the decomposition of the product.

2.5 CONCLUDING REMARKS

This chapter investigated the formation of multicomponent crystals of five 4-aminoquinoline antiplasmodial agents. The compounds were synthesised using literature methods and characterised using NMR, IR, TGA, DSC, PXRD and in the case of **2** and **3**, SCXRD. While the crystal structure of **2** is known, the crystal structure of **3** has not been previously reported. Obtaining this structure allowed us to compare the solid-state interactions of **2** and **3** that provided insight into the differences in intermolecular interactions and solid-state packing between the two compounds.

A total of 19 novel multicomponent forms of the five antiplasmodial agents were obtained, of which 13 were crystalline and 6 of which were amorphous. This resulted in a 38% success rate in the computational screening method. While this figure is lower than the systems described by Hunter and coworkers,[26–28] the systems in this study do not possess as many hydrogen-bonding sites as the ones in their studies. It is also likely that a larger screening pool may have yielded an alternative top ten list that could have resulted in a higher success rate. While not as successful as hoped, the method still proved useful in the choice of coformers.

As the MEPS calculations are carried out in the gas phase and the experiments are carried out in the solid phase, it is possible that this is influencing this success rate. While sublimation (gas-phase) techniques are possible, its use as a screening tool is challenging because of the time involved as well as the optimisation of conditions that would be required to cocrystallise the two materials. Some organic molecules, especially larger ones, are unable to sublime and therefore render this technique impractical in the formation of multicomponent crystals.

Comparing compounds **2** and **3** reveal that the ferrocene moiety (in **2**) has a large influence on its ability to form multicomponent crystals. It could be that the racemic nature of **2** hinders the formation of multicomponent crystals or that the intra-and inter-molecular interactions in **2** are simply more favourable than the potential interactions between **2** and a coformer and this results in no multicomponent product formation.

When comparing compounds **4** and **5**, it was clear that the additional carbon atom in the side chain of **5** played a considerable role in the compound's ability to form multicomponent crystals. This could be due to increased rotational freedom that does not result in efficient packing with coformers, or that the shape complementarity between **5** and the coformer was not favourable.

It is unfortunate that we were unable to obtain single crystals of any of the new products that formed, despite many attempts. This would have provided more detail about the ratio of components and how they interact in the solid state. By studying the FT-IR spectrum of each new product, we were able to suggest that the majority of the new products were salts (i.e. that proton transfer had taken place between the antiplasmodial and the coformer).

While various solution methods were employed in an attempt to form single crystals of these multicomponent products, the use of melt recrystallisation techniques could still yield suitable single crystals. A similar heating-cooling cycle has been used to induce crystallisation in amorphous material.[40] This method could be investigated as a possible way to obtained crystalline materials from the amorphous products that will allow us to study their interactions and properties in more detail. Should suitable single crystals not be obtained for any of the multicomponent products, solving the structure from PXRD (provided the sample is crystalline) is possible, however it would require high quality PXRD patterns (possibly using synchrotron radiation). While theoretically relatively simple, in practice it is considerably more challenging and often requires a great deal of knowledge and experience in the field to accurately determine a crystal structure by PXRD. For these reasons, this was not carried out as part of this work, however, future collaborations with research groups that do have the required facilities and experience would prove useful to further understand the solid-state chemistry of these systems.

The next step would be to investigate the subsequent change in physicochemical properties (such as solubility) of each multicomponent product to determine what effect each coformer has on these properties. In addition, studying the effect that the coformer has on the *in vitro* efficacy and pharmacokinetic profiles of the parent drug molecule would be valuable. This, however, requires exact knowledge of the sample composition. In many of our multicomponent products, thermal analysis indicates that water, methanol or a combination of both are included in the structure. Without single crystal data, it is difficult to ascertain exact ratios of all components.

While it is unfortunate that we were not able to obtain crystal structures of any of the multicomponent products to study them in more detail, this study has nonetheless provided valuable information on the types of coformers that form multicomponent products with these 4-aminoquinoline-based antiplasmodial agents. It also provides an excellent starting point for subsequent studies on other quinoline-based compounds. This study also shows that these systems warrant further investigation and that, in combination with other studies on similar compounds, sufficient insight can be gained that allows us to be one small step closer to the point where prediction of multicomponent product formation may be possible, at least for these types of systems.

2.6 REFERENCES

(1)   Burckhalter, J. H.; Tendick, F. H.; Jones, E. M.; Jones, P. A.; Holcomb, W. F.; Rawlins, A. L. *J. Am. Chem. Soc.* **1948**, *70* (4), 1363–1373.

(2)   Biot, C.; Nosten, F.; Fraisse, L.; Ter-Minassian, D.; Khalife, J.; Dive, D. *Parasite* **2011**, *18* (3), 207–214.

(3)   Blackie, M. A. L.; Yardley, V.; Chibale, K. *Bioorg. Med. Chem. Lett.* **2010**, *20* (3), 1078–1080.

(4)   De, D.; Krogstad, F. M.; Byers, L. D.; Krogstad, D. J. *J. Med. Chem.* **1998**, *41*, 4918–4926.

(5)   Tripathy, S.; Roy, S. *Asian Pac. J. Trop. Med.* **2014**, *7* (9), 673–679.

(6)   Sanofi: *Dose ranging study of Ferroquine with Artesunate in African adults and children with uncomplicated Plasmodium Falciparum malaria.* Available at: https://clinicaltrials.gov/ct2/show/NCT00988507 (accessed Oct 22, 2018).

(7)   Aakeröy, C. B.; Wijethunga, T. K.; Desper, J. *J. Mol. Struct.* **2014**, *1072* (1), 20–27.

(8)   Nath, B.; Baruah, J. B. *Mol. Cryst. Liq. Cryst.* **2012**, *562* (1), 242–253.

(9)   Sánchez-Delgado, R. A.; Navarro, M.; Pérez, H.; Urbina, J. A. *J. Med. Chem.* **1996**, *39* (5), 1095−1099.

(10)   Jacobs, L.; de Kock, C.; de Villiers, K. A.; Smith, P. J.; Smith, V. J.; van Otterlo, W. A. L.; Blackie, M. A. L. *ChemMedChem* **2015**, *10* (12), 2099–2110.

(11)   Biot, C.; Glorian, G.; Maciejewski, L. A.; Brocard, J. S.; Domarle, O.; Blampain, G.; Millet, P.; Georges, A. J.; Lebibi, J. *J. Med.Chem.* **1997**, *40* (23), 3715–3718.

(12)   Blackie, M. A. L. PhD thesis: *New mono and bimetallic chloroquine derivatives: Synthesis and evaluation as antiparasitic agents*, University of Cape Town, 2002.

(13)   Marquarding, D.; Klusacek, H.; Gokel, G.; Hoffmann, P.; Ugi, I. *J. Am. Chem. Soc.* **1970**, *92* (18), 5389–5393.

(14)   Delhaes, L.; Biot, C.; Berry, L.; Delcourt, P.; Maciejewski, L. A.; Camus, D.; Brocard, J. S.; Dive, D. *ChemBioChem* **2002**, *3* (5), 418–423.

(15)   Dubar, F.; Egan, T. J.; Pradines, B.; Kuter, D.; Ncokazi, K. K.; Forge, D.; Paul, J. F.; Pierrot, C.; Kalamou, H.; Khalife, J.; Buisine, E.; Rogier, C.; Vezin, H.; Forfar, I.; Slomianny, C.; Trivelli, X.; Kapishnikov, S.; Leiserowitz, L.; Dive, D.; Biot, C. *ACS Chem. Biol.* **2011**, *6* (3), 275–287.

(16)   de Souza, M. V. N.; Pais, K. C.; Kaiser, C. R.; Peralta, M. A.; Ferreira, M. D. L.; Lourenço, M. C. S. *Bioorg. Med. Chem.* **2009**, *17* (4), 1474–1480.

(17)   Generally regarded as safe (GRAS). Available at: http://www.accessdata.fda.gov/scripts/fdcc/?set=GRASNotices (accessed 14 April 2015).

(18)   Everything added to food in the United States (EAFUS). Available at: http://www.accessdata.fda.gov/scripts/fcn/fcnNavigation.cfm?rpt=eafusListing (accessed 14 April 2015).

(19)   Mukherjee, A. *Cryst. Growth Des.* **2015**, *15* (6), 3076–3085.

(20)   Fábián, L. *Cryst. Growth Des.* **2009**, *9* (3), 1436–1443.

(21)   Braga, D.; Grepioni, F.; Maini, L.; D'Agostino, S. *IUCrJ* **2017**, *4*, 369–379.

(22)   Taylor, C. R.; Day, G. M. *Cryst. Growth Des.* **2018**, *18* (2), 892–904.

(23)   Calero, C. S.; Farwer, J.; Gardiner, E. J.; Hunter, C. A.; MacKey, M.; Scuderi, S.; Thompson, S.; Vinter, J. G. *Phys. Chem. Chem. Phys.* **2013**, *15* (41), 18262–18273.

(24)   Hunter, C. A. *Angew. Chem. Int. Ed.* **2004**, *43* (40), 5310–5324.

(25)   Musumeci, D.; Hunter, C. A.; Prohens, R.; Scuderi, S.; McCabe, J. F. *Chem. Sci.* **2011**, *2* (5), 883–890.

(26)   Grecu, T.; Hunter, C. A.; Gardiner, E. J.; McCabe, J. F. *Cryst. Growth Des.* **2014**, *14* (1), 165−171.

(27)   Grecu, T.; Adams, H.; Hunter, C. A.; McCabe, J. F.; Portell, A.; Prohens, R. *Cryst. Growth Des.* **2014**, *14* (4), 1749–1755.

(28)   Grecu, T.; Prohens, R.; McCabe, J. F.; Carrington, E. J.; Wright, J. S.; Brammer, L.; Hunter, C. A. *CrystEngComm* **2017**, *19* (26), 3592–3599.

(29)   Frisch, A.; Frisch, M. J.; Clemente, F. R.; Trucks, F. W. *Gaussian 09 User's Reference*; Gaussian, Inc: Wallingford, CT, USA, 2009.

(30)   *AIMAll* (Version 17.11.14), Keith, T. A. TK Gristmill Software: Overland Park KS, USA 2017.

(31)   Karagianni, A.; Malamatari, M.; Kachrimanis, K. *Pharmaceutics* **2018**, *10* (1), 1–30.

(32)   Friščić, T. *J. Mater. Chem.* **2010**, *20* (36), 7599-7605.

(33)   Descamps, M.; Willart, J. F. *Adv. Drug Deliv. Rev.* **2016**, *100*, 51–66.

(34)   Newman, A.; Hastedt, J. E.; Yazdanian, M. *AAPS Open* **2017**, *3* (1), 7.

(35)   Vrani, E. *Bosn. J. Basic Med. Sci.* **2004**, *4* (3), 35–39.

(36)   Hancock, B. C.; Zografi, G. *J. Pharm. Sci.* **1997**, *86* (1), 1–12.

(37)   Jayasankar, A.; Somwangthanaroj, A.; Shao, Z. J.; Rodríguez-Hornedo, N. *Pharm. Res.* **2006**, *23* (10), 2381–2392.

(38)   Karimi-Jafari, M.; Padrela, L.; Walker, G. M.; Croker, D. M. *Cryst. Growth Des.* **2018**, *18*, 6370–6387.

(39)   Childs, S. L.; Stahly, G. P.; Park, A. *Mol. Pharm.* **2007**, *4* (3), 323–338.

(40)   Liu, X.; Lu, M.; Guo, Z.; Huang, L.; Feng, X.; Wu, C. *Pharm. Res.* **2012**, *29* (3), 806–817.

CHAPTER 3

Synthesis of ferrocene-containing analogues of lapatinib

3.1 INTRODUCTION

Since the formation of multicomponent crystals of five known antiplasmodial agents was successful using the combined computational and experimental approach described in Chapter 2, we decided to synthesise five novel antiplasmodial compounds and apply the knowledge gained through the computational and experimental techniques to form multicomponent crystals of these novel compounds. In this way we could study the structures and properties, such as efficacy and solubility, of these new compounds, as well as investigate their ability to form multicomponent crystals, and compare the properties of any multicomponent crystals obtained with those of the original compounds.

Taking inspiration from the Pollastri laboratory in Boston, USA, we set out to make use of a target class repurposing strategy to synthesise derivatives of lapatinib as potential antiplasmodial agents. As previously discussed in Chapter 1 (page 11), target class repurposing involves the use of a previously-approved drug (used to treat a specific disease or pathogen) as a starting point to synthesise new drug molecules. Lapatinib has been shown to inhibit *Plasmodium* species and therefore a series of medicinal chemistry optimisations have been performed to identify similar analogues with improved *in vitro* properties.[1,2] While the target class repurposing approach hinders the option for "rational design", it does provide the option to explore a broader target range and gives the opportunity to identify novel modes of action.[3]

Through a target class repurposing strategy, extensive structure-activity relationship studies have been carried out on lapatinib by Pollastri and coworkers, on what is known as the "head" group (4-amino substituent), the "tail" (furan) group as well as the core scaffold (quinazoline).[2,4,5] These three regions are illustrated in Figure 3.1, along with some examples of substituents that have replaced each region, in an attempt to improve some of the physicochemical properties. It has been shown that replacing the quinazoline core scaffold with a thiopyrimidine or an isoquinoline moiety decreases the efficacy against *P. falciparum*, whereas switching to a quinoline retains the efficacy.[5,6] This suggests that β-hematin inhibition is at least one of the targets of these compounds; however, no studies have yet been performed to determine the targets or modes of action of these compounds. It should be noted that the EC_{50} values (concentration of a compound where 50% of its maximal effect is observed) for these compounds are still in the low micromolar range, indicating that there is most likely more than one target. Replacing the head group with more polar moieties, such as pyrimidines, pyridines and thiazoles, successfully improves solubility of these compounds; however, results in diminished efficacies.[4] The tail region,

however, has been shown to be more tolerable to changes and a variety of substituents have replaced the furan tail of lapatinib without a substantial loss in efficacy. In most cases, substituted phenyl rings improve efficacies, while removing the group all together decreases efficacy against *P. falciparum*.[2]
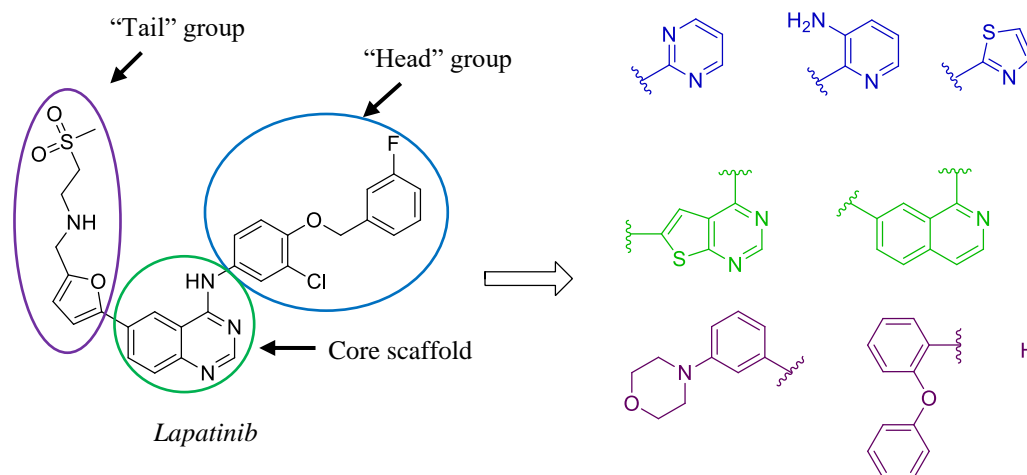
Figure 3.1: Structure of lapatinib (left) and various substituents that have been used to replace each region on the molecule in structure-activity relationship studies.

While a great deal of work has been carried out in this area, the use of metallocenes as "tail" moieties has not yet been studied. Motivated by the literature on ferrocenes and other metallocenes in antiplasmodial drug discovery[7–9] we sought to investigate the effect of substituting the lapatinib furan tail with a substituted ferrocene moiety, as shown in Figure 3.2. As our goal was to improve the solubility through formation of multicomponent crystals, we opted for the head group that displayed the best efficacy, even if it meant that the solubility would not be optimal. Therefore, the lapatinib head group would be retained, as it shows the best efficacy against *P. falciparum*.
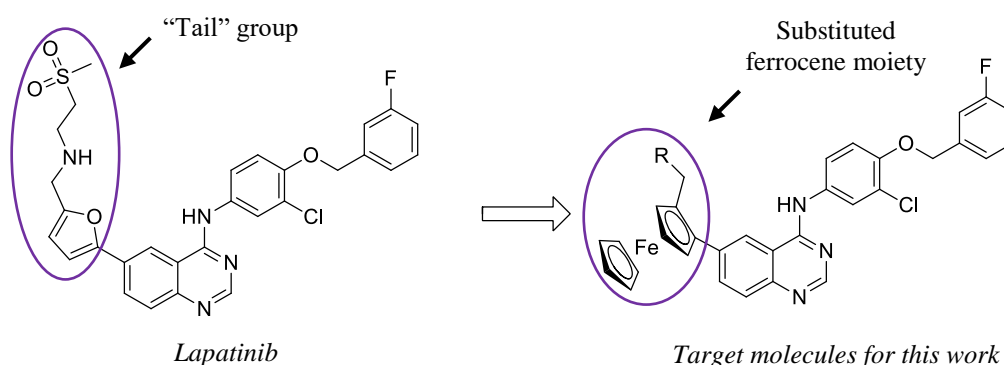
Figure 3.2: Structure of lapatinib (left) and the incorporation of an aminoferrocene moiety (right) into the tail region (purple) of the structure.

It has been shown that the ferrocene moiety plays an important role in the efficacy of ferroquine and that its position within the molecule is crucial.[10,11] Furthermore, it has been established that it needs to be covalently bound to the molecule for improved efficacies against *P. falciparum*.[12] Therefore, forming multicomponent crystals of drug molecules with coformers, such as aminoferrocenes, is not worthwhile. Rather, the incorporation of the moiety into the molecule prior to the formation of multicomponent crystals with these molecules could be more beneficial.

The tail moieties in the majority of the lapatinib analogues described above were introduced onto the core scaffold by means of a palladium-catalysed Suzuki-Miyaura coupling reaction.[5] This well-known reaction makes use of a palladium catalyst to form a carbon-carbon bond between an aryl halide fragment and an organoboronic acid species.[13,14] The catalytic cycle (Figure 3.3) begins with the oxidative addition of the aryl halide species to the Pd(0) catalyst to form a Pd(II) complex. The boronic acid species is activated by the base, where after the transmetallation step takes place. Lastly, reductive elimination takes place, which yields the coupled product and regenerates the palladium(0) catalyst.
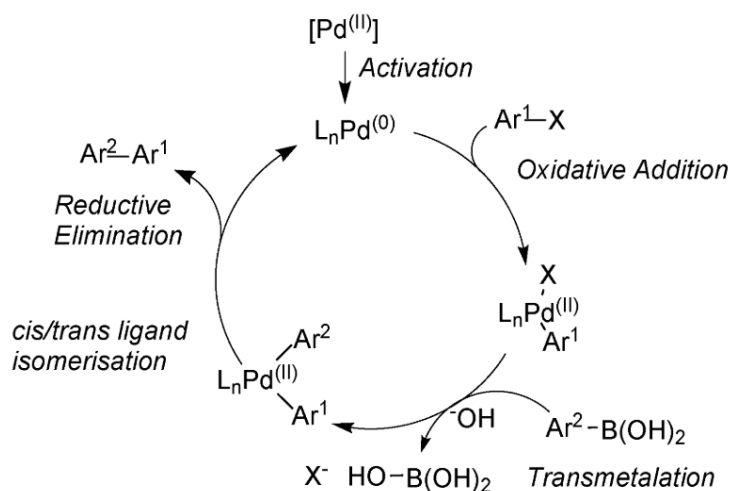
Figure 3.3: The general reaction mechanism proposed by Lennox and Lloyd-Jones for the Suzuki-Miyaura coupling reaction.[14]

Our goal was therefore to synthesise the following five compounds (Figure 3.4, **15a-e**) through a palladium-catalysed Suzuki-Miyaura coupling reaction between boronic acids **16** and aryl halide **17**. These amines were chosen as previous work conducted by members of our research group have shown improved efficacies with these amines (with other linkers).[15,16] While ferroquine makes use of the dimethyl substituent (**a**), work by the Pollastri group that makes use of amino-substituted phenyl linkers have shown that the piperidyl (**d**) and morpholinyl (**e**) substituents also result in improved efficacies.[2] We were also interested in studying a series of these compounds to determine what effect small changes, such as these amine substituents, would have on the solid-state properties of these compounds, in addition to their efficacious properties. It should be noted that compounds **15a-e**, like ferroquine, are

chiral due to the di-substitution on the ferrocene ring, as discussed in Chapter 2 (page 45). We would once again work with the racemic mixture in all cases.
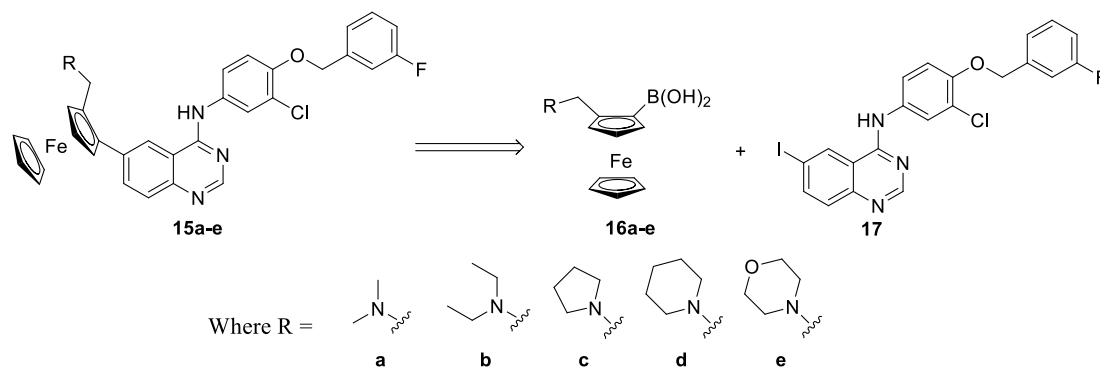
Figure 3.4: Target compounds for this study (**15a-e**) shown by way of retrosynthetic disconnection.

Once synthesised and fully characterised, the compounds would be sent to the Pollastri group and their collaborators for efficacy testing against *P. falciparum* and also for solubility testing. We would then make use of the computational screening method described in the previous chapter to identify the coformers that would most likely form multicomponent crystals. Experimental screening with liquid-assisted grinding would then be carried out with **15a-e** and the structures and physicochemical properties of any multicomponent crystals obtained would be studied in detail.

With our synthetic strategy in hand, we set out to synthesise the precursor molecules that would then be coupled together.

3.2 SYNTHESIS OF THE PRECURSOR FRAGMENTS

While an overview of the synthesis of these compounds is described here, full experimental details for each compound can be found in Chapter 6 (page 150 – 160). Fragment **17** and similar derivatives of **16** have been previously reported in the literature[2,17] and as a result, the synthesis of these compounds proceeded without incident and with minimal optimisation of reaction conditions required. For ease of reading, the synthesis has been divided into three parts – synthesis of the quinazoline core scaffold including the lapatinib head group (aryl halide fragment **17**), the tail fragment (boronic acid fragment **16**) and finally, the Suzuki-Miyaura reaction to couple the two fragments.

3.2.1 The aryl halide fragment ("core scaffold and head group")

The synthesis of the aryl halide fragment follows that described in the literature for the synthesis of lapatinib.[5,17] In some instances, the literature procedures were modified and this is described here. The

formation of the quinazoline core scaffold could be achieved in a three-step synthesis as shown in Scheme 3.1.
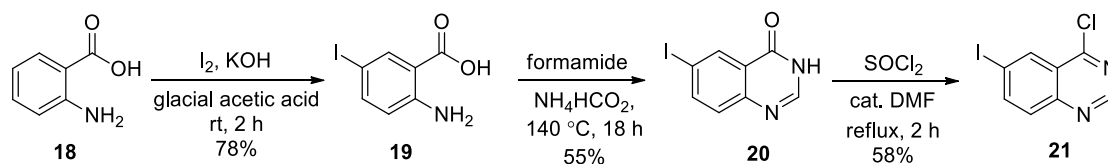
Scheme 3.1: Three-step synthesis of 4-chloro-6-iodoquinazoline (**21**).

In the first step, commercially available anthranillic acid (**18**) was treated with an iodine solution under buffered conditions and allowed to stir at room temperature. After neutralisation, the crude product was recrystallised from hot MeOH to yield a brown crystalline solid in good yield (78%). Subsequent ring-closure with formamide and ammonium formate afforded compound **20** as a brown crystalline solid in moderate yields (55%) after recrystallisation from hot methanol.
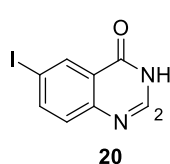
The ^{1}H NMR and FT-IR spectroscopic analysis confirmed that the formation of the desired product was successful. The proton at position 2 on the quinazolinone ring was observed as a singlet at 8.12 ppm on the ^{1}H NMR spectrum. Three peaks were observed in the aromatic region, each integrating to 1H, which correspond to the remaining protons on the molecule. The spectroscopic data correlated well with that reported in the literature.[2]

In addition, X-ray diffraction was utilised to obtain a crystal structure of **20** and confirms the position of the iodine atom on the molecule, as well as that the ring-closure was successful. The asymmetric unit and packing diagrams are shown in Figure 3.5. This compound was studied further in a separate project and its crystal structure will be discussed in more detail in Chapter 4.

(a)   (b)
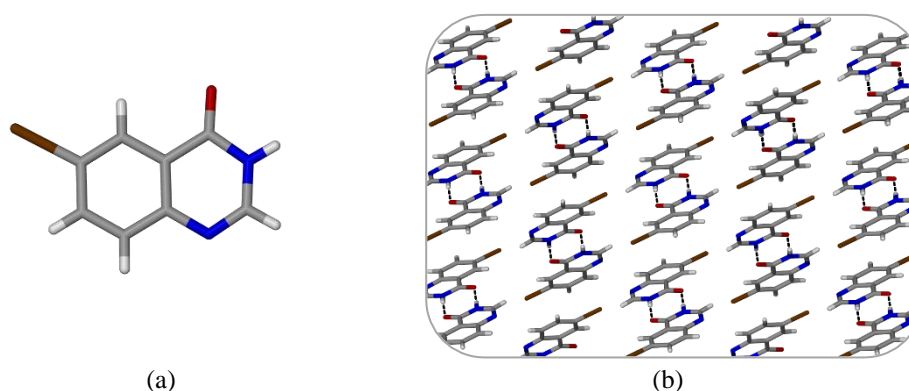
Figure 3.5: Structure of **20**: (a) asymmetric unit and (b) packing diagram viewed down the *b* axis.

It should be noted that **20** exists as a tautomer, as can be seen in Figure 3.6. In the solid state, analysis of the bond length of the carbonyl moiety and the C–N bonds of the ring indicates that only tautomer 1 is observed. In solution however, the amide peak of tautomer 2 can be seen by ^{1}H NMR spectroscopy

at 12.4 ppm, when polar/protic solvents such as CD_3OD or DMSO-d_6 are used. While non-polar/non-protic solvents (such as $CDCl_3$) may give a different outcome, this could not be tested as **20** is insoluble in $CDCl_3$.
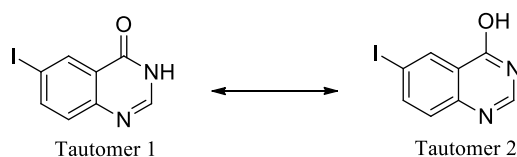
Figure 3.6: Two tautomers of **20**.

Finally, **20** was refluxed in thionyl chloride (with catalytic DMF) under a nitrogen atmosphere for 2 hours to give 6-iodo-4-chloroquinazoline (**21**) in moderate yield (58%).
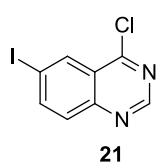
Analysis of the ^{1}H NMR spectrum of **21** shows four aromatic peaks, each integrating for 1H that corresponds to the four protons on the molecule. The absence of the carbonyl stretch in the IR spectrum is also noted. As expected, the spectroscopic data correlates well with the literature.[2]

The next step was to synthesise the head group that would later be added onto the core scaffold. This required a two-step synthesis as shown in Scheme 3.2, starting from commercially available starting materials, **22** and **23**.
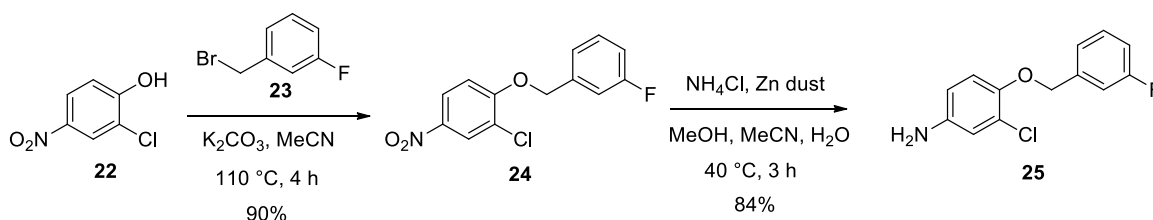
Scheme 3.2: Two-step synthesis of the head group to be attached to the quinazoline scaffold.

Compound **22** was added dropwise to a solution of **23** and potassium carbonate in acetonitrile, and after stirring for 3 hours at 75 °C, the product was extracted and purified to give a pale yellow crystalline solid in excellent yields (90%). Subsequently, the reduction of the nitro group was carried out with zinc powder and ammonium chloride in a mixed solvent system to aid in the solubility of the reagents and yielded **25** in 84% yield. The spectroscopic data corresponds well with that in the literature.[2]

The final step in the synthesis of the aryl halide fragment **17** was to couple **21** and **25** via a nucleophilic substitution reaction as shown in Scheme 3.3. The two fragments were stirred at 30 °C in 2-propanol overnight to yield a bright yellow product in good yield (81%). Spectroscopic data correlates well with that in the literature.[2]
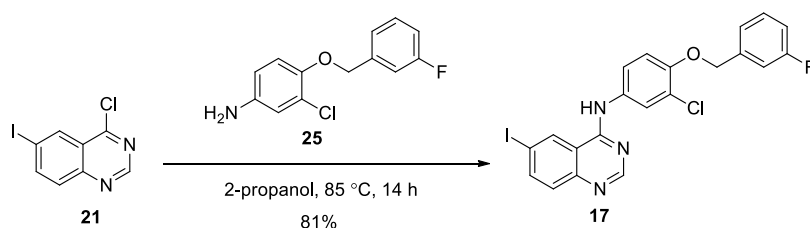
Scheme 3.3: Coupling the head group (**25**) to the core quinazolinone scaffold (**21**).

It should be noted that while the quinazoline scaffold has effectively two positions for substitution (either at the position of the chlorine or iodine atom), substitution only occurs at the 4-position in this reaction. Similarly to quinoline scaffolds, the 4-position is significantly more reactive toward nucleophilic substitution when compared to the 6- or 7-positions. This is because of the nitrogen atoms present in the ring that facilitate a more favourable intermediate, as shown in Figure 3.7. While substitution at the 6-position on **21** is possible, it would require specialised reaction conditions (for example palladium-catalysed aminations.)[18]
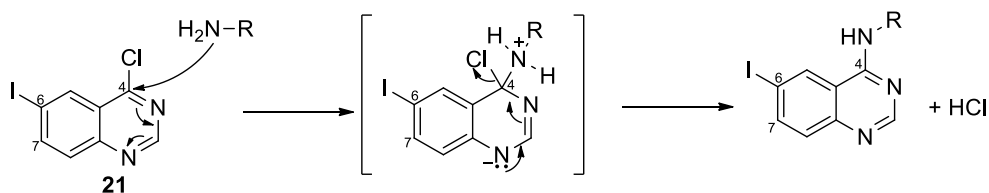
Figure 3.7: Mechanism for the nucleophilic substitution at the 4-position of **21**.

Having successfully synthesised the aryl halide fragment, we moved onto the synthesis of the boronic acid fragment.

3.2.2 The boronic acid fragment

The synthesis of the required boronic acid fragments could be carried out in two steps, as seen in Scheme 3.4. Initially only two fragments (**16a,d**) were synthesised and used in subsequent steps. Once the Suzuki-Miyaura reaction was optimised, the other boronic acid fragments (**16b,c,e**) would be synthesised.
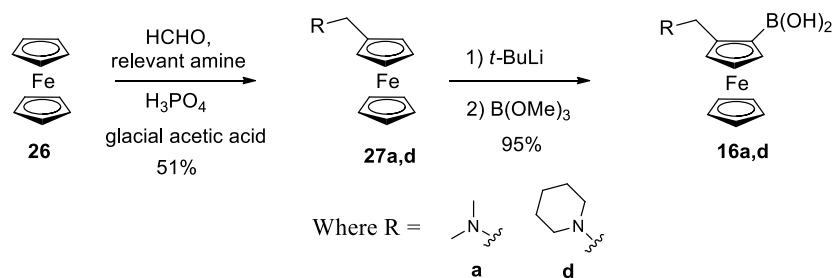
Scheme 3.4: Two-step synthesis of the various ferrocene boronic acid fragments.

N,N-dimethylaminomethyl ferrocene (**27a**) is commercially available and had already been purchased for the synthesis of ferroquine (**2**) in the previous chapter. Therefore, it was not necessary to synthesise this analogue. The synthesis of **27d** was carried out using a procedure described by Wu *et al*.[3] They report the use of formaldehyde, pyrrolidine and phosphoric acid in acetic acid to form an iminium intermediate that reacts with ferrocene (**26**) via electrophilic aromatic substitution to form the desired amine product. Although a thorough attempt at optimising the reaction was carried out, they report low yields (<50%) due to the formation of a by-product (dipyrrolidinylmethane). We made use of their optimised reaction conditions to form **27d** in comparable yields (51%), using piperidine rather than pyrrolidine.
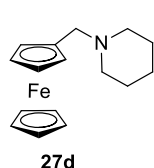
Analysis of the ¹H NMR spectrum for **27d** showed the characteristic Cp singlet of the ferrocene at 4.11 ppm, integrating for 5H, as well as the methylene protons as a singlet at 3.37 ppm, integrating for 2H. All other protons are accounted for. This data compares well with that in the literature.[3,4]

It is well-known that the amine group on these ferrocene analogues acts as a strong *ortho*-director in lithiation reactions.[19,20] As discussed in the previous chapter, *t*-BuLi is the preferred choice of metalation reagent over *n*-BuLi for these reactions due to shorter reaction times, leading to higher yields.[21] Aminoferrocenes **27a** and **27d** were thus treated with *t*-BuLi in diethyl ether at 0 °C, forming a bright orange precipitate (Scheme 3.4). After 2 hours, the reaction was quenched with trimethyl borate. Following workup, the boronic acid **16a** and **16d** were isolated in excellent yields. The spectroscopic data for **16a** compared well with the literature values.[5,6]
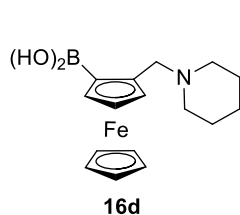
The ¹H NMR spectroscopic analysis of **16d** showed the Cp singlet of the ferrocene at 4.16 ppm (integrating for 5H) as well as the methylene protons at 3.73 ppm, integrating for 2H. All other protons were accounted for. LC-MS showed a product mass correlating to [M+H]⁺ of 287.94 m/z, which compared well with the calculated value of 287.96 m/z.

Having successfully synthesised the aminoferrocene boronic acid derivatives, we were ready to attempt the coupling reaction to provide the target compounds.

3.3 COUPLING THE FRAGMENTS TOGETHER

While the Suzuki-Miyaura reaction is a robust and versatile method of performing carbon-carbon coupling reactions, it is known to frequently require substantial optimisation before the reaction produces the desired product in acceptable yields.[22] Suzuki-Miyaura reactions require the use of a palladium catalyst, a base and a thoroughly degassed solvent system. For many cases, heat is also required to increase reaction rates and yields. The strength and amount of the base used plays an important role in the transmetallation step.[23] The solvent choice influences not only the dissolution of starting materials, but can play a role in the reaction rate and/or selectivity of the reaction. In addition, it has been shown that by not degassing the solvent sufficiently, the yield can decrease dramatically or even promote the formation of unwanted side-products.[24] The choice of catalyst has also been shown to have an effect on the yield of the desired product.[25]

While deoxygenated reaction conditions are necessary, anhydrous conditions are not, and often these reactions make use of water as a co-solvent to facilitate the dissolution of reagents, especially the base.[26] Our initial attempt (shown in Scheme 3.5) made use of the reaction conditions carried out by Woodring *et al.* as they make use of the same aryl halide fragment (**17**).[27] For this reaction, a solvent system of dimethoxyethane (DME), dioxane and water was used, along with potassium carbonate as a base and palladium tetrakis(triphenylphosphine) – Pd(PPh$_3$)$_4$ – as a catalyst. After heating at 80 °C overnight, TLC analysis indicated that a new product had formed. After workup and purification, ^{1}H NMR analysis confirmed that the product obtained was not the desired product, but rather the dehalogenated starting material (Scheme 3.5, **15-H**). This was also confirmed by mass spectrometry. Unfortunately, this product is a common occurrence with Suzuki-Miyaura reactions and reaction conditions need to be optimised in order to eliminate or at least reduce the formation of this unwanted product.[28,29]
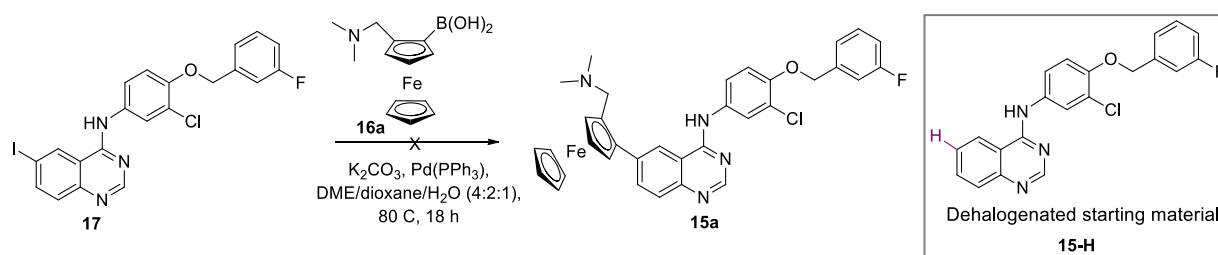
Scheme 3.5: Initial attempt at the Suzuki-Miyaura reaction to couple **17** and **16a**. Insert (right): dehalogenated starting material (**15-H**) obtained instead of the desired product.

The literature reports that the choice of base and solvent can have a large effect on the formation of the dehalogenated product.[28] In addition, other factors such as temperature and increased equivalents of the boronic acid species have also been shown to reduce the formation of side-products and to improve

yields of the desired product.[30] We investigated a number of solvent mixtures, bases and catalysts in an attempt to obtain the desired product (Table 3.1). The use of a nickel catalyst was also attempted as recent literature has shown that these catalysts have been successfully used in some Suzuki-Miyaura reactions.[31,32] Microwave reaction conditions are also popular in the literature as it allows for higher temperatures in comparison to conventional heating and faster reactions times that could lead to the reduction of by-product formation or degradation.[33,34] We therefore also made use of this technique in our optimisation process. Disappointingly, we were unable to obtain any of the desired product from these attempts.

At this point we were planning a three-month research visit to the Pollastri laboratory in Boston and we decided to make use of their expertise and knowledge of similar reactions in an attempt to understand what was happening in our reactions and how we could obtain the desired product. Starting materials were synthesised in our laboratory and couriered there. It should be noted that their laboratory makes use of in-house LC-MS analysis to monitor reactions (rather than TLC analysis as in our case). This allows us to more accurately track even trace quantities of product formation that would not be possible using TLC analysis. This has the advantage of quickly and reliably determining all products that are formed.

Table 3.1: Conditions for Suzuki coupling of **16** and **16a**.
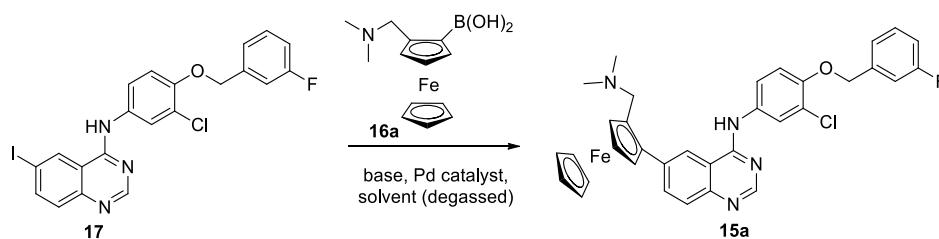
Attempt	Solvent system[a]	Base (3 eq)	Catalyst (10 mol%)	Reaction conditions[b]	Outcome (according to TLC analysis)
1	DME/dioxane/H$_2$O	K$_2$CO$_3$	Pd(PPh$_3$)$_4$	80 °C, 18 h	**15-H**
2	Dioxane/EtOH/H$_2$O	Cs$_2$CO$_3$	Pd(PPh$_3$)$_4$	80 °C, 18 h	**15-H**
3	DME/EtOH/H$_2$O	Cs$_2$CO$_3$	Pd(dppf)Cl$_2$	80 °C, 18 h	**15-H**
4	DME/EtOH/H$_2$O	NaOH	Pd(dppf)Cl$_2$	70 °C, 18 h	**15-H**
5	DMF/H$_2$O	K$_2$CO$_3$	Pd(dppf)Cl$_2$	100 °C, 2 d	starting material and **15-H**
6	Dry EtOH/ Toluene	Et$_3$N	Pd(dppf)Cl$_2$	85 °C, 18 h	starting material
7	Dry EtOH/Toluene	Et$_3$N	Pd(PPh$_3$)$_4$	85 °C, 18 h	starting material
8	Dry dioxane	K$_2$CO$_3$	Pd(dppf)Cl$_2$	115 °C, 18 h	**15-H**
9	Dioxane/MeOH	K$_3$PO$_4$	1,2-Ni(dppe)Cl$_2$	110 °C, 24 h	starting material
10[c]	DME/dioxane/H$_2$O	K$_2$CO$_3$	Pd(dppf)Cl$_2$	MW, 110 °C, 30 min	starting material
11[c]	DMF/H$_2$O	K$_2$CO$_3$	Pd(dppf)Cl$_2$	MW, 150 °C, 2 h	degradation – multiple spots on TLC
12[c]	EtOH/H$_2$O	K$_2$CO$_3$	Pd(PPh$_3$)$_4$	MW, 110 °C, 30 min	dehalogenation and starting material

[a] Solvent and reagent mixture was degassed using the freeze-pump-thaw method (4 cycles) before catalyst was added.

[b] Reactions were carried out in a Schlenk tube that had been purged and refilled with nitrogen gas before use.

[c] Reactions carried out in a microwave reactor.

Initially, the reaction depicted by entry 1 in Table 3.1 was repeated to confirm that dehalogenation occurs and that it is indeed the only product that forms. Our next step was to determine which fragment (the aryl halide or ferrocene boronic acid) was hindering the formation of the desired product. To this regard,

two small-scale test reactions were performed, as shown in Scheme 3.6. In each case, the solvent system was degassed by bubbling nitrogen gas through the mixture for 20 minutes before adding the reagents. Commercially available PdCl$_2$(dppf)·DCM adduct was used as the catalyst and potassium carbonate as the base. The reaction was heated to 80 °C overnight, after which LC-MS was used to analyse the product mixture.
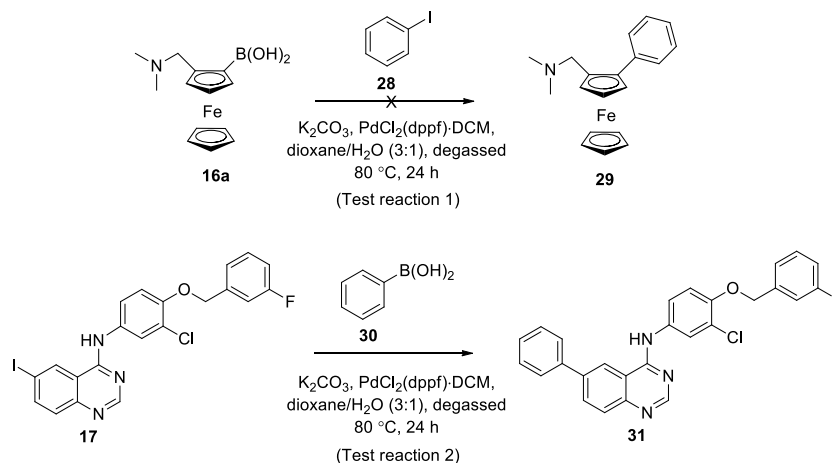
Scheme 3.6: Two test reactions performed to determine which fragment was hindering the formation of the desired product in the Suzuki reactions.

LC-MS analysis confirmed that only starting material remained in test reaction 1. It should be noted that the dehalogenated product (in this case benzene) is not observable by LC-MS or TLC analysis and therefore we cannot say whether this product is forming or not. The conversion of **17** to **31** (test reaction 2) has been previously carried out by the Pollastri group,[27] but was performed again to confirm that the catalyst and reaction conditions were adequate for these types of reactions. Because the focus was on reaction optimisation to yield desired products, **31** was not isolated and purified; however, LC-MS confirmed that the dehalogenated by-product was not forming and that the desired product was obtained ([M+H]$^+$ = 457.0 m/z). These reactions were also performed under microwave conditions, where the reaction mixture was irradiated at 100 °C for 30 minutes with stirring. LC-MS analysis yielded similar results to that of the conventional heating method. As the microwave reactions provided the same outcome in substantially shorter reaction times, this method was used for future reaction optimisations. These two reactions seemed to indicate that the problem was not the halide fragment, but rather the ferrocene boronic acid that was perhaps not undergoing the transmetallation or reductive elimination step in the required manner to facilitate the formation of the coupling. Instead, the favoured reaction seems to be the incorporation of a proton instead of the ferrocene moiety. This could be due to a number of reasons, some of which could include electronics of the system, sterics at that site or simply unfavourable reaction conditions.

We therefore set out to perform a series of test reactions with various reaction conditions to see if this was possibly the culprit. Table 3.2 summarises our attempts at forming the desired product with this simpler system. Each of these reaction conditions were obtained from literature that reports Suzuki coupling with similar ferrocene systems.[35–39] While the use of the more common reaction conditions (attempts 1 – 2) did not yield any of the desired product, the use of barium hydroxide as the base and palladium acetate as the ligand-free catalyst proved to be successful, with the desired product mass detected with LC-MS analysis of the crude product mixture ($[M+H]^+$ = 320.14 m/z). Unfortunately, starting material also remained even after prolonged reaction times. A second attempt at this reaction using a higher temperature (140 °C instead of 100 °C) did not result in reaction completion either.

Table 3.2: Conditions for Suzuki coupling of **16a** and **28**.
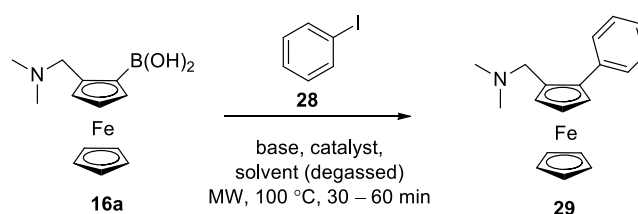
Attempt	Solvent system*	Base	Catalyst	Outcome (according to LC-MS analysis)
1	Dioxane/H_2O	K_2CO_3	$PdCl_2$(dppf)·DCM	Starting material
2	Dioxane/H_2O	NaOH	$PdCl_2$(dppf)·DCM	Starting material
3	Dioxane/H_2O	Ba(OH)$_2$	$PdCl_2$(dppf)·DCM	Starting material
4	EtOH/H_2O	Ba(OH)$_2$	Pd(OAc)$_2$	**29** as well as starting material

*Solvent was degassed by bubbling nitrogen gas through the mixture for 20 minutes.

Satisfied that we had found reaction conditions for this system that allowed the formation of the desired product, albeit without reaction completion, we attempted the coupling reaction between **16a** and **17** to form **15a**, but this time using these new reaction conditions (Scheme 3.7). Unfortunately, it seems that this system is more complicated than initially suspected, as again none of the desired product was formed. Once again, dehalogenation of **17** seemed to be favoured.
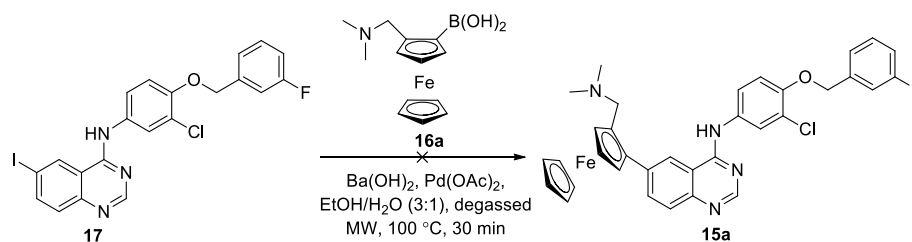
Scheme 3.7: Repeating the coupling between **2a** and **3** with new reaction conditions.

With this outcome, we decided that perhaps it would be more worthwhile to modify our approach. Our next strategy was to switch the coupling partners to see if this would be more successful. To this end, we would need to synthesise an iodoferrocene derivative, as well as convert the aryl halide to the corresponding aryl boronic acid, before carrying out the Suzuki reaction. The same product would be obtained, but it was hoped that this approach favours the formation of **15**, instead of the dehalogenated product.

3.4 PLAN B - SWITCHING THE COUPLING PARTNERS

The synthesis of the iodoferrocene fragment follows similar chemistry to that used to synthesise the boronic acid fragment, however, instead of using trimethyl borate as the electrophile, 1,2-diiodoethane was used (Scheme 3.8). This resulted in the formation of the desired product in quantitative yields. As more of **27d** was available at the time, this was used for the synthesis of the iodoferrocene (**32**) required for the Suzuki-Miyaura reaction.
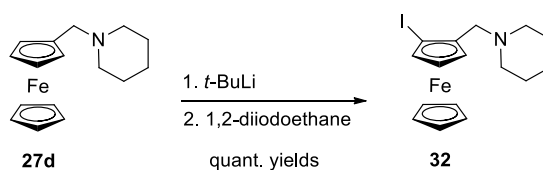
Scheme 3.8: Synthesis of iodoferrocene **32**.
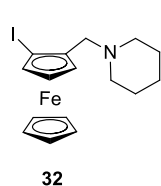
The ^{1}H NMR spectroscopic analysis of **32** shows the characteristic Cp singlet of ferrocene at 4.17 ppm that integrates for 5H. The protons associated with the piperidyl ring are accounted for, along with all other protons. LC-MS [M+H]$^+$ gives 410.07 m/z; calculated gives [M+H]$^+$ = 410.09 m/z. The desired product was obtained as a dark red-brown deliquescent solid. The material was stored under high vacuum and weighed out quickly into the reaction vial when needed for subsequent reactions.

With our iodoferrocene fragment in hand, we initially set out to perform test reactions with a simple system – similar to that carried out earlier – to determine whether this modification would lead to the preferential formation of the desired product over the dehalogenated product. To this end, **32** was reacted with phenyl boronic acid **30** using the reaction conditions outlined in Scheme 3.9 and the reaction monitored using LC-MS. The reaction yielded roughly a 1:1 ratio of desired product to dehalogenated product as determined by the areas under each peak on the LC-MS. While the dehalogenated product still forms, it is in lower amounts in comparison to previous reactions and therefore this route seemed to at least partially solve some of our initial challenges.
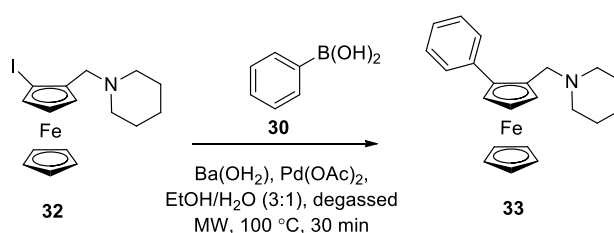
Scheme 3.9: Suzuki-Miyaura reaction with **32** and phenyl boronic acid (**30**).

With this reaction proving more successful than previous ones, we continued on to the next step of synthesising the aryl boronic acid fragment. While synthesising this fragment has been carried out before, the Pollastri group recommended a one-pot borylation and Suzuki coupling instead, as the isolation and purification of the boronic acid can be challenging.[27] This involved synthesising boronic ester **34** and then performing the Suzuki-Miyaura coupling with **32** without first purifying **34**, as shown in Scheme 3.10.
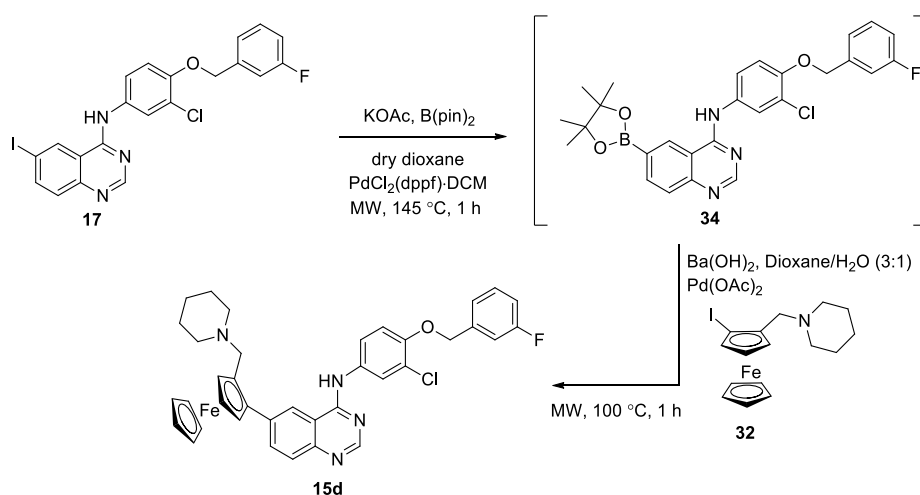
Scheme 3.10: One-pot borylation and Suzuki-Miyaura coupling reaction to form **15d**.

Bis(pinacolato)diboron was used as the borylating agent because it has been shown to be one of the more stable boronate species.[40] The borylation was carried out under inert microwave conditions using

dry dioxane, potassium acetate and PdCl$_2$(dppf)·DCM. After heating for 1 hour, LC-MS confirmed that the reaction had gone to completion and that the desired product was obtained. The reaction mixture was then filtered through Celite, concentrated under reduced pressure and the second step of the reaction was carried out. After heating for 30 minutes, the reaction was cooled and LC-MS analysis revealed that, while the reaction had not yet gone to completion, the desired product mass was detected (Figure 3.8). Unfortunately, the dehalogenated product was also obtained. Despite some optimisation attempts, including longer reaction times and increased catalyst loading, the reaction never went to completion.

While we were disappointed that we were unable to further optimise the reaction, we were nonetheless happy that we were finally able to detect the desired product. Our next step was to isolate and purify the product. Unfortunately, we were unable to isolate the product by flash column chromatography. It is suspected that either the product degraded on the column (many peaks were observed on the chromatogram) or that the product yield was simply too low to isolate using this method. Upscaling the reaction to 500 mg-scale did not improve the outcome. Attempts were also made to purify the product by means of preparative HPLC, but again the product could not be isolated.
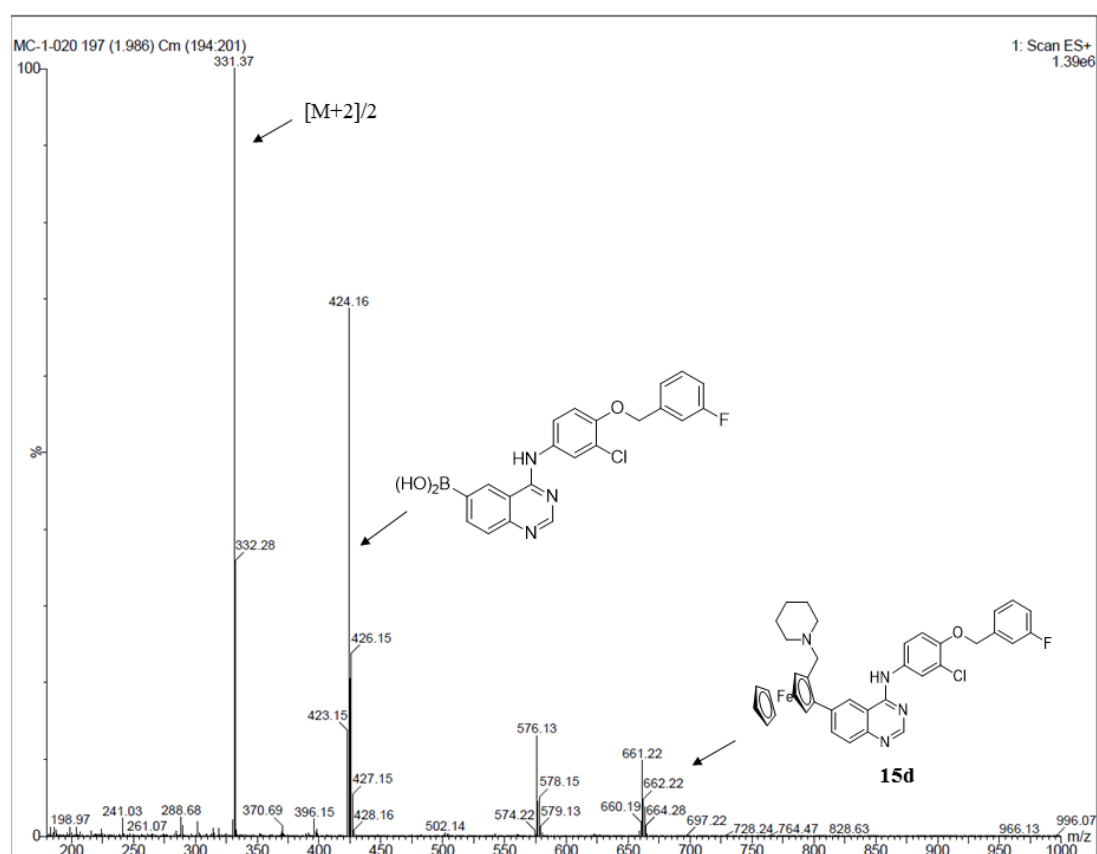
Figure 3.8: Mass spectrum of the peak corresponding to product formation. Peaks identified include that of **15d** ([M+H]$^+$ = 662.22 m/z), hydrolysed boronic acid starting material ([M+H]$^+$ = 424.16 m/z) and the [M+2]/2 fragment associated with **15d**. The peak at 567.13 m/z does not correspond to the fragmentation of any of the reagents or the desired product.

Having been unable to isolate **15d**, and having to leave the Pollastri laboratory, it was decided to abandon further attempts at the synthesis of these compounds. Given that we had only been able to confirm the product formation through LC-MS analysis, any optimisation of these reactions without easy and frequent access to an LC-MS instrument would be challenging.

Other methods to obtain the desired product include the use of a Negishi reaction that makes use of a zinc chloride intermediate instead of the boronic acid fragment in a similar palladium-catalysed coupling reaction.[41,42] Furthermore, the use of mechanochemistry – the use of mechanical force to perform reactions – has also become popular in organic synthesis as a faster and greener way of synthesising compounds.[43,44] In addition, it has been shown that the use of mechanochemistry has led to the formation of desired products when conventional solution methods fail.[45,46] While both these methods were also investigated in our attempt to synthesise **15d**, neither yielded any fruitful outcome; therefore they are not discussed further in this thesis. It was therefore decided to modify our target compounds slightly to include a linker between the quinazoline scaffold and aminoferrocene in the hope that it would aid in the coupling of the two fragments.

3.5 MODIFYING OUR TARGET COMPOUNDS

Instead of a direct carbon-carbon bond linking the two fragments, it was thought that making use of an amine (**35**) or amide (**36**) linker could be worthwhile. Looking at the retrosynthesis of these compounds (Figure 3.9), it can be seen that in both cases, an amine moiety on the quinazoline scaffold would be necessary. For the synthesis of **35**, an aldehyde would be needed to perform the reductive amination reaction to yield the amine-linked product, while in the case of **36**, a carboxylic acid would be needed in the amidation reaction to give the amide-linked product. While the coupling partners could also be switched (having the amine moiety on the ferrocene fragment and the carbonyl moiety on the quinazoline scaffold), the proposed approach has the benefit of only requiring the synthesis of three fragments instead of four. In addition, the ferrocene chemistry performed in reactions described previously (Schemes 3.4 and 3.8) could also be applied to the synthesis of **37** and **39**. Lastly, the formation of the carbonyl group at the 6-position of the quinazoline ring would be far more challenging than incorporating an amine into this position.
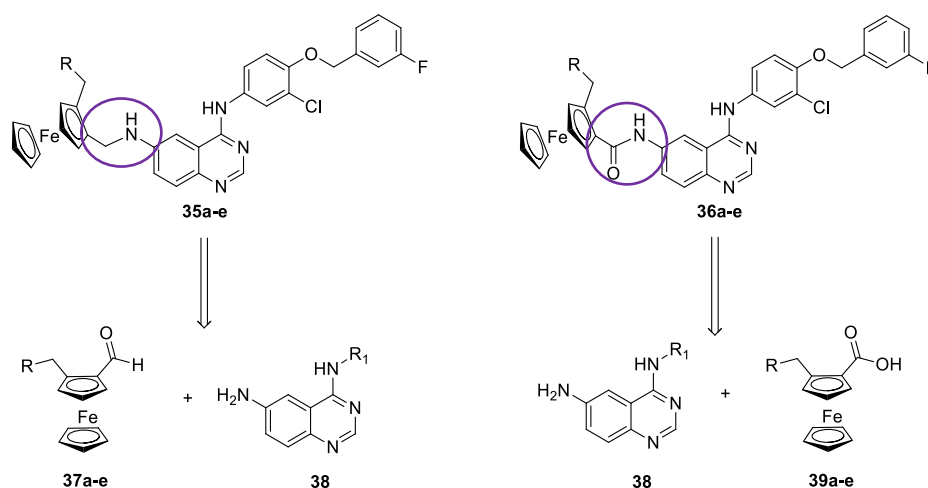
Figure 3.9: Retrosynthetic strategy to form **35** and **36** where **a-e** are the derivatives with each of the amines discussed previously.

With our new targets and synthetic strategy in mind, we set off to synthesise the two new fragments. The synthesis of ferrocene carboxaldehyde **37a** had already been carried out and ferrocene carboxylic acid **39a** has been previously reported in the literature.[21]

While the synthesis of **38** follows a similar procedure to aryl halide fragment **17**, slightly different procedures were initially followed to introduce a nitro moiety that would later be reduced to the amine derivative. In this case, the quinazolinone ring scaffold was first formed by reacting **18** with formamide and ammonium formate before carrying out the electrophilic aromatic substitution reaction to incorporate the nitro group (Scheme 3.11). Spectroscopic data for **40** and **41** correspond well with that obtained in the literature.[47]
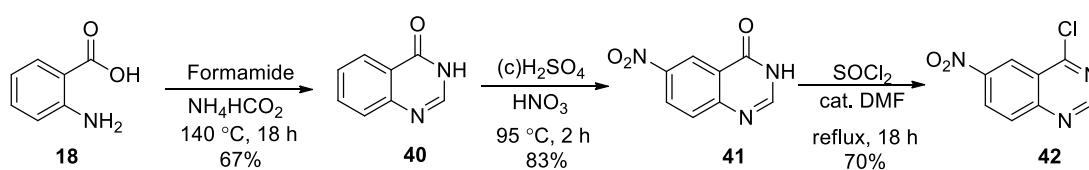
Scheme 3.11: Three-step synthesis of **42** starting from commercially available anthranilic acid (**18**).

The chlorination of **41** to yield **42** using thionyl chloride and catalytic DMF initially gave poor yields (<40%); however, first recrystallising **41** from MeOH resulted in a substantial improvement of the yield to above 70%. During one of these recrystallisation attempts, it was noticed that two differently-shaped crystals grew in the same vial (Figure 3.10). Analysis of the ^{1}H NMR spectrum of this sample confirmed that there was no contaminant, with a small amount of methanol solvent present. Single crystal X-ray diffraction of the block and needle-shaped crystals revealed that a close-packed (**41**) and solvated form (**41·MeOH**) had grown from the same solution. The asymmetric unit and packing diagram for each form can be seen in Figure 3.10, but these structures will only be discussed in more detail in Chapter 4.

Needle-shaped crystals

Block-shaped crystals
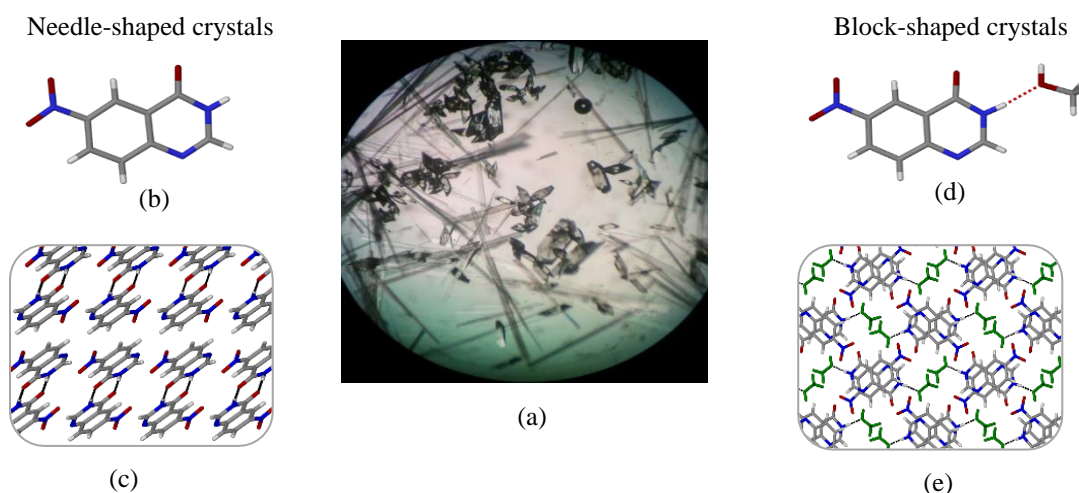
Figure 3.10: (a) Photograph of the crystallisation vial containing the two forms of **41**, (b) asymmetric unit of **41**, (c) packing diagram of **41** viewed down the *a* axis, (d) asymmetric unit of **41·MeOH**, (e) packing diagram of **41·MeOH** viewed down the *a* axis with MeOH molecules shown in green for clarity.

Because the solvent within **41·MeOH** would influence the yield of the chlorination reaction, attempts were made to obtain only the close-packed form in order to continue our synthetic strategy. It was found that by dissolving crude **41** in hot MeOH and placing the vial in the fridge overnight, only the close-packed form was obtained. Further discussion on this, as well as attempts in obtaining only the solvated form can be found in Chapter 4.

As shown in Scheme 3.12, once **42** had been synthesised and purified, the head group could be attached in a similar procedure described previously (Scheme 3.3). This afforded **43** in good yields of 86%. Finally, the reduction of the nitro group would yield the desired amine fragment. For this we made use of the same procedure as described in Scheme 3.4. Unfortunately, this was unsuccessful and only starting material remained after 24 hours. Increasing the temperature from 40 °C to 60 °C also did not result in the formation of any product. The use of the more standard combination of Pd/C and H_2 (or hydrazine) as a reducing agent could not be used in this case as the fluorobenzyl moiety would be cleaved from the head group in a benzyl deprotection-type reaction.[48]
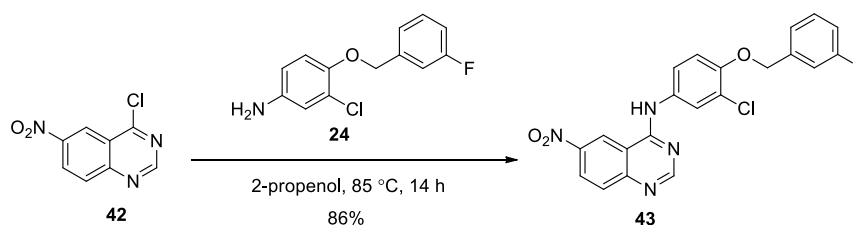
Scheme 3.12: Coupling head group **24** to **42**.

We therefore decided to attempt the reduction before adding the head group (Scheme 3.9). Initially we attempted the reduction on **41** using zinc and ammonium chloride, but again only starting material

remained, even at elevated temperatures (60 °C). Using Pd/C and hydrazine as the reducing agent also did not result in the formation of the desired product **42**.
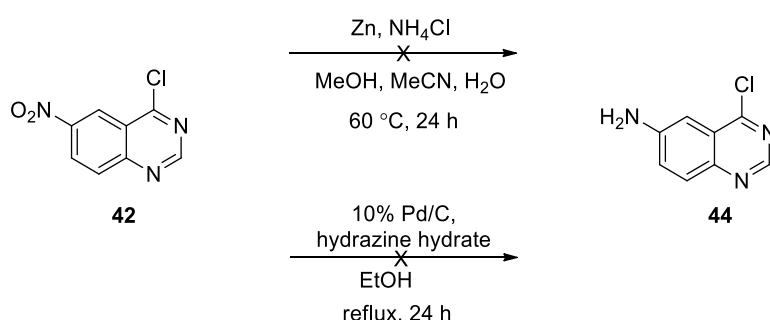
Scheme 3.13: Two methods for the reduction of **42**.

Carrying out the reduction on **41** to give 4-amino-quinazolinone **45** using Pd/C and hydrazine was somewhat successful (23% yield), however the remaining steps in the synthesis (especially the chlorination step) could not be performed with the amine present and therefore this route was not useful for obtaining the required aminoquinazoline fragment.
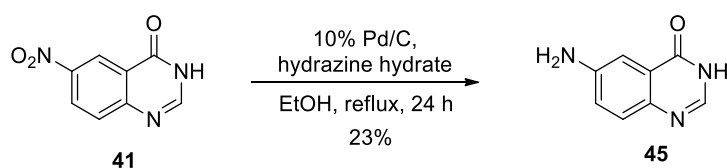
Scheme 3.14: Two methods for the reduction of **41**.

3.6 CONCLUDING REMARKS

This chapter describes our attempts toward the synthesis of novel lapatinib analogues that contain an aminoferrocene substituent. Our initial strategy employed a Suzuki-Miyaura reaction to couple the aminoferrocene boronic acid fragment to the 6-iodoquinazoline scaffold using a palladium catalyst. After numerous attempts at modifying the reaction conditions, including the use of various solvent systems, bases and catalysts, the desired product could not be obtained. Instead, only the dehalogenated quinazoline by-product or a mixture of starting materials was obtained.

Our next approach was to switch the coupling partners where the iodo-aminoferrocene fragment was reacted with the pincolboronate quinazoline scaffold. After a number of attempts, we were finally able to detect the desired product mass using LC-MS, when Pd(OAc)$_2$ was used as a catalyst together with Ba(OH)$_2$ as a base and EtOH/H$_2$O (3:1) as the solvent system. However, even after additional optimisation of the reaction conditions as well as simply upscaling the reaction, the desired product

could not be isolated. This is most likely because the amount of product produced was in trace amounts and the purification techniques used were just not sensitive enough to detect (and isolate) the desired product. It is currently unclear as to why this reaction does not produce higher yields. While it would be interesting to study this system further to pinpoint where the problem lies, it was not within the objectives of this work to spend time on this. As the focus was on the formation of multicomponent crystals, we rather turned our focus to similar analogues that could provide us with sufficient amounts of product to carry out cocrystallisations.

We therefore set out to synthesise an amine-linked analogue that made use of reductive amination to couple the aminoferrocene carboxaldehyde to the 6-aminoquinazoline scaffold. Again problems were faced, but this time in the synthesis of the aminoquinazoline scaffold. After several attempts at performing the reduction reaction to convert the nitro group into the required amine, we were once again forced to abandon this strategy.

There are multiple other methods that could potentially be used to synthesise some of the desired compounds or analogues thereof, but we were not hopeful that they would prove successful. Many of these other methods such as Sonigashira coupling (using an aryl halide and an alkyne) or Stille coupling (using an aryl halide and an alkyl tin reagent) all make use of palladium chemistry in a similar manner to that of the Suzuki-Miyaura reaction. While we cannot say for certain that these reactions wouldn't work, we felt that our resources could be better spent elsewhere.

1.6 REFERENCES

(1)   Mehta, N.; Ferrins, L.; Leed, S. E.; Sciotti, R. J.; Pollastri, M. P. *ACS Infect. Dis.* **2018**, *4* (4), 577–591.

(2)   Patel, G.; Karver, C. E.; Behera, R.; Guyett, P. J.; Sullenberger, C.; Edwards, P.; Roncal, N. E.; Mensa-Wilmot, K.; Pollastri, M. P. *J. Med. Chem.* **2013**, *56* (10), 3820–3832.

(3)   Klug, D. M.; Gelb, M. H.; Pollastri, M. P. *Bioorg. Med. Chem. Lett.* **2016**, *26* (11), 2569−2576.

(4)   Woodring, J. L.; Bachovchin, K. A.; Brady, K. G.; Gallerstein, M. F.; Erath, J.; Tanghe, S.; Leed, S. E.; Rodriguez, A.; Mensa-Wilmot, K.; Sciotti, R. J.; Pollastri, M. P. *Eur. J. Med. Chem.* **2017**, *141*, 446–459.

(5)   Devine, W.; Woodring, J. L.; Swaminathan, U.; Amata, E.; Patel, G.; Erath, J.; Roncal, N. E.; Lee, P. J.; Leed, S. E.; Rodriguez, A.; Mensa-Wilmot, K.; Sciotti, R. J.; Pollastri, M. P. *J. Med. Chem.* **2015**, *58* (14), 5522–5537.

(6)   Woodring, J. L.; Patel, G.; Erath, J.; Behera, R.; Lee, P. J.; Leed, S. E.; Rodriguez, A.; Sciotti, R. J.; Mensa-Wilmot, K.; Pollastri, M. P. *MedChemComm* **2015**, *6* (2), 339–346.

(7)   Salas, P. F.; Herrmann, C.; Orvig, C. *Chem. Rev.* **2013**, *113* (5), 3450–3492.

(8)   Navarro, M.; Gabbiani, C.; Messori, L.; Gambino, D. *Drug Discovery Today* **2010**, *15* (23–24), 1070–1078.

(9)   Blackie, M. A. L.; Chibale, K. *Met. Based. Drugs* **2008**, 2008, 1–10.

(10)   Biot, C.; Daher, W.; Ndiaye, C. M.; Melnyk, P.; Pradines, B.; Chavain, N.; Pellet, A.; Fraisse, L.; Pelinski, L.; Jarry, C.; Brocard, J.; Khalife, J.; Forfar-Bares, I.; Dive, D. *J. Med. Chem.* **2006**, *49* (15), 4707–4714.

(11)   Biot, C.; Taramelli, D.; Forfar-bares, I.; Maciejewski, L. A.; Boyce, M.; Nowogrocki, G.; Brocard, J. S.; Basilico, N.; Olliaro, P.; Egan, T. J. *Mol. Pharm.* **2005**, *2* (3), 185–193.

(12)   Roux, C.; Biot, C. *Future Med. Chem.* **2012**, *4* (6), 783–797.

(13)   Suzuki, A. *Angew. Chem. Int. Ed.* **2011**, *50* (30), 6723–6733.

(14)   Lennox, A. J. J.; Lloyd-Jones, G. C. *Chem. Soc. Rev.* **2014**, *43* (1), 412–443.

(15)   Hamann, A. R.; de Kock, C.; Smith, P. J.; van Otterlo, W. A. L.; Blackie, M. A. L. *Bioorg. Med. Chem. Lett.* **2014**, *24*, 5466–5469.

(16)   Taleli, L.; de Kock, C.; Smith, P. J.; Pelly, S. C.; Blackie, M. A. L.; van Otterlo, W. A. L. *Bioorg. Med. Chem.* **2015**, *23* (15), 4163–4171.

(17)   Erickson, G.; Guo, J.; McClure, M.; Mitchell, M.; Salaun, M. C.; Whitehead, A. *Tetrahedron Lett.* **2014**, *55* (43), 6007–6010.

(18)   Smith, J. A.; Jones, R. K.; Booker, G. W.; Pyke, S. M. *J. Org. Chem.* **2008**, *73* (22), 8880–8892.

(19)   Jacobs, L.; De Kock, C.; De Villiers, K. A.; Smith, P. J.; Smith, V. J.; van Otterlo, W. A. L.; Blackie, M. A. L. *ChemMedChem* **2015**, *10* (12), 2099–2110.

(20)   Picart-goetgheluck, S.; Delacroix, O.; Maciejewski, L.; Brocard, J. *Synthesis* **2000**, 10, 1421−1426.

(21)   Blackie, M. A. L. PhD thesis: *New mono and bimetallic chloroquine derivatives: Synthesis and evaluation as antiparasitic agents*, University of Cape Town, 2002.

(22)   Reizman, B. J.; Wang, Y. M.; Buchwald, S. L.; Jensen, K. F. *React. Chem. Eng.* **2016**, *1* (6), 658–666.

(23)   Thomas, A. A.; Denmark, S. E. *Science.* **2016**, *352* (6283), 329–332.

(24)   Adamo, C.; Amatore, C.; Ciofini, I.; Jutand, A.; Lakmini, H. *J. Am. Chem. Soc.* **2006**, *128* (21), 6829–6836.

(25)   Nikishkin, N. I.; Huskens, J.; Verboom, W. *Org. Biomol. Chem.* **2013**, *11*, 3583–3602.

(26)   Liu, C.; Zhang, Y.; Liu, N.; Qui, J. *Green Chem.* **2012**, *14*, 2999–3003.

(27)   Woodring, J. L. PhD thesis: *Enhancing Physicochemical Properties through Synthesis and Formulation of Piclamislast- and Lapatinib-Derived Analogues*, Northeastern University. 2014.

(28)   Jedinák, L.; Zátopková, R.; Zemánková, H.; Šustková, A.; Cankař, P. *J. Org. Chem.* **2017**, *82* (1), 157–169.

(29)   Ahmadi, Z.; McIndoe, J. S. *Chem. Commun.* **2013**, *49* (98), 11488–11490.

(30)   Maluenda, I.; Navarro, O. *Molecules* **2015**, *20* (5), 7528–7557.

(31)   Dequirez, G.; Bourotte, M.; Porras de Francisco, E.; Remuiñan Blanco, M. J.; Déprez, B.; Willand, N. *ChemistrySelect* **2017**, *2* (28), 8841–8846.

(32)   Ge, S.; Hartwig, J. F. *Angew. Chem. Int. Ed.* **2012**, *51* (51), 12837–12841.

(33)   Lidström, P.; Tierney, J.; Wathey, B.; Westman, J. *Tetrahedron* **2001**, *57* (45), 9225–9283.

(34)   Wang, S.; Guo, R.; Li, J.; Zou, D.; Wu, Y.; Wu, Y. *Tetrahedron Lett.* **2015**, *56* (24), 3750–3753.

(35)   Mamane, V. *Mini. Rev. Org. Chem.* **2008**, *5* (4), 303–312.

(36)   Mamane, V.; Riant, O. *Tetrahedron* **2001**, *57* (13), 2555–2561.

(37)   Jensen, J. F.; Søtofte, I.; Sørensen, H. O.; Johannsen, M. *J. Org. Chem.* **2003**, *68* (4), 1258–1265.

(38)   Imrie, C.; Loubser, C.; Engelbrecht, P.; McCleland, C. W. *J. Chem. Soc. Perkin Trans. 1* **1999**, 0, 2513–2523.

(39)   Braga, D.; Polito, M.; Bracaccini, M.; D'Addario, D.; Tagliavini, E.; Sturba, L.; Grepioni, F. *Organometallics* **2003**, *22* (10), 2142–2150.

(40)   Thomas, A. A.; Zahrt, A. F.; Delaney, C. P.; Denmark, S. E. *J. Am. Chem. Soc.* **2018**, *140* (12), 4401–4416.

(41)   Utepova, I. A.; Chupakhin, O. N.; Serebrennikova, P. O.; Musikhina, A. A.; Valery N Charushin. *J. Org. Chem.* **2014**, *79*, 8659–8667.

(42)   Horikoshi, R.; Nambu, C.; Mochida, T. *Inorg. Chem.* **2003**, *42*, 6868–6875.

(43)   James, S. L.; Adams, C. J.; Bolm, C.; Braga, D.; Collier, P.; Friščić, T.; Grepioni, F.; Harris, K. D. M.; Hyett, G.; Jones, W.; Krebs, A.; Mack, J.; Maini, L.; Orpen, A. G.; Parkin, I. P.; Shearouse, W. C.; Steed, J. W.; Waddell, D. C. *Chem. Soc. Rev.* **2012**, *41* (1), 413–447.

(44)   Wang, G. W. *Chem. Soc. Rev.* **2013**, *42* (18), 7668–7700.

(45)   Do, J. L.; Friščić, T. *ACS Cent. Sci.* **2017**, *3* (1), 13–19.

(46)   Hernández, J. G.; Friščić, T. *Tetrahedron Lett.* **2015**, *56* (29), 4253–4265.

(47)   Fernandes, C.; Oliveira, C.; Gano, L.; Bourkoula, A.; Pirmettis, I.; Santos, I. *Bioorg. Med. Chem.* **2007**, *15*, 3974–3980.

(48)   Gaunt, M. J.; Yu, J.; Spencer, J. B. *J. Org. Chem.* **1998**, *63*, 4172–4173.

CHAPTER 4

Forming multicomponent crystals of quinazolinones

4.1 INTRODUCTION

To remind the reader, one of the synthetic strategies carried out in the previous chapter is shown in Scheme 4.1 below. During the synthesis of the precursor analogues described in the previous chapter, an interesting observation was noted. In an attempt to purify **41**, the crude material was dissolved in hot methanol and allowed to stand overnight to recrystallise. Upon returning, two differently-shaped crystals were observed in the same vial and, after using single crystal X-ray diffraction to obtain their structures, it was confirmed that two different forms of **41** grew concomitantly from the solution (see Figure 3.10 on page 86). The two forms (Figure 4.1) were the close-packed structure of **41** (needle-shaped crystals) and a methanol solvate of **41** (block-shaped crystals).
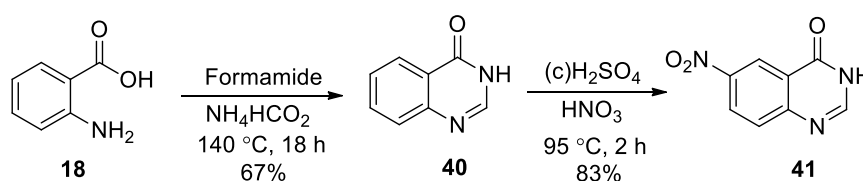
Scheme 4.1: Two-step synthesis of **41** starting from commercially available anthranilic acid (**18**).
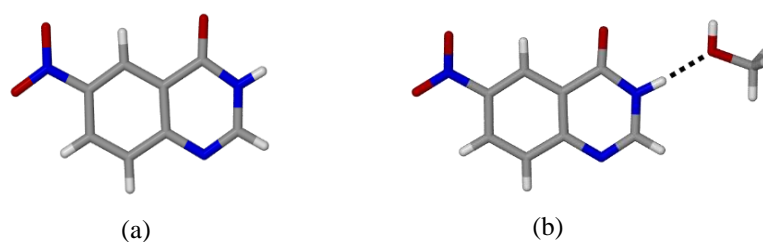
Figure 4.1: Structure of (a) **41** and (b) **41·MeOH** obtained from single crystal data.

As mentioned in the previous chapter, other derivatives of this quinazolinone have been synthesised as part of this thesis. We were able to obtain single crystal data for two other derivatives, namely the 6-iodoquinazolinone (**20**) and 6-aminoquinazolinone (**45**). The unsubstituted quinazolinone (**40**) was also synthesised, however single crystals could not be obtained, despite numerous attempts. This included using various solvents (and layering techniques) as well as the use of sublimation. In each case, no crystals suitable for single crystal X-ray diffraction were obtained.

We therefore have a series of 6-substituted quinazolinones (Figure 4.2) that we can use in order to study what effect small changes to the molecule has on its ability to form multicomponent crystals. Before beginning this study, we searched the Cambridge Structural Database (CSD) to see whether these compounds' crystal structures have been reported before, and whether they have been used to form multicomponent crystals with small organic coformers. In addition, we searched for similar derivatives that have been studied to potentially compare to any results we obtain.
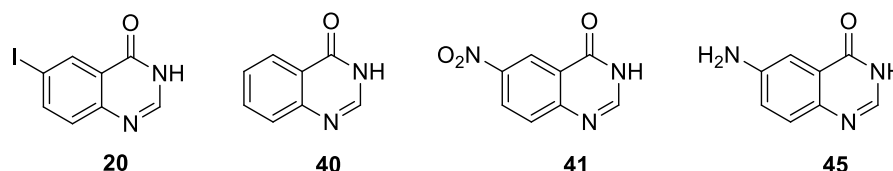
Figure 4.2: Structures of the four quinazolinones used in this study.

Compound **40** forms three multicomponent crystals with terephthalic acid (CSD refcode: AYIWIQ), picric acid (CSD refcode: OWIXAU) and 5-aminoisophthalic acid (CSD refcode: WEFKID). In each of the three multicomponent crystals, there is a hydrogen-bond between the carboxylic acid moiety of the coformer and the tertiary nitrogen atom of the quinazolinone. In the case of picric acid, proton transfer has occurred, resulting in a charge-assisted hydrogen bond. Figure 4.3 shows the main hydrogen-bonding interactions linking each molecule in the structure. No crystal structures were found for any of the quinazolinones by themselves or for any multicomponent crystals with **20**, **41**, and **45**.

(a)

(b)

(c)
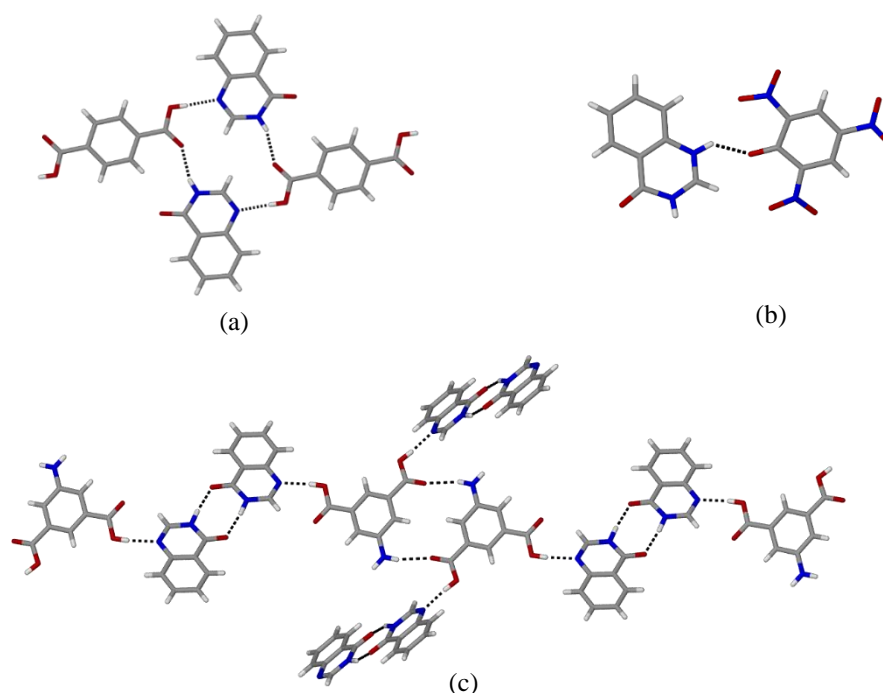
Figure 4.3: Main hydrogen-bonding interactions in (a) AYIWIQ, (b) OWIXAU and (c) WEFKID.

While these specific quinazolinone derivatives have not been tested for their efficacy against *P. falciparum*, various substituted quinazolin-4-(3*H*)-ones have been reported in the literature to have moderate to good efficacies.[1,2] Therefore studying the solid-state properties of compounds such as the ones described above, as well as their ability to form multicomponent crystals, are warranted and would be valuable. Investigating the types of intermolecular interactions formed by these quinazolinones will contribute to the current knowledge in the crystal engineering field that will one day allow for accurate predictions and tailored multicomponent crystals.

4.2 THE 6-SUBSTITUTED QUINAZOLINONES

4.2.1   6-Nitroquinazolinone – *41* and *41·MeOH*

The close-packed form of **41** grew as needles in the triclinic space group PĪ. An amide-amide hydrogen bond links two molecules to form a dimer with a N–H···O bond distance of 2.789 Å. These dimers then pack alongside each other to form a sheet, and these sheets stack to form the three dimensional structure. (Figure 4.4). Weaker interactions, such as the two C–H···O hydrogen bonds (3.416 Å and 3.530 Å) between the oxygen atoms of the nitro moiety and the C–H moiety of a second molecule of **41**. In addition, offset π-π interactions (centroid to centroid distance of 3.906 Å) between two molecules contribute to the overall packing of this molecule in the solid state. Additional hydrogen-bonding interactions can be found in Chapter 6, page 160. Selected crystallographic details for this structure can be found in Table 4.1.

<div align="center">(a)   (b)</div>
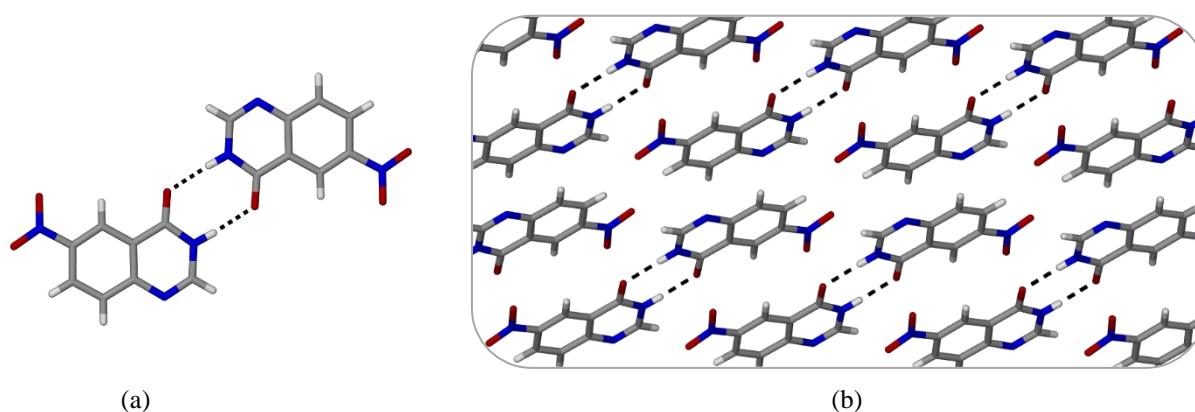
Figure 4.4: (a) Hydrogen-bonded dimer of **41** and (b) packing diagram of **41** viewed down the *a* axis.

The methanol solvate, **41·MeOH**, packs in the monoclinic space group *P*21/*c* with one molecule of **41** and one molecule of MeOH per asymmetric unit (Figure 4.5). Instead of the amide-amide hydrogen bond (as in the close-packed form), an N–H···O hydrogen bond (2.773 Å) links **41** to the methanol molecule, which, in turn, hydrogen bonds to a second molecule of **41** (via the tertiary quinazolinone nitrogen atom) to form chains of molecules. There is also an additional hydrogen bond between the

carbonyl oxygen atom of one molecule of **41** and the C–H between the two quinazolinone nitrogen atoms of a second molecule. These chains pack alongside each other to form layers, which is held together by face-to-face π-π interactions (with centroid to centroid distances of 3.984 Å). Additional hydrogen-bonding interactions can be found in Chapter 6, on page 168. Selected crystallographic information can be found in Table 4.1.

The quinazolinone molecules pack in such a way as to incorporate the methanol molecules in channels that run down the *a* axis. By deleting these methanol molecules in Mercury[3–5] and mapping the contact surface using a probe radius of 1.2 Å and a grid spacing of 0.7 Å, it can be seen that the molecules indeed do form channels (volume of 194 Å^3), as shown in Figure 4.5c.

(a)

(b)

(c)
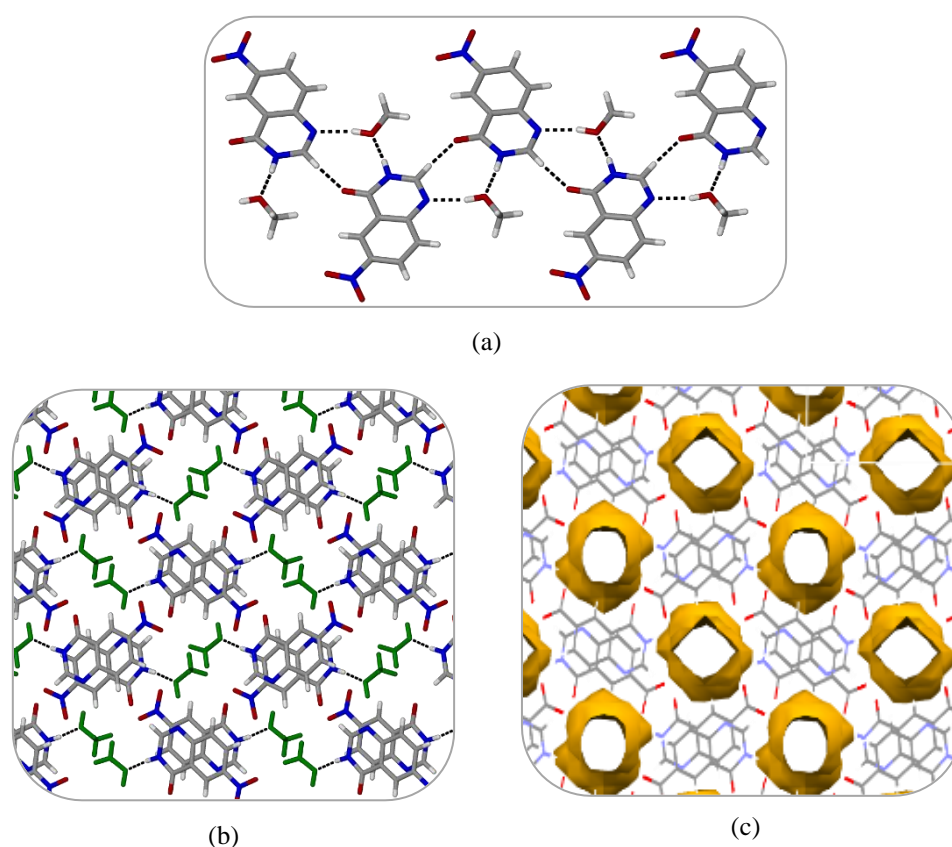
Figure 4.5: (a) Hydrogen-bonded chain of **41** and **MeOH** molecules; (b) packing diagram of **41·MeOH** viewed down the *a* axis, with MeOH molecules shown in green for clarity; (c) packing diagram of **41·MeOH** viewed down the *a* axis that shows the contact surface (in yellow) of the channels calculated in Mercury using a probe radius of 1.2.

Initially we investigated whether we could obtain the two forms separately. To this end, we dissolved 20 mg of the crude powder in hot methanol and placed the vial in the fridge (4 °C) overnight. The next morning, only needle-shaped crystals were obtained (as confirmed by unit cell and PXRD analysis). Attempts were then made to obtain only the methanol solvate. Because the close-packed form appears to be the kinetically favoured product, we opted for a slower cooling period. The nitroquinazolinone

powder was dissolved in methanol at 60 °C in an oil bath. Once **41** was completely dissolved, the heat was turned off, but the vial was left in the oil bath to slowly cool to room temperature. This unfortunately resulted in the formation of a mixture of the forms, even when recrystallised **41** was used instead of the crude powder. It was later found that by eliminating water from the solution (by using dry methanol and a Schlenk tube filled with nitrogen) as well as by seeding the solution with crystals of the solvate, we were able to increase the amount of the solvate produced, but never form it exclusively, even when using the slow-cooling method described above.

Despite the methanol being hydrogen bonded to the framework, the solvent appears to readily escape, as the crystals become opaque after a few hours after removing them from the mother liquor. This was confirmed by thermogravimetric analysis (TGA), where a mass loss roughly correlating to one methanol molecule per asymmetric unit is observed (see Chapter 6, page 170) Once the methanol is removed, the framework reverts to the close-packed form, as confirmed by PXRD.

4.2.2   6-Aminoquinazolinone – **45**

Compound **45** (Figure 4.6) packs in the orthorhombic space group *Pca*2_1 with two molecules per asymmetric unit. A similar hydrogen-bonding pattern between the amide moieties can be seen for **45** as was seen for **41** (Figure 4.4 and Figure 4.5), with a N–H···O hydrogen bond distance of 2.814 Å and 2.828 Å. The dimers are linked via an N–H···N hydrogen bond between the amino moiety of one molecule and one of the quinazoline nitrogen atoms of a second molecule. Pairs of hydrogen-bonded molecules stack to form columns, held together by offset π-π interactions (with centroid to centroid distance of 3.564 Å). Alternating columns are at 90° to each other. The columns are linked by the N–H···N hydrogen bonds.

| (a) | (b) |
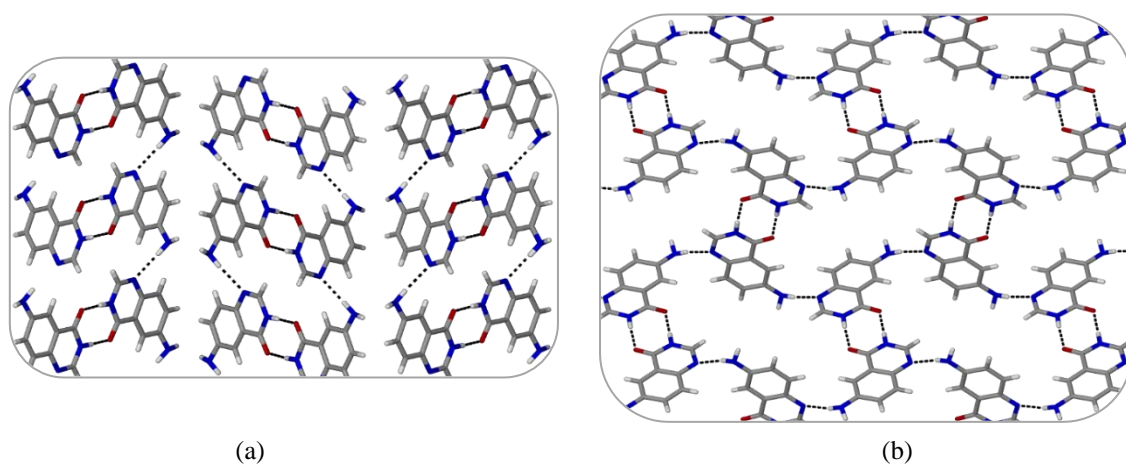
Figure 4.6: (a) Packing of **45** viewed down *b* axis and (b) hydrogen-bonded sheet of molecules of **45** viewed down the *c* axis.

4.2.3   6-Iodoquinazolinone – *20*

Compound **20** packs in the monoclinic space group *P*2$_1$/*n* with one molecule in the asymmetric unit. Similar hydrogen bonding between the amide moieties can be seen for **20** as in **41** (Figure 4.7), with a N–H···O hydrogen bond distance of 2.778 Å. Similarly to **45**, the dimers π-stack (centroid to centroid distance of 3.493 Å) in alternating columns down the *a* axis, but here are linked together by halogen bonds between the iodine atom of a molecule in one column and one of the nitrogen atoms of a molecule in a neighbouring column (N···I bond distance of 3.057 Å) (Figure 4.7).

(a)

(b)

(c)
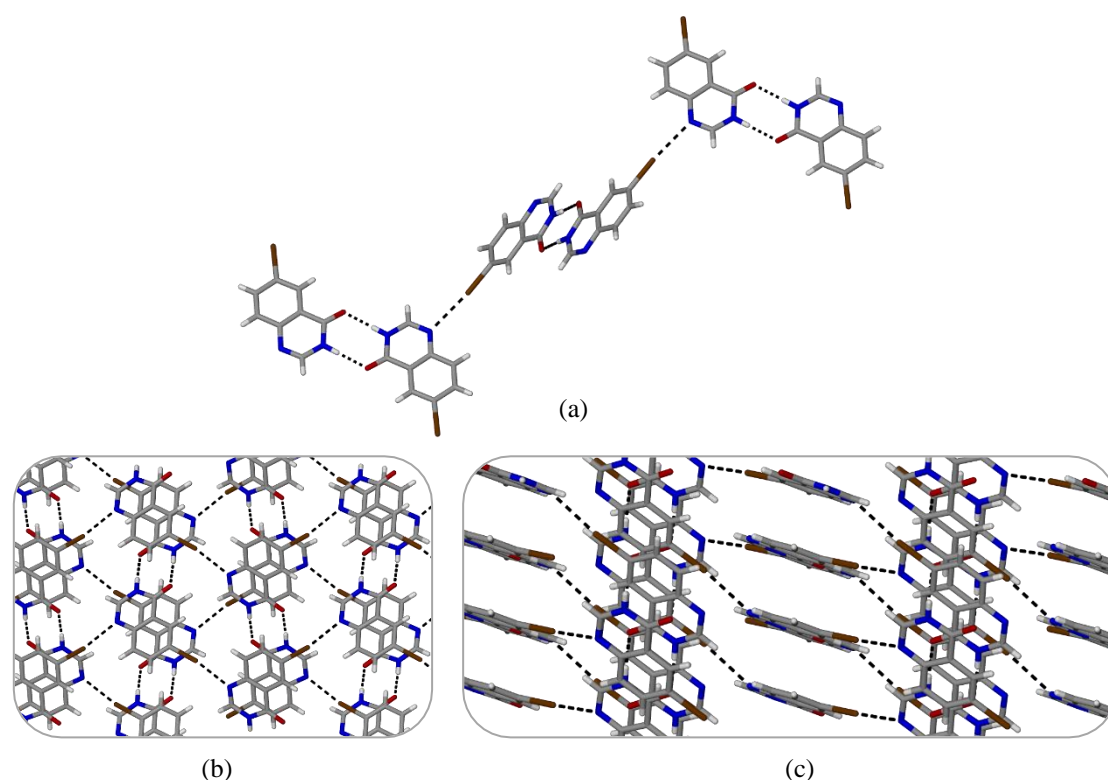
Figure 4.7: (a) Hydrogen-bonded chain of **20**; (b) packing of **20** viewed down the *a* axis; (c) packing of **20** viewed down [1 -2 0].

Table 4.1: Selected crystallographic details for **41**, **41·MeOH**, **45** and **20**.

	41	41·MeOH	45	20
Molecular formula	$C_8H_5N_3O_3$	$C_8H_5N_3O_3 \cdot CH_4O$	$C_8H_7N_3O$	$C_8H_7IN_2O$
Formula weight	191.15	223.19	161.17	272.04
Crystal system	Triclinic	Monoclinic P	Orthorhombic	Monoclinic
Space group	$P\bar{1}$	$P2_1/c$	$Pca2_1$	$P2_1/n$
Z	2	4	8	4
a (Å)	5.5097(2)	7.829(2)	13.3387(1)	7.9429(8)
b (Å)	8.6412(3)	10.876(3)	4.9229(4)	7.1808(7)
c (Å)	8.6508(3)	11.669(3)	21.4414(2)	14.3395(1)
α (°)	105.456(1)	90	90	90
β (°)	90.777(2)	94.037(3)	90	91.833(1)
γ (°)	99.774(2)	90	90	90
Volume ($Å^3$)	390.46(2)	991.2(4)	1407.95(2)	817.45
Temperature (K)	100(2)	100(2)	100(2)	100(2)
R_{int}	0.024	0.046	0.035	0.013
R1 [I>2σ(I)]	0.043	0.038	0.034	0.015
wR$_2$	0.140	0.098	0.090	0.036
GoF	1.11	1.04	1.06	1.10

Each quinazolinone shows the same amide-amide hydrogen bond motif, however these motifs pack in different ways to form the solid state structure. In addition, π-π interactions between the quinazolinone molecules also play an important role in the stabilisation and packing of each structure. Compound **45** and **20** show additional interactions (through the 6-position substituent) that contribute to the overall packing and stability of the solid-state structure.

Initially, each quinazolinone was dissolved in various organic solvents in an attempt to form solvates similarly to **41·MeOH**, however, in each case, only the close-packed structures (described above) were obtained. While we were able to obtain the methanol solvate of **41**, it does not seem to be very stable, and appears to convert over time to the close-packed structure. Therefore, it is not too surprising that we did not obtain any other solvates.

We did, however, have more hope for the formation of multicomponent crystals with organic coformers, given the precedent for them on the CSD. While there were only three multicomponent forms of **40**, it provided precedent for our pursuit for the formation of multicomponent crystals of these quinazolinone

derivatives. For this, we would need to select coformers in which to carry out the experimental screening.

4.3 SELECTION OF COFORMERS

By studying the crystal structures of **41**, **45** and **20**, it can be seen that the amide-amide interactions, as well as the π-π interactions, are central to the packing of these molecules in the solid state. In order to form multicomponent crystals, the interactions formed between the quinazolinone and the coformer would need to be more favourable than the interactions present in each individual component. While the crystal structure of **40** could not be obtained, it is not unreasonable to assume that similar amide-amide interactions to those of **41**, **45** and **20** are present in the packing of these molecules in the solid state. By studying the three multicomponent crystals of **40** that were found in the CSD, it can be seen that in each case, a hydrogen bond between the quinazolinone nitrogen atom and the OH moiety of the coformer links the two molecules in the multicomponent crystal.

Therefore, the use of carboxylic acid coformers, as well as aromatic acids or phenols, would be a good choice in coformer in the formation of multicomponent crystals with this series of quinazolinones. We decided to make use of the same MEPS approach that was used in Chapter 2 to choose coformers for this study. In this way we could further validate the usefulness of this approach for the appropriate choice of coformers. This method proves especially useful in this study over other computational methods as the crystal structure of **40** is not known.

The same 32 coformers were used for this study as described in Chapter 2. The advantage of this is that the geometry optimisation and identification of the local minima and maxima on the electrostatic potential map for each coformer has already been performed (Chapter 2). This allowed for a substantially faster processing time, as only the quinazolinone compounds needed to be optimised (and local minima and maxima identified) before the change in energy for each system could be calculated. The ten coformers with the highest ΔE values for **40**, **41** and **45** are given in Table 4.2. The full list for each compound and the corresponding ΔE values for each coformer is tabulated in Chapter 6, page 164.

Table 4.2: Ranked list of the top ten coformers for **40**, **41** and **45**.

40		41		45	
Coformer*	**-ΔE (kJ mol⁻¹)**	**Coformer***	**-ΔE (kJ mol⁻¹)**	**Coformer***	**-ΔE (kJ mol⁻¹)**
OXA	10.4	OXA	9.6	OXA	12.1
DHBA	6.2	*p*-ABA	9.5	TRIM	7.1
MGAL	6.1	EDA	9.0	PAM	7.0
FUM	5.4	DHBA	8.1	EDA	6.5
TRIM	5.4	MGAL	7.3	DHBA	6.2
PAM	5.0	RES	6.6	FUM	5.9
p-ABA	4.9	TRIM	6.5	RES	5.5
RES	4.4	BENZ	6.4	PIP	5.5
IND	4.2	PIP	6.2	PYZ	4.9
BENZ	3.1	PAM	5.3	BIPY	4.4

*Coformer codes: OXA – oxalic acid, DHBA – 3,5-dihydroxybenzoic acid, MGAL – methyl gallate, FUM – fumaric acid, TRIM – trimesic acid, PAM – pamoic acid, *p*-ABA – *p*-aminobenzoic acid, RES – resorcinol, IND – indole, BENZ – benzamide, EDA – 1,3-ethylenediamine, PIP – piperazine, PYZ – pyrazine, BIPY – 4,4-bipyridine

One of the disadvantages of the MEPS approach is that the same basis set must be used in the geometry optimisations for both components (both the quinazolinone and the coformer) for the calculations to be sufficiently accurate. Up until now, this has not been problematic as the B3LYP/6-31+G* basis set was used for all components. This basis set, however, does not allow for the geometry optimisation of **20**, due to the presence of the iodine atom in the molecule. Instead, the LanL2DZ basis set needed to be used for this compound to accommodate the heavy atom.[6] This unfortunately meant that the calculations for **20** could not be carried out unless all coformers were re-optimised using this basis set. As we were merely trying to narrow down our list of coformers, we simply opted to only perform the liquid-assisted grinding with the coformers that were present in the top ten list for the other quinazolinone compounds. As each quinazolinone's top ten list was similar, this would not yield an unreasonable list of coformers for **20**.

For this study, we also investigated different stoichiometry between the quinazolinones and coformer in these calculations. The values for a 2:1 or 1:2 ratio (quinazolinone to coformer) were comparable to the 1:1 ratio and the ranking of the coformers remained mostly the same. Similar conclusions were made by Musumeci *et al.* in their study.[7,8] We therefore proceeded with a 1:1 ratio for the experimental screening.

4.4 FORMATION OF MULTICOMPONENT CRYSTALS

The formation of multicomponent crystals for these compounds followed a similar procedure as for those in Chapter 2. Initially, each quinazolinone was ground individually in a mortar and pestle for 5 minutes with a few drops of MeOH to determine whether a new product (solvate, hydrate, polymorph etc.) could be formed simply from these conditions, without a coformer present. In the case of **20**, **40**, and **45**, the PXRD pattern obtained after grinding the compound matched that of the pre-ground material, indicating that no new product is obtained from grinding the compound under these conditions. The PXRD of **41**, however, showed that after grinding, the material becomes partially amorphous. Extending the grinding time to 10 minutes resulted in a completely amorphous product.

For the purpose of this study, the top ten coformers were chosen to perform the experimental screening. Stoichiometric amounts (1:1 ratio) of each compound (10 mg) and coformer were ground together in a mortar and pestle for 5 minutes with a few drops of methanol. PXRD was used to determine whether a new product was obtained, or if merely a mixture of starting materials was present.

4.4.1   Outcome of liquid-assisted grinding experiments

For each grinding experiment, the PXRD pattern of the product was compared to those of the individual components to determine whether or not a new product had been obtained. The PXRD patterns of the successful attempts can be found in Chapter 6 (page 165 to 167). The remaining combinations only yielded starting material after liquid-assisted grinding, even after grinding for an additional 5 minutes.

As an example, the formation of **40·SAL** is discussed here in more detail. In Figure 4.8, the powder patterns of **40** (shown in blue), salicylic acid (shown in green) and the product obtained after LAG (maroon) is shown. It is clear that the product after LAG is not simply a mixture of the two starting components. Single crystals of **40·SAL** were obtained (discussed later in this chapter) and the calculated pattern obtained from the single crystal data (shown in black in Figure 4.8) matches the experimentally obtained pattern for **40·SAL**.

Analysis of the PXRD patterns of **40·OXA** and **40·FUM** after grinding for 5 minutes in a 1:1 ratio (**40**:coformer) showed that a new product had formed, however there were still peaks corresponding to **40** present. As no coformer peaks were present, it indicated that the ratio of 1:1 was likely incorrect. Repeating the grinding experiment in a 2:1 ratio (**40**:coformer) resulted in a seemingly pure product (see Figure 6.48 and Figure 6.49 on page 165).
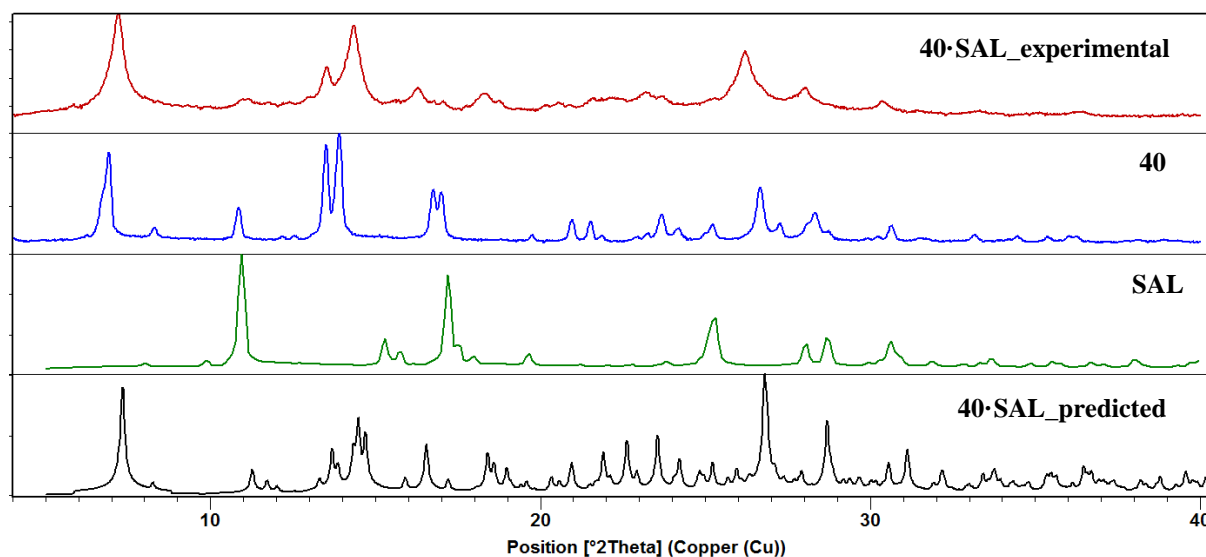
Figure 4.8. Comparison of the PXRD patterns of **40·SAL** (maroon), **40** (blue), salicylic acid (**SAL**, green) and the predicted PXRD pattern of **40·SAL** obtained from single crystal data (black).

Out of the top ten coformers, only oxalic acid, fumaric acid and resorcinol formed multicomponent crystals with **40**, while, surprisingly, no new multicomponent crystals were obtained when any of the other quinazolinones were ground together with the various coformers. For grinding experiments with **41** and each coformer, a powder pattern corresponding to the same amorphous material obtained when grinding **41** individually, was obtained. It was therefore concluded that a new multicomponent product was not obtained. We extended the experimental screening to all 32 coformers for **40** to see whether we could obtain any other multicomponent crystals. To our delight, we were able to obtain an additional four multicomponent crystals (with salicylic acid, succinic acid, glutaric acid and benzoic acid).

We then extended the experimental screening of the other three quinazolinones to include the coformers that were successful in forming multicomponent crystals with **40**, but this did not yield a fruitful outcome.

In addition, we also tried grinding the four quinazolinones with each other (for example grinding **40** with **41**). All of the possible combinations were tried; however, in each case, only a physical mixture of the two components was obtained, even after extended grinding times.

Table 4.3: Ranked list of the 32 coformers and corresponding outcome after LAG with **40**

Coformer*	-(ΔE) (kJ mol⁻¹)	LAG outcome**	Coformer*	-(ΔE) (kJ mol⁻¹)	LAG outcome**
OXA	10.4	MCC	PIP	2.1	SM
DHBA	6.2	SM	HYD	1.9	SM
MGAL	6.1	SM	SUC	1.5	MCC
FUM	5.4	MCC	SAC	1.2	SM
TRIM	5.4	SM	MOR	1.0	SM
PAM	5.0	SM	BIPY	0.7	SM
p-ABA	4.9	SM	GLU	0.7	MCC
RES	4.4	MCC	THEO	0.6	SM
IND	4.2	SM	CAF	0.6	SM
BENZ	3.1	SM	VAN	0.5	SM
TERE	3.1	MCC	NAPH	0.4	SM
EDA	3.1	SM	NIC	0.3	SM
MAL	2.7	SM	PYZ	0.3	SM
SAL	2.6	MCC	BEN	0.2	MCC
TAR	2.5	SM	MEN	0.1	SM
THY	2.3	SM	NICO	0.1	SM

*Coformer code: OXA – oxalic acid, DHBA – 3,5-dihydroxybenzoic acid, MGAL – methyl gallate, FUM – fumaric acid, TRIM – trimesic acid, PAM – pamoic acid, *p*-ABA – *p*-aminobenzoic acid, RES – resorcinol, IND – indole, BENZ – benzamide, TERE – terephthalic acid, EDA – 1,3-ethylenediamine, MAL – malonic acid, SAL – salicylic acid, TAR – tartaric acid, THY – thymine, PIP – piperazine, HYD – hydroquinone, SUC – succinic acid, SAC – saccharin, MOR – morpholine, BIPY – 4,4-bipyridine, GLU – glutaric acid, THEO – theophylline, CAF – caffeine, VAN – vanillin, NAPH – naphthalene, NIC – nicotinic acid, PYZ – pyrazine, BEN – benzoic acid, MEN – menthol, NICO – nicotinic acid.
**LAG outcome: MCC = multicomponent crystal; SM = starting material

The products obtained after LAG were then dissolved in MeOH (with gentle heating and stirring) in an attempt to form single crystals of the multicomponent product. The vials were placed on a shelf, away from movement and vibration, and the solution was left to slowly evaporate. If crystals or powder formed in the vial, PXRD was used to ascertain whether or not this product matched that of the outcome of LAG. Single crystals of new products were used to obtain crystal structure data to study the packing and association of these molecules in the solid state.

4.4.2 Obtaining crystal structures of the multicomponent crystals

We were able to obtain crystal structures of three of the multicomponent crystals formed with **40** – those formed with oxalic acid, fumaric acid and salicylic acid as coformers. Selected crystallographic parameters for each crystal structure are given in Table 4.4. The PXRD pattern obtained from single

crystal data matched that of the bulk sample obtained from solution as well as the product obtained from the LAG experiments. This confirmed that in each case, the same multicomponent product was obtained from grinding and solution methods.

Compound **40** forms a 2:1 salt with oxalic acid (**40·OXA**) that crystallises in the monoclinic space group $C2/c$. There is one molecule of **40** and half an oxalic acid molecule per asymmetric unit. The amide-amide hydrogen bond is no longer seen between two molecules of **40**. An N–H⋯O hydrogen bond (2.877 Å) between the quinazolinone NH atoms and the carbonyl oxygen atom of oxalic acid and an N–H⋯O (2.583 Å) between the tertiary nitrogen atom of the quinazolinone and one of the oxygen atoms of oxalic acid is observed. These two hydrogen bonds link molecules of **40** together into columns down the c axis. Additionally, π-π interactions between pairs of molecules of **40** (centroid to centroid distance of 3.753 Å) are observed. The hydrogen atom of the carboxylic acid was located in the electron density difference map. The C=O and C–O bond lengths (1.227 Å and 1.287 Å, respectively) of the carboxylic acid moiety indicate that only partial proton transfer has taken place. After several refinements, the hydrogen atom appears slightly closer to the nitrogen atom of the quinazolinone than to the oxygen atom of the coformer (1.228 Å versus 1.338Å) and therefore is depicted as a salt in Figure 4.9.

(a)   (b)   (c)
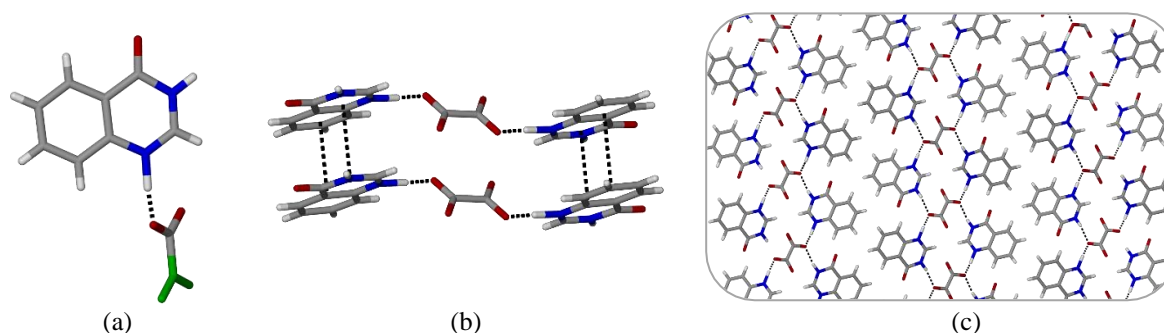
Figure 4.9: (a) Asymmetric unit of **40·OXA** with the symmetry-generated half of the oxalic acid molecule shown in green for clarity; (b) π-π interactions between molecules of **40** and N–H⋯O hydrogen bond between **40** and oxalic acid and (c) packing of **40·OXA** viewed down the *b* axis.

Compound **40** also forms a 2:1 cocrystal with fumaric acid (**40·FUM**) that packs in the monoclinic space group $P2_1/n$ with one molecule of **40** and half a molecule of fumaric acid per asymmetric unit. Similarly to **40·OXA**, the amide-amide hydrogen bond is not seen in **40·FUM**, but rather the O–H⋯N hydrogen bond (2.619 Å) between the OH moiety of fumaric acid and one of the quinazolinone nitrogen atoms. An additional N–H⋯O hydrogen bond (2.838 Å) is observed between the secondary nitrogen atom of the quinazolinone molecule and the carbonyl oxygen atom of neighbouring molecules of **40**.

(a)   (b)
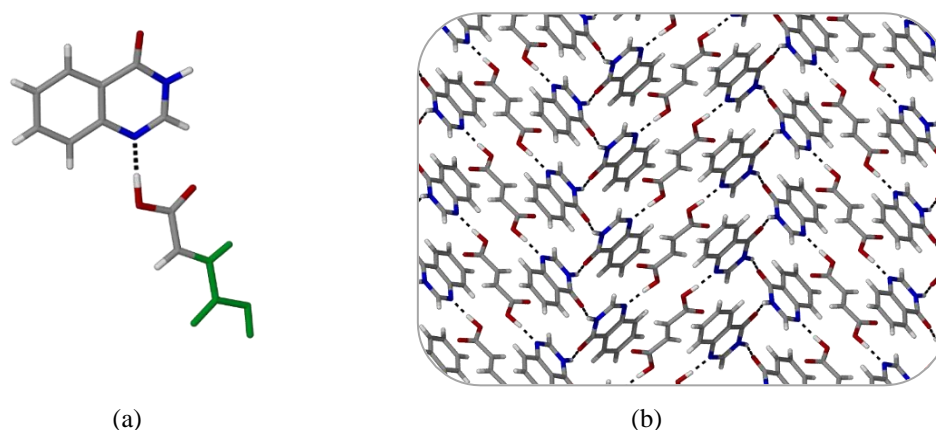
Figure 4.10: (a) Asymmetric unit of **40·FUM** with the symmetry-generated half of fumaric acid shown in green for clarity and (b) packing of **40·FUM** viewed down the *b* axis.

Compound **40** forms a 1:1 cocrystal with salicylic acid (**40·SAL**) that packs in the triclinic space group *P*$\bar{1}$, with two molecules of each component present in the asymmetric unit. While it appears that there could be additional symmetry present in this structure, the molecules are slightly offset and this disrupts the symmetry that would result in a different space group. The structure was analysed in Platon[9] using the "addsym" function, which did not detect additional symmetry. Interestingly, in this multicomponent crystal, the amide-amide hydrogen bonding motif between the **40** molecules is observed with a hydrogen-bond distance of 2.784 Å and 2.784 Å. A second hydrogen bond (2.633 Å) between the carboxylic acid moiety and the tertiary quinazolinone nitrogen atom links the molecules into tetramers. These tetramers pack in sheets perpendicular to the *a* axis.

(a)   (b)
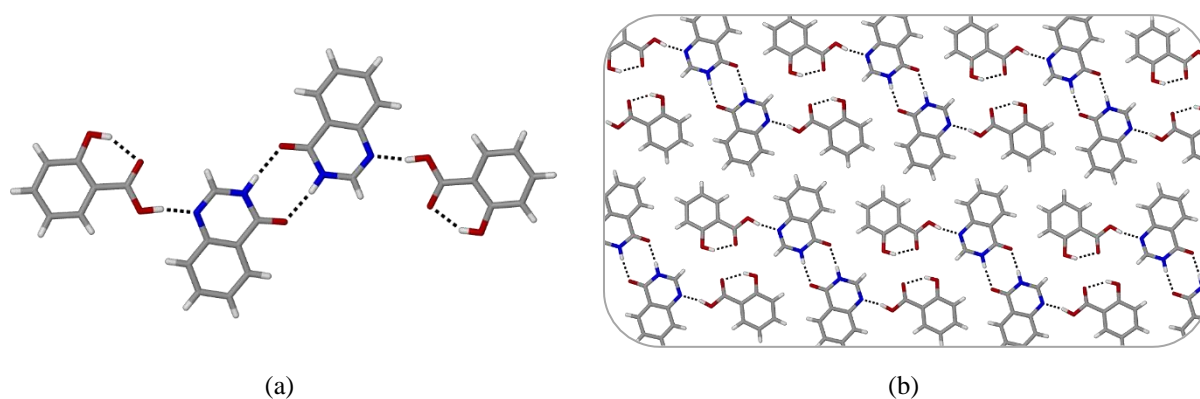
Figure 4.11: (a) Asymmetric unit of **40·SAL** and (b) hydrogen-bonded sheet of **40·SAL** viewed down the *a* axis.

Table 4.4: Selected crystallographic details for the multicomponent crystals obtained with **40**

	40·OXA	**40·FUM**	**40·SAL**
Molecular formula	$C_8H_6N_2O \cdot 0.5(C_2H_4O_4)$	$C_8H_6N_2O \cdot 0.5(C_4H_4O_4)$	$C_8H_6N_2O \cdot C_7H_6O_3$
Formula weight	190.16	204.18	284.27
Crystal system	Monoclinic	Monoclinic	Triclinic
Space group	$C2/c$	$P2_1/n$	$P\bar{1}$
Z	8	4	4
a (Å)	30.794(1)	12.5466(4)	8.1396(6)
b (Å)	3.7535(1)	5.6384(2)	12.9286(1)
c (Å)	13.872(5)	14.1431(5)	13.4391(1)
α (°)	90	90	109.609(1)
β (°)	104.263(7)	111.521(2)	102.898(1)
γ (°)	90	90	93.278(1)
Volume (Å³)	1553.9(1)	932.08(6)	1285.10(1)
Temperature (K)	100(2)	100(2)	100(2)
R_{int}	0.085	0.045	0.028
R1 [I>2σ(I)]	0.062	0.034	0.038
wR_2	0.155	0.091	0.107
GoF	1.14	1.07	1.04

Unfortunately, we were unable to form single crystals of the remaining multicomponent products, despite numerous attempts. The use of various solvents, including solvent mixtures and layering techniques, were tried, but resulted either in no product forming or the powdered multicomponent product. Both the pre-formed multicomponent product as well as the individual components were used in these attempts but no single crystals were obtained. In addition to solution methods, sublimation techniques were also tried, using either the pre-formed product or the two individual components, however this resulted only in the formation of two bands of powder/crystals, which PXRD analysis confirmed to be the two individual components.

Unfortunately, using infrared spectroscopy to identify whether proton transfer has taken place during the formation of these multicomponent crystals was not feasible, because the amide stretch of the quinazolinone overlaps with the carbonyl stretching peak of the carboxylic acid/carboxylate moiety.

One of the methods used to assist in the prediction of whether a coformer is likely to produce a cocrystal or a salt if a multicomponent product is obtained is the ΔpKa rule. This method has been used extensively in the literature and is based on the difference in the pKa values of the two components.[10–13] If ΔpKa is greater than 3, then a salt is expected to form, while if ΔpKa is less than 0, then a cocrystal is expected.

There is uncertainty in whether a salt or cocrystal will form (or even if a product in which partial proton transfer occurs) when the ΔpKa value lies between 0 and 3.

Because the majority of the multicomponent products obtained in this work contained carboxylic acid coformers, we decided to make use of this tool to see whether the predicted outcomes matched that of the experimental outcomes for the multicomponent products for which crystal structures are available. The results of this are summarised in Table 4.5. The pKa values for the quinazolinones and coformers were calculated using Advanced Chemistry Development (ACD/Labs) Software (V11.02).

Table 4.5: Using the ΔpKa rule to assess whether the multicomponent products of **40** are likely to be salts or cocrystals.

Coformer*	ΔpKa	Predicted outcome	Experimental outcome
OXA	1.31	Salt/cocrystal	Partial proton transfer
FUM	-0.46	Cocrystal	Cocrystal
SAL	-0.32	Cocrystal	Cocrystal
GLU	-1.64	Cocrystal	N/A
SUC	-1.55	Cocrystal	N/A
BEN	-1.51	Cocrystal	N/A
RES	-6.63	Cocrystal	N/A
TERE	-0.8	Cocrystal	Cocrystal**
PIC	2.39	Salt/cocrystal	Salt**
AISO	-6.17	Cocrystal	Cocrystal**

*Coformer codes: OXA – oxalic acid, FUM – fumaric acid, SAL – salicylic acid, GLU – glutaric acid, SUC – succinic acid, BEN – benzoic acid, RES – resorcinol, TERE – terephthalic acid, PIC – picric acid, AISO – 5-aminoisophthalic acid.
**Crystal structures available on the CSD (described at the beginning of this chapter); N/A = no crystal structure obtained.

From the table above, it is clear that the prediction was accurate for each crystal structure obtained in this study (oxalic acid, fumaric acid and salicylic acid), as well as for the three multicomponent crystals obtained from the CSD (terephthalic acid, picric acid and 5-aminoisophthalic acid). Therefore, it is likely that the prediction would be correct for the remaining four multicomponent products for which we could not obtain single crystals. However, without single crystal data, this cannot be confirmed.

4.5 WHY DOES ONLY COMPOUND 40 FORM MULTICOMPONENT CRYSTALS?

It is surprising that only the unsubstituted quinazolinone (**40**) forms multicomponent crystals with these coformers. While we did expect that the substituent may have some influence, we did not expect it to

completely hinder the compounds' ability to form multicomponent crystals with these coformers. By studying the crystal structures and the MEPS of these compounds in more detail we could perhaps find a possible explanation.

Etter's rule, which has been used extensively in crystal engineering and prediction studies in the literature, states that the strongest hydrogen-bond donor will interact with the strongest hydrogen-bond acceptor site.[14,15] We therefore studied the MEPS of each compound and some of the coformers in more detail to determine whether the strongest donor-acceptor interaction would be between two different components or two of the same components. Shown in Figure 4.12 is the MEPS for **40**, **41** and **45,** as well as for the coformer, salicylic acid (**SAL**). This example was chosen as salicylic acid forms a multicomponent crystal with **40**, and the crystal structure had been obtained and therefore we were able to study the interactions that result in its formation.
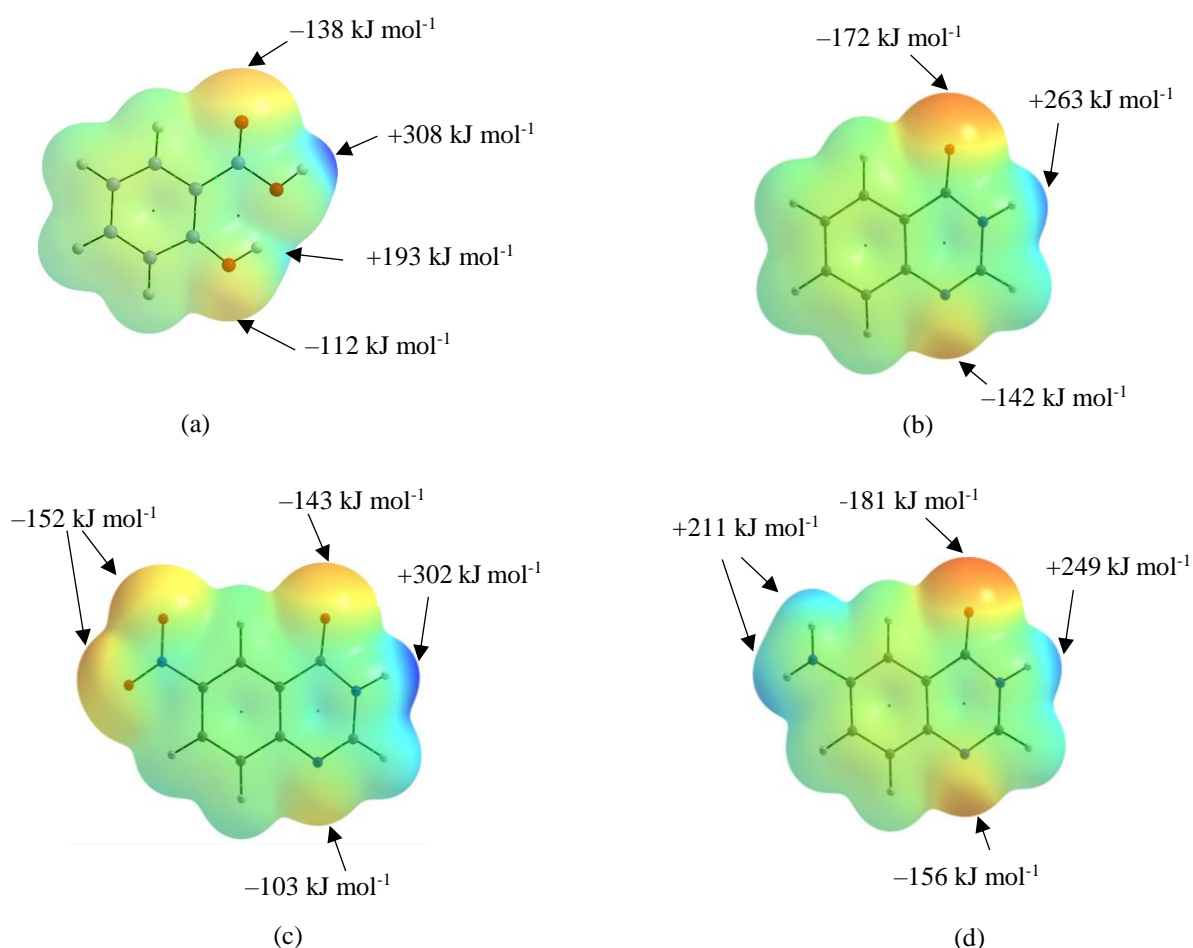
Figure 4.12: MEPS of (a) salicylic acid, (b) **40**, (c) **41** and (d) **45** mapped onto the 0.002 Bohr A^{-3} isosurface (blue +315 kJ mol^{-1} to red -225 kJ mol^{-1}).

When looking at the combination of **40** and **SAL**, the strongest hydrogen-bond donor site between both molecules is +308 kJ mol^{-1} (carboxylic acid OH group on **SAL**), while the strongest hydrogen-bond acceptor site is -172 kJ mol^{-1} (carbonyl oxygen atom of **40**). Following Etter's rules, it is predicted that

this combination would likely form a multicomponent crystal through that interaction. While we did indeed form a multicomponent crystal with this combination, the main hydrogen-bonding interaction between **40** and **SAL** in the crystal structure is between the strongest donor on the coformer and the second strongest acceptor (tertiary nitrogen atom) on **40**. In addition, a second hydrogen bond is observed between the second strongest donor (NH moiety of **40**) and the strongest acceptor (carbonyl oxygen atom of **40**). These interactions are both found on the same molecule and therefore result in an amide-amide dimeric interaction between two molecules of **40**.

If these are the interactions observed in the formation of **40·SAL**, then one might expect these to be the favoured interactions should a multicomponent product form between **41** and **SAL**. Looking at the combination of **41** and **SAL**, the strongest hydrogen-bond donor site on **41** (NH moiety, 302 kJ mol^{-1}) has very similar strength to that of the strongest hydrogen-bond donor site on **SAL** (carboxylic acid OH moiety, 308 kJ mol^{-1}). As these are of comparable strength and the tertiary quinazolinone nitrogen atom acceptor is a weaker acceptor than in **40**, this may result in the favoured formation of only the amide-amide dimer between two molecules of **41**, rather than the O–H···N interaction between **41** and **SAL**, resulting in no multicomponent product being obtained. Although the nitro group is the strongest acceptor, this does not seem to be favoured as a hydrogen-bond acceptor as it is not involved in hydrogen bonding in either of the crystal structures of **41** obtained (**41** and **41·MeOH**).

For the combination of **45** and **SAL**, there is now the presence of another relatively strong hydrogen-bond donor on the quinazolinone. In the crystal structure of **45**, the strongest hydrogen-bond donor (NH moiety of the amide) and the strongest hydrogen-bond acceptor (carbonyl oxygen atom) interact, forming the amide-amide dimer. The second strongest donor (NH$_2$ moiety) interacts with the second strongest acceptor (tertiary nitrogen atom). It seems that these two interactions are more favourable than an interaction between **45** and a coformer and therefore no multicomponent products are obtained.

In the other multicomponent products obtained with **40**, **40·FUM** and **40·OXA**, a different packing arrangement is observed to that in **40·SAL**, in which the amide-amide interaction is not present. Despite this, in these combinations of hydrogen-bond donors and acceptors, a similar trend is still observed as in **40·SAL**, with the strongest hydrogen-bond donor on the coformer interacting with the second strongest hydrogen-bond acceptor (tertiary nitrogen atom on **40**).

The difference in the arrangement of these combinations lies not with this O–H···N hydrogen-bonding interaction, but rather in the additional hydrogen bond present. The second hydrogen bond between the second strongest donor (NH moiety on **40**) and strongest acceptor (carbonyl oxygen atom on **40**) no longer occurs as an amide-amide hydrogen bond between two molecules of **40** (forming the amide-amide dimer). In the case of **40-FUM**, this N–H···O hydrogen bond now links three molecules of **40** together, rather than just two (each with separate N–H···O hydrogen bonds). In the case of **40·OXA**, this N–H···O hydrogen bond no longer occurs, but rather a different N–H···O hydrogen bond linking

two **40·OXA** dimers together, again in the pattern of strongest hydrogen bond donor (NH moiety of **40**) interacting with the second strongest hydrogen-bond acceptor (oxygen atom of the OH moiety on the coformer).

So far, the focus has been directed toward hydrogen-bonding interactions. To test whether this applies to other intermolecular interactions such as halogen bonding, we carried out LAG experiments in which each of the quinazolinones were ground with 1,4-diiodotetrafluorobenzene and a few drops of MeOH. This compound is known to form halogen bonds with other molecules and has the potential to form halogen bonds with our quinazolinone series.[11,16,17] Once again, only the unsubstituted quinazolinone (**40**) formed a multicomponent product (as analysed by PXRD), while the remaining three quinazolinones (**41**, **45** and **20**) yielded only a physical mixture of starting materials after grinding.

The most plausible interaction occurring in this multicomponent product would be a halogen bond between the tertiary nitrogen atom of **40** and one of the iodine atoms on the coformer as this seemed to be most favourable for the hydrogen bond linking **40** and the other coformers, however, without single crystal data, this cannot be confirmed. This indicates that it is most likely that both hydrogen- and halogen-bonding interactions are influenced by the substituents at the 6-position of these quinazolinone molecules. While we have explored a number of commonly-accepted explanations for interactions in crystal engineering ("rule of thumb" type ideas), none of them provide a satisfactory explanation for the variation that is observed here.

4.6 CONCLUDING REMARKS

This study began with the serendipitous discovery of two forms of 6-nitroquinazolinone (**41**) that grew concomitantly from MeOH. Other 6-subsituted derivatives of quinazolin-4-(3*H*)-one had been synthesised in our pursuit for novel lapatinib analogues (Chapter 3) including the amino- and iodo-derivatives (**45** and **20**), as well as the unsubstituted derivative (**40**). While the antiplasmodial efficacy of these compounds has not been established, some quinazolinones have been shown to display adequate efficacies. Studying these simpler systems could provide insight into what effect that small changes on the molecule have on its ability to form multicomponent crystals and the types of interactions that occur in such structures.

The formation of multicomponent crystals with a series of four 6-substituted quinazolinones and small organic coformers was investigated. Once again, the MEPS approach was used to select coformers by studying their surface-site interaction pairing energies. After simple calculations, a ranked list of the coformers was obtained that gave an indication of which coformers were more likely to form multicomponent crystals with each quinazolinone. This study highlighted one of the complications of the MEPS approach, in that heavy atoms such as iodine influences the choice of basis set to use during

the geometry optimisation step. Calculations could therefore not be performed with **20** and its list of top coformers. It was also evident that while the MEPS approach did provided a ranked list, it did not seem to be accurate for these systems, since the coformers that resulted in multicomponent products of **40** were scattered across the entire list of 32 coformers.

Eight novel multicomponent crystalline products of **40** and one methanol solvate of **41** were obtained by liquid-assisted grinding of each quinazolinone with selected coformers. Of these nine forms, four were obtained as single crystals (after use of solvent evaporation methods) and therefore their crystal structures could be studied, giving insight into the packing and association of these molecules in the solid state. In all except one case, cocrystals were obtained (no proton transfer between the quinazolinone and coformer).

Unexpectedly, the other quinazolinones did not form multicomponent products with any of these coformers. Instead, only starting material was obtained after grinding. We studied the molecular electrostatic potential surfaces of each quinazolinone and coformer more closely to see if we could pinpoint a reason for this; however, no conclusive information was obtained. Van der Waals forces and other weaker interactions may be playing a more significant role than initially suspected and a more extensive computational study would be needed to provide more information on the interactions present between the quinazolinone and coformer. It appears that small changes, at least in these molecules, seem to have a profound effect on the compound's ability to form multicomponent products.

It would be interesting to synthesise other 6-substituted quinazolinones that, for example, contain a hydroxyl or methyl moiety at that position, to determine whether these would form multicomponent crystals. Unfortunately these compounds would be slightly more challenging to synthesise. Perhaps moving the substituent to other positions on the quinazolinone ring (for example, to the 7-position) would alter the electrostatics of the molecule to an extent where multicomponent formation is possible with a range of substituents.

This study supports the current knowledge that the formation of multicomponent crystals is controlled by many factors, including sterics, 'best donor…best acceptor' guidelines and other weaker interactions, and a delicate balance between them dictates the self-assembly of these molecules. It is evident from this study that these systems are not as simple as initially thought and that there is still a great deal of information that needs to be obtained in order to fully understand the balance between these factors and to be able to predict combinations of molecules that are likely to result in multicomponent crystal formation.

4.7 REFERENCES

(1)   Rajput, R.; Mishra, A. P. *Int. J. Pharm. Pharm. Sci.* **2012**, *4* (2), 66–70.

(2)   Sharma, P. C.; Kaur, G.; Pahwa, R.; Sharma, A; Rajak, H. *Curr. Med. Chem.* **2011**, *18* (31), 4786–4812.

(3)   Macrae, C. F.; Edgington, P. R.; McCabe, P.; Pidcock, E.; Shields, G. P.; Taylor, R.; Towler, M.; Van De Streek, J. *J. Appl. Crystallogr.* **2006**, *39* (3), 453–457.

(4)   Macrae, C. F.; Bruno, I. J.; Chisholm, J. A.; Edgington, P. R.; McCabe, P.; Pidcock, E.; Rodriguez-Monge, L.; Taylor, R.; Van De Streek, J.; Wood, P. A. *J. Appl. Crystallogr.* **2008**, *41* (2), 466–470.

(5)   Bruno, I. J.; Cole, J. C.; Edgington, P. R.; Kessler, M.; Macrae, C. F.; McCabe, P.; Pearson, J.; Taylor, R. *Acta Crystallogr. Sect. B Struct. Sci.* **2002**, *58*, 389–397.

(6)   Frisch, M. J.; Trucks, G. W.; Schlegel, H. B.; Scuseria, G. E.; Robb, M. A.; Cheeseman, J. R.; Scalmani, G.; Barone, V.; Petersson, G. A.; Nakatsuji, H.; Li, X.; Caricato, M.; Marenich, A.; Bloino, J.; Janesko, B. G.; Gomperts, R.; Mennucci, B.; Hratchian, H. P.; Ortiz, J. V.; Izmaylov, A. F.; Sonnenberg, J. L.; Williams-Young, D.; Ding, F.; Lipparini, F.; Egidi, F.; Goings, J.; Peng, B.; Petrone, A.; Henderson, T.; Ranasinghe, D.; Zakrzewski, V. G.; Gao, J.; Rega, N.; Zheng, G.; Liang, W.; Hada, M.; Ehara, M.; Toyota, K.; Fukuda, R.; Hasegawa, J.; Ishida, M.; Nakajima, T.; Honda, Y.; Kitao, O.; Nakai, H.; Vreven, T.; Throssell, K.; Montgomery, J. A.; Peralta, J. E.; Ogliaro, F.; Bearpark, M.; Heyd, J. J.; Brothers, E.; Kudin, K. N.; Staroverov, V. N.; Keith, T.; Kobayashi, R.; Normand, J.; Raghavachari, K.; Rendell, A.; Burant, J. C.; Iyengar, S. S.; Tomasi, J.; Cossi, M.; Milliam., J. M.; Klene, M.; Adamo, C.; Cammi, R.; Ochterski, J. W.; Martin, R. L.; Morokuma, K.; Farkas, O.; Foresman, J. B.; Fox, D. J. Gaussian, Inc: Wallingford, CT, USA 2016

(7)   Musumeci, D.; Hunter, C. A.; Prohens, R.; Scuderi, S.; McCabe, J. F. *Chem. Sci.* **2011**, *2* (5), 883–890.

(8)   Grecu, T.; Adams, H.; Hunter, C. A.; McCabe, J. F.; Portell, A.; Prohens, R. *Cryst. Growth Des.* **2014**, *14* (4), 1749–1755.

(9)   Spek, A. L. *Acta Crystallogr. Sect. D Biol. Crystallogr.* **2009**, *65* (2), 148–155.

(10)   Bhogala, B. R.; Basavoju, S.; Nangia, A. *CrystEngComm*, **2005**, 7, 551–562.

(11)   Delori, A.; Galek, P. T. A; Pidcock, E.; Jones, W. *Chem. – Eur. J.* **2012**, *18* (22), 6835–6846.

(12)   Delori, A.; Galek, P. T. A.; Pidcock, E.; Patni, M.; Jones, W. *CrystEngComm* **2013**, *15*, 2916−2928.

(13)   Cruz-Cabeza, A. *CrystEngComm*, **2012**, 14, 6362–6365.

(14)   Etter, M. C. *J. Phys. Chem.* **1991**, *95* (12), 4601–4610.

(15)   Etter, M. C.; Adsmond, D. A. *J. Chem. Soc. Chem. Commun.* **1990**, *589* (8), 589–591.

(16)   Choquesillo-Lazarte, D.; Nemec, V.; Cinčić, D. *CrystEngComm* **2017**, *19* (35), 5293–5299.

(17)   Forni, A.; Metrangolo, P.; Pilati, T.; Resnati, G. *Cryst. Growth Des.* **2004**, *4* (2), 291–295.

CHAPTER 5
Conclusions and future work

The aim of this project was to investigate the formation of multicomponent crystals of known and novel antiplasmodial agents. By doing so, we aimed to contribute to the current knowledge in the crystal engineering field that would ultimately allow for accurate predictions of multicomponent crystals with tailor-made properties. Studying the intermolecular interactions formed between particular combinations of antiplasmodials and coformers, gives us insight into the relationship between the structure of the antiplasmodial agent and the types of multicomponent products that would form.

The objectives of this project were, therefore, to investigate a series of known antiplasmodial agents to determine what effect various moieties have on the formation of intra- and inter-molecular interactions, how these molecules pack in the solid state and what types of multicomponent crystals form, if any. Using this knowledge, we could then expand this strategy to novel systems.

Our initial strategy was to select, from the literature, five 4-aminoquinoline antiplasmodial agents that have similar features, but with sufficient difference to ensure difference in three dimensional crystalline structures. This allowed us to study what effect these differences have on the ability of the compounds to form multicomponent crystals and what types of intermolecular interactions are formed. We made use of molecular electrostatic potential surfaces (MEPS) to calculate the pairing energies of the multicomponent product. This provided a list of coformers, ranked according to their likelihood of forming multicomponent crystals, which narrowed down our choice of coformers for each antiplasmodial agent.

The top ten coformers were then chosen to carry out liquid-assisted grinding experiments to form multicomponent products. A total of 19 novel multicomponent products were obtained, 6 of which were amorphous and 13 of which were crystalline. This resulted in a 38% success rate of the MEPS method for choosing coformers. While this value is lower than hoped, this method still proved useful in narrowing down the list of coformers. It is likely that a larger pool of coformers may have yielded an alternative top ten list. This could be facilitated by the development of a computational high throughput screen. It is likely that these kinds of resources will become more widely available in the next decade.

Comparing the outcomes of the experimental study, it was found that compounds **2** and **5** form only amorphous products, while compounds **3** and **4** yield only crystalline multicomponent products with the chosen coformers. Compound **1** forms mostly crystalline products; however, one amorphous product was also obtained. It was noted that the racemic nature of **2**, as well as the likelihood of more favourable intramolecular hydrogen-bonding of **2**, could be as least partially contributing to the outcome of

amorphous products. It is also likely that the bulky ferrocene moiety is playing a role in the packing of molecules, more so than the phenyl group of **3**, and could be influencing the outcome of cocrystallisation. The additional carbon atom in the side chain of **5** (in comparison to the side chain of **4**) leads to increased rotational freedom that could be resulting in the amorphous nature of the multicomponent forms of **5**.

One of the assumptions made by the MEPS method is that the shape and long-range packing of the molecules in the solid state are of secondary importance (with intermolecular interactions being most important) when analysing whether these molecules are likely to form multicomponent crystals. This study indicates that, while intermolecular interactions do play a primary role in the formation of multicomponent crystals, the shape and long-range packing have a larger role than initially thought. This warrants further attention and a more detailed study on similar compounds, where the shape complementarity is taken into consideration, should be carried out.

Developing an *in silico* high throughput screening tool for coformer selection would certainly be useful for the formation of multicomponent products of drug molecules. Currently, there is insufficient knowledge in predictions, such that the formation of multicomponent crystals is still deemed non-obvious in patent terminology. Having said this, it is likely that in the upcoming years such predictions may be possible and *in silico* screening may become a viable method of predicting the formation of multicomponent crystals.

Being able to study the types of intermolecular interactions taking place in these multicomponent products would be useful. Unfortunately, single crystals of these multicomponent crystals were not obtained, despite considerable effort. Solving the crystal structures of some of these products by PXRD data could be helpful in this regard.[1] For the amorphous products, pair distribution function (PDF) analysis could also be investigated to gain more detailed knowledge of these products.[2] The use of cryo-electron microscopy (cryoEM) technology would also be advantageous.[3]

Having successfully formed a range of multicomponent products with these known antiplasmodial agents, our next strategy was to apply similar techniques to form multicomponent crystals with a series of novel compounds. To this end, a target repurposing strategy was employed to design aminoferrocene-containing lapatinib analogues as potential antiplasmodial agents. A series of five compounds (**15a-e**), differing in the amino moiety on the ferrocene ring, were designed to study what effect that group has on the antiplasmodial efficacy, as well as on its ability to form multicomponent crystals. The use of a Suzuki-Miyaura reaction to carry out a carbon-carbon coupling reaction between an aminoferrocene boronic acid fragment and the 6-iodoquinazoline scaffold was investigated; however, the desired products could not be formed, despite extensively modifying reaction conditions. Instead, only a mixture of starting materials or the dehalogenated quinazoline by-product was obtained in each case.

Our next approach involved switching the coupling partners (i.e. using an iodoferrocene fragment and a boronate quinazoline scaffold). After numerous attempts, we were able to synthesis the desired product (as detected by LC-MS); however, we were unable to isolate it, most likely because only trace quantities were formed. It is suspected that there are various factors that influence this lack of reactivity and investigating this further through computational studies to ascertain which factor contributes most would be valuable. Owing to the complexity of these molecules, this would be challenging and would require substantial effort, but could provide the necessary information that will allow us to redesign our synthetic pathway or reaction conditions to form the desired product in higher yields.

As the direct carbon-carbon coupling reaction did not give a favourable outcome, we turned to synthesising amine-linked analogues where reductive amination was used to couple the aminoferrocene carboxaldehyde and 6-aminoquinazoline fragments. Unfortunately, problems in the synthesis of the aminoquinazoline scaffold forced us to abandon this strategy too. While other methods are reported in the literature for coupling similar fragments, many of them make use of palladium chemistry in a similar coupling-type reaction and therefore they were not investigated further.

During the synthesis of the abovementioned compounds, a series of quinazolinones were also synthesised that provided an opportunity to study the formation of multicomponent crystals of simpler systems in more detail. While the antiplasmodial efficacy of these compounds has not been established, there are quinazolinone derivatives in the literature that have been shown to have moderate to good efficacy. By studying these simpler systems we expected to obtain detailed information on what effect the substituent has when forming multicomponent products with small organic coformers.

Four 6-substituted quinazolin-4-($3H$)-ones were synthesised and the crystal structures of three of them were obtained and compared. We once again made use of the MEPS approach to select coformers that would be most likely to form multicomponent crystals with each quinazolinone. After liquid-assisted grinding experiments were performed, it was discovered that only the unsubstituted quinazolinone (**40**) formed multicomponent crystals with the selected coformers. Solution cocrystallisation methods were employed to obtain single crystals of each multicomponent product. This was successful for three of the products, and their structures were compared. We investigated possible reasons for why only the unsubstituted quinazolinone forms multicomponent crystals, but no clear reason was identified. This led to the conclusion that these systems are more intricate than initially thought and that there is a delicate balance between various factors that ultimately drive the formation of multicomponent crystals.

It is evident from this work that the use of MEPS to select coformers, while robust and straight forward to carry out, may not be as simple as initially thought and that additional experimental factors are playing a large role in the outcome of multicomponent forms, which are not taken into account in the calculations. It is likely that the shape and packing of the molecules in the solid state play a more

significant role than described by Hunter and coworkers[4–6] in the use of MEPS to identify appropriate coformers, at least in the systems described in this work.

The work discussed in this thesis provides evidence that both quinoline- and quinazolinone-based antiplasmodial compounds have potential to form multicomponent crystals and warrants further investigation. This study has given insight into the types of intermolecular interactions that can be formed with a variety of small organic coformers and provides additional information that is useful for selecting coformers for similar systems.

While this project focused on the formation of multicomponent crystals, studying the physicochemical properties of these new products would provide insight into how cocrystallisation effects the *in vitro* properties and the pharmacokinetic profile of these compounds. The compounds discussed in Chapter 2 have the potential to be studied further in this regard, provided that more detail can be provided by single crystal structure determination. Being able to determine what effect various coformers have on the pharmacokinetic profile of the drug molecule would provide further insight into the viability of this method to improve physicochemical properties.

Recently, the use of Cryo-electron microscopy (cryoEM) and microcrystal electron diffraction (microED) has been shown to provide one-Ångstrom and even sub-Ångstrom resolution structural data from powdered samples, with minimum sample preparation and experiment time.[3,7] This technique, while still in its infancy for small molecule applications, will most likely radically change the manner in which we analyse powered samples in the future. It should be noted that there are certainly limitations with this technique and single crystal data is still more powerful in studying intermolecular interactions. However, for samples where single crystals cannot be obtained, such as those in this thesis, this method is certainly an option to study those products further.

The formation of multicomponent forms of drug molecules is receiving increased attention and has the potential to solve at least some of the current problems that cause many compounds to be discarded from the drug discovery pipeline. Perhaps once sufficient knowledge is available in the field, we could see a revival of drug candidates that were previously discarded due to poor physicochemical properties. This study contributes to this knowledge pool that can be used, ideally in combination with other studies, to provide a more complete understanding of how these types of molecules interact in the solid state. This could potentially aid in a faster drug discovery process that could allow for more drug molecules to reach the market place.

Being able to eradicate malaria is a challenging endeavour and it is evident that no strategy will be successful alone. Rather, a combined effort between the chemistry, biology and education sectors (both in industry and academia) will be necessary to one day eliminate this debilitating disease.

REFERENCES

(1)   David, W. I. F.; Shankland, K.; McCusker, L. B.; Baerlocher, C. *Acta Crystallogr., Sect. A: Found. Crystallogr.* **2008**, *A64*, 52–64.

(2)   Einfal, T.; Planinšek, O.; Hrovat, K. *Acta Pharm.* **2013**, *63* (3), 305–334.

(3)   Jones, C. G.; Martynowycz, M. W.; Hattne, J.; Fulton, T. F.; Stoltz, B. M.; Rodriquez, J. A.; Nelson, H. M.; Gonen, T. *ACS Cent. Sci.* **2018**, Advanced Online Release. DOI: 10.1021/acscentsci.8b00760.

(4)   Hunter, C. A. *Angew. Chem. Int. Ed.* **2004**, *43* (40), 5310–5324.

(5)   Musumeci, D.; Hunter, C. A.; Prohens, R.; Scuderi, S.; McCabe, J. F. *Chem. Sci.* **2011**, *2* (5), 883–890.

(6)   Grecu, T.; Hunter, C. A.; Gardiner, E. J.; McCabe, J. F. *Cryst. Growth Des.* **2014**, *14* (1), 165−171.

(7)   Nannenga, B. L.; Gonen, T. *Emerg. Top. Life Sci.* **2018**, *2* (1), 1–8.

CHAPTER 6
Experimental Information

Note to the reader:

The experimental details pertaining to the work carried out in chapters 2, 3 and 4 are described here. *Addendum A* (starting on page 173 of this thesis) contains work carried out as part of a research visit to Prof Pollastri's research laboratory in Boston, USA. The experimental details for that work are included in the addendum, and not as part of this chapter. *Addendum B* (electronic supplementary information) contains the input files, wavefunction files and log files for the MEPS work. It also contains the CIFs and RES files for all crystal structures obtained in this study as well as the FT-IR spectra described in Chapter 2.

6.1 GENERAL INFORMATION

6.1.1 Chemicals

All chemicals used in this project were obtained from Sigma Aldrich / Merck South Africa. Chemicals were used without further purification in most cases, unless otherwise stated, in which case they were purified according to standard literature procedures.[1] Solvents that were required to be free from water were dried using the techniques listed in Table 6.1 below.

Table 6.1: Purification and drying methods for various solvents

Solvent	*Purification technique*
Methanol (MeOH)	Distilled under nitrogen from I_2/Mg turnings
Ethanol (EtOH)	Distilled under nitrogen from I_2/Mg turnings
Tetrahydrofuran (THF)	Distilled under nitrogen from sodium ribbons and benzophenone as indicator
1,4-Dioxane	Distilled under nitrogen from CaH
Diethyl ether	3Å molecular sieves for three days prior to use
N,N-Dimethylformamide (DMF)	3Å molecular sieves for three days prior to use

Ethyl acetate (EtOAc), hexane and dichloromethane (DCM) that were used for silica gel chromatography were purchased from Protea Chemicals and bulk distilled in air prior to use. All solvents used for crystallisation experiments were purchased from Sigma Aldrich South Africa and were of HPLC grade and stored on 3Å molecular sieves for two days prior to use.

Alkyl lithium reagents were titrated prior to use using the following procedure:[2]

An oven-dried Schlenk tube was evacuated and filled with nitrogen three times, following which freshly distilled THF (8.0 mL), menthol (0.100 g, 0.640 mmol, 1.00 equivalent) and 2,2-bipyridine (4 – 5 mg as indicator) were added. The reaction mixture was cooled to -78 °C (dry ice/acetone bath) and the alkyl lithium reagent was added dropwise via an oven-dried glass syringe until the colour changed to a persistent deep red within one drop. The volume of alkyl lithium used was recorded and used to calculate the molar concentration. The experiment was repeated in triplicate for accuracy.

6.1.2 Instrumentation and related software

Microwave reactions were performed using a CEM Focused Microwave Synthesis System, Discover SP, using either 10 mL or 35 mL microwave vials and Teflon coated stir bars.

Flash column chromatography was performed using a CombiFlash Rf+ 150 Teledyne ISCO automated purification instrument fitted with a UV detector (200 – 400 nm). All chromatography was performed using 230 – 400 mesch Merck silica gel. Thin layer chromatography was carried out using Macherey-Nagel Alugram® Xtra SIL G/UV$_{254}$ TLC sheets pre-coated with silica gel 60. Spots were visualised using a UV lamp or stains (ninhydrin, 2,6-dinitrophenyl hydrazine or bromocresol green)

LC-MS analysis was performed using a Waters Alliance reverse phase HPLC (columns Waters SunFire C18 4.6 × 50 mm) with single-wavelength UV−visible detector and Waters Micromass ZQ detector (electrospray ionisation).

Mechanochemistry was performed either manually in a mortar and pestle or with a FTS1000 Shaker Mill with stainless steel jars and stainless steel milling balls (size: 6 mm).

Nuclear Magnetic Resonance (NMR) spectroscopy was carried out to confirm the structure and purity of synthesised compounds. Samples were prepared by dissolving 10 – 20 mg of the sample in an appropriate deuterated solvent. In all cases CDCl$_3$ was used, except when samples were not soluble. DMSO-*d$_6$* or CD$_3$OD were used in these cases. All solvents were stored on 3 Å molecular sieves to eliminate the presence of water peaks in the spectrum. ^{1}H and ^{13}C spectra were obtained using a 300 MHz Varian VNMRS (75.5 MHz for ^{13}C), 400 MHz (100 MHz for ^{13}C) or 600 MHz (150 MHz for ^{13}C). Chemical shifts are reported using the residual peaks of deuterated solvents as reference. Spectra were analysed using ACD Labs NMR spectroscopic processing software.[3]

Fourier Transform Infrared Spectroscopy (FTIR) was carried out using a Bruker Alpha spectrometer with platinum ATR attachment. OPUS v7.5 software[4] was use to record spectra, and processing was carried out using KnowItAll freeware.[5] A background scan was acquired before each sample scan.

Powder X-ray diffraction (PXRD) was carried out on a Bruker D2 Phaser powder X-ray diffractometer with 1.54183 Å CuKα radiation, operated at 30 kV and 10 mA. Data were collected from 2θ = 4 to 40° with a scan step of 0.5 seconds per step and a step size of 0.0201 (for multicomponent crystals) or a step size of 0.0161 (for individual components). Data analysis was performed using X'Pert HighScore Plus (v 2.2e).[6]

Single crystal X-ray diffraction (SC-XRD) was used to obtain the solid-state structure of compounds from diffraction-quality single crystals. Crystals were placed in paratone oil on a slide and a suitable crystal was mounted on a MiTeGen mount, which was then placed on the goniometer head of the instrument. A Bruker Apex II DUO CCD area-detector diffractometer was used for **41**, **41·MeOH**, **20**, **45**, **40·OXA** and **40·SAL**, operating with MoKα radiation of wavelength 0.71073 Å produced by an Incoatec I$_{\mu S}$ microsource coupled with a multilayer mirror optics monochromator. An Oxford Crysosystems cryostat (Cryostream Plus 700 Controller) was used for all data collections (100 K). For **3** and **40·FUM**, a Bruker D8 Venture Photon II four-circle diffractometer was used operating with MoKα radiation of wavelength 0.71073 Å produced by an Incoatec I$_{\mu S}$ microsource coupled with a multilayer mirror optics monochromator. Low temperature (100 K) data collections were performed for all structures, making use of an Oxford Cryosystems Cryostream 800 series cryostat. Data were collected and reduced using Bruker SAINT[7] in the ApexIII interface and absorption corrections were carried out with SADABS[8,9] The structures were solved using SHELXT-13 and SHELXT-16[10] using direct methods and refined using SHELXL-16[10] in the Xseed graphical user interface.[11,12] Hydrogen atoms were placed in calculated positions using riding models, except for OH and NH hydrogen atoms, which were placed on maxima found in the electron density difference maps. Images were generated using POV-Ray.[13] CIFs were generated within Xseed and edited with EnCiFer.[14] All CIFs were checked using CheckCIF prior to submission.[15] The CIFs and CIFCheck files are included in this thesis as part of the electronic supplementary information.

Thermogravimetric analysis (TGA) was performed under nitrogen (flow rate: 40 mL/min) using a TA Q500 instrument. Samples (2 – 5 mg) were placed in open aluminium pans and the traces were obtained by heating at 10 °C/min under a N$_2$ gas purge.

Differential Scanning Calorimetry (DSC): was performed using a TA Q20 instrument coupled to an RSC cooling unit. Samples (2 – 5 mg) were placed in non-hermetically sealed aluminium pans with a pinhole in the lid and heated at a rate of 10 °C/min. Analysis of the traces obtained from the TGA and DSC measurements were carried out using the TA Instruments Universal Analysis program.

ConQuest 1.18,[16] as part of the Cambridge Structural Database, was used to search for published crystal structures and hydrogen-bonding motifs.

Mercury CSD 3.9,[16–18] was used to generate the channel mapping image for **41·MeOH** as well as for analysis of intermolecular interactions in the crystal structures described in this these. In addition, it was used to generate the calculated PXRD patterns from single crystal data.

For the molecular electrostatic potential surface calculations, molecules were draw in *ChemCraft* and geometry optimisations carried out with *Gaussian 09*.[19] *AIMAll* and *AIMQB* were used to map the MEPS onto the 0.002 Bohr Å^{-3} isodensity surface and to generate the MEPS images.[20]

6.2 EXPERIMENTAL DATA PERTAINING TO CHAPTER 2

Amodiaquine free base (1)
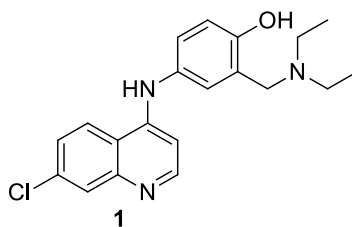
Amodiaquine dihydrochloride dihydrate was purchased from Sigma Aldrich South Africa. The free base was obtained by stirring the salt (0.350 g) in ammonia solution (25%) for 2 hours and then extracting into EtOAc (3×30 mL). The organic layers were combined, dried over anhydrous K_2CO_3, filtered and the filtrate concentrated under reduced pressure. The resulting pale yellow powder was recrystallised from hot methanol (87% yield).

^{1}H NMR (300 MHz, DMSO-d_6) δ 8.88 (s, 1H), 8.42 (d, J = 8.8 Hz, 1H), 8.36 (d, J = 5.6 Hz, 1H), 7.84 (d, J = 2.1 Hz, 1H), 7.51 (dd, J = 8.8, 2.1 Hz, 1H), 7.08 (s, 1H), 7.07 – 7.03 (m, 1H), 6.81 – 6.75 (m, 1H), 6.57 (d, J = 5.6 Hz, 1H), 3.74 (s, 2H), 2.57 (q, J = 7.0 Hz, 4H), 1.04 (t, J = 7.0 Hz, 6H).
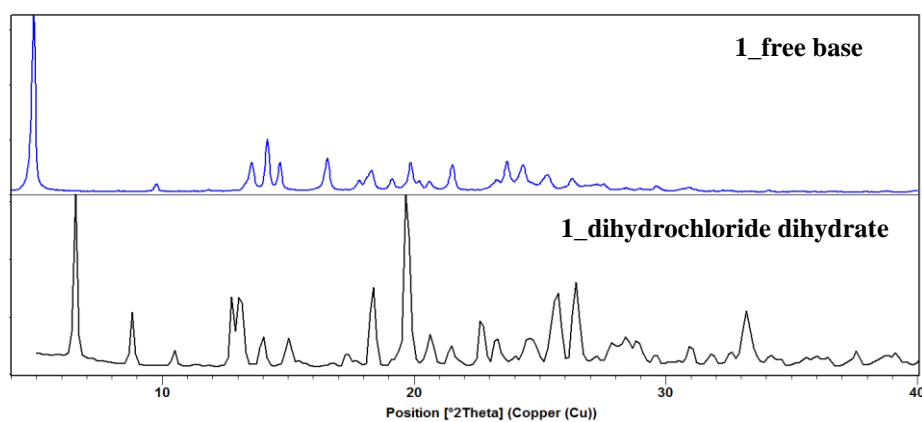
Figure 6.1: Experimental PXRD pattern of **1** (blue) and of commercially available amodiaquine dihydrochloride dihydrate (black).
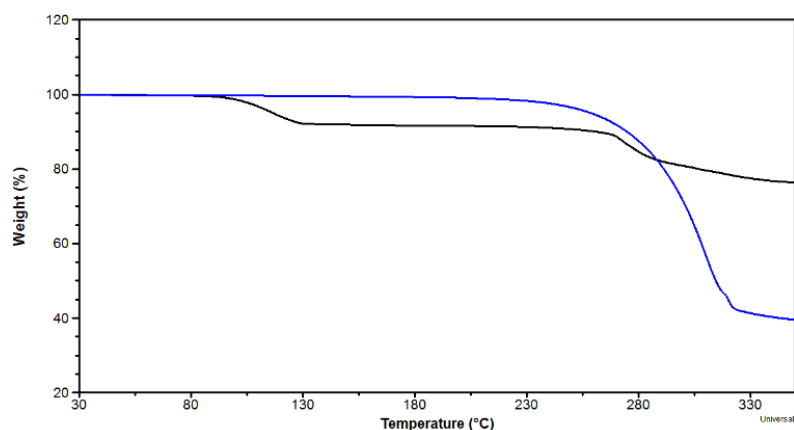
Figure 6.2: TGA trace of **1** (blue) and of commercially available amodiaquine dihydrochloride dihydrate (black).
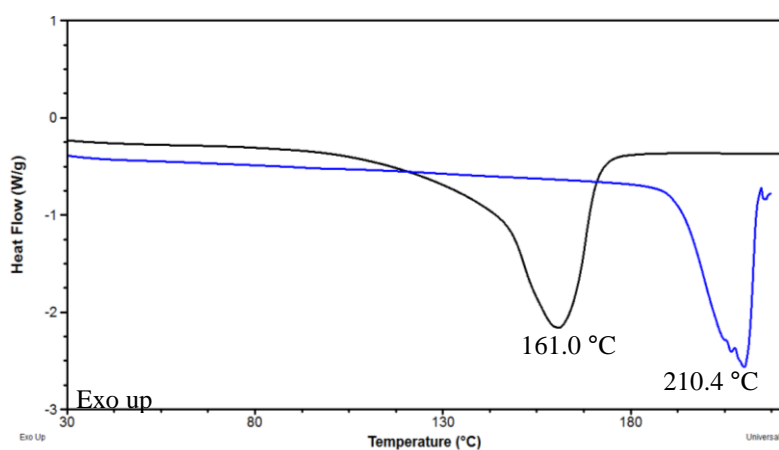
Figure 6.3: DSC trace of **1** (blue) and of commercially available amodiaquine dihydrochloride dihydrate (black).

[(*N, N*-Dimethylamino)methyl]ferrocenecarboxaldehyde (7)
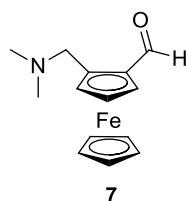
To a dry Schlenk tube that has been evacuated and filled with nitrogen three times was added commercially available *N,N*-dimethylaminomethyl ferrocene (0.3 mL, 1 mmol, 1 equivalent) and anhydrous diethyl ether (6.0 mL). This solution was then cooled to 0 °C and *t*-BuLi (1.5 mL, 1.0 M, 1.1 equivalents) was added dropwise. The ice bath was removed and the bright orange reaction mixture was stirred for a further 2 hours at room temperature. The reaction mixture was then once again cooled to 0 °C and anhydrous DMF (0.1 mL, 1 mmol, 1 equivalent) was added dropwise. The ice bath was once again removed and the reaction stirred at room temperature for a further 2 hours, after which 1.0 mL distilled water was added dropwise to quench the reaction. Additional distilled water (5 mL) was added

and the product was extracted with DCM (3×30 mL). The organic fractions were combined, dried over anhydrous $MgSO_4$ and concentrated under reduced pressure. A quantitative yield of the dark red oil was obtained and used directly in the next reaction without further purification.

TLC (EtOAc/Et$_3$N/MeOH = 95:3:2): R_f = 0.33; DNP (2,4-dinitrophenyl hydrazine) solution stains the aldehyde product an orange colour on the TLC plate. **^{1}H NMR (300 MHz, CDCl$_3$) δ** 10.10 (s, 1H), 4.78 – 4.76 (m, 1H), 4.64 – 4.61 (m, 1H), 4.56 – 4.55 (m, 1H), 4.23 (s, 5H), 3.84 (d, *J* = 12.9 Hz, 1H), 3.38 (d, *J* = 12.9 Hz, 1H), 2.23 (s, 6H). The data compared well with the literature.[21,22]

2-[(*N*,*N*-Dimethylamino)methyl]ferrocenecarboxaldehyde oxime (8)

8
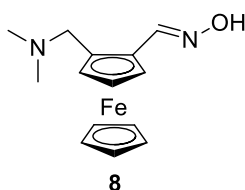
To a 50 mL round-bottomed flask containing [(*N*,*N*-dimethylamino)methyl]ferrocenecarboxaldehyde (**7**) (0.383 g, 1.48 mmol, 1.00 equivalent) was added absolute EtOH (15 mL) and hydroxylamine hydrochloride (0.281 g, 4.00 mmol, 2.70 equivalents). To this mixture was added 2.5 M NaOH solution (4 mL, 6 mmol, 3 equivalents). The reaction was heated under reflux for 3 hours before cooling back to room temperature and neutralising with dry ice until a pH of 7 was obtained. The mixture was diluted with DCM (40 mL) and the product extracted with a further DCM (3×20 mL). The combined organic fractions were washed with brine (30 mL), then dried over anhydrous $MgSO_4$, filtered and the filtrate concentrated under reduced pressure. The product was used directly in the next step without further purification.

TLC (EtOAc/Et$_3$N/MeOH = 95:3:2): R_f = 0.25.

2-[(N,N-Dimethylamino)methyl]ferrocenemethylamine (9)

9
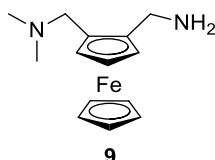
To a two-neck round-bottomed flask containing the crude 2-[(*N*,*N*-dimethylamino)methyl]ferrocenecarboxaldehyde oxime product (**8**) described above (0.420 g, 1.48 mmol, 1.00 equivalent) was added anhydrous THF (8.0 mL) and the mixture stirred under nitrogen until dissolved. LiAlH$_4$ (0.114 g, 3.00 mmol, 2.00 equivalents) was added portion-wise under a positive

pressure of nitrogen. The reaction mixture was then heated under reflux under a nitrogen atmosphere for 18 hours. Once cooled, the reaction mixture was diluted with diethyl ether (40 mL) and excess LiAlH$_4$ was quenched by the slow addition of brine (5 mL). The reaction mixture was transferred to a separatory funnel and additional brine added (10 mL). The product was extracted with diethyl ether (3 × 30 mL), then dried over anhydrous K$_2$CO$_3$, filtered and the filtrate concentrated under reduced pressure to afford the crude product as a dark red oil that was used directly in the next step without further purification.

TLC (DCM/Et$_3$N/EtOH = 80:10:10): R$_f$ = 0.31; Ninhydrin stains amine product an orange colour on TLC. **^{1}H NMR (300 MHz, CDCl$_3$) δ** 4.19 (m, 1H), 4.11 (m, 1H), 4.04 (s, 5H), 4.03 – 4.01 (m, 1H), 3.78 (d, *J* = 13.5 Hz, 1H), 3.59 – 3.61 (m, 1H), 3.65 – 3.64 (m, 1H), 3.50 (br s, 2H), 2.86 (d, *J* = 12.3 Hz, 1H), 2.14 (s, 6H). The data compared well with the literature.[21,22]

Ferroquine (2)
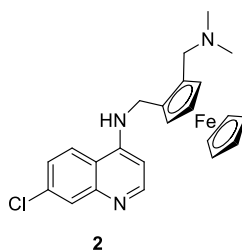
To a 25 mL round-bottomed flask was added crude 2-[(*N*,*N*-dimethylamino)methyl]ferrocenemethylamine (**9**) (0.475 g, 1.75 mmol, 1.00 equivalent) and anhydrous *N*-methylpyrolidinone (NMP, 8.0 mL) under a positive flow of nitrogen. To this was added anhydrous triethylamine (0.3 mL, 2 mmol, 1 equivalents) and K$_2$CO$_3$ (0.393 g, 3.25 mmol, 1.50 equivalents). 4,7-Dichloroquinoline (1.82 g, 9.19 mmol, 5.00 equivalents) was added portion wise to the reaction mixture after which the reaction mixture was stirred at 135 °C for 4 hours. The reaction mixture was cooled to room temperature, diluted with EtOAc (150 mL) and transferred to a separatory funnel where the NMP was extracted with brine (10 × 50 mL). The organic layer was dried over anhydrous MgSO$_4$, filtered and the filtrate concentrated under reduced pressure. Purification by column chromatography (EtOAC/Hexane/Et$_3$N = 45:50:5) afforded the desired product, which was then recrystallised from DCM/Hexane to give orange rod-shaped crystals of diffraction quality in 54% yield.

TLC (EtOAC/Hex/Et$_3$N = 45:50:5): R$_f$ = 0.33. **^{1}H NMR (300 MHz, CDCl$_3$) δ** 8.55 (d, *J* = 5.3 Hz, 1H), 7.92 (d, *J* = 2.4 Hz, 1H), 7.67 (br s, 1H), 7.62 (d, *J* = 8.8 Hz, 1H), 7.29 – 7.28. (m, 1H), 6.46 (d, *J* = 5.3 Hz, 1H), 4.42 – 4.36 (m, 1H), 4.29 – 4.27 (m, 1H), 4.21 – 4.16 (m, 1H), 4.15 (s, 5H), 4.14 – 4.12 (m, 1H), 4.09 – 4.08 (m, 1H), 3.80 (d, *J* = 12.3 Hz, 1H), 2.89 (d, *J* = 12.3 Hz, 1H), 2.23 (s, 6H). **IR (ATR, cm^{-1})** 3170 (br. w, NH), 1574 (s, C=N of quinoline), 797 (C–Cl). **Mp** 201.0 °C (DSC peak). The data compared well with the literature.[23]
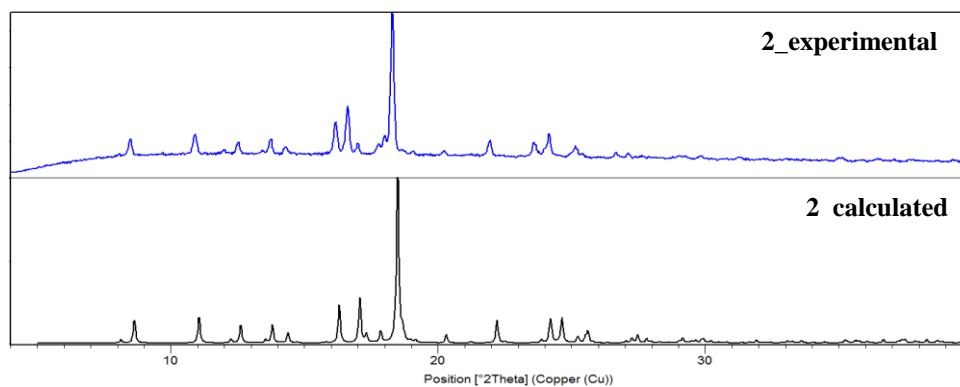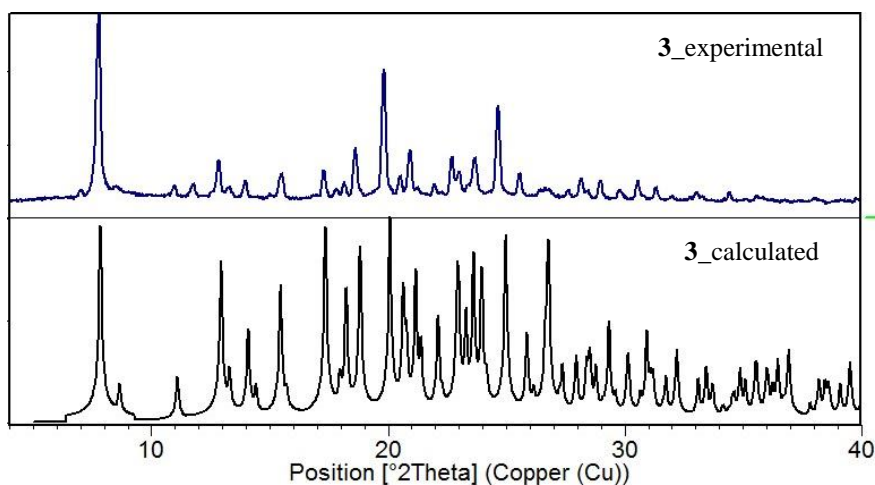
**Figure 6.4**: Experimental PXRD pattern of **2** (blue) and the calculated PXRD pattern obtained from single crystal data (black, CSD refcode: LEZNIO).
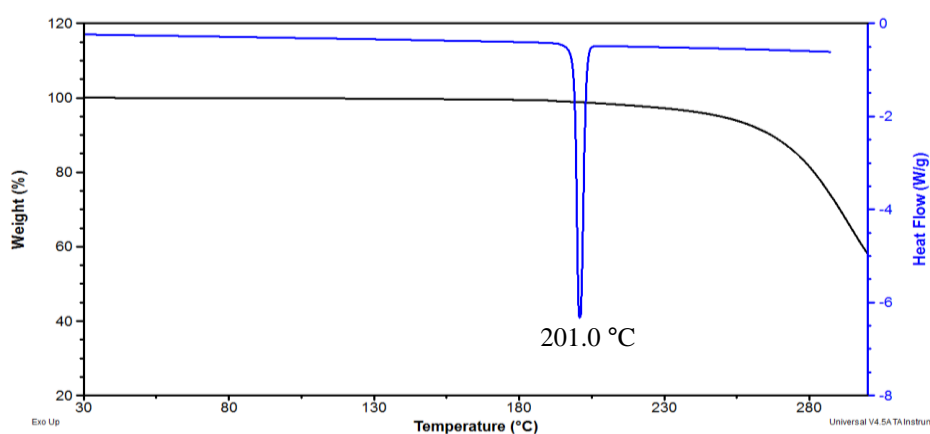
Figure 6.5: TGA trace (black) and DSC trace (blue) of **2**.

2-[(Dimethylamino)methyl]benzaldehyde (12)
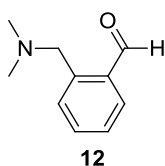
To a dry Schlenk tube that has been evacuated and filled with nitrogen three times was added commercially available *N,N*-dimethyl-1-phenylmethanamine (0.2 mL 2 mmol, 1 equivalent) and anhydrous diethyl ether (8 mL). This solution was then cooled to -78 °C and *n*-BuLi (1.0 mL, 2.0 M, 1.1 equivalents) was added dropwise. The reaction mixture was stirred without the dry ice/acetone bath for a further 18 hours, during which the yellow solution becomes milky. The reaction mixture was cooled to 0 °C and anhydrous DMF (0.1 mL, 2 mmol, 1 equivalents) added dropwise. The ice bath was removed and the reaction stirred at room temperature for a further 2 hours after which distilled water (5 mL) was added dropwise to quench the reaction. The product was extracted with diethyl ether (3 × 30 mL) and

the organic fractions combined, dried over anhydrous MgSO₄ and concentrated under reduced pressure. The product was obtained as a colourless oil in quantitative yield (0.302 g).

TLC (Ether/Hexane/Et₃N = 70:20:10): R_f = 0.75; DNP stains aldehyde product an orange colour on the TLC plate. **^{1}H NMR (300 MHz, CDCl₃) δ** 10.28 (s, 1H), 7.91 (dd, *J* = 8.2, 1.3, 1H), 7.49 – 7.48 (m, 1H) 7.36 – 7.31 (m, overlapping peaks, 2H) 3.61 (s, 2H), 2.19 (s, 6H). The data compared well with the literature.[21,24]

2-[(Dimethylamino)methyl]benzaldehyde oxime (13)

13
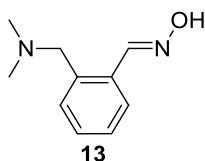
To a 50 mL round-bottomed flask containing 2-((dimethylamino)methyl)benzaldehyde (**12**) (0.302 g, 1.85 mmol, 1.00 equivalent) was added to absolute EtOH (8.0 mL) and hydroxylamine hydrochloride (0.319 g, 2.77 mmol, 1.50 equivalents). To this mixture was added NaOH solution (3.7 mL, 2.5 M, 3.0 equivalents). The reaction was heated under reflux for 18 hours before cooling back to room temperature and neutralising with dry ice until a pH of 7 was obtained. The mixture was diluted with DCM (40 mL) and the product extracted with a further DCM (3 × 20 mL). The combined organic fractions were washed with brine (1 × 30 mL), then dried over anhydrous MgSO₄, filtered and the filtrate concentrated under reduced pressure. The product was used directly in the next step without further purification.

TLC (Ether/Hexane/Et₃N = 70:20:10): R_f = 0.75; DNP stain on the TLC plate confirms that aldehyde starting material was consumed and that the reaction was complete.

1-[2-(Aminomethyl)phenyl]-*N*,*N*-dimethylmethanamine (14)

14
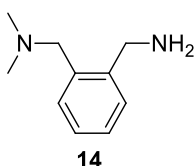
To a 2-neck round-bottomed flask containing the crude oxime product **12** described above (0.328 g, 1.85 mmol, 1.00 equivalent) was added anhydrous THF (6.0 mL) and the mixture stirred under nitrogen until dissolved. LiAlH₄ (0.140 g, 3.69 mmol, 2.00 equivalents) was added portion wise under a positive pressure of nitrogen. The reaction mixture was then heated under reflux under a nitrogen atmosphere for 18 hours. Once cooled, the reaction mixture was diluted with diethyl ether (40 mL) and excess

LiAlH$_4$ was quenched by the slow addition of brine (5 mL). The reaction mixture was transferred to a separatory funnel and additional brine (10 mL) added. The product was extracted with diethyl ether (3 × 30 mL), then dried over anhydrous K$_2$CO$_3$, filtered and the filtrate concentrated under reduced pressure to give a pale yellow oil. The product was used directly in the next step without further purification.

TLC (Ether/Hexane/Et$_3$N = 70:20:10): R$_f$ = 0.68. Ninhydrin was used to visualise the amine product, which stains an orange colour on the TLC plate.

Phenylequine (3)

3
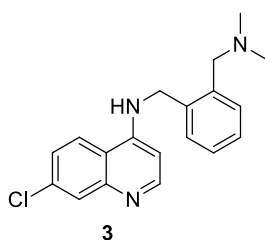
To a 25 mL round-bottomed flask was added 1-[2-(aminomethyl)phenyl]-*N,N*-dimethylmethanamine (**13**) (0.302 g, 1.85 mmol, 1.00 equivalent) and anhydrous NMP (5.0 mL) under a positive flow of nitrogen. To this was added anhydrous triethylamine (0.3 mL, 2 mmol, 1 equivalent) and K$_2$CO$_3$ (0.228 g, 1.65 mmol, 1.50 equivalents). 4,7-Dichloroquinoline (1.09 g, 5.50 mmol, 5.00 equivalents) was added portion-wise to the reaction mixture after which the reaction mixture was stirred at 135 °C for 4 hours. The reaction mixture was cooled to room temperature, diluted with EtOAc (80 mL) and transferred to a separatory funnel where the NMP was extracted with brine (10 × 30 mL). The organic layer was dried over anhydrous MgSO$_4$, filtered and the filtrate concentrated under reduced pressure. Purification by column chromatography and subsequent recrystallisation from DCM/Hexane afforded the desired product in a 48% yield (0.108 g) as an off-white solid.

TLC (EtOAc/Hexane/Et$_3$N = 45:50:5): R$_f$ = 0.56. **^{1}H NMR (300 MHz, CDCl$_3$) δ** 8.56 (d, *J* = 5.5 Hz, 1H), 8.50 (br s, 1H), 7.96 (d, *J* = 1.8 Hz, 1H), 7.63 (d, *J* = 9.4 Hz, 1H), 7.46 – 7.41 (m, 1H), 7.37 – 7.28 (m, 4H), 6.56 (d, *J* = 5.5 Hz, 1H), 4.47 (s, 2H), 3.51 (s, 2H), 2.29 (s, 6H). **IR (ATR, cm^{-1})** 3228 (br. m, NH), 1561 (s, C=N of quinoline), 1489 (m, NCH$_3$). **Mp** 139 – 143 °C. The data compared well with the literature.[25]

Figure 6.6: Experimental PXRD pattern of **3** (blue) and the calculated PXRD pattern obtained from single crystal data (black).
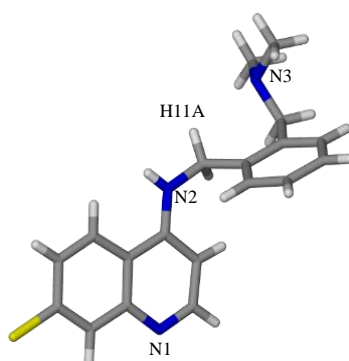
Table 6.2: Hydrogen-bond geometries for **3** from single crystal X-ray diffraction data.

D–H···*A*	*D*–H (Å)	H···*A* (Å)	*D*···*A* (Å)	*D*–H···*A* (°)
C11–H11*A*···N3	0.97	2.68	3.191 (2)	113
N2–H1···N1ⁱ	0.85 (3)	2.09 (3)	2.900 (2)	158 (2)

Symmetry code: (i) y-1/2, x+1/2, z-1/2.

N-(7-Chloroquinolin-4-yl)ethane-1,2-diamine (4)
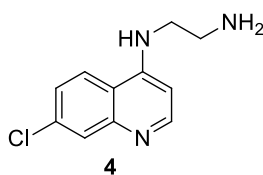
Commercially available 4,7-dichloroquinoline (1.04 g, 5.00 mmol, 1.00 equivalent) and 1,2-diaminoethane (1.3 mL, 20 mmol, 4.0 equivalents) was added to a 50 mL round-bottomed flask and stirred at 80 °C for one hour after which the temperature was increased to 135 °C for a further 5 hours.

The reaction mixture was then cooled to room temperature and diluted with DCM (80 mL). A saturated solution of sodium bicarbonate (20 mL) was added until a pH of 7 was obtained. The organic layer was separated from the aqueous layer and the latter washed with DCM (4 × 30 mL). The organic layers were combined and washed once with brine (30 mL). The organic layer was dried over anhydrous $MgSO_4$, filtered and the filtrate concentrated under reduced pressure to yield a pale yellow powder (0.623 g, 56%).

TLC (EtOAc/Hexane/MeOH/Et$_3$N = 50:30:10:10): R_f = 0.32. **^{1}H NMR (300 MHz, DMSO-d_6) δ** 8.39 (d, *J* = 5.3 Hz, 1H), 8.24 (d, *J* = 9.6 Hz, 1H), 7.78 (d, *J* = 2.0 Hz, 1H), 7.45 (dd, *J* = 9.6, 2.0 Hz, 1H), 6.47 (d, *J* = 5.3 Hz, 1H), 3.31 (t, *J* = 6.6 Hz, 2H), 2.69 (t, *J* = 6.6 Hz, 2H). **IR (ATR, cm^{-1})** 3264 (m, NH), 1610 (m, NH$_2$). **Mp** 137 – 139 °C. The data compared well with the literature.[26,27]

N^1-(7-chloroquinolin-4-yl)propane-1,2-diamine (5)
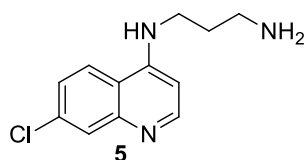
Compound **5** was prepared using the same procedure described above for compound **4** with the same equivalents of 4,7-dichloroquinine and 1,3-diaminopropane to yield a pale yellow powder (0.856 g, 73%).

TLC (EtOAc/Hexane/MeOH/Et$_3$N = 50:30:10:10): R_f = 35. **^{1}H NMR (300 MHz, DMSO-d_6) δ** 8.39 (d, *J* = 5.4 Hz, 1H), 8.23 (d, *J* = 9.0 Hz, 1H), 7.77 (d, *J* = 2.2 Hz, 1H), 7.52 (br s, 1H), 7.45 (dd, *J* = 9.0, 6.7 Hz, 1H), 6.46 (d, *J* = 5.4 Hz, 1H), 3.32 (t, *J* = 6.5 Hz, 2H), 2.68 (t, 6.5 Hz, 2H), 1.73 (m, 2H). **IR (ATR, cm^{-1})** 3285 (m, NH), 1610 (m, NH$_2$). **Mp** 89–92 °C. The data compared well with the literature.[26,27]

Molecular Electrostatic Potential Surfaces (MEPS)

All input and wavefunction files, as well as log files for each compound can be found in Appendix B (electronic data). The coformers used in this study can all be found on either the GRAS or EAFUS lists and were available in the laboratory at the time. Table 6.3 shows the change in energy for each coformer and antiplasmodial agent in descending order of the energy value.

Table 6.3: ΔE values for each antiplasmodial agent and coformer combination.

1		2		3		4		5	
Coformer	-ΔE (kJ mol^{-1})	Coformer	-ΔE (kJ mol^{-1})	Coformer	-ΔE (kJ mol^{-1})	Coformer	-ΔE (kJ mol^{-1})	Coformer	-ΔE (kJ mol^{-1})
oxalic acid	12.1	oxalic acid	24.5	oxalic acid	14.6	oxalic acid	15.5	fumaric acid	22.5
3,5-dihydroxy benzoic acid	9.0	3,5-dihydroxy benzoic acid	19.0	3,5-dihydroxy benzoic acid	10.7	pamoic acid	10.3	oxalic acid	18.4
trimesic acid	8.4	fumaric acid	18.4	fumaric acid	9.1	trimesic acid	10.0	trimesic acid	13.5
fumaric acid	7.6	trimesic acid	17.0	indole	8.5	4,4-bipyridine	9.0	3.5-dihydroxy benzoic acid	13.2
pamoic acid	6.9	malonic acid	16.8	pamoic acid	8.2	pyrazine	8.2	pamoic acid	12.9
resorcinol	6.7	pamoic acid	16.8	trimesic acid	8.1	3,5-dihydroxy benzoic acid	8.1	resorcinol	10.9
indole	6.4	indole	16.2	resorcinol	7.7	fumaric acid	7.7	indole	9.9
malonic acid	4.9	resorcinol	16.1	malonic acid	7.3	indole	7.5	malonic acid	9.2
teraphthalic acid	4.9	teraphthalic acid	15.7	teraphthalic acid	6.6	resorcinol	7.2	teraphthalic acid	8.7
salicylic acid	4.3	succinic acid	15.2	*p*-aminobenzoic acid	6.1	vanillin	6.8	succinic acid	7.7
hydroquinone	4.1	salicylic acid	14.6	succinic acid	6.0	piperazine	6.2	salicylic acid	7.6
p-aminobenzoic acid	4.0	saccharin	13.7	salicylic acid	5.9	ethylenediamine	6.1	hydroquinone	7.2
ethylenediamine	3.8	thymine	13.0	saccharin	5.2	teraphthalic acid	6.0	glutaric acid	6.5
benzamide	3.8	hydroquinone	13.0	hydroquinone	4.7	malonic acid	5.5	*p*-aminobenzoic acid	6.1
succinic acid	3.6	*p*-aminobenzoic acid	13.0	thymine	4.6	saccharin	5.1	saccharin	5.5
saccharin	3.0	methyl gallate	11.6	glutaric acid	4.0	succinic acid	5.0	methyl gallate	5.3
thymine	2.6	glutaric acid	11.2	methyl gallate	3.7	theophylline	4.9	vanillin	5.2
vanillin	2.5	benzamide	10.7	benzamide	3.4	glutaric acid	4.5	tartaric acid	5.0
glutaric acid	2.2	tartaric acid	10.6	vanillin	3.3	salicylic acid	4.5	nicotinic acid	4.8

piperazine	1.7	vanillin	10.4	tartaric acid	2.6	nicotinic acid	4.4	theophylline	4.6
4,4-bipyridine	1.2	nicotinic acid	8.9	benzoic acid	2.6	hydroquinone	4.0	thymine	4.2
methyl gallate	1.2	benzoic acid	8.9	nicotinic acid	2.5	p-aminobenzoic acid	3.2	benzamide	3.8
tartaric acid	1.0	theophylline	8.6	theophylline	2.1	morpholine	3.1	benzoic acid	3.8
morpholine	0.9	nicotinamide	7.1	ethylenediamine	1.5	tartaric acid	3.1	pyrazine	3.1
caffeine	0.9	morpholine	6.0	morpholine	1.3	methyl gallate	2.2	44-bipyridine	2.3
benzoic acid	0.6	ethylenediamine	5.9	nicotinamide	1.2	benzoic acid	2.2	nicotinamide	2.0
nicotinic acid	0.5	caffeine	4.9	naphthalene	0.9	naphthalene	2.0	morpholine	1.8
theophylline	0.4	menthol	4.6	menthol	0.4	benzamide	1.6	piperazine	1.6
naphthalene	0.3	4,4-bipyridine	2.7	pyrazine	0.3	caffeine	1.5	naphthalene	1.1
pyrazine	0.2	piperazine	2.6	piperazine	0.2	thymine	0.9	ethylenediamine	1.0
nicotinamide	0.1	naphthalene	2.5	4,4-bipyridine	0.1	nicotinamide	0.6	menthol	0.8
menthol	0.0	pyrazine	1.9	caffeine	0.1	menthol	0.0	caffeine	0.4

Obtaining multicomponent crystals of 1 – 5 with organic coformers:

Liquid-assisted grinding (with a few drops of MeOH) was used as a screening tool to determine whether multicomponent crystals would form between the respective antiplasmodial agent and the top ten coformers in the list obtained from the virtual screening method. Stoichiometric amounts (1:1) of the antiplasmodial agent (10 mg) and coformer were added to a mortar and pestle and 3 drops of solvent were added. The components were ground together for 5 minutes, occasionally adding an extra drop of MeOH when necessary. PXRD was used to determine whether a mixture of starting components was still present or whether a new product had formed. In cases where starting material was still present, an additional 10 minutes of grinding was carried out and PXRD was once again performed.

PXRD patterns of the individual components and that of the product obtained after 5 minutes of grinding:
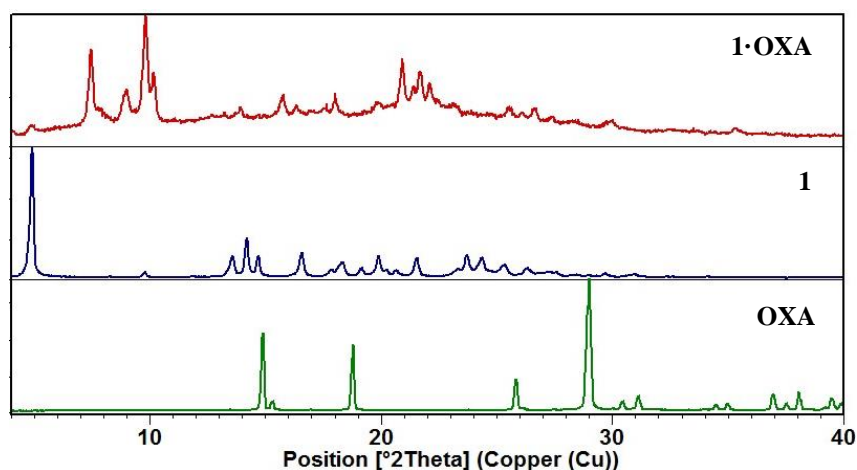
Figure 6.7: Experimental PXRD pattern of amodiaquine (**1**, navy blue), oxalic acid (**OXA**, green) and the new product obtained after grinding for 5 min with a few drops of MeOH (**1·OXA**, maroon).
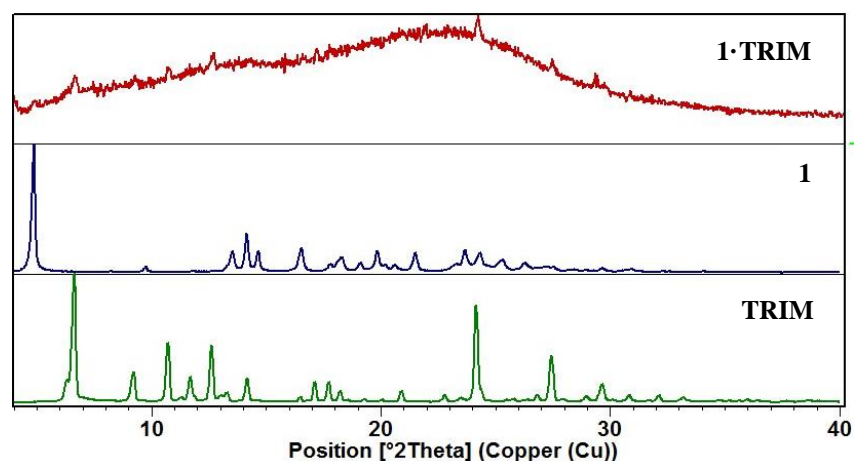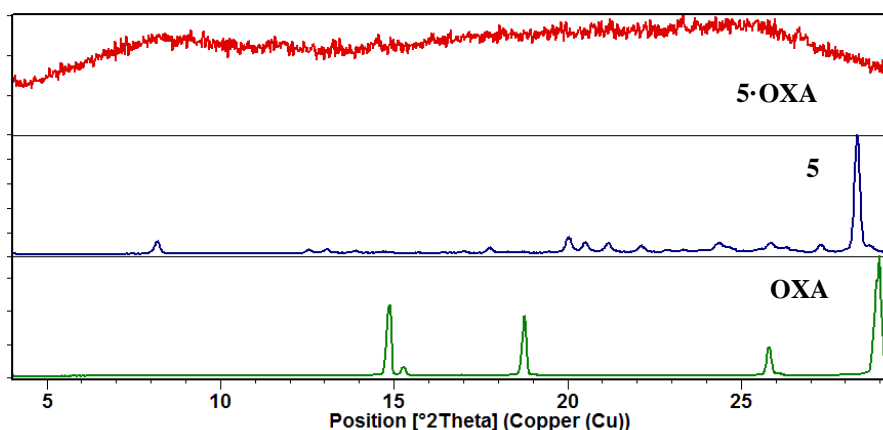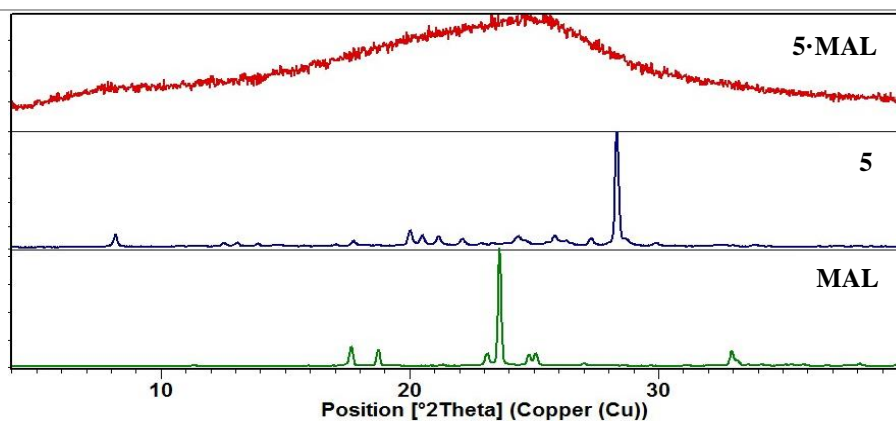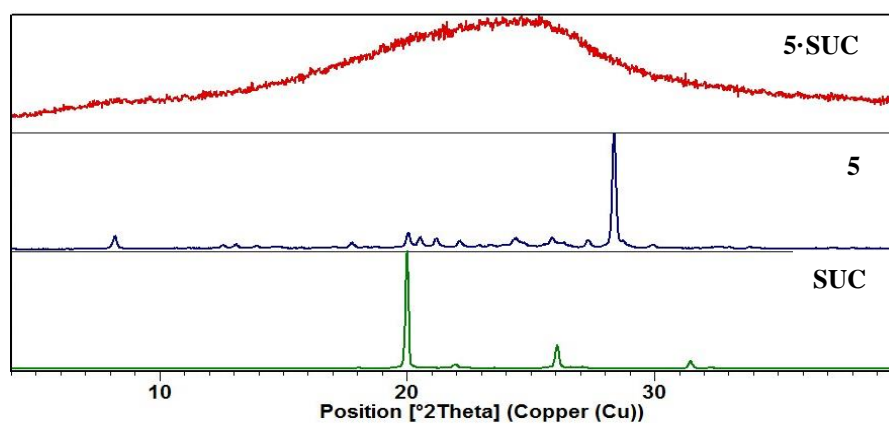

Figure 6.8: Experimental PXRD pattern of amodiaquine (**1**, navy blue), trimesic acid (**TRIM**, green) and the new product obtained after grinding for 5 min with a few drops of MeOH (**1·TRIM**, maroon).
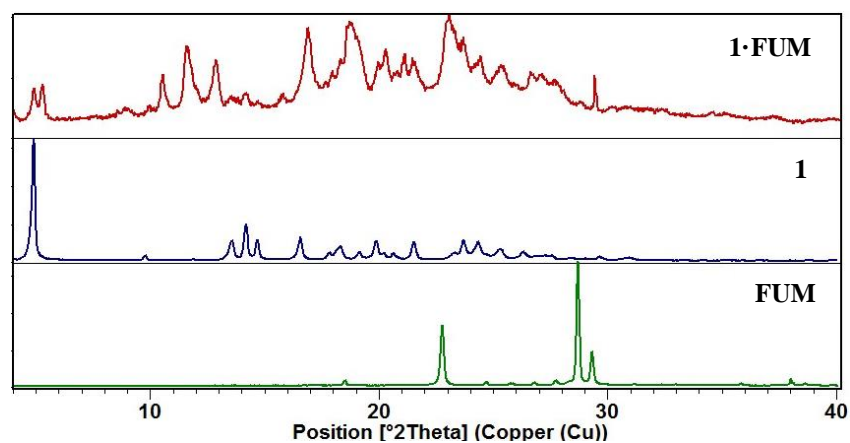
Figure 6.9: Experimental PXRD pattern of amodiaquine (**1**, navy blue), fumaric acid (**FUM**, green) and the new product obtained after grinding for 5 min with a few drops of MeOH (**1·FUM**, maroon).
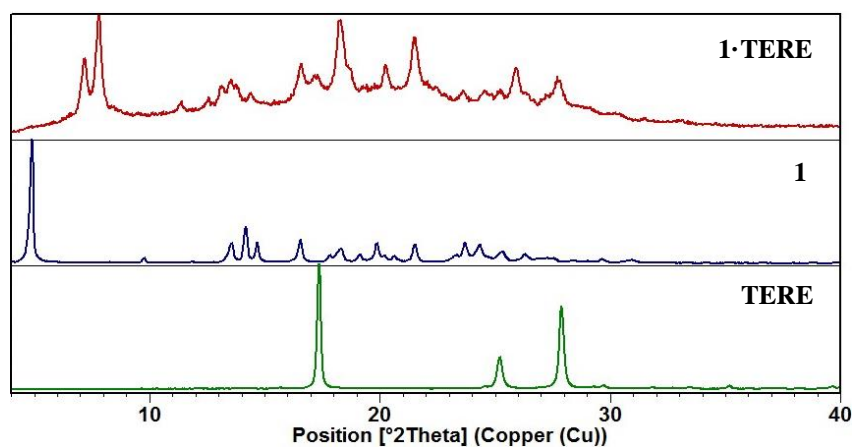
Figure 6.10: Experimental PXRD pattern of amodiaquine (**1**, navy blue), terephthalic acid (**TERE**, green) and the new product obtained after grinding for 5 min with a few drops of MeOH (**1·TERE**, maroon).
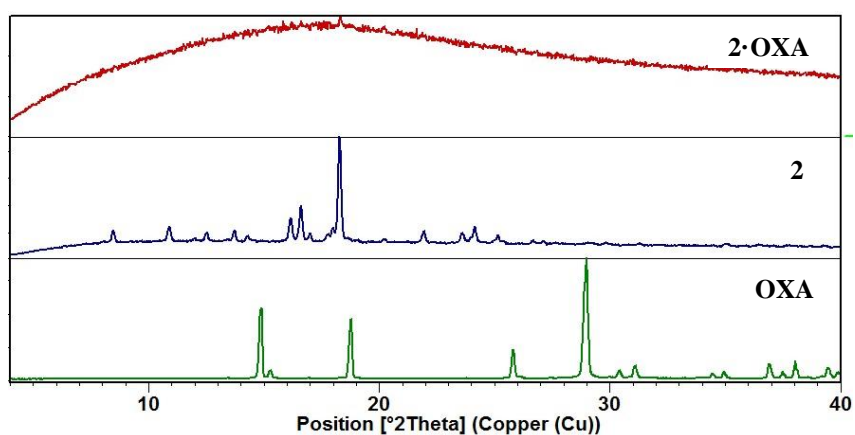
Figure 6.11: Experimental PXRD pattern of ferroquine (**2**, navy blue), oxalic acid (**OXA**, green) and the new product obtained after grinding for 5 min with a few drops of MeOH (**2·OXA**, maroon).
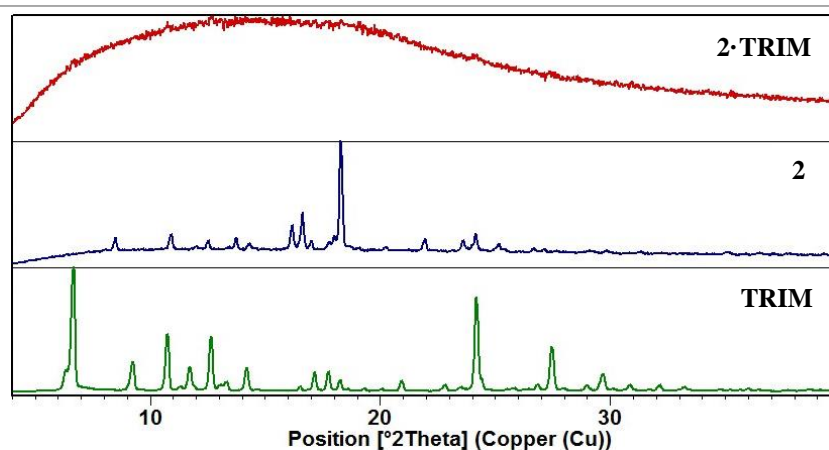
Figure 6.12: Experimental PXRD pattern of ferroquine (**2**, navy blue), trimesic acid (**TRIM**, green) and the new product obtained after grinding for 5 min with a few drops of MeOH (**2·TRIM**, maroon).
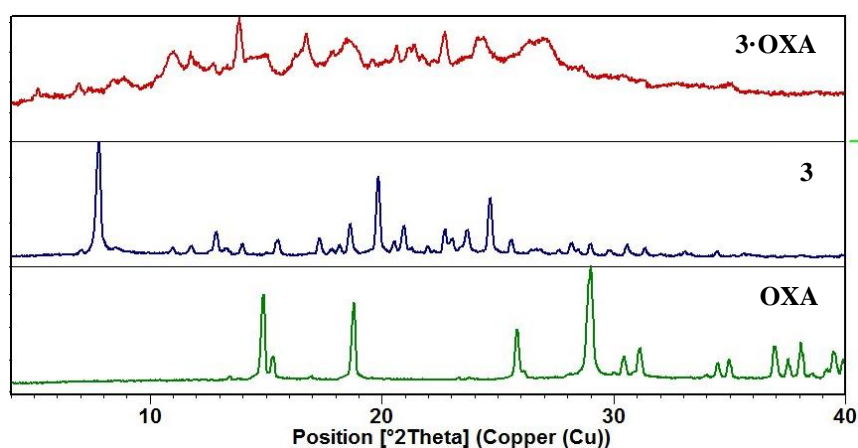
Figure 6.13: Experimental PXRD pattern of phenylequine (**3**, navy blue), oxalic acid (**OXA**, green) and the new product obtained after grinding for 5 min with a few drops of MeOH (**3·OXA**, maroon).
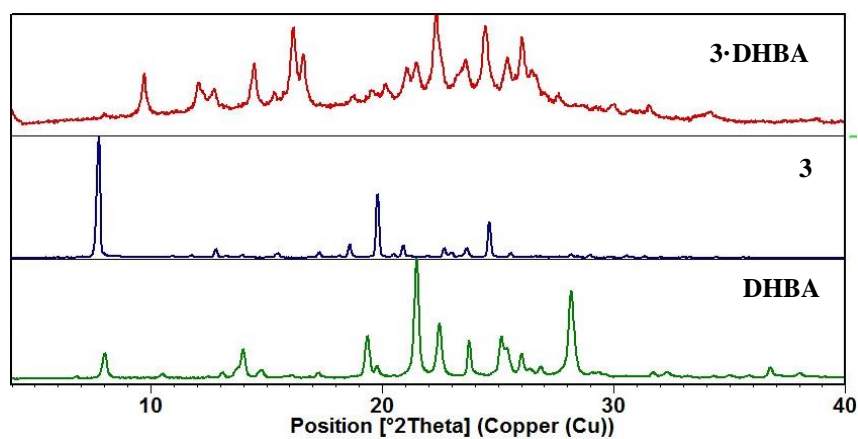
Figure 6.14: Experimental PXRD pattern of phenylequine (**3**, navy blue), 3,5-dihydroxybenzoic acid (**DHBA**, green) and the new product obtained after grinding for 5 min with a few drops of MeOH (**3·DHBA**, maroon).
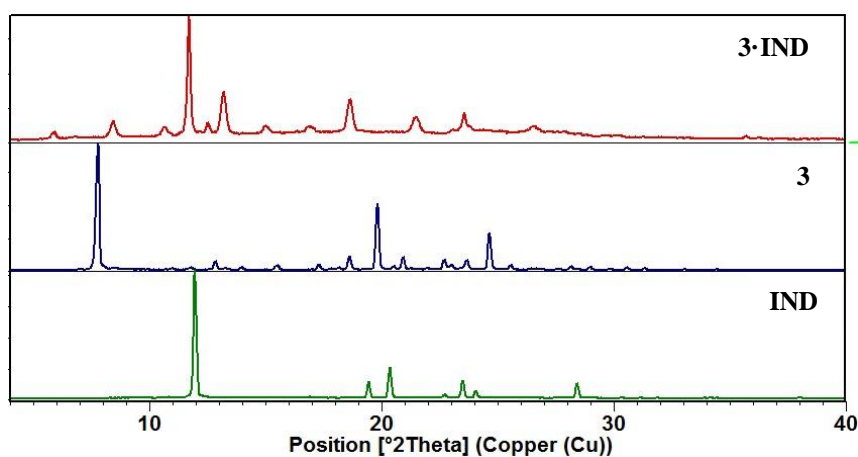
Figure 6.15: Experimental PXRD pattern of phenylequine (**3**, navy blue), indole (**IND**, green) and the new product obtained after grinding for 5 min with a few drops of MeOH (**3·IND**, maroon).
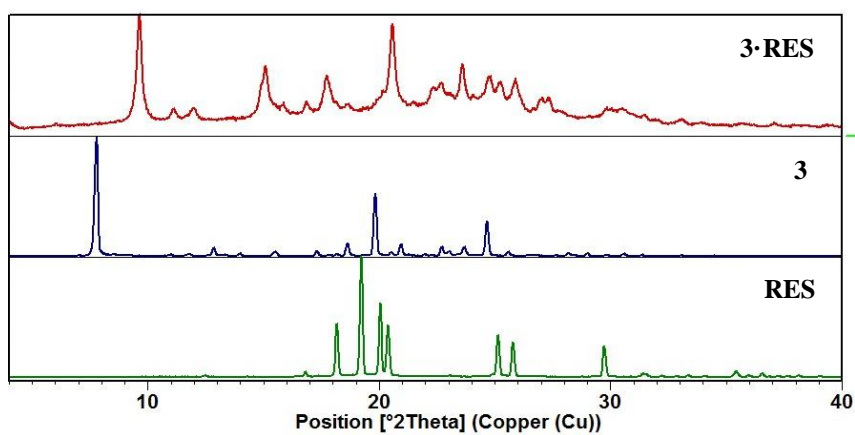
Figure 6.16: Experimental PXRD pattern of phenylequine (**3**, navy blue), resorcinol (**RES**, green) and the new product obtained after grinding for 5 min with a few drops of MeOH (**3·RES**, maroon).
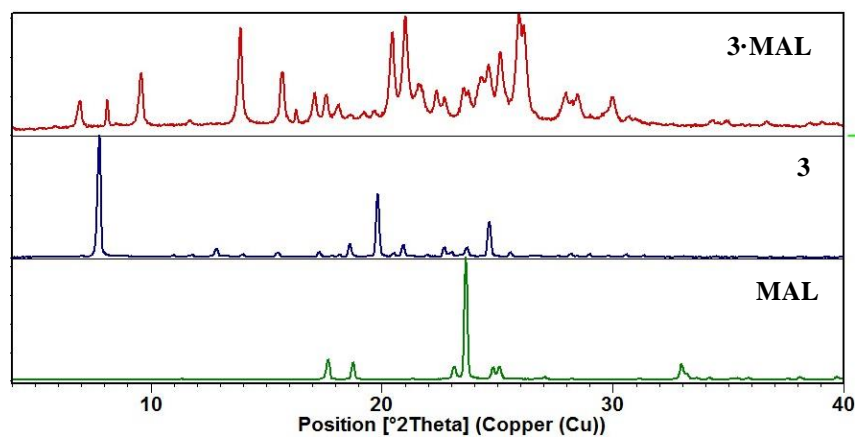
Figure 6.17: Experimental PXRD pattern of phenylequine (**3**, navy blue), malonic acid (**MAL**, green) and the new product obtained after grinding for 5 min with a few drops of MeOH (**3·MAL**, maroon).
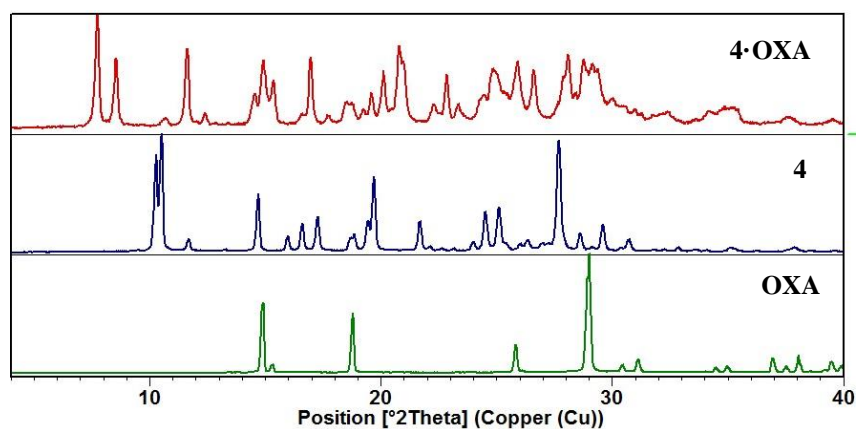
Figure 6.18: Experimental PXRD pattern of N^1-(7-chloroquinolin-4-yl)ethane-1,2-diamine (**4**, navy blue), oxalic acid (**OXA**, green) and the new product obtained after grinding for 5 min with a few drops of MeOH (**4·OXA**, maroon).
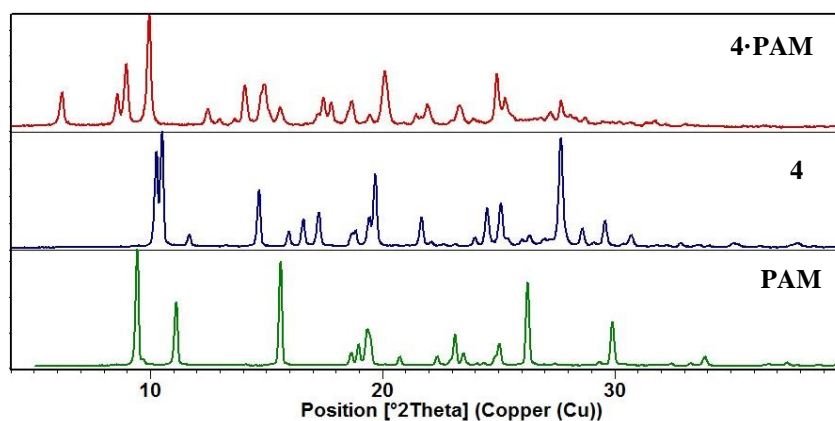
Figure 6.19: Experimental PXRD pattern of N^1-(7-chloroquinolin-4-yl)ethane-1,2-diamine (**4**, navy blue), pamoic acid (**PAM**, green) and the new product obtained after grinding for 5 min with a few drops of MeOH (**4·SUC**, maroon).
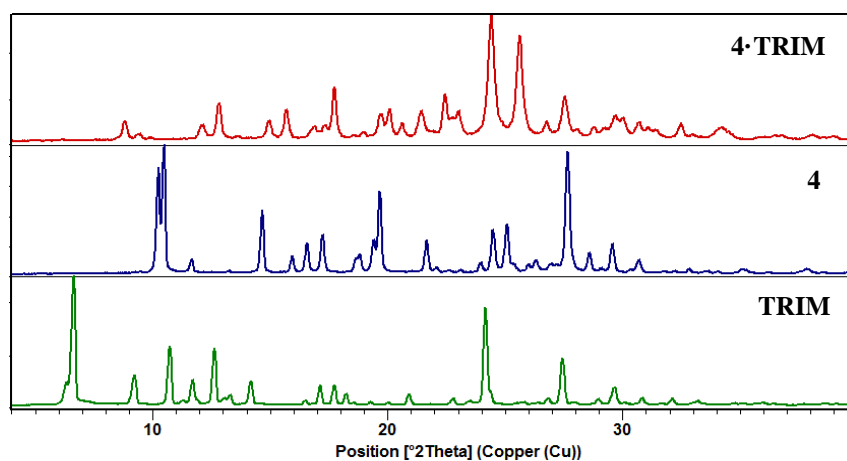
Figure 6.20: Experimental PXRD pattern of N^1-(7-chloroquinolin-4-yl)ethane-1,2-diamine (**4**, navy blue), trimesic acid (**TRIM**, green) and the new product obtained after grinding for 5 min with a few drops of MeOH (**4·TRIM**, maroon).
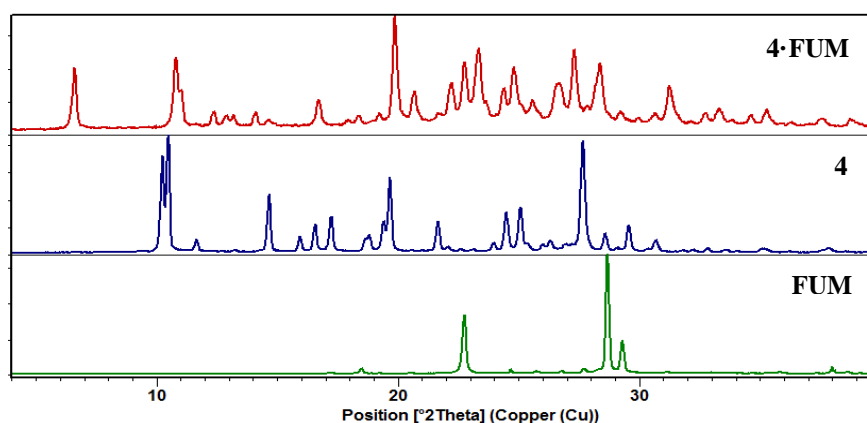
Figure 6.21: Experimental PXRD pattern of N^1-(7-chloroquinolin-4-yl)ethane-1,2-diamine (**4**, navy blue), fumaric acid (**FUM**, green) and the new product obtained after grinding for 5 min with a few drops of MeOH (**4·FUM**, maroon).
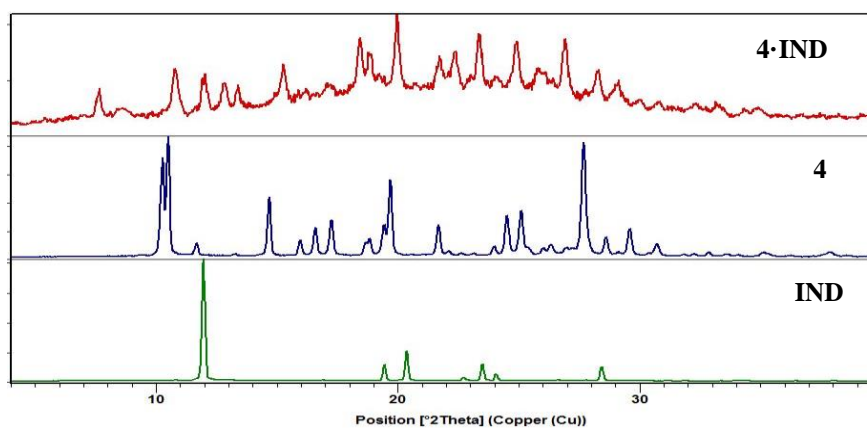
Figure 6.22: Experimental PXRD pattern of N^1-(7-chloroquinolin-4-yl)ethane-1,2-diamine (**4**, navy blue), indole (**IND**, green) and the new product obtained after grinding for 5 min with a few drops of MeOH (**4·IND**, maroon).

Figure 6.23: Experimental PXRD pattern of N^1-(7-chloroquinolin-4-yl)propane-1,2-diamine (**5**, navy blue), oxalic acid (**OXA**, green) and the new product obtained after grinding for 5 min with a few drops of MeOH (**5·OXA**, maroon).

Figure 6.24: Experimental PXRD pattern of *N*-(7-chloroquinolin-4-yl)propane-1,2-diamine (**5**, navy blue), malonic acid (**MAL**, green) and the new product obtained after grinding for 5 min with a few drops of MeOH (**5·MAL**, maroon).

Figure 6.25: Experimental PXRD pattern of *N*-(7-chloroquinolin-4-yl)propane-1,2-diamine (**5**, navy blue), succinic acid (**SUC**, green) and the new product obtained after grinding for 5 min with a few drops of MeOH (**5·SUC**, maroon).

*Thermogravimetric analysis (TGA) and differential scanning calorimetry (DSC) traces:*
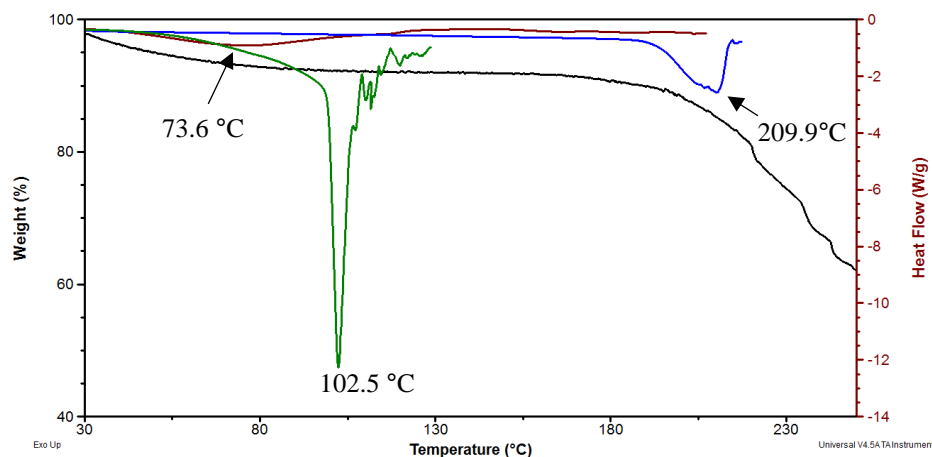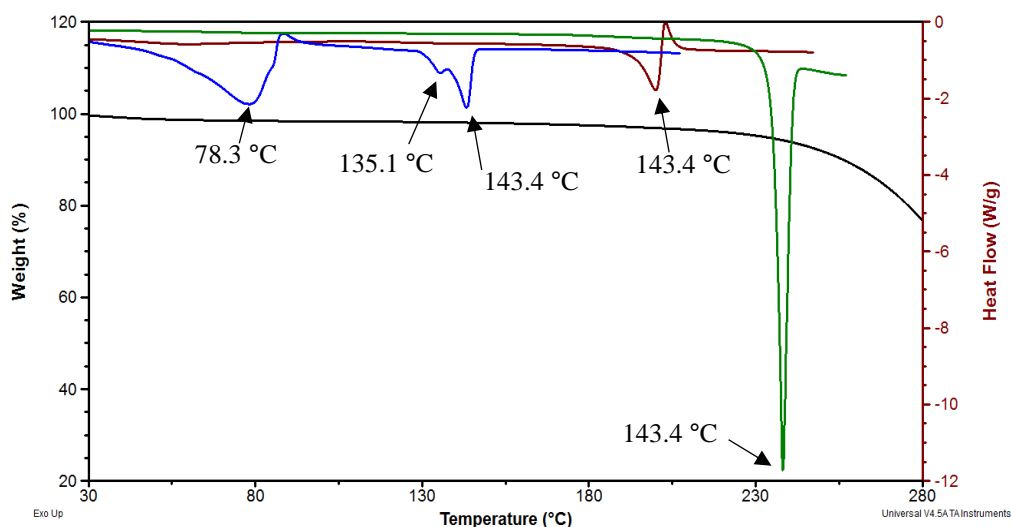

Figure 6.26: Thermal analysis of **1·OXA** in comparison to its individual components. The TGA trace of **1·OXA** is shown in black, the DSC trace of **1·OXA** is shown in maroon, the DSC trace of **1** is shown in blue and the DSC trace of oxalic acid (**OXA**) is shown in green. The initial mass loss on the TGA trace (5.6%) most likely corresponds to the loss of one MeOH molecule (calculated loss: 6.2%) from **1**:OXA:MeOH in a 1:1:1 ratio.
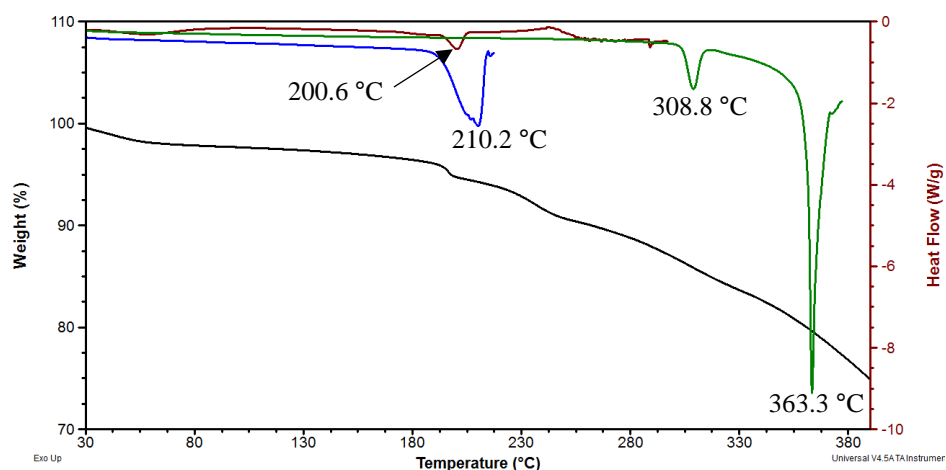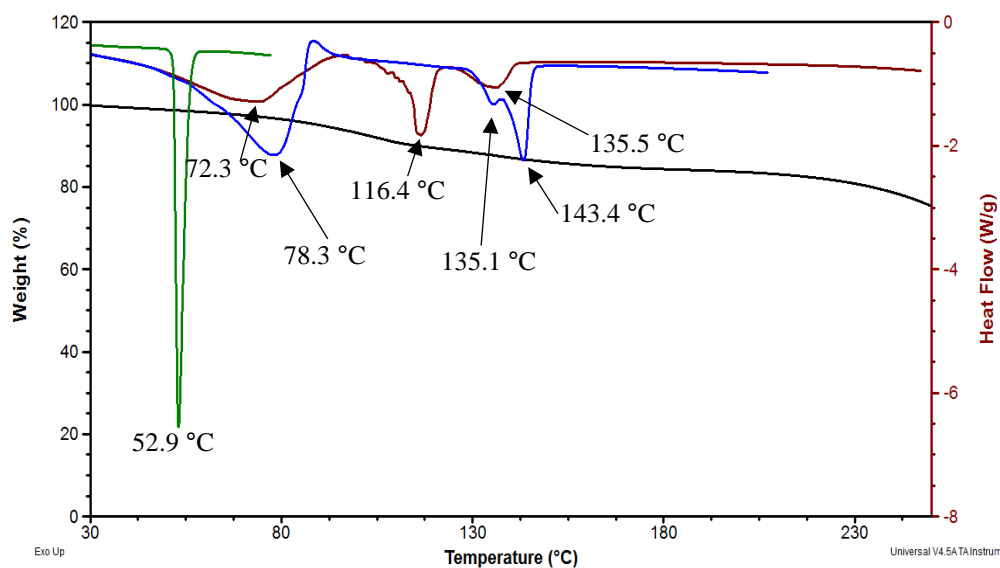

Figure 6.27: Thermal analysis of **1·TRIM** in comparison to its individual components. The TGA trace of **1·TRIM** is shown in black, the DSC trace of **1·TRIM** is shown in maroon, the DSC trace of **1** is shown in blue and the DSC trace of trimesic acid (**TRIM)** is shown in green. The initial mass loss on the TGA trace (2.1%) most likely corresponds to the loss of one H_2O molecule (calculated loss: 3.1%) from **1**:TRIM:H_2O in a 1:1:1 ratio.
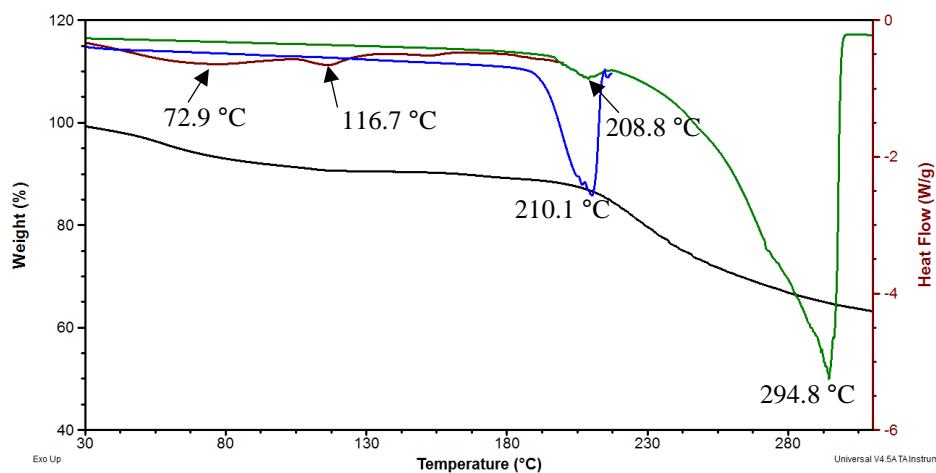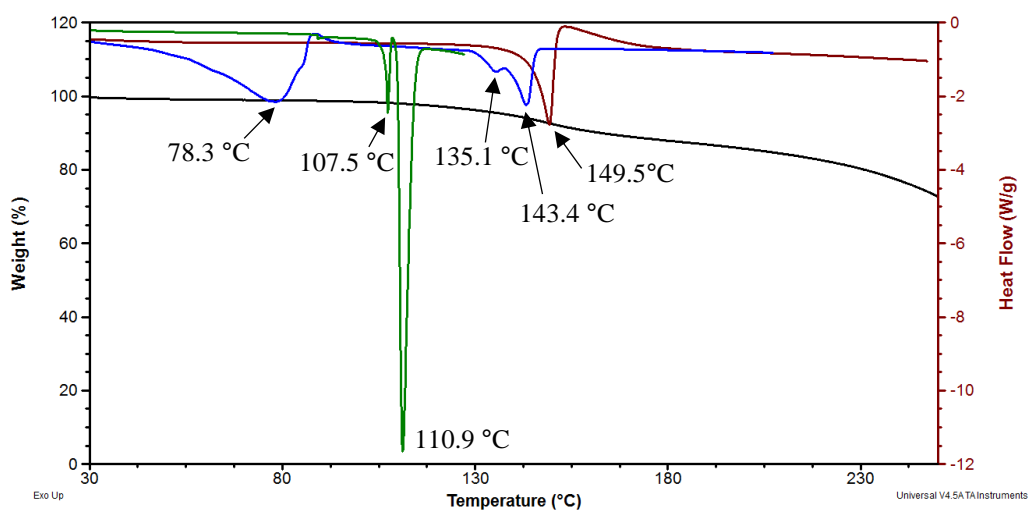
Figure 6.28: Thermal analysis of **1·FUM** in comparison to its individual components. The TGA trace of **1·FUM** is shown in black, the DSC trace of **1·FUM** is shown in maroon, the DSC trace of **1** is shown in blue and the DSC trace of fumaric acid (**FUM**) is shown in green. The initial mass loss on the TGA (8.7%) most likely corresponds to the loss of two H_2O molecules (calculated loss: 7.1%) from **1**:FUM:2H_2O in a 1:1:3 ratio, or the loss of one H_2O and one MeOH molecule (calculated loss: 9.6%) from **1**:FUM:MeOH:H_2O in a 1:1:1:1 ratio.
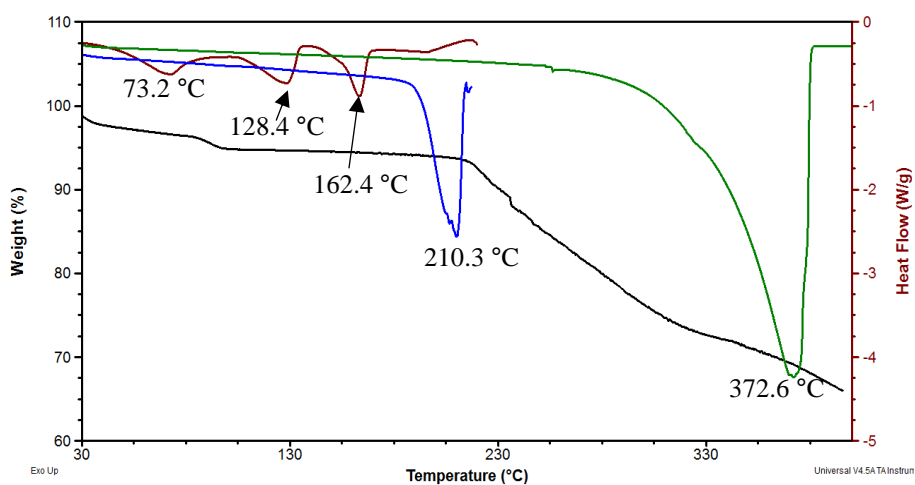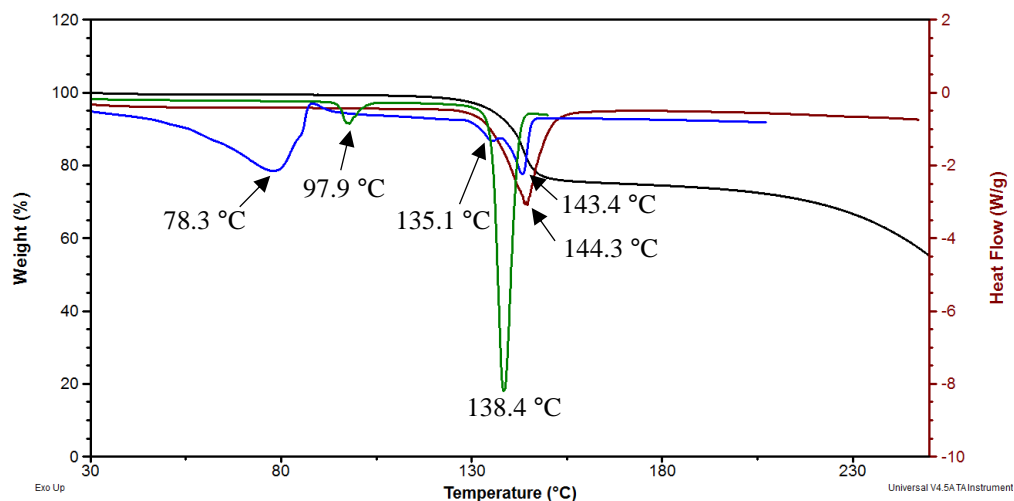

Figure 6.29: Thermal analysis of **1·TERE** in comparison to its individual components. The TGA trace of **1·TERE** is shown in black, the DSC trace of **1·TERE** is shown in maroon, the DSC trace of **1** is shown in blue and the DSC trace of terephthalic acid (**TERE**) is shown in green. The initial mass loss on the TGA (4.1%) most likely corresponds to the loss of one H_2O molecule (calculated loss: 3.3%) from **1**:TERE:H_2O in a 1:1:1 ratio.
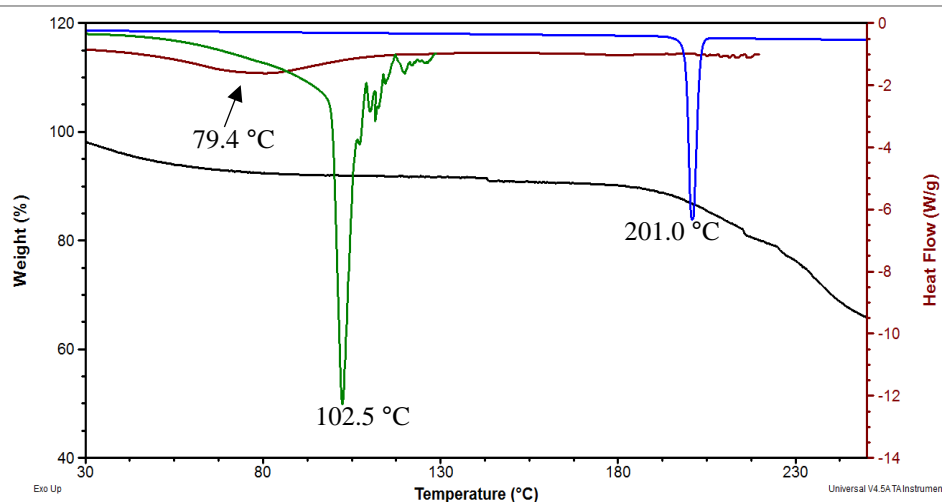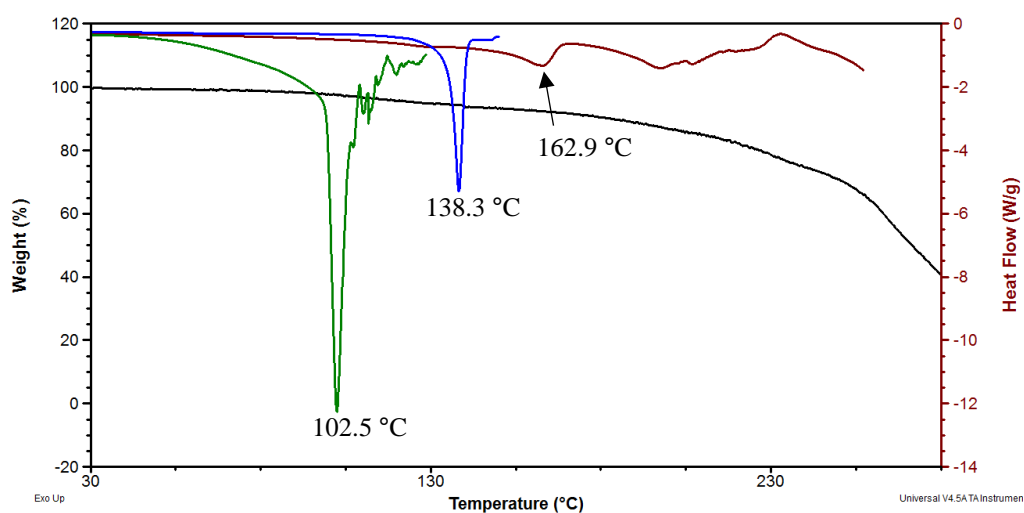
Figure 6.30: Thermal analysis of **2·OXA** in comparison to its individual components. The TGA trace of **2·OXA** is shown in black, the DSC trace of **2·OXA** is shown in maroon, the DSC trace of **2** is shown in blue and th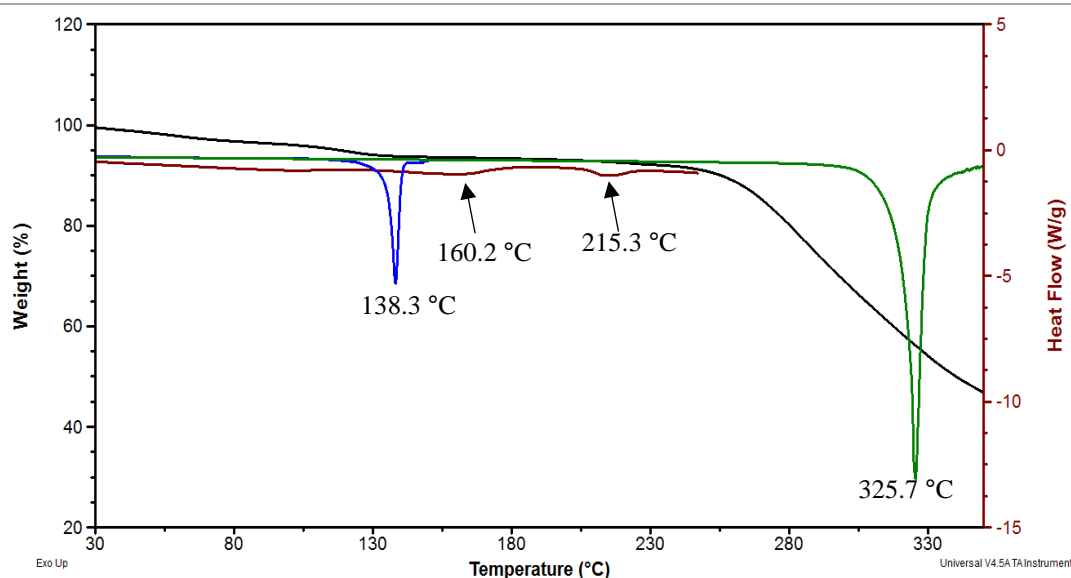e DSC trace of oxalic acid (**OXA**) is shown in green. The initial mass loss on the TGA (6.3%) most likely corresponds to the loss of one MeOH molecule (calculated loss: 5.5%) from **2**:OXA:MeOH in a 1:1:1 ratio.
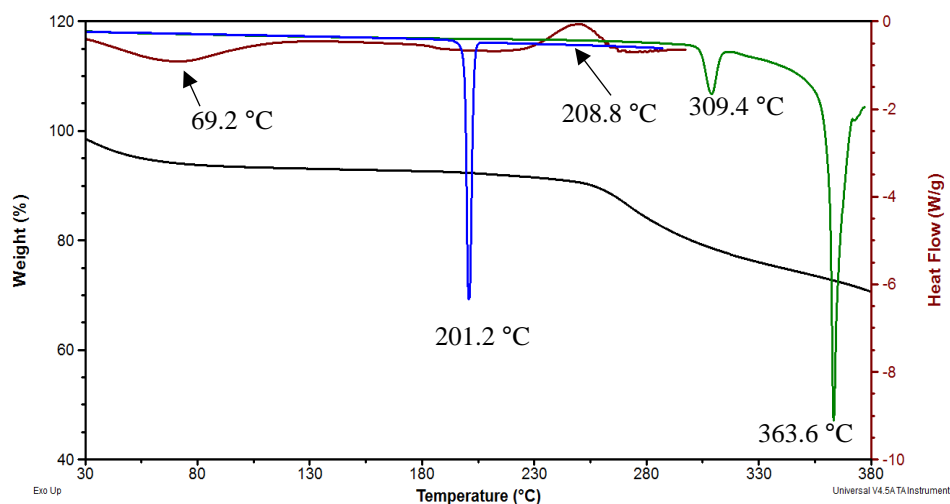
Figure 6.31: Thermal analysis of **2·TRIM** in comparison to its individual components. The TGA trace of **2·TRIM** is shown in black, the DSC trace of **2·TRIM** is shown in maroon, the DSC trace of **2** is shown in blue and the DSC trace of trimesic acid (**TRIM**) is shown in green. The initial mass loss on the TGA (5.1%) most likely corresponds to the loss of one MeOH molecule (calculated loss: 4.8%) from **2**:TRIM:MeOH in a 1:1:1 ratio.
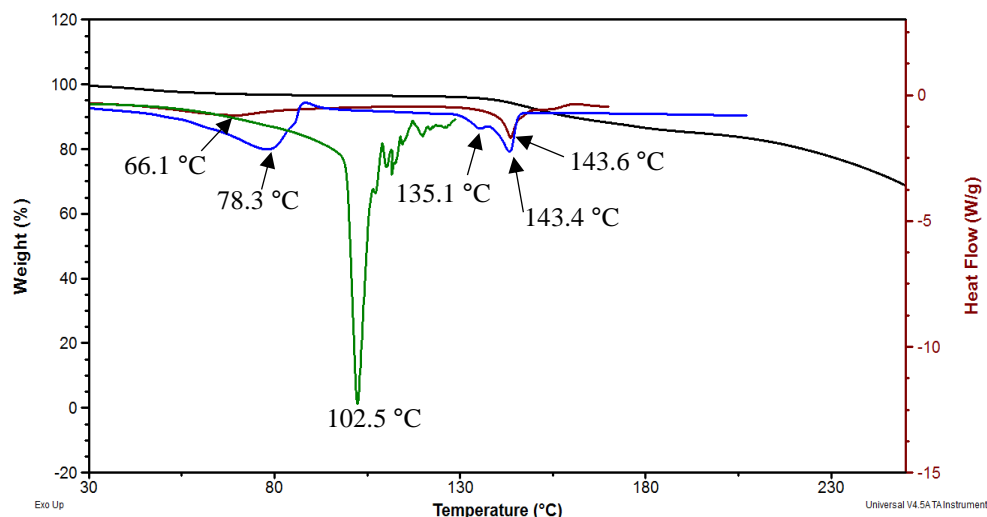
Figure 6.32: Thermal analysis of **3·OXA** in comparison to its individual components. The TGA trace of **3·OXA** is shown in black, the DSC trace of **3·OXA** is shown in maroon, the DSC trace of **3** is shown in blue and the DSC trace of oxalic acid (**OXA**) is shown in green. The initial mass loss on the TGA (2.9%) most likely corresponds to the loss of one H_2O molecule (calculated loss: 3.8%) from **3**:OXA:H_2O in a 1:1:1 ratio.
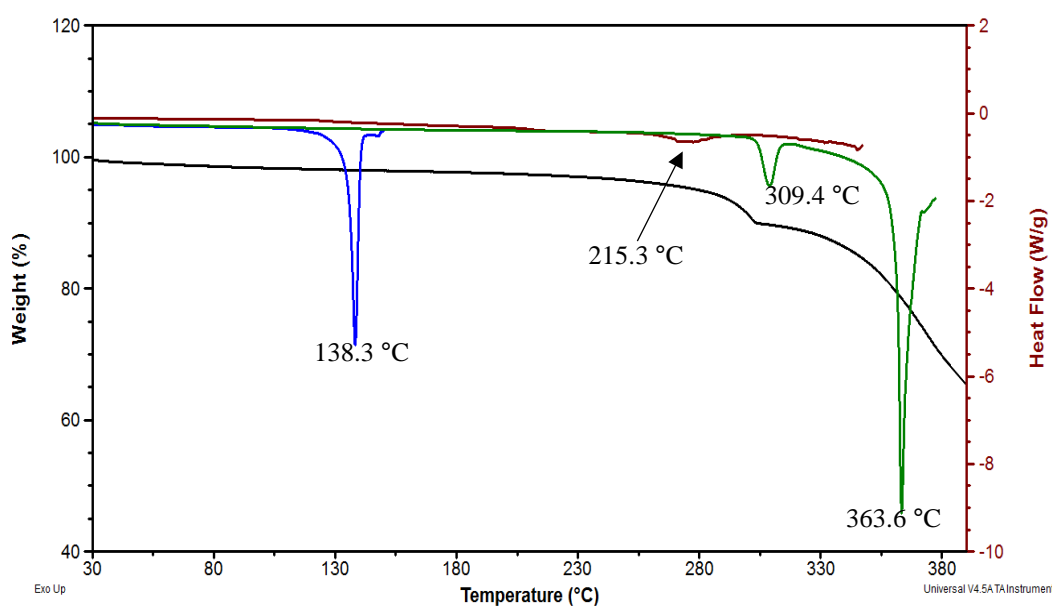

Figure 6.33: Thermal analysis of **3·DHBA** in comparison to its individual components. The TGA trace of **3·DHBA** is shown in black, the DSC trace of **3·DHBA** is shown in maroon, the DSC trace of **3** is shown in blue and the DSC trace of dihydroxybenzoic acid (**DHBA**) is shown in green.
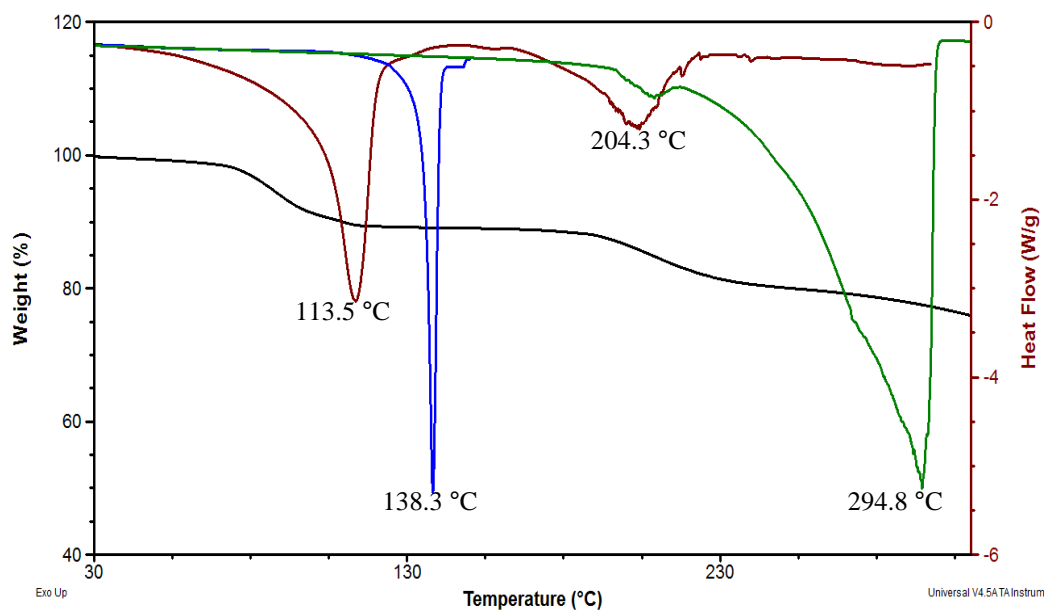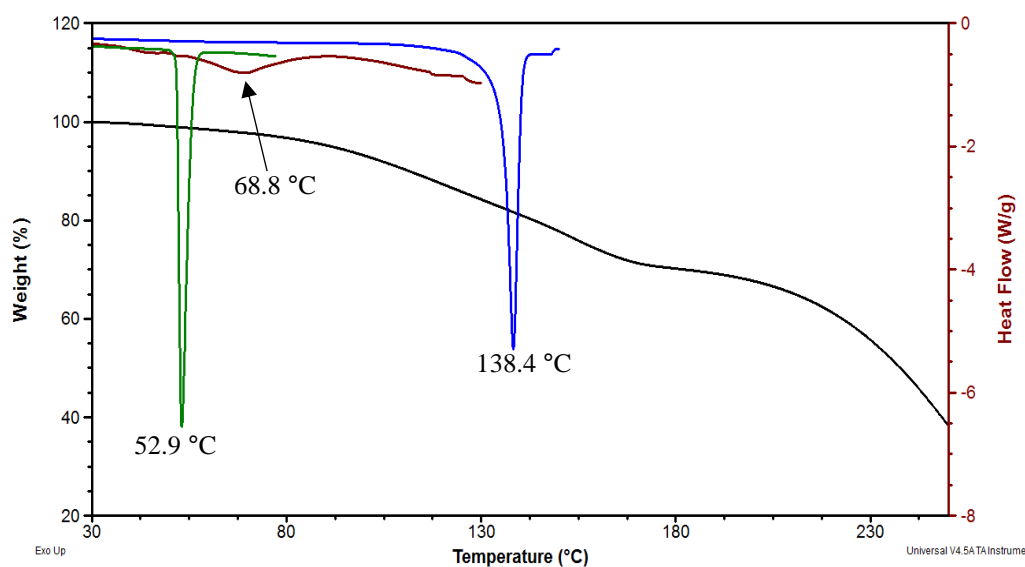
Figure 6.34: Thermal analysis of **3·IND** in comparison to its individual components. The TGA trace of **3·IND** is shown in black, the DSC trace of **3·IND** is shown in maroon, the DSC trace of **3** is shown in blue and the DSC trace of indole (**IND**) is shown in green. The initial mass loss on the TGA (10.4%) most likely corresponds to the loss of one MeOH and one H_2O molecule (calculated loss: 10.2%) from **3**:IND:MeOH:H_2O in a 1:1:1:1 ratip.

Figure 6.35: Thermal analysis of **3·RES** in comparison to its individual components. The TGA trace of **3·RES** is shown in black, the DSC trace of **3·RES** is shown in maroon, the DSC trace of **3** is shown in blue and the DSC trace of resorcinol (**RES**) is shown in green.

Figure 6.36: Thermal analysis of **3·MAL** in comparison to its individual components. The TGA trace of **3·MAL** is shown in black, the DSC trace of **3·MAL** is shown in maroon, the DSC trace of **3** is shown in blue and the DSC trace of malonic acid (**MAL**) is shown in green.
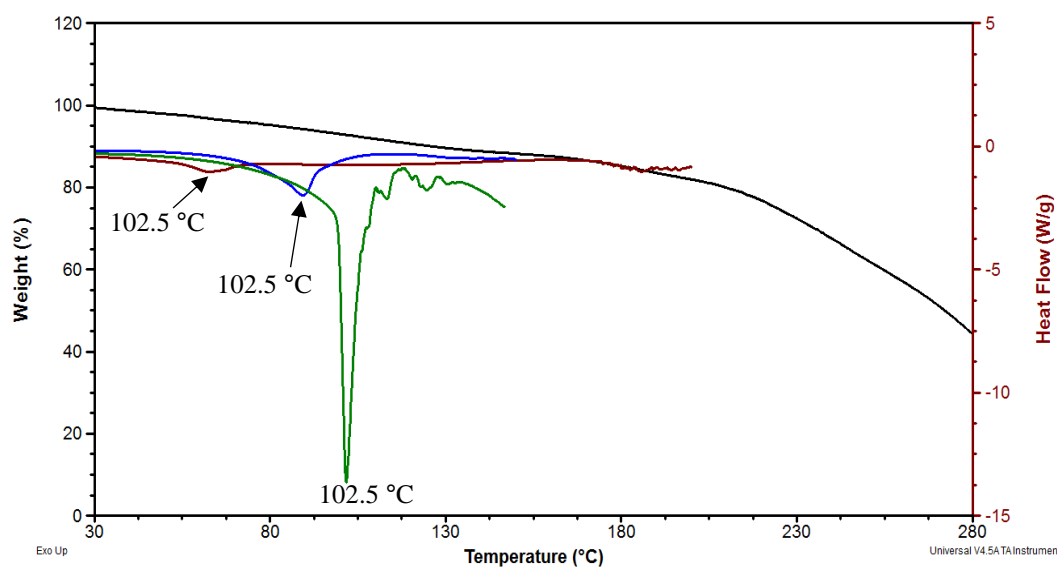

Figure 6.37: Thermal analysis of **4·OXA** in comparison to its individual components. The TGA trace of **4·OXA** is shown in black, the DSC trace of **4·OXA** is shown in maroon, the DSC trace of **4** is shown in blue and the DSC trace of oxalic acid is shown in green.

Figure 6.38: Thermal analysis of **4·PAM** in comparison to its individual components. The TGA trace of **4·PAM** is shown in black, the DSC trace of **4·PAM** is shown in maroon, the DSC trace of **4** is shown in blue and the D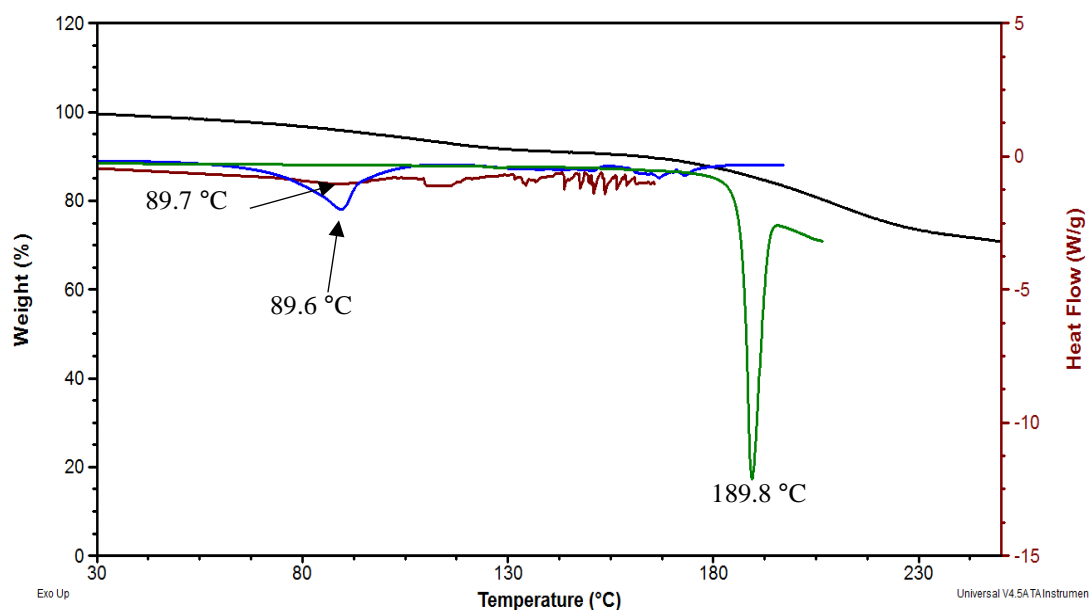SC trace of pamoic acid is shown in green. The initial mass loss on the TGA (5.9%) mostly likely corresponds to the loss of one MeOH molecule (calculated loss: 4.9%) from **4**:PAM:MeOH in a 1:1:1 ratio, or the loss of two H_2O molecules (calculated loss: 5.6%) from **4**:PAM:$2H_2O$ in a 1:1:2 ratio.
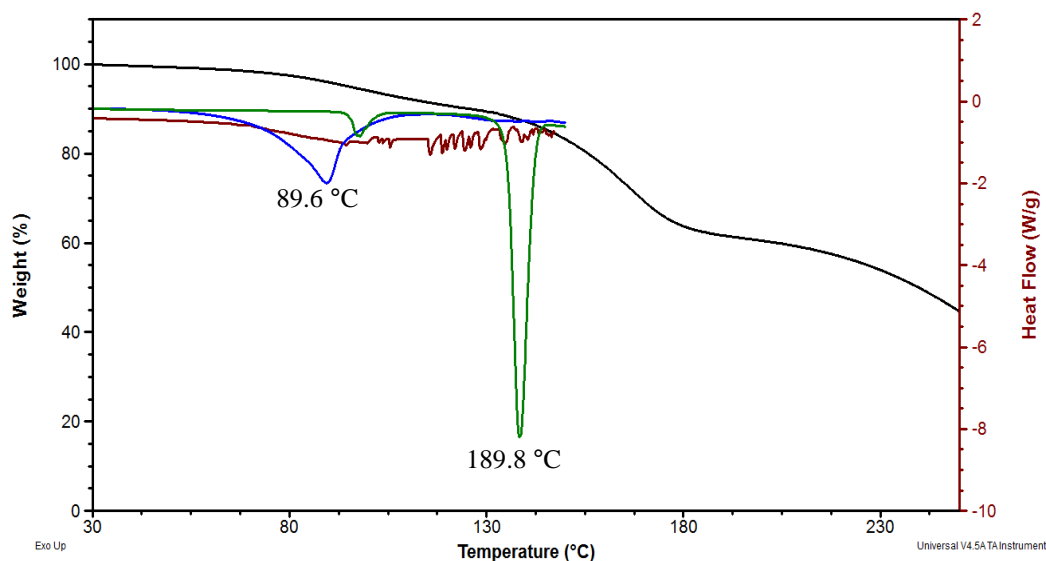

Figure 6.39: Thermal analysis of **4·TRIM** in comparison to its individual components. The TGA trace of **4·TRIM** is shown in black, the DSC trace of **4·TRIM** is shown in maroon, the DSC trace of **4** is shown in blue and the DSC trace of trimesic acid is shown in green.

Figure 6.40: Thermal analysis of **4·FUM** in comparison to its individual components. The TGA trace of **4·FUM** is shown in black, the DSC trace of **4·FUM** is shown in maroon, the DSC trace of **4** is shown in blue and the DSC trace of fumaric acid is shown in green. The initial mass loss on the TGA (10.6%) most likely corresponds to the loss of two H_2O molecules (calculated loss: 9.7%) from **4**:FUM:$2H_2O$ in a 1:1:2 ratio.

Figure 6.41: Thermal analysis of **4·IND** in comparison to its individual components. The TGA trace of **4·IND** is shown in black, the DSC trace of **4·IND** is shown in maroon, the DSC trace of **4** is shown in blue and the DSC trace of indole is shown in green.

Figure 6.42: Thermal analysis of **5·OXA** in comparison to its individual components. The TGA trace of **5·OXA** is shown in black, the DSC trace of **5·OXA** is shown in maroon, the DSC trace of **5** is shown in blue and the DSC trace of oxalic acid is shown in green.

Figure 6.43: Thermal analysis of **5·SUC** in comparison to its individual components. The TGA trace of **5·OXA** is shown in black, the DSC trace of **5·SUC** is shown in maroon, the DSC trace of **5** is shown in blue and the DSC trace of succinic acid is shown in green. The initial mass loss on the TGA (7.9%) most likely corresponds to the loss of one MeOH molecule (8.3%) from **5**:SUC:MeOH in a 1:1:1 ratio.

Figure 6.44: Thermal analysis of **5·MAL** in comparison to its individual components. The TGA trace of **5·MAL** is shown in black, the DSC trace of **5·MAL** is shown in maroon, the DSC trace of **5** is shown in blue and the DSC trace of malonic acid is shown in green. The initial mass loss on the TGA (10.0%) most likely corresponds to the loss of one MeOH molecule (8.6%) from **5**:MAL:MeOH in a 1:1:1 ratio.

6.3 EXPERIMENTAL DATA PERTAINING TO CHAPTER 3

2-Amino-5-iodobenzoic acid (19)
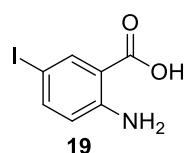
In a 500 mL round-bottomed flask was added 0.58 M KOH solution (1.32 g KOH in 40 mL distilled water) and commercially available 2-aminobenzoic acid (2.01 g, 14.6 mmol, 1.00 equivalents). In a second flask, iodine (3.70 g, 14.6 mmol, 1.00 equivalent) was added portion wise to a 1.7 M KOH solution (1.91 g KOH in 20 mL distilled water) and the mixture stirred until the iodine was completely dissolved. This iodine mixture was then added dropwise to the 2-aminobenzoate solution over 20 minutes, resulting in an orange-brown solution. After 1 hour, glacial acetic acid (8 mL) was added in one portion, followed immediately by distilled water (25 mL). The dark reaction mixture was stirred for 2 hours at room temperature before a saturated solution of sodium thiosulphate (50 mL) was added. The reaction mixture was stirred for further 1 hour, during which the mixture lightened in colour. The precipitate was filtered off and washed with distilled water (4 × 20 mL) and dried in air for 10 minutes using vacuum filtration. The resulting product was recrystallised from hot methanol to afford the title compound in 78% yield (3.01 g) as a brown crystalline solid.

TLC (50% EtOAc/Hexane): R_f = 0.42. **^{1}H NMR (300 MHz, DMSO-d_6) δ** 8.80 (br. s., 3H), 7.92 (d, *J* = 2.2 Hz, 1H), 7.45 (dd, *J* = 8.7, 2.2 Hz, 1H), 6.61 (d, *J* = 8.7 Hz, 1H). **IR (ATR, cm^{-1})** 3500 (s, NH$_2$), 3386 (s, NH$_2$), 1662 (m, C=O), 1227 (s, C–O), 619 (C–I). **Mp** >230 °C (exceeded maximum temperature on melting point apparatus). The data compared well with the literature.[28,29]
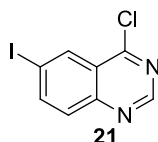
6-Iodoquinazolin-4(3*H*)-one (20)

20

To a 25 mL round-bottomed flask was added 2-amino-5-iodobenzoic acid (**19**) (4.47 g, 16.9 mmol, 1.00 equivalents), formamide (13.5 mL, 509 mmol, 30.0 equivalents) and ammonium formate (1.60 g, 25.5 mmol, 1.50 equivalents). The reaction mixture was stirred at 140 °C for 18 hours. Once the reaction was complete (as indicated by TLC analysis), the mixture was cooled to room temperature and poured into ice cold distilled water (200 mL). The precipitate was filtered and washed with distilled water (4 × 20 mL) and then dried in air for 10 minutes using vacuum filtration. A brown crystalline solid was obtained after recrystallisation from hot methanol (2.96 g, 64% yield).

TLC (80% EtOAc/Hexane): R_f = 0.41. **^{1}H NMR (300 MHz, DMSO-d_6) δ** 12.40 (br s, 1H), 8.38 (d, *J* = 2.3 Hz, 1H), 8.12 (s, 1H), 8.09 (dd, *J* = 8.4, 2.3 Hz, 1H), 7.45 (d, *J* = 8.4 Hz, 1H). **IR (ATR, cm^{-1})** 3165 (w, NH), 1670 (s, C=O), 619 (m, C–I). **Mp** >230 °C (exceeded maximum temperature on melting point apparatus). The data compared well with the literature.[30]

4-Chloro-6-iodoquinazoline (21)

21

A solution of 6-iodo-quinazolin-4(3*H*)-one (**20**) (2.85 g, 7.36 mmol, 1.00 equivalent) in thionyl chloride (15.0 mL) and anhydrous DMF (0.1 mL) was heated under reflux (85 °C) under a nitrogen atmosphere for 2 hours. Upon complete consumption of the starting material (as indicated by TLC analysis), the pale brown translucent reaction mixture was quenched with a saturated solution of sodium bicarbonate (200 mL). The product was extracted into DCM (4 × 30 mL) and washed once with brine (30 mL). The organic fractions were dried over anhydrous MgSO$_4$ and concentrated under reduced pressure. Flash column chromatography was used to purify the product, eluting with 0 – 60% EtOAc/Hexane to give the desired product as a pale yellow powder in a 58% yield (1.36 g).

TLC (50% EtOAc/Hexane): R_f = 0.79. **¹H NMR (300 MHz, CDCl₃) δ** 9.08 (s, 1H), 8.67 (d, *J* = 1.9 Hz, 1H), 8.22 (dd, *J* = 8.8, 1.9 Hz, 1H), 7.81 (d, *J* = 8.8 Hz, 1H). **Mp** 168 – 170 °C. The data compared well with the literature.[30]
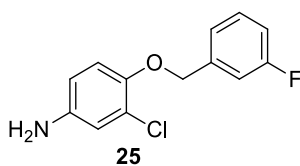
2-Chloro-1-[(3-fluorobenzyl)oxy]-4-nitrobenzene (24)
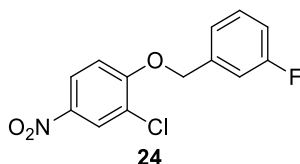
To a 25 mL round-bottomed flask containing commercially available 3-fluorobenzyl bromide (0.3 mL, 3 mmol, 1 equivalent), K_2CO_3 (0.486 g, 3.52 mmol, 1.50 equivalents) and acetonitrile (4 mL) was added a solution of commercially available 2-chloro-4-nitrophenol (0.408 g, 2.35 mmol, 1.00 equivalent) in acetonitrile (3 mL) in a dropwise fashion. The reaction mixture was stirred at 75 °C for 3 hours after which it was cooled to room temperature. The precipitate was filtered off using vacuum filtration and the filtrate was concentrated under reduced pressure. The product was eluted with a 0 – 30% EtOAc/Hexane gradient solvent system to give a pale yellow crystalline solid in 0.592 g yield (90%).

TLC (15% EtOAc/Hexane): R_f = 0.63. **¹H NMR (300 MHz, CDCl₃) δ** 8.34 (d, *J* = 2.8 Hz, 1H), 8.15 (dd, *J* = 9.0, 2.8 Hz, 1H), 7.44 – 7.36 (m, 1H), 7.25 – 7.18 (m, overlapping peaks, 2H), 7.10 – 7.06 (m, 1H), 7.02 (d, *J* = 9.0 Hz, 1H) 5.27 (s, 2H). **IR (ATR, cm⁻¹)** 1511 (s, NO₂), 1051 (s, C–O). **Mp** 90 – 93 °C. The data compared well with the literature.[30]
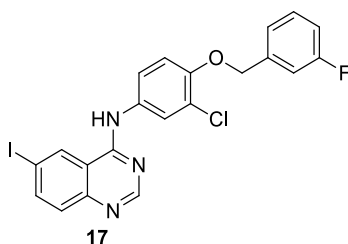
3-Chloro-4-[(3-fluorobenzyl)oxy]aniline (25)

2-chloro-1-[(3-fluorobenzyl)oxy]-4-nitrobenzene (**24**) (0.718 g, 2.55 mmol, 1.00 equivalent), ammonium chloride (1.64 g, 30.6 mmol, 12.0 equivalents), methanol (20 mL), acetonitrile (15 mL), distilled water (10 mL) and zinc powder (1.05 g, 15.3 mmol, 6.00 equivalents) were added to a 100 mL round-bottomed flask and stirred at 30 °C for 4 hours. Once the reaction was complete (as indicated by TLC analysis), the precipitated was filtered off using vacuum filtration and washed well with methanol (4 × 20 mL). The solvent (filtrate) was removed under reduced pressure to yield a brown residue that was purified by recrystallisation from hot methanol to yield a pale brown crystalline solid (0.543 g, 84%).

TLC (15% EtOAc/Hexane): R_f = 0.23. **^{1}H NMR (300 MHz, CD$_3$OD) δ** 7.38 – 7.34 (m, 1H), 7.23 – 7.20 (m, overlapping peaks, 2H), 7.02 – 7.00 (m, 1H), 6.89 (d, *J* = 8.4 Hz, 1H), 6.80 (d, *J* = 2.3 Hz, 1H), 6.60 (dd, *J* = 8.4, 2.3 Hz, 1H), 5.03 (s, 2H). The NH$_2$ protons were not observed. **IR (ATR, cm^{-1})** 3405 (m, NH$_2$), 3318 (m, NH$_2$) 1051 (s, C–O). **Mp** 69 – 71 °C. The data compared well with the literature.[30]

N-{3-Chloro-4-[(3-fluorobenzyl)oxy]phenyl}-6-iodoquinazolin-4-amine (17)

17

To a 50 mL round-bottomed flask was added 4-chloro-6-iodoquinazoline (**21**) (0.520 g, 1.80 mmol, 1.00 equivalent), 2-propanol (20 mL) and 3-chloro-4-[(3-fluoroylbenzyl)oxy]aniline (**25**) (0.500 g, 1.98 mmol, 1.10 equivalents). The reaction mixture was stirred at 85 °C for 14 hours. The bright yellow precipitate was collected and dried *in vacuo* to yield the desired product (0.734 g, 81%). No further purification was carried out.

TLC (50% EtOAc/Hexane): R_f = 0.62. **^{1}H NMR (300 MHz, DMSO-*d$_6$*) δ** 11.38 (s, 1H), 9.26 (d, 1.4 Hz, 1H), 8.95 (s, 1H), 8.37 (d, *J* = 8.8 Hz, 1H), 7.89 (d, *J* = 2.3 Hz, 1H), 7.71 (d, *J* = 8.8 Hz, 1H), 7.67 (d, *J* = 8.8 1H), 7.40 – 7.38 (m, 1H), 7.31 – 7.30 (m, 3H), 7.23 – 7.19 (m, 1H), 5.20 (s, 2H). **IR (ATR, cm^{-1})** 3035 (w, NH), 1059 (m, C–O). **Mp** 202 – 208 °C. **LC-MS** found [M+H]$^+$ = 505.9 *m/z* (C$_{21}$H$_{14}$ClFIN$_3$O); calculated [M+H]$^+$ = 505.9 *m/z*. The data compared well with the literature.[30]

Piperidylaminomethyl ferrocene (27d)

27d
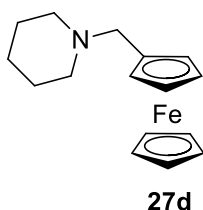
To a 50 mL round-bottomed flask was added formaldehyde solution (34%, 1.3 mL, 20 mmol, 12.5 equivalents) followed by phosphoric acid (85%, 0.1 mL, 2 mmol, 2 equivalents). To this solution, the piperidine (0.2 mL, 2 mmol, 1 equivalent) was added dropwise. Glacial acetic acid (8.0 mL) was added in one portion, followed by ferrocene (0.298 g, 1.60 mmol, 0.800 equivalents). The reaction mixture was stirred at 100 °C for 7.5 hours after which the reaction mixture was cooled and any unreacted ferrocene was extracted with EtOAc (3 × 10 mL). The aqueous layer was neutralised by the addition of

1.0 M NaOH solution (25 mL) and the product was extracted with EtOAc (3 × 30 mL). These organic fractions were combined, dried over anhydrous $MgSO_4$, and concentrated under reduced pressure. Purification by flash column chromatography using EtOAc/Hexane/Et_3N as the eluent provided the desired product moderate yield (0.296 g, 52%).

TLC (EtOAc/Hexane/Et_3N = 45:50:5): R_f = 0.63. **^{1}H NMR (300 MHz, CDCl$_3$) δ** 4.17 – 4.15 (m, 2H), 4.11 – 4.08 (m, overlapping peaks, 7H), 3.36 – 3.35 (m, 2H), 2.33 – 2.30 (m, 4H), 1.53 (quin, *J* = 5.6 Hz, 4H), 1.36 – 1.34 (m, 2H). **Mp** 79 – 82 °C. The data compared well with the literature.[31]

General procedure for the synthesis of di-substituted ferrocenes:

To a dry Schlenk tube that has been evacuated and filled with nitrogen three times was added the relevant amino ferrocene (1.0 equivalent) and anhydrous diethyl ether (8 mL). This solution was then cooled to 0 °C and *t*-BuLi (1.0 M, 1.1 equivalents) was added dropwise. The ice bath was removed and the bright orange reaction mixture was stirred for a further 2 hours. The reaction mixture was once again cooled to 0 °C and the appropriate electrophile (1.1 equivalents) added dropwise. The ice bath was removed and the reaction stirred at room temperature for a further 2 hours after which dilute hydrochloric acid (1.0 mL, 1.0 M) was added dropwise to quench the reaction. The product was extracted with DCM (3 × 30 mL) and the organic fractions combined, dried over anhydrous $MgSO_4$ and concentrated under reduced pressure. No further purification was carried out.

### 2-Dimethylaminomethyl-ferrocene-1-boronic acid (16a)

16a
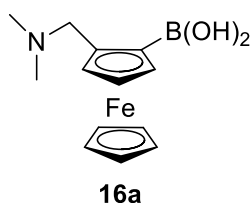
Amino ferrocene: *N,N*-dimethylaminomethyl ferrocene (0.7 mL, 4 mmol, 1 equivalent). Appropriate electrophile: trimethyl borate (0.4 mL, 4 mmol, 1 equivalent). Product obtained as a dark red-brown crystalline solid in quantitative yields (1.01 g).

TLC (EtOAc/Hexane/Et_3N = 45:50:5): R_f = 0.36. **^{1}H NMR (300 MHz, CDCl$_3$) δ** 4.47- 4.44 (m, 1H), 4.25 – 4.21 (m, 2H), 4.12 (s, 5H), 4.07 (d, *J* = 12.5 Hz, 1H), 2.87 (d, *J* = 12.5 Hz, 1H), 2.21 (s, 6H). **IR (ATR, cm^{-1})** 3279 (br, m, OH), 1462 (NCH_3). **Mp** 72 – 74 °C. The data compared well with the literature. [32]

2-Piperidylaminomethyl-ferrocene-1-boronic acid (16d)

16d
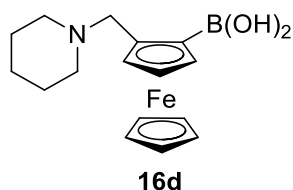
Amino ferrocene: piperidylaminomethyl ferrocene (**27d**) (0.283 g, 0.993 mmol, 1 equivalent). Appropriate electrophile: trimethyl borate (0.1 mL, 1 mmol, 1 equivalent). Product obtained as a dark brown solid in quantitative yield. (0.320 g).

TLC (EtOAc/Hexane/Et$_3$N = 45:50:5): R$_f$ = 0.32. **^{1}H NMR (300 MHz, CDCl$_3$) δ** 4.30 – 4.28 (m, 1H), 4.22 – 4.20 (m, 1H), 4.16 (s, 5H), 4.13 – 4.12 (m, 1H), 3.73 (br s, 2H), 2.66 (br s, 4 H), 1.81 (br s, 4H), 1.49 (br s, 2H). The OH protons of the boronic acid are not observed. **IR (ATR, cm^{-1})** 3272 (br, m, OH), 1465 (NCH$_3$). **Mp** 91 – 94 °C. LCMS found [M+H]$^+$ = 287.94 *m/z* for C$_{16}$H$_{22}$BFeNO$_2$); found [M+H]$^+$ = 287.14 *m/z*.

1-Iodo-2-piperadylmethyl ferrocene (32)
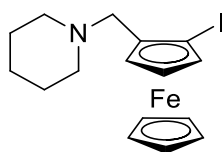
Amino ferrocene: piperadylaminomethyl ferrocene (**27d**) (0.200 g, 0.707 mmol, 1.00 equivalent). Appropriate electrophile: 1,2-diiodoethane (0.258 g, 0.918 mmol, 1.10 equivalents). Product obtained as a deliquescent dark brown solid in quantitative yield (0.288 g,).

TLC (EtOAc/Hexane/Et$_3$N = 45:50:5): R$_f$ = 0.33. **^{1}H NMR (300 MHz, CDCl$_3$) δ** 4.30 – 4.28 (m, 1H), 4.22 – 4.19 (m, overlapping peaks, 2H), 4.15 (s, 5H), 2.66 – 2.64 (m, 4H), 1.81 – 1.79 (m, 4H), 1.49 – 1.48 (m, 2H), 1.26 (s, 2H). **LC-MS** found [M+H]$^+$ = 410.09 *m/z* for C$_{16}$H$_{22}$FeIN; calculated [M+H]$^+$ = 410.09 *m/z*.

Suzuki-Miyaura coupling reaction

General method A: solution synthesis

To a Schlenk tube was added aryl halide (1 equivalent), boronic acid (1 – 2 equivalents), base (2 equivalents) and the respective solvent mixture. The reaction mixture was degassed using the freeze-pump-thaw method (4 cycles) and backfilled with nitrogen gas. The respective palladium catalyst

(10 mol%) was added under a positive pressure of nitrogen. The reaction was then stirred and heated for 18 hours after which it was cooled, filtered through Celite (washing with MeOH) and the filtrate concentrated onto silica gel and purified by flash column chromatography (0 – 100% EtOAc/Hexane)

In most cases, either starting material remained, or the by-product described below formed.

15-H
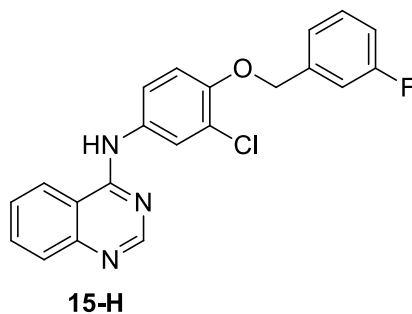
TLC (50% EtOAc/Hexane): R_f = 0.34. **^{1}H NMR (300 MHz, CDCl$_3$) δ** 9.76 (s, 1H), 8.56 (s, 1H), 8.54 (d, *J* = 8.2 Hz, 1H), 8.05 (d, *J* = 2.4 Hz, 1H), 7.91 – 7.90 (m, 1H), 7.79 (d, *J* = 8.2 Hz, 1H), 7.75 (dd, *J* = 8.8, 2.4 Hz, 1H), 7.59 – 7.57 (m, 1H), 7.47 – 7.46 (m, 1H), 7.32 – 7.30 (m, 2H), 7.21 (d, *J* = 8.8 Hz, 1H), 7.15 – 7.13 (m, 1H), 5.26 (s, 2H). **LC-MS** found [M+H]$^+$ = 380.10 *m/z*; calculated [M+H]$^+$ = 380.09 *m/z* for C$_{21}$H$_{15}$ClFNO$_3$. The data compared well with the literature.[30]

*General method B: microwave synthesis of **15d***[30]

15d
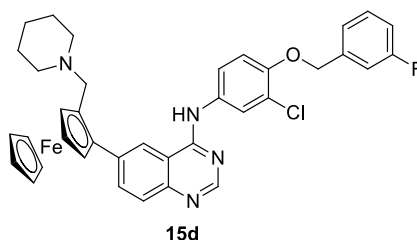
N-{3-chloro-4-[(3-fluorobenzyl)oxy]phenyl}-6-iodoquinazolin-4-amine (1 equivalent) was added to a microwave vial, followed by bis(pinacolato)diboron (1.5 equivalents) and potassium acetate (3.5 equivalents). Anhydrous dioxane was added followed by PdCl$_2$(dppf)·CH$_2$Cl$_2$ (10 mol%). The reaction mixture was degassed by bubbling nitrogen gas through the mixture for 10 minutes. The vial was placed in the microwave and stirred at 145 °C for 1 hour 45 minutes. Once complete, the reaction mixture was filtered through Celite (washing with EtOAc) and concentrated under reduced pressure to give a crude residue that was used directly in the next reaction.

To a second microwave vial was added 2-piperadylaminomethyl ferrocene-1-boronic acid (1.00 equivalent), the crude boronate product above (1.50 equivalents), barium hydroxide (3.00 equivalents), and EtOH/H$_2$O (3:1, 1.3 mL). The reaction mixture was degassed for 10 minutes by

bubbling nitrogen gas through the mixture. The respective palladium catalyst was then added and the reaction mixture degassed for a further 5 minutes. The reaction was stirred in the microwave reactor at the conditions listed in Chapter 3. The mixture was then cooled, filtered through Celite (washing with MeOH) and concentrated under reduced pressure. Purification was carried out with flash column chromatography however the desired product was unable to be isolated. Preparative HPLC on a second reaction also was tried, but without success.

LC-MS found $[M+H]^+$ = 661.22 *m/z*; calculated $[M+H]^+$ = 661.19 *m/z* for $C_{37}H_{34}ClFFeN_4O$.

Quinazolin-4(3*H*)-one (40)

40
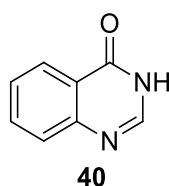
Commercially available anthranilic acid (5.00 g, 19.1 mmol, 1.00 equivalent), ammonium formate (13.8 g, 219 mmol, 6.00 equivalents) and formamide (20 mL) were added to a 50 mL round-bottomed flask and stirred at 140 °C overnight. The pale brown solution was then cooled to room temperature and poured into ice cold water (100 mL), upon which a precipitate was formed. This off-white precipitate was collected by vacuum filtration and washed with distilled water (3 × 20 mL) and dried *in vacuo* for 1 hour. Purification by flash column chromatography eluting with 50 – 100% EtOAc/Hexane resulted in the desired compound as a white solid (3.39 g, 67%).

TLC (15% EtOAc/Hexane): R_f = 0.43. **^{1}H NMR (300 MHz, CDCl₃) δ** 8.30 (dd, *J* = 8.0, 1.1 Hz, 1H), 8.23 (d, *J* =13.7 Hz, 1H), 8.14 (s, 1H), 7.81 – 7.80 (m, 1H), 7.78 – 7.75 (m, 1H), 7.54 – 7.51 (m, 1H). **IR (ATR, cm⁻¹)** 3163 (m, NH), 1660 (s, C=O). **Mp** 142 – 145 °C.

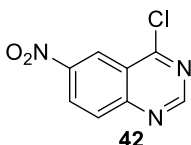### 6-Nitro-quinazolin-4(3*H*)-one (41)

41
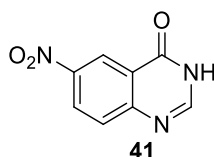
To a 25 mL round-bottomed flask was added conc. H_2SO_4 (8.0 mL, 140 mmol, 6 equivalents), followed by fuming nitric acid (8.0 mL, 140 mmol, 6 equivalents). To this mixture was added quinazolin-4(3*H*)-one (**40**) (3.28 g, 22.5 mmol, 1.00 equivalent) portion wise over 30 minutes. The resulting yellow solution was stirred at 95 °C for 2 hours. The solution was cooled to room temperature and neutralised

by slowly adding the solution to a cold, saturated solution of sodium bicarbonate (150 mL). An additional amount of the sodium bicarbonate solution was added until a pH of approximately 7 was obtained as determined by universal indicator paper (roughly 50 mL). The pale yellow precipitate was collected by vacuum filtration, washed with distilled water (3 × 30 mL) and dried in air overnight. The desired product was obtained as a pale yellow solid in 83% yield (3.56 g). No further purification was necessary.

TLC (50% EtOAc/Hexane): R_f = 0.37. **¹H NMR (300 MHz, DMSO-d_6) δ** 12.75 (br. s., 1H), 8.78 (d, J = 2.4 Hz, 1H), 8.53 (dd, J = 8.8, 2.4 Hz, 1H), 8.30 (s, 1H), 7.85 (d, J = 8.8 Hz, 1H). **IR (ATR cm⁻¹)** 1652 (s, C=O), 1607 (s, NO_2). **Mp** 285 – 287 °C.
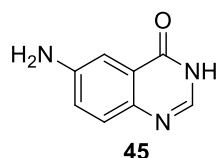
4-Chloro-6-nitro-quinazoline (42)

A solution of 6-nitro-quinazolin-4(3H)-one (**41**) (0.501 g, 2.62 mmol, 1.00 equivalent) in thionyl chloride (10.0 mL, 0.139 mmol, 53.0 equivalents) and anhydrous DMF (0.2 mL, 3 mmol, 1 equivalents) was heated under reflux at 85 °C under a nitrogen atmosphere for 2 hours. Upon complete consumption of the starting material (TLC), the reaction mixture was quenched with a saturated solution of sodium bicarbonate (15 mL). The product was extracted into DCM (4 × 30 mL) and washed once with brine (30 mL). The organic fractions were dried over anhydrous $MgSO_4$ and concentrated under reduced pressure. Flash column chromatography was used to purify the product, eluting with 0 – 60% EtOAc/Hexane to give **42** as a pale yellow powder in a 70% yield (0.384 g).

TLC (50% EtOAc/Hexane): R_f = 0.84. **¹H NMR (300 MHz, CDCl₃) δ** 9.51 (d, J = 2.3 Hz, 1H), 8.55 (m, 1H), 8.10 (s, 1H), 7.90 (d, J = 8.8 Hz, 1H). **Mp** 168 – 170 °C. The data compared well with the literature.[33]

N-{3-Chloro-4-[(3-fluorobenzyl)oxy]phenyl}-6-nitroquinazolin-4-amine (43)

43
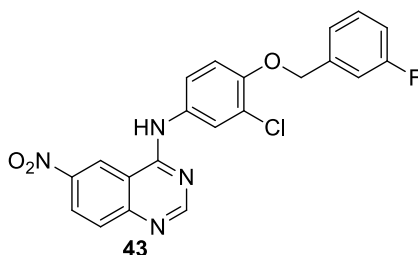
To a 50 mL round-bottomed flask was added 4-chloro-6-nitroquinazoline (**42**) (0.351 g, 1.67 mmol, 1.00 equivalent), 2-propanol (20 mL) and 3-chloro-4-[(3-fluoroylbenzyl)oxy]aniline (**25**) (0.422 g, 1.67 mmol, 1.00 equivalent). The reaction mixture was stirred at 85 °C for 14 hours. The bright yellow precipitate was collected and dried *in vacuo* to yield the desired product (0.726 g, 86%). No further purification was necessary.

TLC (20% MeOH/DCM): R_f = 0.73. **^{1}H NMR (300 MHz, CDCl$_3$) δ** 9.75 (d, *J* = 2.4 Hz, 1H), 8.92 (s, 1H), 8.70 (dd, *J* = 9.4, 2.4 Hz, 1H), 8.05 (d, *J* = 9.4 Hz, 1H), 7.96 (d, *J* = 2.4 Hz, 1H), 7.70 (dd, *J* = 8.8, 2.4 Hz, 1H), 7.41 – 7.37 (overlapping peaks, 2H), 7.29 – 7.(overlapping peaks, 4H), 7.15 – 7.13 (m, 1H), 5.30 (s, 2H).

6-Amino-quinazolin-4-(3*H*)-one (45)

45

Method A: zinc and mildly acidic conditions

6-Nitro-quinazolin-4(3*H*)-one (0.251 g, 1.31 mmol, 1 equivalent), ammonium chloride (0.839 g, 15.7 mmol, 12.0 equivalents), methanol (10 mL), acetonitrile (8 mL), distilled water (5 mL) and zinc powder (0.513 g, 7.85 mmol, 6 equivalents) were added to a 50 mL round-bottomed flask and stirred at 60 °C overnight. Once the reaction was complete, the precipitate was filtered off using vacuum filtration and washed well with methanol (4 × 20 mL). The solvent (filtrate) was removed under reduced pressure to yield a brown residue that was purified by recrystallisation from hot methanol to yield a pale brown crystalline solid (0.0358 g, 17%).

Method B: Hydrazine hydrate and Pd/C[34]

6-Nitro-quinazolin-4(3*H*)-one (0.199 g, 1.04 mmol, 1.0 equivalent) and anhydrous methanol (10 mL) were added to a 50 mL round-bottomed flask, that had been previously dried and flushed with nitrogen.

To this solution was added hydrazine hydrate (0.5 mL, 3 mmol, 3 equivalents) and palladium on carbon (10 mol%). This mixture was heated under reflux under a nitrogen atmosphere for 24 hours, after which the reaction was cooled. The mixture was filtered through Celite and the filtrate concentrated under reduced pressure to give a brown residue that was purified by recrystallisation from hot methanol to give a pale brown crystalline solid (0.0396 g, 23%)

TLC (EtOAc/Hexane/MeOH/Et₃N = 50:30:10:10): R_f = 0.28. Ninhydrin was used to visualise the amine product on the TLC plate. **¹H NMR (300 MHz, CDCl₃) δ** 11.81 (br. s., 1H), 7.76 (s, 1H), 7.38 (d, J = 8.2 Hz, 1H), 7.18 (d, J = 2.4 Hz, 1H), 7.07 (dd, J = 8.2, 2.4 Hz, 1H), 5.61 (br. s., 2H). **IR (ATR, cm⁻¹)** 3426 (w, NH), 3333 (w, NH), 1657 (s, C=O), 1603 (s, NH₂).

6.4 EXPERIMENTAL DATA PERTAINING TO CHAPTER 4

Obtaining single crystals of the quinazolinone derivatives:

To a 20 mL glass vial was added 20 mg of the respective quinazolinone. Methanol was added to dissolve the sample, using gentle heating and stirring to assist with dissolution. The solution was filtered through a microfilter into a clean, labelled vial and the cap replaced. After three days, if no crystals had formed, 2 – 3 holes were poked into the vial cap to aid slow evaporation of the solvent. Diffraction-quality crystals were obtained within 1 week for **41**, **45** and **20**.

In addition to methanol, DMSO, DMF and DMA could also be used to obtain diffraction-quality crystals of each of the quinazolinone derivatives, with the exception of **40**.
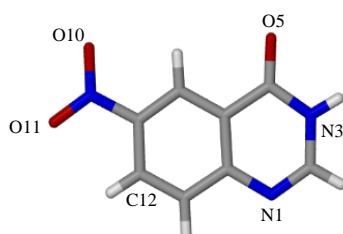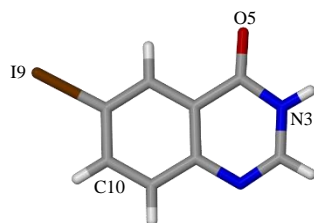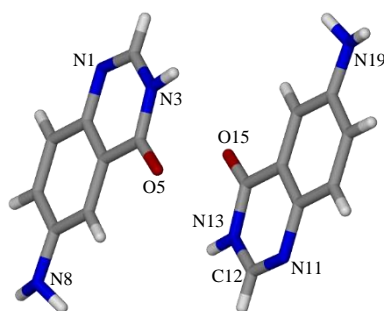
Hydrogen-bonding geometry tables

Table 6.4: Hydrogen-bonding geometries of **41**

D–H···*A*	*D*–H (Å)	H···*A* (Å)	*D*···*A* (Å)	*D*–H···*A* (°)
C13—H13···N1ⁱ	0.95	2.48	3.420 (2)	171
C2—H2···O11ⁱⁱ	0.95	2.50	3.416 (2)	162
C12—H12···O11ⁱⁱⁱ	0.95	2.49	3.388 (2)	157
N3—H3···O5ⁱᵛ	0.87 (2)	1.92 (2)	2.790 (1)	176 (2)

Symmetry codes: (i) −x+2, −y, −z+1; (ii) x+1, y, z+1; (iii) −x+1, −y, −z; (iv) −x+1, −y+1, −z+2.

Table 6.5: Hydrogen-bonding geometries for **20**

D–H···A	D–H (Å)	H···A (Å)	D···A (Å)	D–H···A (°)
C10—H10···I9^{i}	0.95	3.24	4.013 (2)	140
N3—H3···O5^{ii}	0.88 (3)	1.90 (3)	2.778 (2)	175 (2)

Symmetry codes: (i) −*x*+1, −*y*, −*z*+1; (ii) −*x*+2, −*y*+2, −*z*+1.

Table 6.6: Hydrogen-bonding geometries for **45**

D–H···A	D–H (Å)	H···A (Å)	D···A (Å)	D–H···A (°)
C2—H2···O5^{i}	0.93	2.50	3.211 (3)	133
C12—H12···O15^{ii}	0.93	2.48	3.214 (3)	136
N13—H1···O5^{iii}	0.90 (3)	1.92 (3)	2.814 (2)	174 (2)
N3—H7···O15^{iv}	0.92 (3)	1.91 (3)	2.828 (2)	174 (3)
N19—H5···N8^{v}	0.91 (3)	2.53 (3)	3.389 (3)	158 (3)
N8—H3···N1^{ii}	0.92 (3)	2.15 (3)	3.065 (3)	173 (3)
N19—H4···N11^{i}	0.89 (4)	2.24 (4)	3.112 (3)	169 (3)

Symmetry codes: (i) *x*+1/2, −*y*, *z*; (ii) *x*−1/2, −*y*+1, *z*; (iii) *x*, *y*+1, *z*; (iv) *x*, *y*−1, *z*; (v) −*x*+1, −*y*, *z*−1/2.
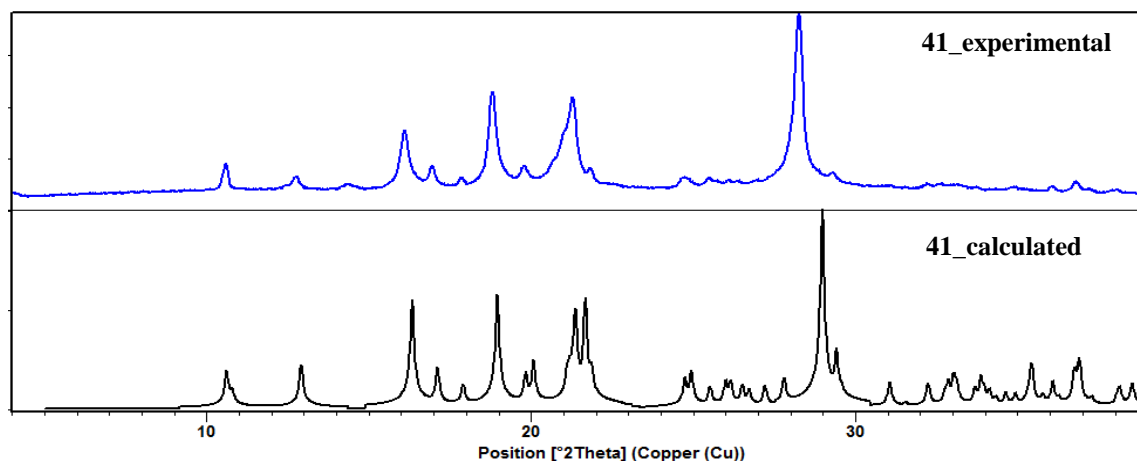
Powder X-ray Diffraction:

Figure 6.45: Comparison of the experimental (blue) and calculated (black) PXRD patterns of **41**. The experimental pattern was recorded at room temperature and the calculated pattern was obtained from crystal structure data collected at 100 K.
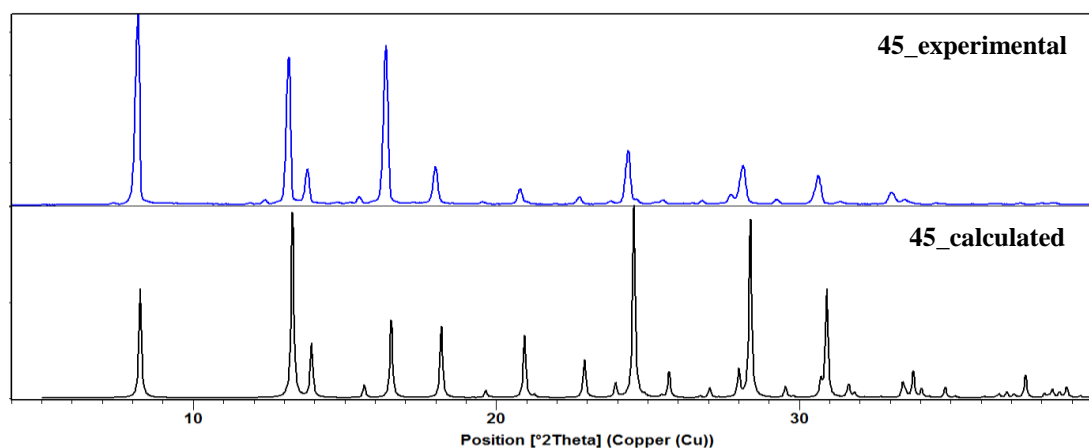

Figure 6.46: Comparison of the experimental (blue) and calculated (black) PXRD patterns of **45**. The experimental pattern was recorded at room temperature and the calculated pattern was obtained from crystal structure data collected at 100 K.
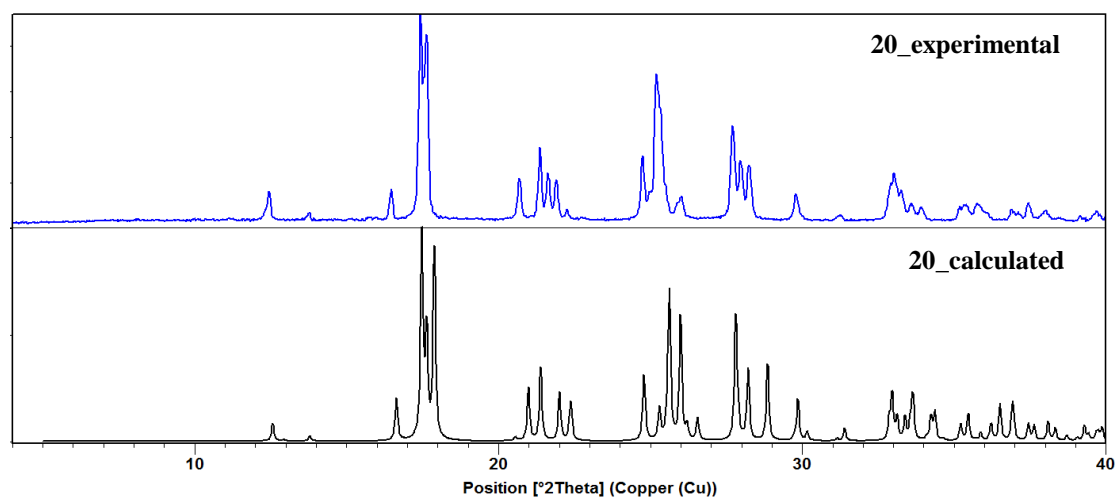
Figure 6.47: Comparison of the experimental (blue) and calculated (black) PXRD patterns of **20**. The experimental pattern was recorded at oom temperature and the calculated pattern was obtained from crystal structure data collected at 100 K.

Molecular Electrostatic Potential Surface (MEPS) calculation results

All input and wavefunction files as well as log files for each compound can be found in Appendix B (electronic data). Table 6.7 lists the 32 coformers and the ΔE value associated with each combination.

Table 6.7: ΔE values for the 1:1 combinations of **40**, **41** and **45** with each coformer.

40		41		45	
Coformer	-ΔE (kJ mol⁻¹)	Coformer	-ΔE (kJ mol⁻¹)	Coformer	-ΔE (kJ mol⁻¹)
Oxalic acid	10.4	Oxalic acid	9.6	Oxalic acid	12.1
3,5-Dihydroxy benzoic acid	6.2	*p*-Aminobenzoic acid	9.5	Trimesic acid	7.1
Methyl gallate	6.1	Ethylenediamine	9.0	Pamoic acid	7.0
Fumaric acid	5.4	3,5-Dihydroxy benzoic acid	8.1	Ethylenediamine	6.5
Trimesic acid	5.4	Methyl gallate	7.3	3,5-Dihydroxy benzoic acid	6.2
Pamoic acid	5.0	Resorcinol	6.6	Fumaric acid	5.9
p-Aminobenzoic acid	4.9	Trimesic acid	6.5	Resorcinol	5.5
Resorcinol	4.4	Benzamide	6.4	Piperazine	5.5
Indole	4.2	Piperazine	6.2	Pyrazine	4.9
Benzamide	3.1	Pamoic acid	5.3	4,4-Bipyridine	4.4
Teraphthalic acid	3.1	Indole	5.3	Tartaric acid	4.3
Ethylenediamine	3.1	Fumaric acid	4.9	Teraphthalic acid	4.2
Malonic acid	2.7	Thymine	4.3	Theophylline	4.0
Salicylic acid	2.6	Tartaric acid	4.2	Malonic acid	3.7
Tartaric acid	2.5	Caffeine	3.5	Salicylic acid	3.3
Thymine	2.3	4,4-Bipyridine	3.2	Succinic acid	3.2
Piperazine	2.1	Hydroquinone	3.0	Hydroquinone	3.0
Hydroquinone	1.9	Teraphthalic acid	2.9	Nicotinic acid	3.0
Succinic acid	1.5	Theophylline	2.6	Indole	2.7
Saccharin	1.2	Malonic acid	2.6	Glutaric acid	2.5
Morpholine	1.0	Salicylic acid	2.5	Saccharin	2.5
4,4-Bipyridine	0.7	Saccharin	2.2	Caffeine	2.3
Glutaric acid	0.7	Morpholine	2.1	Methyl gallate	2.0
Theophylline	0.6	Succinic acid	1.7	Morpholine	1.8
Caffeine	0.6	Pyrazine	1.6	*p*-Aminobenzoic acid	1.4
Vanillin	0.5	Menthol	1.6	Benzoic acid	1.3
Naphthalene	0.4	Vanillin	1.5	Naphthalene	1.1
Nicotinic acid	0.3	Nicotinamide	1.5	Thymine	0.7
Pyrazine	0.3	Glutaric acid	1.1	Vanillin	0.4
Benzoic acid	0.2	Naphthalene	0.6	Benzamide	0.2
Menthol	0.1	Benzoic acid	0.4	Nicotinamide	0.2
Nicotinamide	0.1	Nicotinic acid	0.4	Menthol	0.2

Obtaining multicomponent crystals of 40, 41 and 45 with organic coformers:

Mechanochemistry:

Liquid-assisted grinding (using a few drops of MeOH) was used as a screening tool to determine whether multicomponent crystals would form between the respective quinazolinone and various coformers. Stoichiometric amounts of the quinazolinone (10 mg) and coformer were added to a mortar and pestle and 3 drops of MeOH were added. The components were ground together for 5 minutes. PXRD was used to determine whether a mixture of starting components was still present or whether a new product had formed. In cases where starting material was still observed (by PXRD), an additional 10 minutes of grinding was carried out and PXRD was once again carried out.
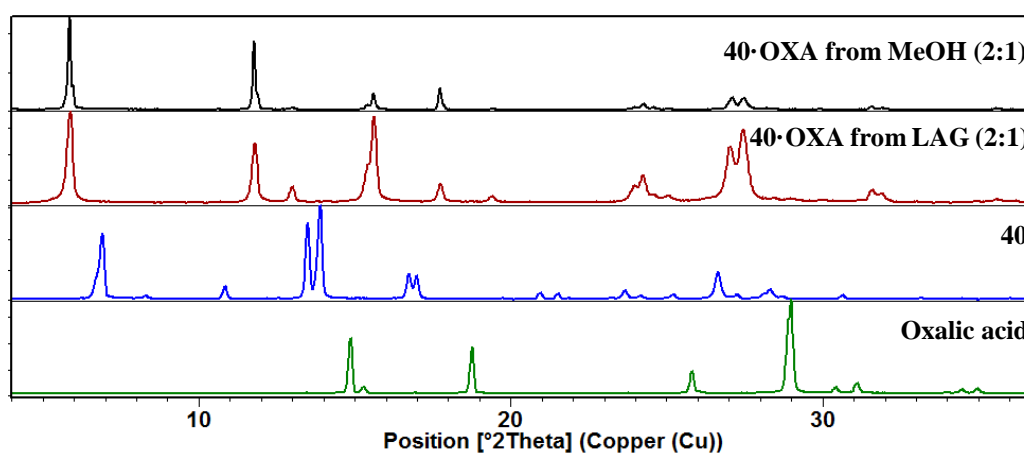
PXRD patterns of successful attempts

Figure 6.48: Comparison of the PXRD patterns of the product obtained from MeOH (**40·OXA** – black), product obtained from LAG (**40·OXA** – maroon), and the two individual components (**40** – blue and oxalic acid – green).
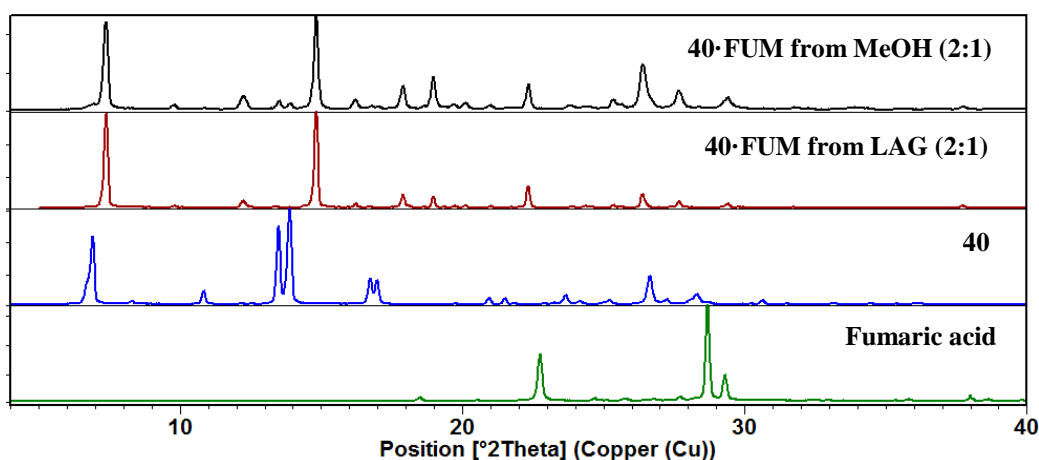

Figure 6.49: Comparison of the PXRD patterns of the product obtained from MeOH (**40·FUM** – black), product obtained from LAG (**40·FUM** – maroon), and the two individual components (**40** – blue and fumaric acid – green).
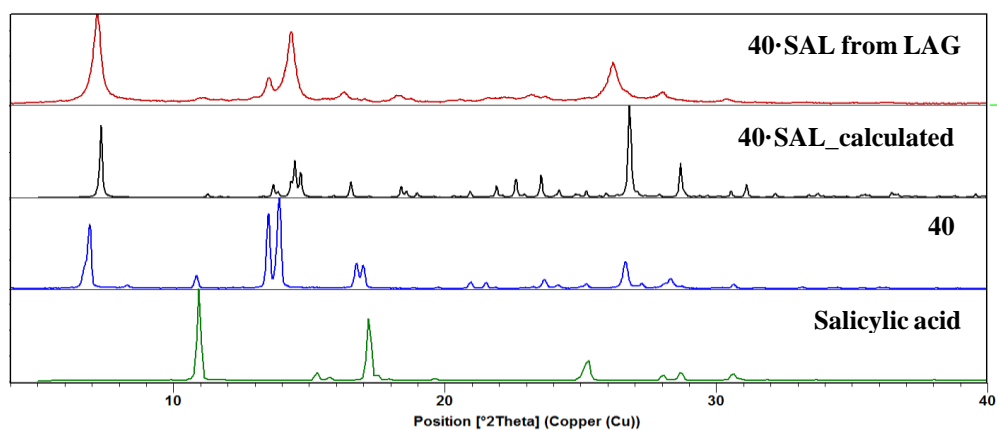
Figure 6.50: Comparison of the experimental PXRD pattern obtained from LAG (**40·SAL** – maroon) and calculated (black) PXRD patterns of **40·SAL**, as well as the two starting components – **40** (blue) and salicylic acid (green).
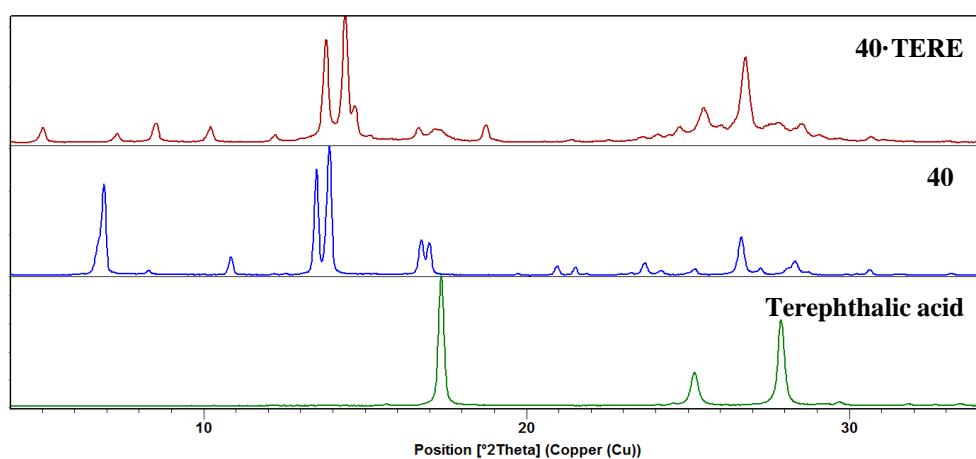

Figure 6.51: Comparison of the PXRD patterns of the product obtained from LAG (**40·TERE** – maroon) and the two individual components (**40** – blue and terephthalic acid – green).
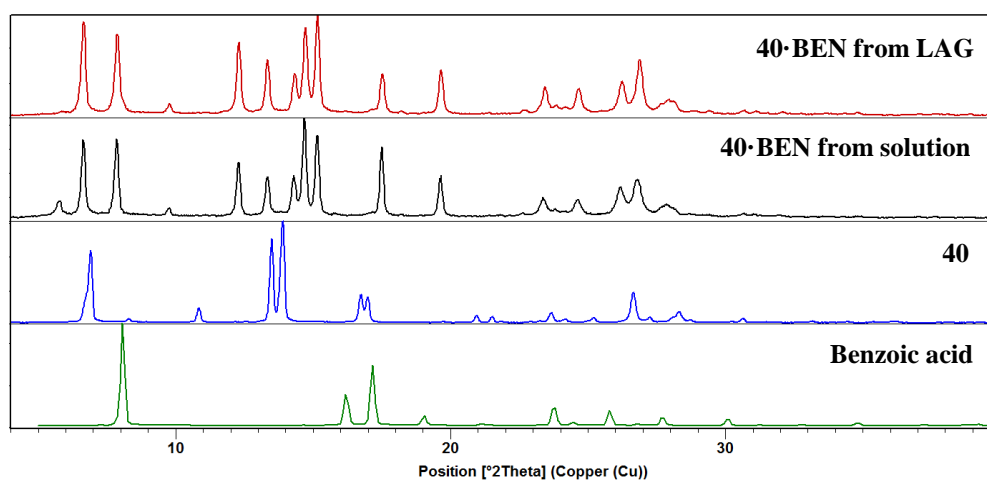

Figure 6.52: Comparison of the PXRD patterns of the product obtained from LAG (**40·BEN** – maroon), product obtained from MeOH (**40·BEN** – black), and the two individual components (**40** – blue and benzoic acid – green).
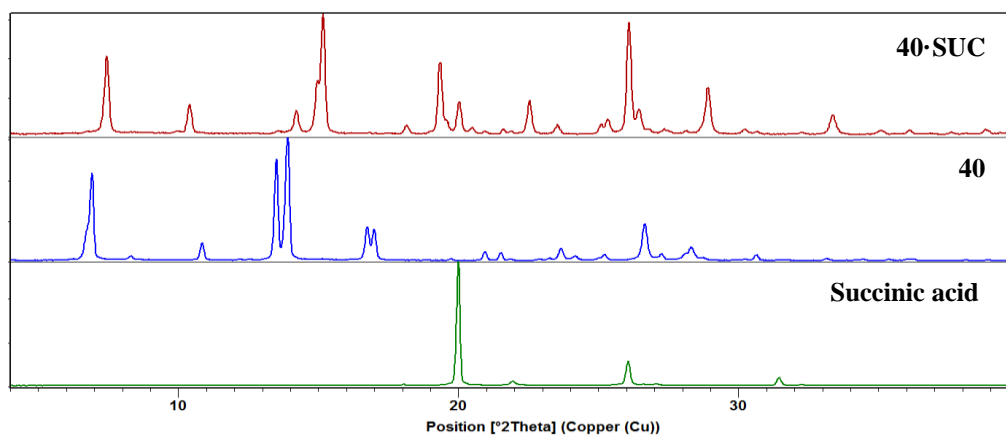
Figure 6.53: Comparison of the PXRD patterns of the product obtained from LAG (**40·SUC** – maroon) and the two individual components (**40** – blue and succinic acid – green).
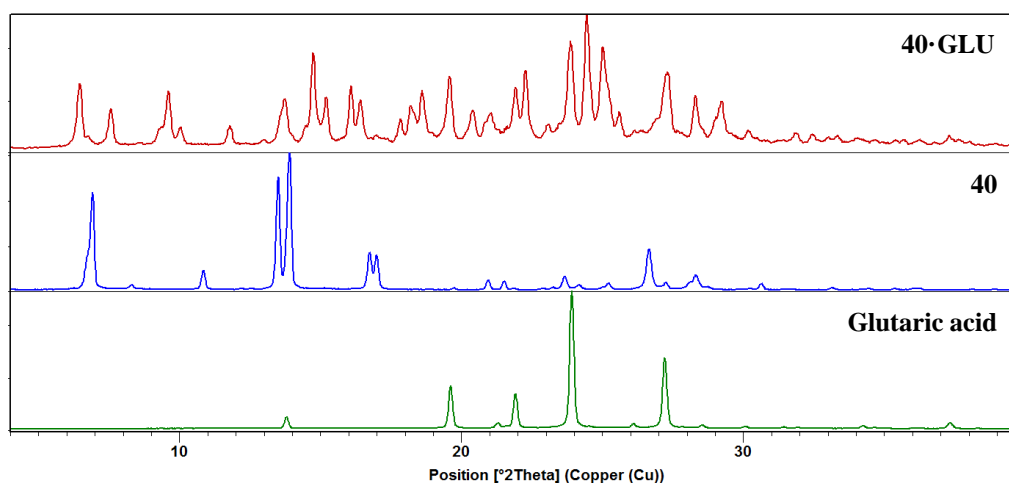

Figure 6.54: Comparison of the PXRD patterns of the product obtained from LAG (**40·GLU** – maroon) and the two individual components (**40** – blue and glutaric acid – green).
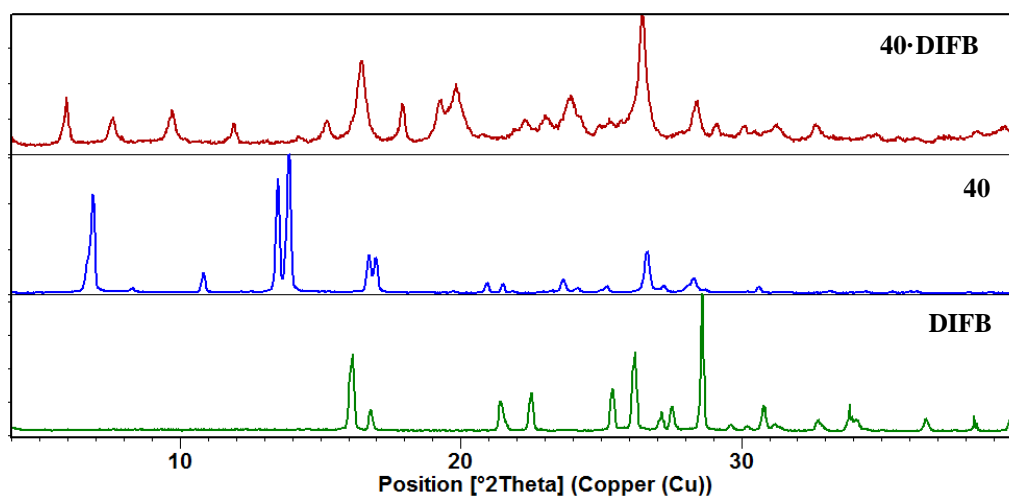

Figure 6.55: Comparison of the PXRD patterns of the product obtained from LAG (**40·DIFB** – maroon) and the two individual components (**40** – blue and 1,4-diiodotetrafluorobenzene (DIFB) – green).

Solution cocrystallisation:

Stoichiometric amounts of the quinazolinone (10 mg) and coformer were added to a vial and the appropriate solvent (MeOH or DMSO) was added. Gentle heating and stirring ensured that the minimum amount of solvent needed was used to dissolve the components. Vials were then placed on a shelf and the solvent allowed to slowly evaporate. Crystals/solid material was obtained after 1 – 18 days. If diffraction-quality crystals were obtained, single-crystal X-ray diffraction was used to determine the unit cell (and therefore whether the crystal was one of either starting component or something new). If only poor quality crystals or powders were obtained from solution, PXRD was used to identify the solid material.

Hydrogen-bonding geometry tables
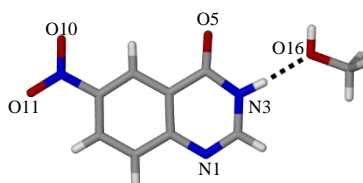
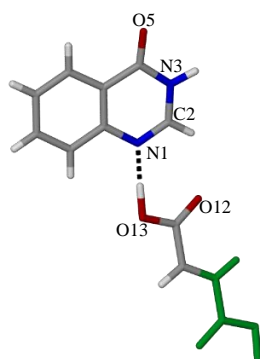**Table 6.8**: Hydrogen-bonding geometries for **41·MeOH**

D–H⋯*A*	*D*–H (Å)	H⋯*A* (Å)	*D*⋯*A* (Å)	*D*–H⋯*A* (•)
C2—H2⋯O5[i]	0.95	2.21	3.136 (2)	166
C12—H12⋯O10[ii]	0.95	2.34	3.213 (2)	152
N3—H1⋯O16	0.91 (2)	1.87 (2)	2.773 (2)	175.1 (2)
O16—H3⋯N1[iii]	0.88 (2)	1.97 (2)	2.839 (2)	170.4 (2)

Symmetry codes: (i) −*x*+1, *y*+1/2, −*z*+3/2; (ii) −*x*+2, *y*+1/2, −*z*+1/2; (iii) −*x*+1, *y*−1/2, −*z*+3/2.
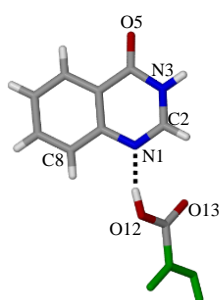
Table 6.9: Hydrogen-bonding geometries for **40·OXA**

D–H⋯*A*	*D*–H (Å)	H⋯*A* (Å)	*D*⋯*A* (Å)	*D*–H⋯*A* (•)
C2—H2⋯O13[i]	0.93	2.44	3.013 (4)	120
C8—H8⋯O11[ii]	0.93	2.43	3.130 (4)	132
N3—H1⋯O12[iii]	0.92 (5)	1.98 (5)	2.877 (4)	164 (5)
N3—H1⋯O13[i]	0.92 (5)	2.38 (5)	2.949 (4)	120 (4)
O12—H3⋯N1	0.91 (2)	1.69 (3)	2.583 (4)	166 (8)

Symmetry codes: (i) −*x*+1, *y*+1, −*z*+1/2; (ii) *x*, −*y*+1, *z*−1/2; (iii) *x*, −*y*+2, *z*+1/2.

Table 6.10: Hydrogen-bonding geometries for **40·FUM**

D–H⋯*A*	*D*–H (Å)	H⋯*A* (Å)	*D*⋯*A* (Å)	*D*–H⋯*A* (°)
C2—H2⋯O12	0.93	2.52	3.177 (2)	128
N3—H1⋯O11[i]	0.912 (2)	1.99 (2)	2.833 (1)	154.3 (1)
O13—H3⋯N1	1.03 (2)	1.59 (2)	2.619 (1)	175 (2)

Symmetry code: (i) −*x*+3/2, *y*+1/2, −*z*+1/2.
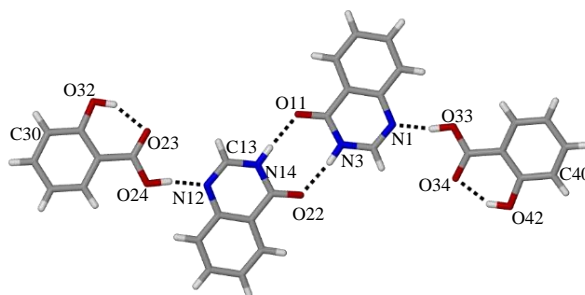
Table 6.11: Hydrogen-bonding geometries for **40·SAL**

D–H⋯*A*	*D*–H (Å)	H⋯*A* (Å)	*D*⋯*A* (Å)	*D*–H⋯*A* (°)
C40—H40⋯O11	0.93	2.59	3.470 (2)	159
C2—H2⋯O32[i]	0.93	2.47	3.350 (2)	158
C30—H30⋯O22[ii]	0.93	2.53	3.402 (2)	156
C13—H13⋯O42	0.93	2.36	3.280 (1)	169
N3—H1⋯O22	0.91 (2)	1.88 (2)	2.784 (2)	172 (2)
N14—H9⋯O11	0.89 (2)	1.89 (2)	2.782 (2)	174 (2)
O32—H3⋯O23	0.89 (2)	1.84 (2)	2.644 (1)	150 (2)
O32—H3⋯O34[iii]	0.89 (2)	2.46 (2)	3.009 (2)	120 (2)
O42—H4⋯O23[iv]	0.89 (2)	2.48 (2)	3.016 (1)	120 (2)
O42—H4⋯O34	0.89 (2)	1.82 (2)	2.630 (1)	150 (2)
O24—H10⋯N12[iii]	0.95 (2)	1.67 (3)	2.606 (2)	168 (2)
O33—H11⋯N1[v]	0.94 (2)	1.71 (2)	2.633 (2)	166 (2)

Symmetry codes: (i) *x*, *y*, *z*−1; (ii) *x*, *y*, *z*+1; (iii) *x*−1, *y*, *z*; (iv) *x*+1, *y*, *z*; (v) *x*+1, *y*, *z*+1.
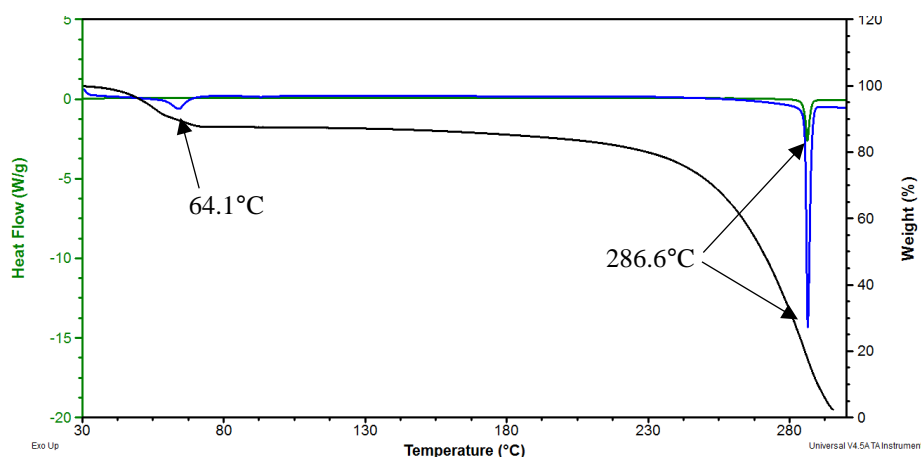
Figure 6.56: Comparison of the TGA trace of **41·MeOH** (black) and the DSC trace of **41** (blue) and **41·MeOH** (green). The mass loss on the TGA (12.3%) corresponds to the loss of one MeOH molecule (calculated loss: 14.4%)

6.5 REFERENCES

(1)   Armarego, W. L. F.; Chai, C. L. L. *Purification of Organic Chemicals*, 7th edition.; Elsevier Inc.: United Kingdom, 2013.

(2)   Lin, H.; Paquette, L. A. *Synth. Commun.* **1994**, *24* (17), 2503–2506.

(3)   *ACD Labs/NMR Processor Academic Edition*, version 12.01, Advanced Chemistry Development, Inc., 2010.

(4)   *OPUS 7.5, build: 7, 5, 18 (20140810)*, Bruker Optik GmbH, 2014.

(5)   *KnowItAll Informatics System Academic Edition*, Bio-Rad Laboratories Inc. Philadelphia, Pennylvania, USA 2018.

(6)   *X'Pert Highscore Plus, version 2.2e*, PANalytical B.V, The Netherlands, 2009.

(7)   *SAINT Data Collection Software, version V7.99A*, Bruker AXS Inc, Madison, WI, 2012.

(8)   Blessing, R. H. *Acta Crystallogr. Sect. A: Found. Crystallogr.* **1995**, *51*, 33–55.

(9)   *SADABS, version 2012/1*, Bruker AXS Inc, Madison, WI, 2012.

(10)   Sheldrick, G. M. *Acta Crystallogr. Sect. C Cryst. Struct. Commun.* **2015**, *71*, 3–8.

(11)   Atwood, J. L.; Barbour, L. J. *Cryst. Growth Des.* **2003**, *3*, 3–8.

(12)   Barbour, L. J. *J. Supramol. Chem.* **2001**, *1*, 189–191.

(13)   *POV-RayTM for Windows*, version 3.6, Persistence of Vision Raytracer Pty. Ltd: Williamstown, Australia, 2004.

(14)   Allen, F. H.; Johnson, O.; Shields, G. P.; Smith, B. R.; Towler, M. *J. Appl. Crystallogr.* **2004**, *37* (2), 335–338.

(15)   Spek, A. L. *Acta Crystallogr. Sect. D: Biol. Crystallogr.* **2009**, *65* (2), 148–155.

(16)   Bruno, I. J.; Cole, J. C.; Edgington, P. R.; Kessler, M.; Macrae, C. F.; McCabe, P.; Pearson, J.; Taylor, R. *Acta Crystallogr. Sect. B: Struct. Sci.* **2002**, *58* (3 PART 1), 389–397.

(17)   Macrae, C. F.; Bruno, I. J.; Chisholm, J. A.; Edgington, P. R.; McCabe, P.; Pidcock, E.; Rodriguez-Monge, L.; Taylor, R.; Van De Streek, J.; Wood, P. A. *J. Appl. Crystallogr.* **2008**, *41* (2), 466–470.

(18)   Macrae, C. F.; Edgington, P. R.; McCabe, P.; Pidcock, E.; Shields, G. P.; Taylor, R.; Towler, M.; Van De Streek, J. *J. Appl. Crystallogr.* **2006**, *39* (3), 453–457.

(19)   Frisch, M. J.; Trucks, G. W.; Schlegel, H. B.; Scuseria, G. E.; Robb, M. A.; Cheeseman, J. R.; Scalmani, G.; Barone, V.; Petersson, G. A.; Nakatsuji, H.; Li, X.; Caricato, M.; Marenich, A.; Bloino, J.; Janesko, B. G.; Gomperts, R.; Mennucci, B.; Hratchian, H. P.; Ortiz, J. V.; Izmaylov, A. F.; Sonnenberg, J. L.; Williams-Young, D.; Ding, F.; Lipparini, F.; Egidi, F.; Goings, J.; Peng, B.; Petrone, A.; Henderson, T.; Ranasinghe, D.; Zakrzewski, V. G.; Gao, J.; Rega, N.; Zheng, G.; Liang, W.; Hada, M.; Ehara, M.; Toyota, K.; Fukuda, R.; Hasegawa, J.; Ishida, M.; Nakajima, T.; Honda, Y.; Kitao, O.; Nakai, H.; Vreven, T.; Throssell, K.; J. A. Montgomery, J.; Peralta, J. E.; Ogliaro, F.; Bearpark, M.; Heyd, J. J.; Brothers, E.; Kudin, K. N.; Staroverov, V. N.; Keith, T.; Kobayashi, R.; Normand, J.; Raghavachari, K.; Rendell, A.; Burant, J. C.; Iyengar, S. S.; Tomasi, J.; Cossi, M.; M., J. M.; Klene, M.; Adamo, C.; Cammi, R.; Ochterski, J. W.; Martin, R. L.; Morokuma, K.; Farkas, O.; Foresman, J. B.; Fox, D. J. Gaussian, Inc: Wallingford, CT, USA 2016.

(20)   *AIMAll, version 17.11.14*, Keith, T. A. TK Gristmill Software: Overland Park KS, USA, 2017.

(21)   Blackie, M. A. L. PhD thesis: *New mono and bimetallic chloroquine derivatives: Synthesis and evaluation as antiparasitic agents*; University of Cape Town, 2002.

(22)   Jacobs, L. MSc thesis: *Synthesis and Biological Evaluation of Novel Ferroquine and Phenylequine Analogues*; Stellenbosch University, 2013.

(23)   Biot, C.; Glorian, G.; Maciejewski, L. A.; Brocard, J. S.; Domarle, O.; Blampain, G.; Millet, P.; Georges, A. J.; Lebibi, J. *J. Med. Chem.* **1997**, *40* (23), 3715–3718.

(24)   Jacobs, L.; De Kock, C.; De Villiers, K. A.; Smith, P. J.; Smith, V. J.; Van Otterlo, W. A. L.; Blackie, M. A. L. *ChemMedChem* **2015**, *10* (12), 2099–2110.

(25)   Blackie, M. A. L.; Yardley, V.; Chibale, K. *Bioorg. Med. Chem. Lett.* **2010**, *20* (3), 1078−1080.

(26)   De, D.; Krogstad, F. M.; Byers, L. D.; Krogstad, D. J. *J. Med. Chem.* **1998**, *41*, 4918–4926.

(27)   De Souza, M. V. N.; Pais, K. C.; Kaiser, C. R.; Peralta, M. A.; Ferreira, M. D. L.; Lourenço, M. C. S. *Bioorg. Med. Chem.* **2009**, *17* (4), 1474–1480.

(28)   Klemme, C. J.; Hunter, J.H.; *J. Org. Chem.* **1939**, *1*, 227–234.

(29)   Singh, T.; Sharma, S.; Srivastava, V. K.; Kumar, A. *Indian J. Chem.* **2006**, *45B*, 2558–2565.

(30)   Patel, G.; Karver, C. E.; Behera, R.; Guyett, P. J.; Sullenberger, C.; Edwards, P.; Roncal, N. E.; Mensa-Wilmot, K.; Pollastri, M. P. *J. Med. Chem.* **2013**, *56* (10), 3820–3832.

(31)   Wu, M.; Shaw, G.-S.; Jong, S.-J. *J. Organomet. Chem.* **1985**, *297*, 205–209.

(32)   Marr, G.; R.E., M.; Rockett, B. W. *J. Chem. Soc.* **1968**, *24*, 24–27.

(33)   Fernandes, C.; Oliveira, C.; Gano, L.; Bourkoula, A.; Pirmettis, I.; Santos, I. *Bioorg. Med. Chem.* **2007**, *15*, 3974–3980.

(34)   Li, F.; Frett, B.; Li, H. *Synth. Lett.* **2014**, *25* (10), 1403–1408.

Addendum A
Synthesis of quinoline derivatives as antischistosomal agents

Note to the reader:

This work was carried out in the Pollastri laboratory at Northeastern University, Boston, USA between August and October 2017. While only the work that I carried out is reported herein, additional information based on the larger project is given where necessary for completeness. This work forms part of a manuscript currently being prepared by the Pollastri group.

A.1 INTRODUCTION

Neglected tropical diseases (NTDs) are classified as a group of seventeen communicable diseases that affect the lives of over 1 billion people globally that live in tropical and subtropical regions, but have received little attention from pharmaceutical companies in terms of drug discovery, simply because of a lack of financial interest.[1] The Pollastri research group focusses on three of these diseases, namely American trypanosomiasis (chagas disease), human African trypanosomiasis (African sleeping sickness) and leishmaniasis (black fever).[2–4] As these diseases are all caused by protozoan parasites, many of the compounds that are screened against NTDs are potent against more than one parasite. While not technically classified as a NTD by the World Health Organisation, malaria is still one of the deadliest infectious protozoan diseases.[5,6] Therefore, compounds used to treat NTDs are also tested against the chloroquine-susceptible and chloroquine-resistant strains of *P. falciparum*.[7] More recently, the Pollastri group has included a fourth NTD, schistosomiasis (bilharzia), to their list of disease targets. While schistosomiasis is caused by trematodes (blood flukes or worms) and not protozoa, there are similar features in their life cycles and potential drug targets. For example, as for protozoa of the *Plasmodium* genus, the detoxification of heme through hemozoin formation occurs in tremadoes of the *Schistosoma* genus too.

With over 200 million people infected worldwide in 2016, the World Health Organisation considers schistosomiasis to be a major public health concern.[8] There are three main species of *Schistosoma* that infect humans, namely *S. japonicum*, *S. haematobium* and *S. mansoni*, of which *S. mansoni* is most prevalent. Similarly to malaria, the parasite requires a human as well as animal host to complete its life cycle (Figure A.1). Schistosome eggs hatch in water and the larvae (miracidia) penetrate freshwater snails (animal host) where, after several weeks of growth, cercariae are released from the snail into the surrounding water. These cercariae are then able to penetrate human skin and subsequently move to the liver where they mature into adult worms. After maturation, the worms move through the

bloodstream to either the abdominal cavity or urinary tract where they reproduce. Some of the eggs that are produced escape through the bladder or bowel, while the others are trapped in the tissue of the host. The eggs that are released from the human host are then once again able to infect freshwater snails and the cycle repeats.[9,10]
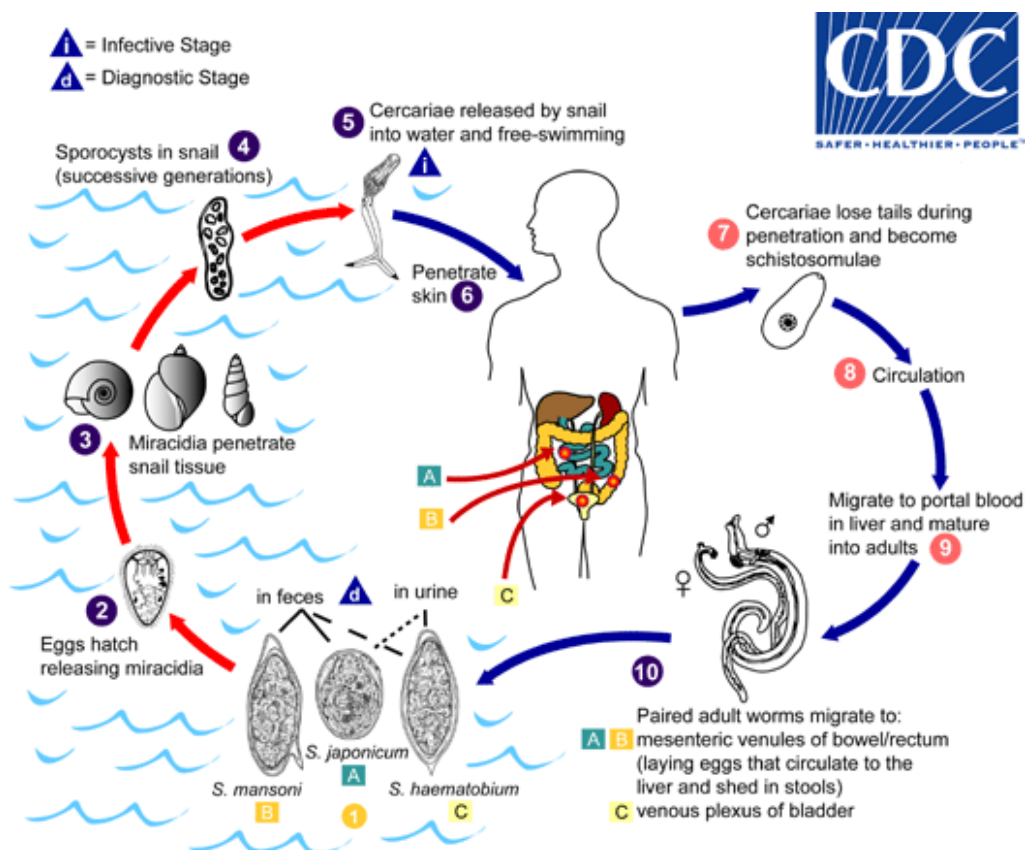

Figure A.1: Life cycle of *Schistosoma* worms. Image taken from the Centre for Disease Control (CDC) website.[10]

Remarkably, we have relied on just one drug as treatment for this disease – praziquantel (Figure A.2).[8] After its discovery in the early 1970s, Bayer marketed the drug as Biltricide; however, at a cost beyond the affordability of developing nations. Soon after, Shin Poong (a South Korean pharmaceutical company) patented a new synthetic procedure for praziquantel and the cost was reduced dramatically to the point where mass production was feasible for the treatment of the disease.[11] Since then, little attention has been paid to finding alternative treatment options. While clinically-relevant resistance has not yet emerged, the recent increased usage of the drug could change this.[9] There is therefore a genuine concern regarding the absence of an alternative treatment option, should praziquantel no longer be effective. This warrants the search for novel agents to target this disease.
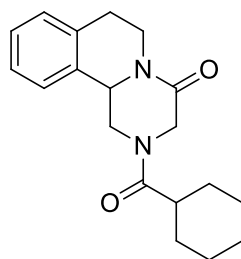
Figure A.2: Structure of praziquantel.

S. mansoni, in its adult stage, is known to digest human host blood to obtain the required nutrients needed for growth and sexual development.[12] In order to do this, *S. mansoni* degrades host hemeoglobin, similarly to *P. falciparum*, and in the process forms heme – a toxic by-product. The biocrystallisation of heme to hemeozoin has evolved as a method of detoxification and evidence of these hemeozoin crystals has been observed within the gut of the adult female worms.[13,14] Initial tests with chloroquine and other quinoline-based antimalarial agents have shown inhibition of hemeozoin formation in mice livers,[15] which indicates a potential drug target in *S. mansoni* similar to that of *P. falciparum*. However, it has been reported that for some of these antimalarial agents, the excellent efficacy did not in fact correlate well with their hemeozoin inhibition potencies.[12] This suggests that there is possibly an alternative mechanism by which these drugs inhibit hemeozoin formation that is not adequately modelled by the assay, or even that there is an additional target. A number of repurposed compounds have been explored for the treatment of schistosomiasis and some are showing promise.[16–18] These include natural products, such as artemisinin, plumbagin and sanguinarine, and metal-based compounds, such as ferroquine and ferrocene derivatives of praziquantel (Figure A.3).

(a)   (b)   (c)

(d)   (e)
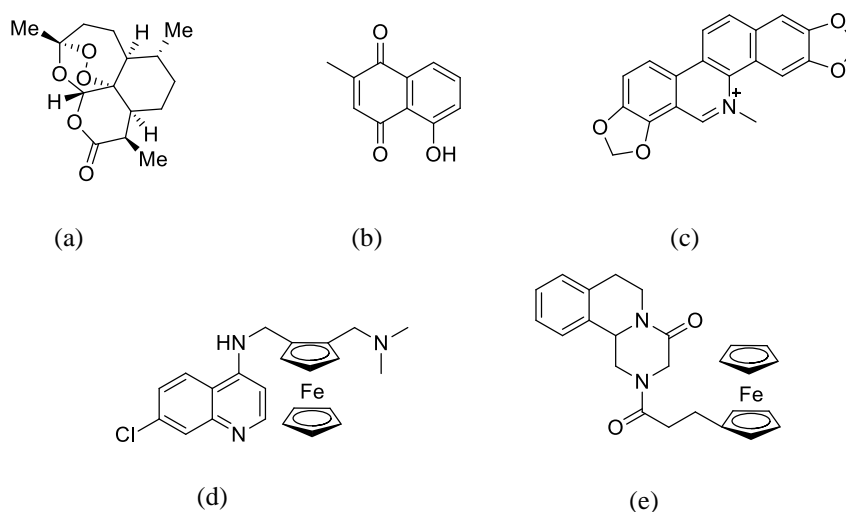
Figure A.3: Structure of (a) artemisinin, (b) plumbagin, (c) sanguinarine, (d) ferroquine, (e) ferrocene derivative of praziquantel.

Addendum A: Synthesis of quinoline derivatives as antischistosomal agents

As part of the target class repurposing strategy discussed in Chapter 3, the Pollastri group have synthesised a large number of compounds mainly targeting trypanosomes; however, all compounds that they synthesise are tested against the other four parasitic diseases mentioned above. For example, one project found that a quinoline analogue, shown in Figure A.4 (**NEU1953**), exhibited reasonable potency in preliminary screens against adult *S. mansoni* worms. Additionally, introducing a methyl substituent onto the 8-position of the quinoline ring further increased the potency against *S. mansoni* (currently unpublished results).

One of the drawbacks, however, was the poor aqueous solubility of these compounds (especially **NEU1953**).[7] For a drug to be orally administered, a reasonable solubility is required for acceptable bioavailability. For NTDs especially, any other route of delivery of the drug is simply not viable in terms of cost and access to treatment centres. Previous work on similar compounds has shown that the incorporation of a homopiperazine (1,4-diazacycloheptane) moiety, instead of a piperizine or other cyclic amine group substantially improved the solubility of the compound without a significant loss in efficacy against trypanosomes.[19] In addition, preliminary unpublished work using similar analogues has shown that increasing the length of the side chain attached to the amino tail group leads to an increase in efficacy toward the adult worms.
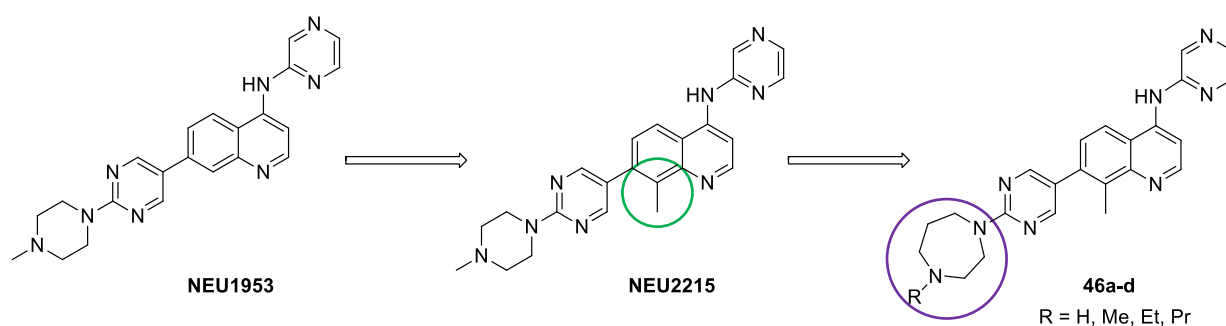

Figure A.4: The incorporation of a methyl substituent at the 8-position on the quinoline scaffold (**NEU2215**) increases potency against *S. mansoni*. This work investigates incorporating a homopiperazine derivative instead of the piperazine derivative (this work: **46a-d**) to potentially improve solubility. H (**46a**), Me = methyl (**46b**), Et = ethyl (**46c**) and Pr = propyl (**46d**) chain.

Therefore, the goal of this work was to resynthesise **NEU2215** to confirm the phenotypic observation, as well as to synthesise compounds **46a-d** (Figure A.4) to explore the effect of the homopiperazine and alkyl chain lengths on the Adsorption, Distribution, Metabolism and Excretion (ADME) profile and potency against *S. mansoni*. These compounds will also be compared to other analogues synthesised by the Pollastri group to investigate the structure-activity relationships of these compounds.

A.2 SYNTHESIS OF THE PRECURSOR FRAGMENTS

The synthesis of these compounds is briefly discussed here; however, full experimental details and characterisation data can be found in Section A.6 (page 186). Similarly to the synthesis discussed in Chapter 3, the synthesis of these compounds can be divided into three parts – synthesis of the quinoline scaffold, synthesis of the tail group and finally the Suzuki-Miyaura reaction to couple the two fragments.

A.2.1 Synthesis of the quinoline scaffold

As shown in Scheme A.1, the synthesis begun with a condensation-type reaction where commercially available 2-methyl-3-bromo-aniline (**47**) was reacted with diethyl-2-(ethoxymethylene)malonate (**48**) to form compound **49**. This reaction had been previously performed by another member of the Pollastri group and product **49** was received from them (roughly 5 g) when I arrived. Cyclisation of **49** to form quinolone **50** was carried out by refluxing **49** in diphenyl ether (DPE) for 4 hours. Monitoring the reaction with LC-MS analysis showed that the reaction was complete after 4 hours and that the desired product had formed. In addition, by-products were also observed, one of which was the decarboxylated quinolone **52**. As this was the product of a subsequent reaction, we decided not to separate out the products at this stage, but rather to work with the crude mixture for the following steps. This was also because the solubility of these compounds is rather poor and this made column chromatography challenging. The crude mixture of **50** was saponified, followed by decarboxylation to give **52**, which, after chlorination using phosphorous oxychloride (POCl$_3$) yielded quinoline scaffold **53** in a yield of 35% over four steps.
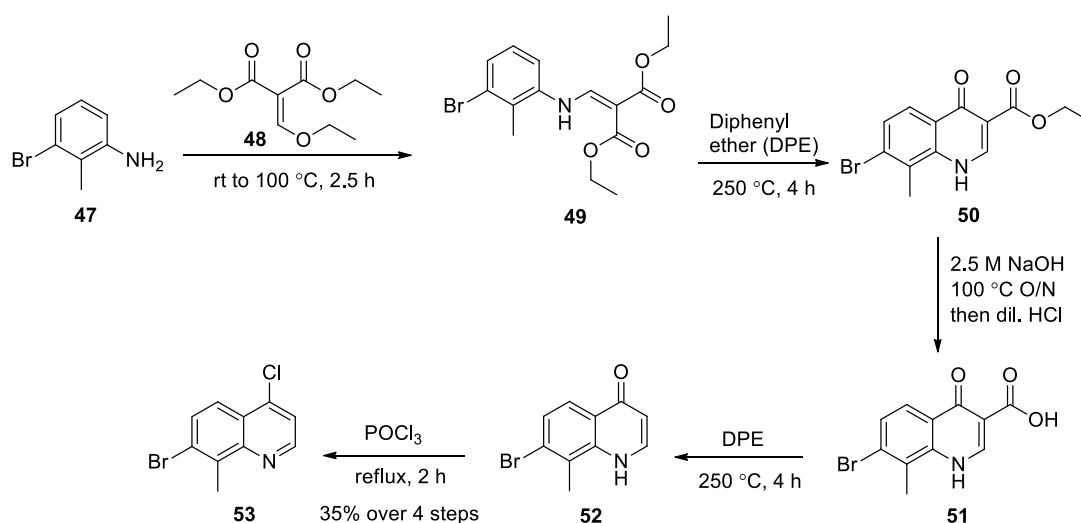

Scheme A.1: Synthesis of the core quinoline scaffold **53** starting from commercially available aniline **47**.
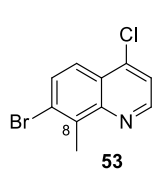
¹H NMR spectroscopic analysis of **53** showed a singlet, integrating to 3H, at 2.94 ppm that corresponds to the methyl group at the 8-position. Four peaks are observed in the aromatic region, each integrating for 1H, which correspond to the remaining protons on the molecule. LC-MS found an [M+H]⁺ of 258.0 *m/z*, which corresponds well with the calculated [M+H]⁺ of 257.9 *m/z*.

Once the quinoline scaffold had been synthesised, the head group could be introduced to the 4-position on the quinoline ring in a similar substitution reaction to that in Chapter 3 (page 74). The regioselectivity of the substitution to the 4-position and not the 7-position (i.e. at the chlorine and not the bromine) is due to the presence of the heteroatom in the quinoline ring, as explained in a similar example in Chapter 3 on page 74. This reaction was carried out as shown in Scheme A.2 and the bright yellow product was obtained in a moderate 61% yield.
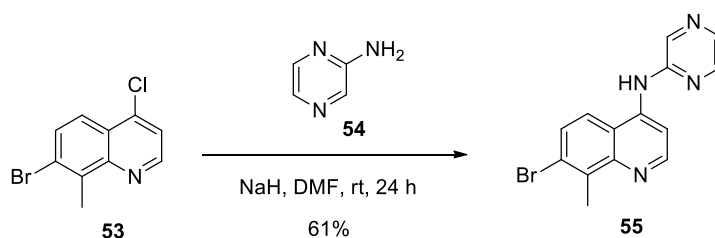
Scheme A.2: Substitution reaction to introduce 2-aminopyrazine (**54**) onto quinoline scaffold **53**.
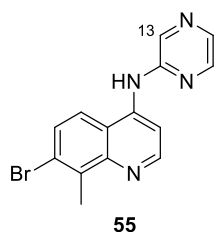
Characterisation of **55** was carried out using NMR and LC-MS. Analysis of the ¹H NMR spectrum showed a singlet integrating to 3H at 2.82 ppm that corresponds to the methyl group at the 8-position of the quinoline ring. The singlet at 9.79 ppm, integrating for 1H, corresponds to the protons at position 13 (on the pyrazine ring). The remaining aromatic protons were all accounted for. Analysis of the LC-MS chromatogram showed one peak, with a corresponding *m/z* value of 317.1 [M+2H]²⁺; the calculated [M+2H]²⁺ is 317.1 *m/z*.

With the quinoline scaffold in hand, we moved on to the synthesis of the various tail fragments.

A.2.2 Synthesis of the tail fragments

The methyl derivatives of the tail fragments (**56** and **57**) could be synthesised using commercially available starting material in a one-step reaction under microwave conditions (Scheme A.3). 5-Bromo-2-chloro-pyrimidine (**58**) and either *N*-methylpiperidine (**59**) or *N*-methylhomopiperidine (**60**) were heated to 150 °C while stirring together with diisopropylethylamine (DIPEA) in *tert*-butanol. LC-MS analysis confirmed that the reaction had gone to completion within 30 minutes. Purification was

carried out using flash column chromatography (using a 1 – 10% MeOH/DCM gradient solvent system) and compounds were characterised by ^{1}H NMR and LC-MS.
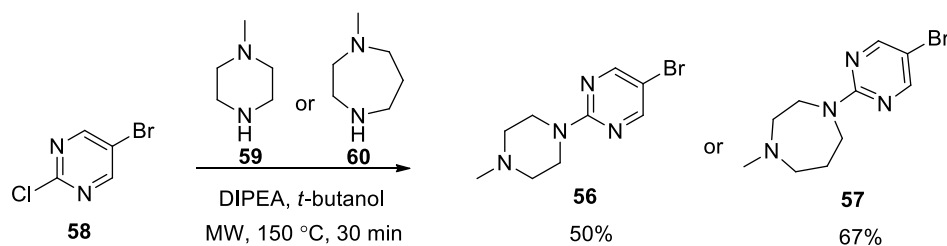
Scheme A.3: Synthesis of tail compounds **56** and **57**.
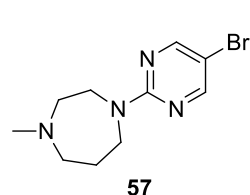
^{1}H NMR spectral analysis of **57** shows a singlet integrating to 3H at 2.53 ppm that corresponds to the methyl protons on the homopiperazine moiety, as well as a singlet integrating to 2H at 8.45 ppm that corresponds to the two aromatic protons on the pyrimidine ring. All other protons are accounted for. LC-MS analysis of the product shows the desired mass peak ($[M+H]^+ = 351.1$ *m/z*). Similar spectroscopic data was obtained for **56**.

For the ethyl and propyl derivatives of **57**, an additional two steps were required in the synthetic route (Scheme A.4). Making use of a commercially available boc-protected homopiperidine **61**, the coupling reaction could be performed, followed by deprotection with 4 M HCl in dioxane to afford **63** in good yields. This product could then be reacted with the relevant alkyl iodides to give the tail fragments **64** and **65**, as shown in Table A.1.
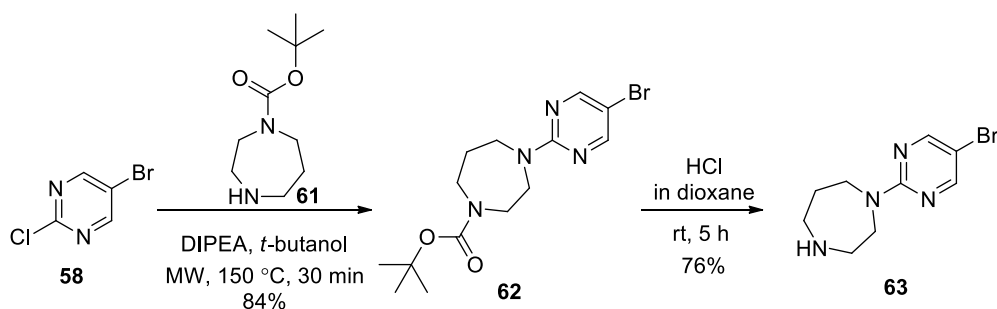
Scheme A.4: Synthesis of **62** that could then be further derivatised to give the desired ethyl and propyl analogues.

Table A.1: Yields obtained for the synthesis of **64** and **65**.

	Alkyl	R group	Yield (%)
64	Ethyl iodide		76%
65	Propyl iodide		79%
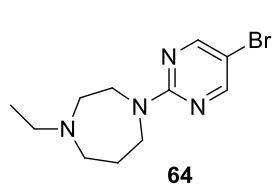
For compound **64**, ^{1}H NMR spectral analysis shows a triplet integrating to 3H at 1.07 ppm and a quartet at 2.56 ppm, which confirms the incorporation of the ethyl chain. The singlet at 8.28 ppm integrating to 2H confirms the presence of the pyrimidine protons. All other protons are accounted for. LC-MS confirms the desired product: $[M+H]^+$ = 285.2 *m/z* (calculated $[M+H]^+$: 285.1 *m/z*).

With both the quinoline scaffold and the desired tail fragments in hand, the next step was to perform the Suzuki-Miyaura reaction to couple them together.

A.3 THE SUZUKI-MIYAURA REACTION

The Suzuki-Miyaura reaction was carried out under microwave conditions in a similar two-step, one-pot procedure as described in Chapter 3 (page 82). The reaction began with the borylation of the tail fragment using bis(pinacolato)diboron in anhydrous dioxane under microwave reaction conditions (Scheme A.5). This product was used directly in the next step without purification to afford **46a-d** in low yields.
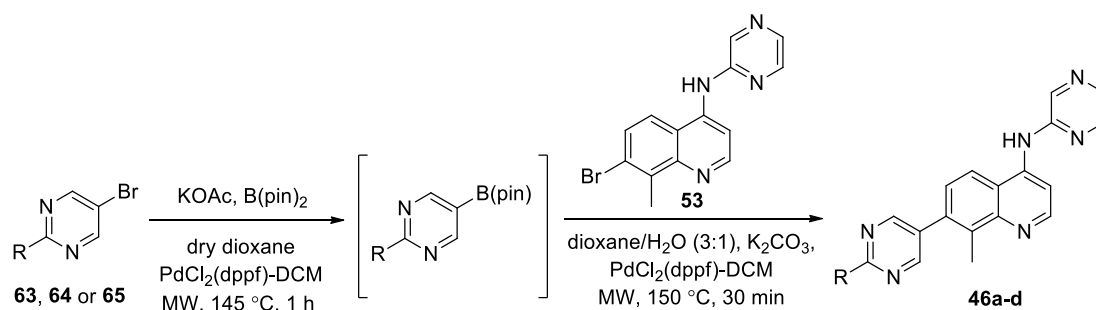
Scheme A.5: Suzuki-Miyaura reaction to couple fragments **63-65** and **53** together to form **46a-d**.

Table A.2 shows the synthesised compounds **46a-d** as well as the yields obtained for each product. While improving the yield would be imperative if these compounds were to move on to *in vivo* testing, it was not deemed necessary at this point to optimise the reaction until initial *in vitro* testing showed promising results. Unfortunately, compound **46c** was not isolated in sufficient quantities for characterisation or biological testing. As this was a short research visit, time constraints did not allow for the compound to be resynthesised. This would be done by another member of the group at a later stage. Compounds **46a-d** were fully characterised using NMR, LC-MS and IR spectroscopy, with the exception of **46c**.

Table A.2: Yields obtained for the synthesis of **NEU2215** and **46a-d.**

	R group	Yield (%)
NEU2215		31
46a		19
46b		26
46c		Trace*
46d		15

* Product lost during workup; insufficient time during research visit
to synthesise more.

In **46b**, ^{1}H NMR spectral analysis showed two singlets integrating to 3H each at 2.81 ppm and 2.71 ppm that correspond to the two methyl groups on the molecule (corresponding to the protons attached to carbon 18 and 29). The singlet at 8.48 ppm integrating to 2H corresponds to the protons at positions 20 and 21. All other protons are accounted for. ^{13}C NMR spectroscopy showed two methyl carbons at 46.6 ppm and 16.2 ppm corresponding to C-29 and C-18, respectively. All other carbon atoms were accounted for. LC-MS found [M+H]$^+$ to be 427.3 which compares well to the calculated *m/z* value for [M+H]$^+$ of 427.5. Similar spectroscopic data was obtained for **46a** and **46d** with differences in the spectrum for the peaks associated with the protons of the alkyl chain.

Having confirmed that the desired products were obtained in high purity (>95% based on LC-MS), samples were sent to collaborators for biological testing, as well as to determine certain physicochemical properties.

A.4 *IN VITRO* TESTING

NEU2215 as well as **46a, 46b** and **46d** were sent to collaborators at the University of California, Los Angeles, for testing against adult worms of *S. mansoni*. In their assays, adult worms are subjected to 10 µM of the drug (made up in a DMSO solution) and a combination of manual and semi-automated methods are used to record the phenotypic response of the worms after 1 hour, 5 hours, 24 hours and 48 hours. Descriptors are used at each time interval to evaluate the observed worms, and based on these, a severity score between 0 and 4 (with 0 corresponding to no effect, and 4 being very potent) is assigned.[20] Some of these descriptors include changes in movement, shape, ability of the worm to adhere to the culture dish surface, as well as tegument ("skin" of worm) damage and death. The higher the score and the earlier phenotypic observations are made, the more effective the drug. It should be noted that the assay used forms part of a high throughput screening, where the compounds are screened for activity without an assigned EC_{50} value. Should compounds display adequate severity scores, further *in vitro* tests can be carried out to more accurately determine their efficacy profiles. The severity scores for each compound in this work can be seen in Table A.3.

NEU2215 was potent against *S. mansoni*, with a severity score of 4 after 48 hours. Compound **46b** was inactive against the trematodes, but compound **46d** – with the longer alkyl side chain – showed improved potency, with a severity score of 4 after 24 hours. Surprisingly, compound **46a** displayed the highest potency in this series, with a severity score of 3 after just 5 hours and a score of 4 after 24 hours. Although increasing the length of the side chain was expected to increase the efficacy (based on previous unpublished work), these results seem to contradict this hypothesis.

Because these compounds are quinoline-based they would most likely exhibit some efficacy against the malaria parasite. Therefore, these compounds were also sent for testing against the chloroquine-sensitive D6 strain of *P. falciparum*. In Table A.3, the EC_{50} value (the half maximal effective concentration) for each compound is given. While the values are all in the low micromolar range ($EC_{50} = 0.069 – 0.374$ µM), they were still at least an order of magnitude larger than the benchmark standard, chloroquine ($EC_{50} = 0.005$ µM).

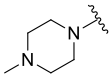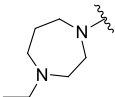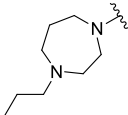**Table A.3**. *In vitro* biological data for **NEU2215** and **1a-d**.

Code	R group	*S. mansoni* severity score*				*P. falciparum* D6 strain EC$_{50}$ (μM)
		1 h	**5 h**	**24 h**	**48 h**	
NEU2215		0	1	3	4	0.069
46a		0	3	4	4	0.299
46b		0	0	0	0	0.312
46c		N/D				N/D
46d		1	1	4	4	0.374
chloroquine		-				0.005

*Assays were performed in duplicate. Each phenotypic descriptor observed was given a score of 1 and the scores were added to a maximum of 4. Descriptors: no effect = 0; worms darken = 1; male suction impaired = 1; overactive = 1; rounded = 1; slow = 1; uncoordinated = 1; degenerating = 4; tegument damage = 4; dead = 4.

The compounds were also sent to AstraZeneca to determine their ADME profile, with specific focus on aqueous solubility and metabolic stability. As can be seen in Table A.4, the aqueous solubility for the homopiperazine analogues (**46a**, **b**, **d**) all show substantial improvement over **NEU2215**. An in-house target threshold of 100 μM is considered adequate, while a value higher than 100 μM is preferred. Compound **46b** showed roughly a 2-fold increase in solubility in comparison to **46a** and **46d**. The human protein-plasma binding (PPB) percentage of drug was also determined. This value is reported as the percentage of bound drug and should be as low as possible (desired range <95%) as only unbound drug molecules are active against the parasite. Overall, the homopiperazine analogues showed improved values in comparison to **NEU2215**, with **46a** showing the lowest binding value (76%). Metabolic stability – intrinsic clearance from both human liver microsomes (HLM) and rat hepatocytes was also established. Metabolic stability refers to the susceptibility of a compound to react or degrade *in vivo* and provides an indication of the stability, elimination rate by metabolism as well as toxicity of the compound. The studies are carried out on both human and rat cell lines in order to

ensure that there is no significant difference between the two that could give misleading *in vivo* results when the compound advances to rat studies. In this study, once again, **46a** outperformed **NEU2215** and the other homopiperazine analogues.

Table A.4: ADME data obtained for **NEU2215** and **46a-d**.

Code	R group	Aqueous solubility (µM)	Human PPB (%)	HLM Cl$_{int}$ (µL/min/mg)	Rat hepatocyte Cl$_{int}$ (µL/min/10^6 cells)
Desired range[7]		>100	<95	<90	<50
NEU2215		5	97	115	51.8
46a		465.1	76	41.1	5.31
46b		861.9	82	121	27.3
46c		N/D	N/D	N/D	N/D
46d		445.7	94.4	300	35.7

Compound **46a** displayed particularly favourable results against *S. mansoni*, with excellent severity scores after 5 hours. In addition, **46a** had physicochemical properties that surpassed the benchmark minimums of appropriate ADME profiles (profile aqueous solubility and metabolic stability). Although **46d** displayed excellent severity scores against *S. mansoni*, this inhibition was only achieved after 24 hours as compared to 5 hours for **46a**. The ADME profile of **46d** (aqueous solubility and metabolic stability) was however not as good as that of **46a**.

The compounds performed reasonably well against the chloroquine-sensitive strain (D6) of *P. falciparum*, with values in the low micromolar range. Compound **46a** displayed the best EC$_{50}$ value of the three compounds sent for testing, but was still two orders of magnitude less effective than chloroquine.

A.5 CONCLUDING REMARKS

This chapter describes the synthesis and biological data of a small library of quinoline-based compounds. The synthesis was carried out in three stages – firstly synthesis of the quinoline scaffold from commercially available 5-bromo-2-chloro-pyrimidine, secondly the synthesis of various amine tail groups and lastly the Suzuki-Miyaura coupling reaction to combine the two fragments. While these reactions were successful, the yields of the final compounds are poor. Having said that, there was sufficient material available to test these compounds against *S. manoni*, as well as obtain physicochemical data that describe the ADME profile of the compounds, excluding **46c**. Some of the compounds were also sent for testing against *P. falciparum*.

The replacement of the piperazine moiety with a homopiperazine proved to be valuable, with a substantial improvement to the ADME properties in comparison to NEU2215. Interestingly, the hypothesis of a longer alkyl chain that improves efficacy against adult worms was not validated with these compounds, as **46a** (with no alkyl chain) displayed the greatest severity score. Compound **46a** warrants further investigation as it displayed the greatest *in vitro* activity against *S. mansoni* as well as excellent ADME properties.

Since leaving their laboratory, other derivatives have been synthesised by members of the Pollastri group. These include the *NH*-piperidine analogue of **46a** (Figure A.5(a)), as well the morpholinyl derivative (Figure A.5b). The morpholinyl derivative, however, was found to be inactive in comparison to **46a**. This indicates that the basic nitrogen atom of the piperidine or homopiperidine moiety is important in the potency of these compounds. This could hint at a pH-trapping mechanism similar to that of β-hematin inhibitors for *P. falciparum* as part of the mode of action of these compounds against *S. mansoni*,[21] but this would require further studies before any conclusive statement can be made. They have also explored the effect of moving the methyl group from the 8-position on the quinoline to the 5- and 6-positions (Figure A.5c). While the head group has been optimised for appropriate ADME profiles,[22] exploring small substituents on the pyrazine ring could be carried out to increase potency (Figure A.5d). Lastly, replacing the quinoline scaffold with an isoquinoline or a quinazoline ring could also be valuable to enrich the structure-activity relationship study of these compounds against *S. mansoni* (Figure A.5e).
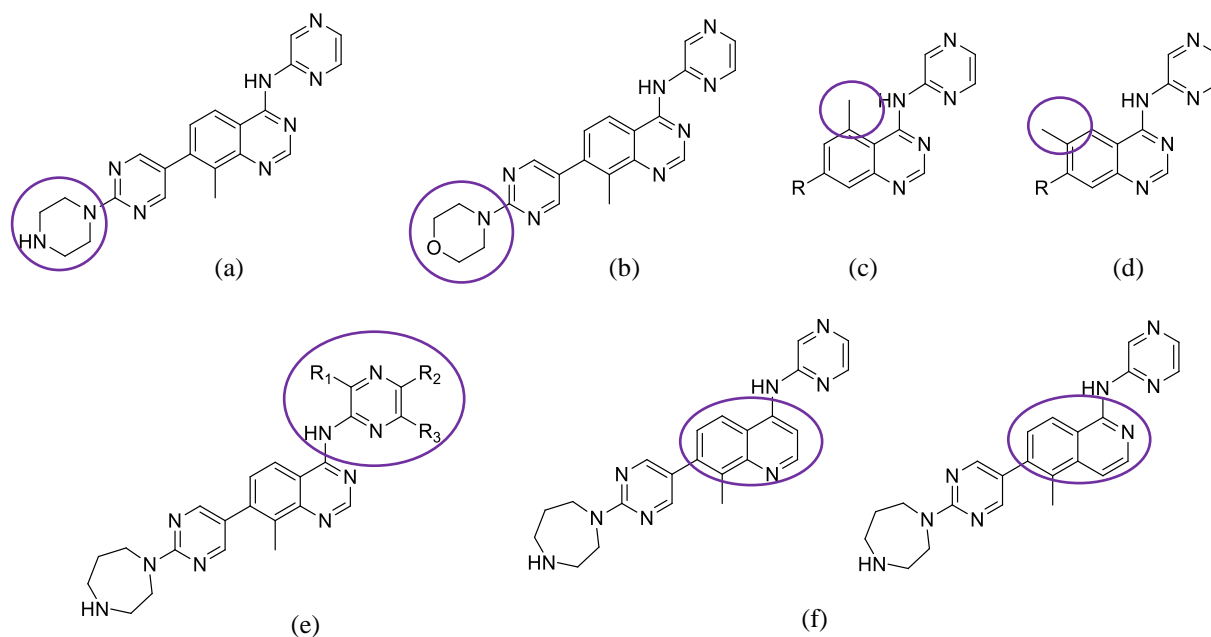
Figure A.5: Derivatives of **46b** that have been synthesised by the Pollastri group based on the work in this chapter: (a) *NH*-piperazine analogue; (b) morpholinyl derivative; (c) 5-and 6-position methyl substituent analogues; (d) various substitutions on the pyrazine ring; (e) quinoline and isoquinoline analogues.

Since some quinoline-containing antimalarials have been shown to be potent against *S. mansoni* and they have been shown to inhibit the formation of β-hematin, it is possible that compounds **46a-d** could be targeting the biocrystallisation of hemeozoin pathway at least as part of its mode of action.[15] Other studies on quinazolines, isoquinolines and benzamide derivatives amongst others, have shown that protein kinases have potential as targets for schistosomal drug development.[9] Our compounds, originally stemming from lapatinib (a kinase inhibitor), could also be targeting certain protein kinases in *S. mansoni*.[9] However, since the assays used in this study to determine potency are purely phenotypic, we cannot say for certain what the mode of action is of these drug molecules without carrying out extensive mechanistic studies.

A.6 EXPERIMENTAL DETAILS

A.6.1 General

All starting materials were commercially obtained and were used without further purification, unless otherwise specified. Reaction solvents were purified by passage through alumina columns on an Innovative Technology (Newburyport, MA) purification system. NMR spectra were obtained on Varian NMR systems (500 MHz) and processed with ACDLabs software. LC-MS analysis was performed using a Waters Alliance reverse phase HPLC (columns Waters SunFire C18 4.6 × 50 mm) with single-wavelength UV−visible detector and Waters Micromass ZQ detector (electrospray

ionisation). Final compounds were purified by preparative reverse phase HPLC (columns Waters Symmetry RP8 30 × 50 mm, 5 μm column), with a single wavelength UV−visible detector and Waters Micromass ZQ (electrospray ionization) and have purities greater than 95% based upon LC-MS analysis.

A6.2 ADME experiment protocols (carried out by AstraZeneca)

Aqueous pH 7.4 Solubility. Compounds are dried down from 10 mM DMSO solutions using centrifugal evaporation technique. Phosphate buffer (0.1 M pH 7.4) added and StirStix inserted in the glass vials, shaking is then performed at a constant temperature of 25 °C for 20–24 h. This step is followed by double centrifugation with a tip wash in between, to ensure that no residues of the dried compound are interfering. The solutions are diluted before analysis and quantification using LC-MS-MS is performed.

Log $D_{7.4}$. Shake-flask octanol-water distribution coefficient at pH 7.4 (Log $D_{7.4}$). The aqueous solution used is 10 mM sodium phosphate pH 7.4 buffer. The method has been validated for Log $D_{7.4}$ ranging from -2 to 5.0.

Human Plasma Protein Binding (PPB). PPB is determined using equilibrium dialysis (RED device) to separate free from bound compound. The amount of compound in plasma (10 μM initial concentration) and in dialysis buffer (pH 7.4 phosphate buffer) is measured by LC-MS-MS after equilibration at 37°C in a dialysis chamber. The fraction unbound (fu) is reported.

Human Liver Microsomal Cl_{int}. In vitro intrinsic clearance determined from human liver microsomes using a standard approach.[6] Following incubation and preparation, the samples are analysed using LC-MS-MS. Refined data are uploaded to IBIS and are displayed as Cl_{int} (intrinsic clearance) in μL/min/mg.

Rat Hepatocyte Cl_{int}. In vitro intrinsic clearance determined from rat hepatocytes using a standard approach. Following incubation and preparation, the samples are analysed using LC/MS/MS. Refined data are uploaded to IBIS and are displayed as Cl_{int} (intrinsic clearance) μL/min/1 million cells.

A6.3 Synthesis of compounds

Ethyl-7-bromo-8-methyl-4-oxo-1,4-dihydroquinoline-3-carboxylate (50)

50
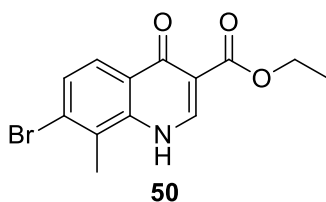
Diethyl-2-{[(3-bromo-2-methylphenyl)amino]methylene}malonate **49** (2.02 g, 5.61 mmol) was added to a 25 mL round-bottomed flask containing diphenyl ether (9.0 mL). The flask was fitted with a condenser and the reaction mixture stirred at 250 °C for 8 hours. The orange-brown solution was then cooled to room temperature, upon which a pale brown precipitate formed. The mixture was quantitatively transferred to a 100 mL beaker containing hexane (20 mL). The precipitate was triturated with hexane (4 × 25 mL) and then filtered and washed with a further hexane (2 × 20 mL). The precipitate was dried in air on a Buchner funnel for 10 minutes before drying *in vacuo* for a further 2 hours to yield a beige solid (1.32 g) that was used directly in the next step without further purification.
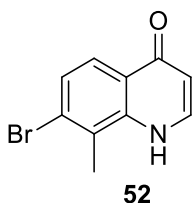
TLC (50% EtOAc/Hexane): R_f = 0.48. **LC-MS** found [M+H]$^+$= 311.1 *m/z*; calculated [M+H]$^+$ = 311.2 *m/z* for $C_{13}H_{12}BrNO_3$.

7-Bromo-8-methyl-4-oxo-1,4-dihydroquinoline-3-carboxylic acid (51)


51
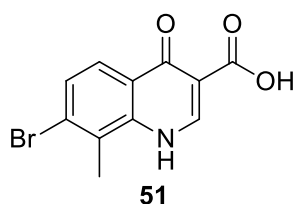
Ethyl-7-bromo-8-methyl-4-oxo-1,4-dihydroquinoline-3-carboxylate (**50**) (1.32 g, 4.26 mmol) was added to a 50 mL round-bottomed flask containing a solution of sodium hydroxide (1.02 g, 25.5 mmol, 6.00 equivalents) in distilled water (12.0 mL). The heterogenous reaction mixture was heated to 110 °C and stirred overnight. Upon completion, the reaction mixture was cooled and then poured into of 1.0 M HCl (15 mL). An additional of 1.0 M HCl (15 mL) was added until a pH of 3 − 4 was obtained. The precipitate was filtered using a Buchner funnel and washed with distilled water (3 × 30 mL). The dried product (1.25 g) was used without further purification in the next step.

LC-MS found [M+H]$^+$ = 283.3 *m/z*; calculated [M+H]$^+$ = 283.1 *m/z* for $C_{11}H_8BrNO_3$.

Addendum A: Synthesis of quinoline derivatives as antischistosomal agents

---

7-Bromo-8-methylquinolin-4(1*H*)-one (52)

52

To a 50 mL round-bottomed flask was added 7-bromo-8-methyl-4-oxo-1,4-dihydroquinoline-3-carboxylic acid (**51**) (1.25 g, 4.44 mmol) and diphenyl ether (22.0 mL). The heterogenous reaction mixture was stirred overnight at 250 °C. Once the reaction was complete (LC-MS; TLC), the solution was cooled to room temperature and quantitatively transferred to a 250 mL beaker containing hexane (60 mL). The precipitate was triturated with hexane (3 × 30 mL). The precipitate was filtered using a Buchner funnel and washed with a further hexane (3 × 25 mL) and allowed to air dry (Buchner vacuum filtration) for 15 minutes before being dried *in vacuo* overnight. The beige solid (0.963 g) was used in the next step without further purification.

TLC (10% MeOH/EtOAc): R_f = 0.62. **LC-MS** found $[M+H]^+$ = 239.01 *m/z*; calculated $[M+H]^+$ = 239.01 *m/z* for $C_{10}H_8BrNO$.

7-Bromo-4-chloro-8-methylquinoline (53)

53
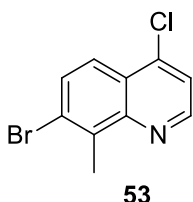
To a nitrogen-purged three-neck flask fitted with a reflux condenser was added 7-bromo-8-methylquinolin-4(1*H*)-one (**52**) (0.963 g, 4.05 mmol) and phosphorous oxychloride (7.0 mL, 81 mmol, 20 equivalents). The reaction was heated under reflux at 110 °C for 6 hours, during which the reaction mixture turned a dark brown colour. Upon reaction completion (LC-MS, TLC analysis), the reaction mixture was cooled to room temperature. Excess phosphorous oxychloride was quenched by the slow addition of the reaction mixture to a saturated solution of sodium bicarbonate (200 mL) on ice. The pH was adjusted by adding more sodium bicarbonate solution (approximately 250 mL) until a pH of 7 – 8 was obtained. The yellow solution was decanted into a separatory funnel and the product extracted with DCM (5 × 50 mL). The organic layers were combined, washed once with brine (50 mL), dried over anhydrous $MgSO_4$, filtered and the filtrate concentrated under reduced pressure. The product was purified by flash column chromatography, eluting with a 0 – 15% EtOAc/Hexane solution. The

desired product was obtained as an off-white powder in 35% (0.702 g, 2.74 mmol) yield over four steps.

TLC (10% EtOAc/Hexane): R_f = 0.71. **¹H NMR (500 MHz, CDCl₃) δ** 8.80 (d, *J* = 4.6 Hz, 1H), 7.97 (d, *J* = 9.3 Hz, 1H), 7.79 – 7.76 (m, 1H), 7.51 (d, *J* = 4.6 Hz, 1H), 2.94 (s, 3H). **LC-MS** found [M+H]⁺ = 257.9 *m/z*; calculated [M+H]⁺ = 257.9 *m/z* for $C_{10}H_7BrNCl$.

7-Bromo-8-methyl-*N*-(pyrazine-2-yl)quinoline-4-amine (55)
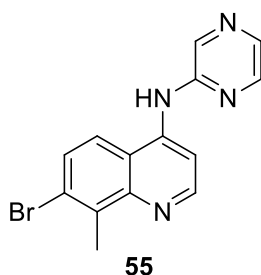
Anhydrous DMF (7.0 mL) was added to a 25 mL two-neck round-bottomed flask that had been purged with nitrogen. Commercially available 2-aminopyrazine (0.651 g, 6.86 mmol, 2.50 equivalents) was added to the flask, followed by sodium hydride (0.383 g, 60% dispersion in oil, 9.58 mmol, 3.50 equivalents). This bright yellow reaction mixture was stirred at room temperature for 30 minutes before adding a solution of 7-bromo-4-chloro-8-methylquinoline (**53**) (0.702 g, 2.74 mmol, 1.00 equivalent) in anhydrous DMF (6.0 mL) dropwise over three minutes. The reaction mixture was stirred at room temperature overnight before being quenched with a saturated solution of ammonium chloride (100 mL). The bright yellow precipitate was collected using a Buchner funnel and washed with distilled water (3 × 20 mL). The precipitate was dried in air for 15 minutes before being purified by flash column chromatography, eluting with a 1 – 10% MeOH/DCM mixture. The desired product was obtained as a bright yellow powder in 61% yield (0.529 g, 1.68 mmol).

TLC (10% MeOH/DCM): R_f = 0.52. **¹H NMR (500 MHz, DMSO-d₆) δ** 9.79 (s, 1H), 8.74 (d, *J* = 5.4 Hz, 1H), 8.69 (s, 1H), 8.35 (d, *J* = 5.4 Hz, 1H), 8.30 – 8.31 (m, 1H), 8.27 (d, *J* = 8.8 Hz, 1H), 8.17 (d, *J* = 2.8 Hz, 1H), 7.78 (d, *J* = 9.3 Hz, 1H), 2.82 (s, 3H). **LC-MS** found [M+H]⁺ = 316.08 *m/z*; calculated [M+H]⁺ = 316.02 *m/z* for $C_{14}H_{11}BrN_4$.

General procedure for the synthesis of the amine tail groups:

The relevant amine (1.55 mmol, 1.20 equivalents) and diisopropylethylamine (DIPEA) (1.68 mmol, 1.30 equivalents) were added to a microwave vial containing *tert*-butanol (5 mL). To this, was added

5-bromo-2-chloropyrimidine (1.29 mmol, 1.00 equivalent). The microwave vial was sealed and stirred at 150 °C for 30 minutes. The orange-brown reaction mixture was then concentrated under reduced pressure and purified by flash column chromatography, eluting with 0 – 7% MeOH/DCM to afford the desired products described below.
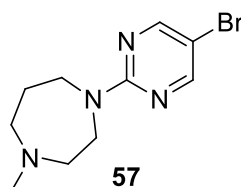
5-Bromo-2-(4-methylpiperazin-1-yl)pyrimidine (56)

56
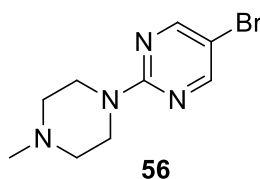
Relevant amine: *N*-methylpiperazine (0.172 mL, 1.55 mmol, 1.20 equivalents). The desired product was obtained as an off-white solid in 67% yield (0.221 g, 0.859 mmol).

TLC (5% MeOH/DCM): R_f = 0.31. **^{1}H NMR (500 MHz, DMSO-d_6) δ** 8.51 (s, 2H), 3.82 (br s, 4H), 2.78 (br s, 4H), 2.48 (br s, 3H, buried under DMSO-d_6 peak). **LC-MS** found $[M+H]^{2+}$ = 258.02; calculated $[M+H]^+$ = 258.04 *m/z* for $C_9H_{13}BrN_4$.

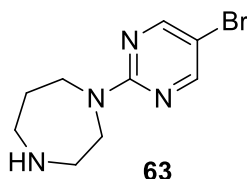## 1-(5-Bromopyrimidin-2-yl)-4-methyl-1,4-diazepane (57)

57

Relevant amine: 1-(5-bromopyrimidin-2-yl)4-methyl-1,4-diazepane (0.192 mL, 1.55 mmol, 1.20 equivalents). The desired product was obtained as an off-white solid in 50% yield (0.176 g, 0.647 mmol).

TLC (5% MeOH/DCM): R_f = 0.31. **^{1}H NMR (500 MHz, DMSO-d_6) δ** 8.45 (s, 2H), 3.87 (br s, 2H), 3.71 – 3.69 (m, 2H), 3.07 – 2.93 (m, 4H), 2.53 – 2.50 (m, 3H), 2.02 (br s, 2H). **LC-MS** found $[M+H]^+$ = 272.10 *m/z*; calculated $[M+H]^+$ = 272.05 *m/z* for $C_{10}H_{15}BrN_4$.

Tert-butyl-5-(5-bromopyrimidin-2-yl)-1,4-diazepane-1-carboxylate (62)
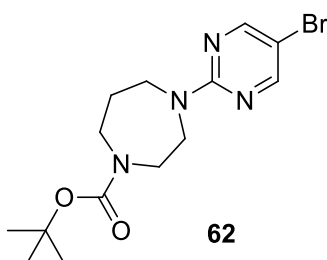
Relevant amine: tert-butyl-1,4-diazepane-1-carboxylate (1.2 mL, 6.2 mmol, 1.2 equivalents). The desired product was obtained as a white powder in 84% yield (1.56 g, 4.36 mmol).

TLC (5% MeOH/DCM): R_f = 0.62. **^{1}H NMR (500 MHz, CDCl$_3$) δ** 8.29 (s, 2H), 3.86 – 3.81 (m, 2H), 3.75 – 3.71 (m, 2H), 3.55 – 3.53 (m, 2H), 3.38 – 3.36 (m, 2H), 3.28 – 3.26 (m, 2H), 1.42 (s, 9H). **LC-MS** found [M+H]$^+$ = 358.11 *m/z*; calculated [M+H]$^+$ = 358.08 *m/z* for C$_{14}$H$_{21}$BrN$_4$O$_2$.
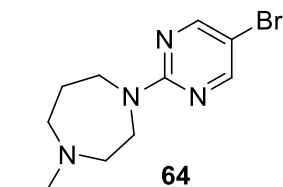
1-(5-Bromopyrimidin-2-yl)-1,4-diazepane (63)

Tert-butyl-5-(5-bromopyrimidin-2-yl)-1,4-diazepane-1-carboxylate (**62**) (1.50 g, 4.20 mmol) was dissolved in a 4.0 M HCl solution in dioxane (11.0 mL) and stirred at room temperature overnight. The milky-white precipitate was filtered off using a Buchner funnel and washed with dioxane (2 × 20 mL). The sticky solid was then dissolved in a minimum amount of distilled water (10 – 15 mL) and basified using a saturated solution of sodium bicarbonate until a pH of 7 – 8 was obtained (about 20 mL). The product was extracted with DCM (5 × 20 mL). The organic layers were combined, washed once with brine (20 mL), dried over anhydrous MgSO$_4$, filtered, and the filtrate concentrated under reduced pressure to yield the desired product as a pale yellow powder in 76% yield (0.824 g, 3.20 mmol). No further purification was necessary.

TLC (5% MeOH/DCM): R_f = 0.16. **^{1}H NMR (500 MHz, CDCl$_3$) δ** 8.28 (s, 2H), 3.83 – 3.90 (m, 4H), 3.03 – 3.01 (m, 2H), 2.88 – 2.86 (m, 2H), 2.16 (br. s., 1H), 1.91 – 1.86 (m, 2H). **LC-MS** found [M+H]$^+$ = 257.10 *m/z*; calculated [M+H]$^+$ = 257.03 *m/z* for C$_9$H$_{13}$BrN$_4$.

Addendum A: Synthesis of quinoline derivatives as antischistosomal agents


General procedure for alkylation of the amino group:

The appropriate secondary amine was dissolved in MeOH (5 mL). To this was added DIPEA (8.0 equivalents) and alkyl halide (5.0 equivalents). The reaction was allowed to stir at room temperature for 48 hours. Upon reaction completion, the mixture was concentrated under reduced pressure and then diluted with DCM (50 mL). The solution was washed with a saturated solution of sodium bicarbonate (1 × 50 mL) and the product was extracted with DCM (2 × 30 mL). The organic layers were combined, dried over anhydrous $MgSO_4$, filtered and the filtrate concentrated under reduced pressure to give the desired product. No further purification was necessary.

1-(5-Bromopyrimidin-2-yl)-4-ethyl-1,4-diazepane (64)

Appropriate secondary amine: 1-(5-bromopyrimidin-2-yl)-1,4-diazepane (**63**) (0.248 g, 0.964 mmol, 1.00 equivalent). Alkyl halide: iodoethane (0.4 mL, 5 mmol, 5 equivalents). Desired product was obtained as a pale yellow powder in 76% yield (0.210 g, 0.738 mmol).

TLC (5% MeOH/DCM): R_f = 0.21. **^{1}H NMR (500 MHz, CDCl$_3$) δ** 8.28 (s, 2H), 3.87 – 3.85 (m, 2H), 3.77 (t, *J* = 6.4 Hz, 2H), 2.75 – 2.73 (m, 2H), 2.61 – 2.60 (m, 2H), 2.56 (q, *J* = 7.2 Hz, 2H), 1.98 – 1.94 (m, 2H), 1.07 (t, *J* = 7.2 Hz, 3H). **LC-MS** found $[M+H]^+$ = 286.17 *m/z*; calculated $[M+H]^+$ = 286.06 *m/z* for $C_{11}H_{17}BrN_4$.

1-(5-Bromopyrimidin-2-yl)-4-propyl-1,4-diazepane (65)
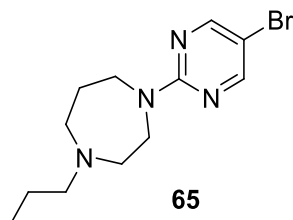
Appropriate secondary amine: 1-(5-bromopyrimidin-2-yl)-1,4-diazepane (0.300 g, 1.17 mmol, 1.00 equivalent). Alkyl halide: iodopropane (0.6 mL, 6 mmol, 5 equivalents). Desired product was obtained as a pale yellow powder in 79% yield (0.278 g).

TLC (5% MeOH/DCM): R_f = 0.31. **^{1}H NMR (500 MHz, CDCl$_3$) δ** 8.27 (s, 2H), 3.90 – 3.88 (m, 2H), 3.77 (t, *J* = 6.4 Hz, 2H), 2.81 – 2.80 (m, 2H), 2.70 – 2.67 (m, 2H), 2.51 – 2.48 (m, 2H), 2.02 (td, *J* = 11.1, 5.9 Hz, 2H), 1.58 – 1.51 (m, 2H), 0.89 (t, *J* = 7.3 Hz, 3H). **LC-MS** found [M+H]$^+$ = 299.11 *m/z*; calculated [M+H]$^+$ = 299.08 *m/z* for C$_{12}$H$_{19}$BrN$_4$.

General procedure for the Suzuki-Miyaura reaction between 7-bromo-8-methyl-N-(pyrazine-2-yl)quinoline-4-amine and the relevant tail compound:

The relevant bromopyrimidine derivative (1.0 equivalent) was added to a microwave vial that had been evacuated and filled with nitrogen three times. Anhydrous dioxane (2.8 mL) was then added, followed by bis(pinacolato)diboron (1.5 equivalents), KOAc (3.5 equivalents) and PdCl$_2$(dppf)·CH$_2$Cl$_2$ (5 mol%). The reaction mixture was degassed with nitrogen for 10 minutes, after which the vial was placed in the microwave for 1 hour at 145 °C. LC-MS confirmed the completion of the reaction as well as the formation of the desired product. The dark brown reaction mixture was then filtered through Celite, concentrated under reduced pressure and used directly in the next reaction without further purification.

The crude boronate compound was then dissolved in 3:1 dioxane/water (3.1 mL) in a microwave vial. K$_2$CO$_3$ (3.00 equivalents) and 7-bromo-8-methyl-*N*-(pyrazine-2-yl)quinoline-4-amine (**55**) (1.00 equivalent) were then added and the reaction mixture degassed for 10 minutes with nitrogen gas. PdCl$_2$(dppf)·CH$_2$Cl$_2$ (10 mol%) was then added and the mixture stirred in the microwave for 40 minutes at 130 °C. LC-MS confirmed the completion of the reaction and that the desired product had formed. The reaction mixture was then filtered through Celite, concentrated under reduced pressure and purified by flash column chromatography, eluting with 1 – 50% (MeOH + 5% NH$_4$OH)/EtOAc. A second purification using preparative HPLC was performed, eluting with 5 – 70% MeCN/H$_2$O.

8-Methyl-7-[2-(4-methylpiperazine-1-yl)pyrimidin-5-yl]-*N*-(pyrazine-2-yl)quinoline-4-amine (NEU2215)

NEU2215
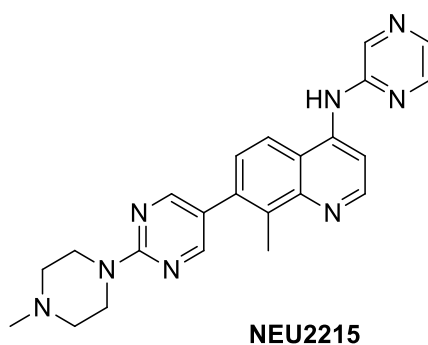
Tail compound used: 5-bromo-2-(piperazin-1-yl)pyrimidine (**56**) (0.070 g, 0.27 mmol, 1.0 equivalent). Desired product was obtained as a pale yellow powder in 31% yield (0.028 g, 0.067 mmol).

TLC (10% (MeOH + 5% NH$_4$OH)/EtOAc): R$_f$ = 0.47. **^{1}H NMR (500 MHz, CD$_3$OD) δ** 8.71 (d, *J* = 5.6 Hz, 1H), 8.61 (s, 1H), 8.50 (s, 2H), 8.47 (d, *J* = 5.6 Hz, 1H), 8.34 – 8.33 (m, 2H), 8.17 (s, 1H), 7.51 (d, *J* = 8.8 Hz, 1H), 4.14 – 4.09 (m, 4H), 3.14 (t, *J* = 5.0 Hz, 4H), 2.78 (s, 3H), 2.69 (s, 3H). **^{13}C NMR (150 MHz, CD$_3$OD) δ** 161.6, 159.3, 153.4, 150.6, 148.3, 146.7, 142.9, 137.8, 137.5, 137.4, 134.9, 128.8, 125.7, 121.4, 120.6, 108.8, 55.1, 44.9, 43.4, 15.9 **LC-MS** found [M+H]$^+$ = 413.81 *m/z*; calculated [M+H]$^+$ = 413.21 *m/z* for C$_{23}$H$_{24}$N$_8$.

8-Methyl-7-[2-(4-methyl-1,4-diazepan-1yl)pyrimidin-5-yl]-*N*-(pyrazine-2-yl)quinoline-4-amine (46a)
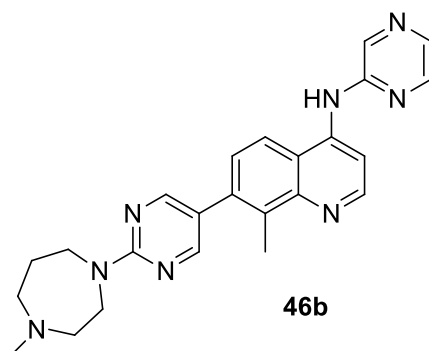

46a
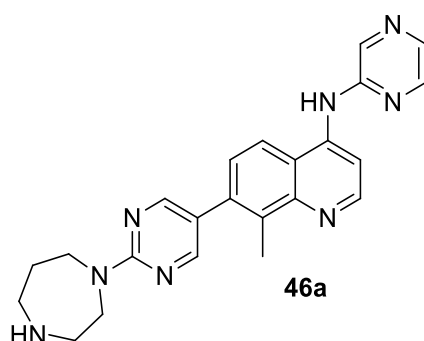
Tail compound used: 1-(5-bromopyrimidin-2-yl)-1,4-diazepane (**63**) (0.085 g, 0.33 mmol, 1.0 equivalent). Desired product was obtained as a pale yellow-brown powder in 19% yield (0.020 g, 0.051 mmol).

TLC (30% (MeOH + 5% NH$_4$OH)/EtOAc): R$_f$ = 0.65. **^{1}H NMR (500 MHz, DMSO-*d$_6$*) δ** 8.75 – 8.74 (m, 1H), 8.67 – 8.66 (m, 1H), 8.49 (s, 2H), 8.37 – 8.36 (m, 2H), 8.28 – 8.25 (m, 1H), 8.13 – 8.10 (m, 1H), 7.50 – 7.47 (m, 1H), 3.95 – 3.91 (m, 2H), 3.91 – 3.86 (m, 2H), 3.71 (s, 4H), 3.10 – 3.06 (m, 2H),

2.97 – 3.92 (m, 2H), 2.69 (s, 3H), 1.96 – 1.90 (m, 2H). **¹³C NMR (150 MHz, CD₃OD) δ** 161.5, 159.5, 153.7, 151.1, 149.1, 146.2, 143.0, 137.6, 137.48, 137.3, 135.4, 128.8, 125.7, 121.6, 120.7, 109.1, 47.1, 46.7, 46.7, 44.8, 27.2, 16.2. **LC-MS** found [M+H]⁺ = 413.20 *m/z*; calculated [M+H]⁺ = 413.21 *m/z* for C₂₃H₂₄N₈.

8-Methyl-7-[2-(4-methyl-1,4-diazepan-1yl)pyrimidin-5-yl]-*N*-(pyrazine-2-yl)quinoline-4-amine (46b)

46b

Tail compound used: 1-(5-bromopyrimidin-2-yl)-4-methyl-1,4-diazepane (**57**) (0.070 g, 0.26 mmol, 1.0 equivalent). Desired product was obtained as a pale yellow-brown powder in 25% yield (0.023 g, 0.052 mmol).

TLC (10% (MeOH + 5% NH₄OH)/EtOAc): R_f = 0.34. **¹H NMR (500 MHz, CD₃OD) δ** 8.72 (d, *J* = 5.4 Hz, 1H), 8.58 (s, 1H), 8.48 (s, 2H), 8.42 (d, *J* = 5.4 Hz, 1H), 8.32 (s, 1H), 8.29 (d, *J* = 8.8 Hz, 1H), 8.12 (s, 1H), 7.48 (d, *J* = 8.8 Hz, 1H), 4.15 – 4.13 (m, 2H), 3.98 (t, *J* = 6.2 Hz, 2H), 2.81 (s, 3H), 2.71 (s, 3H), 2.24 (br. s., 2H), 1.19 (s, 3H). **¹³C NMR (150 MHz, CD₃OD) δ** 161.7, 159.4, 153.8, 151.2, 149.2, 146.2, 143.0, 137.63, 137.4, 137.3, 135.5, 128.8, 125.3, 121.6, 120.7, 109.2, 58.6, 57.8, 46.6, 45.9, 44.71, 27.0, 16.2. **LC-MS** found [M+H]⁺ = 427.20 *m/z*; calculated [M+H]⁺ = 427.23 *m/z* for C₂₄H₂₆N₈.

8-Methyl-7-[2-(4-propyl-1,4-diazepan-1yl)pyrimidin-5-yl]-*N*-(pyrazine-2-yl)quinoline-4-amine (46d)
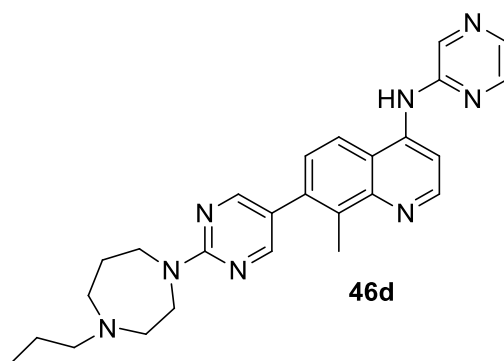
Tail compound used: 1-(5-bromopyrimidin-2-yl)-4-propyl-1,4-diazepane (**65**) (0.090 g, 0.30 mmol, 1.0 equivalent). Desired product was obtained as a pale yellow powder in 7% yield (0.008 g, 0.002 mmol).

TLC (20% (MeOH + 5% NH$_4$OH)/EtOAc): R$_f$ = 0.58. **^{1}H NMR (500 MHz, CD$_3$OD) δ** 8.69 (d, *J* = 5.4 Hz, 1H), 8.56 (s, 1H), 8.44 (s, 2H), 8.39 (d, *J* = 4.9 Hz, 1H), 8.31 – 8.29 (m, 1H), 8.25 (d, *J* = 8.8 Hz, 1H), 8.11 (d, *J* = 2.9 Hz, 1H), 7.44 (d, *J* = 8.8 Hz, 1H), 4.14 – 4.10 (m, 2H), 3.95 (t, *J* = 6.4 Hz, 2H), 3.26 (d, *J* = 3.9 Hz, 2H), 3.20 – 3.15 (m, 2H), 2.93 – 2.88 (m, 2H), 2.68 (s, 3H), 2.66 (s, 5H), 2.22 – 2.16 (m, 2H), 1.75 – 1.67 (m, 2H), 0.98 (t, *J* = 7.3 Hz, 3H). Insufficient material was obtained to carry out the ^{13}C NMR analysis. **LC-MS** found [M+H]$^+$ = 455.23 *m/z*; calculated [M+H]$^+$ = 455.26 *m/z* for C$_{26}$H$_{30}$N$_8$.

A.7 REFERENCES

(1)   World Health Organisation. *Neglected Tropical Diseases*; Available at: http://www.who.int/neglected_diseases/diseases/en/ (accessed 10 October 2018).

(2)   Devine, W.; Woodring, J. L.; Swaminathan, U.; Amata, E.; Patel, G.; Erath, J.; Roncal, N. E.; Lee, P. J.; Leed, S. E.; Rodriguez, A.; Mensa-Wilmot, K.; Sciotti, R. J.; Pollastri, M. P. *J. Med. Chem.* **2015**, *58* (14), 5522–5537.

(3)   Patel, G.; Karver, C. E.; Behera, R.; Guyett, P. J.; Sullenberger, C.; Edwards, P.; Roncal, N. E.; Mensa-Wilmot, K.; Pollastri, M. P. *J. Med. Chem.* **2013**, *56* (10), 3820–3832.

(4)   Woodring, J. L.; Patel, G.; Erath, J.; Behera, R.; Lee, P. J.; Leed, S. E.; Rodriguez, A.; Sciotti, R. J.; Mensa-Wilmot, K.; Pollastri, M. P. *MedChemComm* **2015**, *6* (2), 339–346.

(5)   World Health Organisation. *Global technical strategy for malaria 2016-2030*; Available at: http://www.who.int/malaria/publications/atoz/9789241564991/en/ (accessed 26 August 2018).

(6)   World Health Organisation. *World Malaria Report 2017*; Available at: http://apps.who.int/iris/discover?query=world+malaria+report+2017 (accessed 26 August 2018).

(7)   Mehta, N.; Ferrins, L.; Leed, S. E.; Sciotti, R. J.; Pollastri, M. P. *ACS Infect. Dis.* **2018**, *4* (4), 577–591.

(8)   World Health Organisation. *Schistosomiasis*; Available at: http://www.who.int/schistosomiasis/epidemiology/table/en/ (accessed 10 October 2018).

(9)   Beckmann, S.; Leutner, S.; Gouignard, N.; Dissous, C.; Grevelding, C. G. *Curr. Pharm. Des.* **2012**, *18* (24), 3579–3594.

(10)   Centres for Disease Control and Prevention. *Schistosomiasis life cycle;* Available at: https://www.cdc.gov/parasites/schistosomiasis/biology.html (accessed 10 October 2018).

(11)   Dömling, A.; Khoury, K. *ChemMedChem* **2010**, *5* (9), 1420–1421.

(12)   Okombo, J.; Singh, K.; Mayoka, G.; Ndubi, F.; Barnard, L.; Njogu, P. M.; Njoroge, M.; Gibhard, L.; Brunschwig, C.; Vargas, M.; Keiser, J.; Egan, T. J.; Chibale, K. *ACS Infect. Dis.* **2017**, *3* (6), 411–420.

(13)   Xiao, S. hua; Sun, J. *Int. J. Parasitol.* **2017**, *47* (4), 171–183.

(14)   Chen, M. M.; Shi, L.; Sullivan, D. J. *Mol. Biochem. Parasitol.* **2001**, *113* (1), 1–8.

(15)   Oliveira, M. F.; d'Avila, J. C. P.; Tempone, A. J.; Corrêa Soares, J. B. R.; Rumjanek, F. D.; Ferreira-Pereira, A.; Ferreira, S. T.; Oliveira, P. L. *J. Infect. Dis.* **2004**, *190* (4), 843–852.

(16)   Moraes, J. de. *Future Med. Chem.* **2016**, *7* (6), 801–820.

(17)   Hess, J.; Keiser, J.; Gasser, G. *Future Med. Chem.* **2015**, *7* (6), 821–830.

(18)   Keiser, J.; Utzinger, J. *Curr. Pharm. Des.* **2012**, *18*, 3531–3538.

(19)   Bachovchin, K. A.; Sharma, A.; Bag, S.; Klug, D.; Schneider, K. M.; Singh, B.; Jalani, H. B.; Buskes, M. J.; Metha, N.; Tanghe, S.; Momper, J. D.; Sciotti, R. J.; Rodriguez, A.; Mensa-Wilmot, K.; Pollastri, M. P.; Ferrins, L. *Manuscript under revision.*

(20)   Long, T.; Neitz, R. J.; Beasley, R.; Kalyanaraman, C.; Suzuki, B. M.; Jacobson, M. P.; Dissous,

C.; McKerrow, J. H.; Drewry, D. H.; Zuercher, W. J.; Singh, R.; Caffrey, C. R. *PLoS Negl. Trop. Dis.* **2016**, *10* (1), 1–21.

(21)   Bogitsh, B. J.; Davenport, G. R. *J. Parasitol.* **1991**, *77* (2), 187–193.

(22)   Woodring, J. L.; Bachovchin, K. A.; Brady, K. G.; Gallerstein, M. F.; Erath, J.; Tanghe, S.; Leed, S. E.; Rodriguez, A.; Mensa-Wilmot, K.; Sciotti, R. J.; Pollastri, M. P. *Eur. J. Med. Chem.* **2017**, *141*, 446–459.